The Design and Evaluation of a Microfluidic Cell Sorting Chip

by

Jay Kendall Taylor

A thesis
presented to the University of Waterloo
in fulfillment of the
thesis requirement for the degree of
Master of Applied Science
in
Mechanical Engineering

Waterloo, Ontario, Canada, 2007

Author's Declaration

I hereby declare that I am the sole author of this thesis. This is a true copy of the thesis, including any required final revisions, as accepted by my examiners.

I understand that my thesis may be made electronically available to the public.

Abstract

Many applications for the analysis and processing of biological materials require the enrichment of cell subpopulations. Conventional cell sorting systems are large and expensive with complex equipment that necessitates specialized personnel for operation. Employing microfluidics technology for lab-on-a-chip adaptation of these devices provides several benefits: improved transport control, reduced sample volumes, simplicity of operation, portability, greater accessibility, and reduced cost. The designs of microfluidic cell sorting chips vary widely in literature; evaluation and optimization efforts are rarely reported. This study intends to investigate the primary components of the design to understand the effect of various parameters and to improve the performance of the microfluidic chip. Optimized individual elements are incorporated into a proposed cell sorter chip with the ability to dynamically sort target cells from a non-homogeneous solution using electrical driving forces.

Numerical and experimental results are used to evaluate the sample focusing element for controlled cell dispensing, the sorting configuration for target cell collection, and the flow elements for reduced pressure effects and prevention of flow blockages. Compact models are adapted to solve the potential field and flow field in the chip and to predict the focused sample stream width. A commercial CFD package is used to perform 2-D simulations of the potential, velocity, and concentration fields. A fluorescence microscopy visualization system is implemented to conduct experiments on several generations of chip designs. The data from sample focusing experiments, performed with fluorescent dye samples, is analyzed using a Gaussian distribution model proposed in this work. A technique for real-time monitoring of fluorescent microspheres in the microfluidic chip enables the use of dynamic cell sorting to emulate fully autonomous operation. The performance values obtained from these experiments are used to characterize the various design configurations.

Sample focusing is shown to depend largely on the relative size of the sheath fluid channel and the sample channel, but is virtually independent of the junction shape. Savings in the applied potential can be achieved by utilizing the size dependency. The focusing performance also provides information for optimizing the widths of the channels relative to the cell size. Successful sorting of desired cells is demonstrated for several designs. Key parameters that affect the sorting performance are discussed; a design employing the use of supplemental fluid streams to direct the particle during collection is chosen due to a high sorting evaluation and a low sensitivity to flow anomalies. The

necessary reduction of pressure influences to achieve reliable flow conditions is accomplished by introducing channel constrictions to increase the hydrodynamic resistance. Also, prolonged operation is realized by including particle filters in the proposed design to prevent blockages caused by the accumulation of larger particles.

A greater understanding of the behaviour of various components is demonstrated and a design is presented that incorporates the elements with the best performance. The capability of the microfluidic chip is summarized based on experimental results of the tested designs and theoretical cell sorting relationships. Adaptation of this chip to a stand-alone, autonomous device can be accomplished by integrating an optical detection system and further miniaturization of the critical components.

Acknowledgements

I would like to offer my sincere gratitude to my supervisor, Prof. Carolyn Ren, from whom I learned immensely during my studies. Her support and encouragement helped me reach my educational goals and are truly appreciated.

The collected and insightful advice imparted by Prof. Gordon Stubley will be carried through many facets of my future. I would like to thank him for his assistance and his dedication to enhancing the learning experience for all students.

The knowledge and efforts of my colleagues in the Microfluidics and Biochip Research Group provided a resource that was valuable for successful completion of this project. In particular, Tom Glawdel, Razim Samy, and Dr. Lin Gui are thanked for their contributions in creating a successful research facility.

I would like to thank Arthur F. Church for his financial support through a Graduate Scholarship. Also, support provided by the Ontario government through the Ontario Graduate Scholarship in Science and Technology (OGSST) Program is gratefully acknowledged.

The loving support of my family and friends can not be underestimated. These individuals provide the fun and enjoyment essential for a balanced and healthy life. I'd like to extend a special thank you to Brian Taylor, Glennis Taylor, Tierre Taylor, Andrew Pettersen, Tyler Davis, Marc Maistrelli, Jill Osborne, and Meta Zylicz.

Table of Contents

List of Figures

List of Tables

Nomenclature

Acronyms:

CCD	Charged Coupled Device
CFD	Computational Fluid Dynamics
CTC	Circulating Tumor Cell
DI	De-Ionized
DPI	Dots Per Inch
E. coli	*Escherichia coli*
EDL	Electrical Double Layer
FACS	Fluorescence-Activated Cell Sorter
FWHM	Full-Width at Half-Maximum
HV	High-Voltage
LED	Light Emitting Diode
MEMS	Micro Electro-Mechanical Systems
NA	Numerical Aperture
PCR	Polymerase Chain Reaction
PEB	Post Exposure Bake
PMT	Photo-Multiplier Tube
PDMS	Poly (dimethylsiloxane)
µAPD	Micro Avalanche Photo Diode
µFACS	Micro Fluorescence-Activated Cell Sorter
µPIV	Micro Particle Image Velocimetry
µTAS	Micro Total Analysis System

Mathematical Symbols:

A_c	Channel cross-sectional area
c_i	Molar concentration of the i^{th} species
$c_4^{\max}$	Maximum concentration at outlet section 4
C_d	Drag coefficient
d	Focused sample stream width
d_p	Particle diameter
D	Diffusion coefficient of ions in EDL
D_i	Diffusion coefficient of species i
e	Magnitude of a proton or electron charge (e = 1.602 x 10^{-19} C)

$\boldsymbol{E}$, $\vec{E}$	Electric field vector
E_x, E_y, E_z	Electric field strength in x-, y-, and z-directions
E	Sorting efficiency
$f_1(\kappa a)$	Electrophoretic mobility shape correction factor
h, H	Channel height
k	Thermal conductivity
k_b	Boltzmann constant (k_b = 1.381 x 10^{-23} m^2kg/s^2K)
k_d	Shape factor for drag coefficient
ℓ_τ	Length scale
L	Channel length
$\dot{m}_i$	Mass flow through section i
n	Index of refraction
$n_{i\infty}$	Bulk ionic concentration of the i^{th} species
p	Pressure
P	Purity of enriched sample
Pe	Peclet number
q	Particle charge
Q	Volumetric flow rate
r	Particle arrival rate
$r_{\max}$	Maximum particle arrival rate
r_m	Radius of meniscus
R	Rate of sorting
$R_{\max}$	Maximum rate of sorting
R_p	Particle radius
$R_{reservoir}$	Reservoir radius
R_{hyd}	Hydrodynamic resistance of microchannel
R_V	Electrical resistance of microchannel
R_i	Volumetric rate of generation of the i^{th} species by reaction
Re	Reynolds number
s	Target cell fraction
T_{abs}	Absolute temperature
T	Time required to perform a sorting event
$\boldsymbol{u}$, $\vec{u}$	Fluid velocity vector
$\overline{u}$, $\overline{u}_{ave}$	Average velocity
u_{eof}	Helmholtz-Smoluchowski velocity
u_{ep}	Electrophoretic velocity
u_{obs}	Observed velocity
u_{slip}	Slip velocity

v_f	Relative velocity of the particle in the bulk fluid
v_p	Particle velocity
$\bar{v}_i$	Average velocity in channel *i*
V_∞	Bulk fluid velocity
V_p	Particle volume
w, W	Channel width
z_i	Valence of ion
ε	Dielectric permittivity of fluid
ε_r	Dielectric constant
ε_0	Permittivity of a vacuum (ε_0 = 8.854 x 10^{-12} C/Vm)
ε_c	Channel aspect ratio
ϕ	Electric potential
ϕ_{foc}	Electric focusing potential ratio ($\phi_{foc} = \phi_{sheath} / \phi_{sample}$)
γ	Surface tension
η	Ratio of sheath channel width to sample channel width ($\eta = W_{sheath} / W_{sample}$)
κa	Ratio of particle radius to Debye-Huckel length
λ_D	Debye-Huckel parameter
μ	Dynamic viscosity of fluid
μ_{eof}	Electroosmotic mobility
μ_{ep}	Electrophoretic mobility
μ_{obs}	Observed mobility
θ	Half-cone angle of light
θ_{ca}	Contact angle at fluid-solid interface
ρ	Mass density of fluid
ρ_p	Particle mass density
ρ_e	Net charge density
σ	Electrical conductivity of solution (Chapters 2 & 4)
σ	Standard deviation of concentration profile curve (Chapter 6)
τ	Time constant of particle acceleration
ψ	Electrostatic potential due to surface charge
ζ	Zeta potential

Chapter 1

Introduction

1.1 Background

Devices for the analysis of biological materials and the generation of chemicals have widespread importance in the field of life sciences. The conventional systems used to accomplish these tasks have limited accessibility due to the complexity of the equipment, which often requires specialists to operate, and due to the subsequent high cost. With the burden on health care increasing and inadequate numbers of health-care professionals available, there is motivation to develop methods for point-of-care diagnosis or to improve the processing rate of current analysis techniques. Microfluidics, taking advantage of microfabrication advancements in the microelectronics and micro electro-mechanical systems (MEMS) industries, has the potential to change the landscape of drug discovery, drug delivery, clinical diagnostics, genetics research, bioweapons detection, and immunology [Fitzgerald (2002)].

The miniaturization of bio-analysis systems has several benefits, which have fueled a recent surge in exposure and research efforts. The life sciences component of microfluidics technology was estimated to be 640 million US dollars at the time of a 2002 market study and growth was projected to 1.8 billion US dollars by 2008 [Ducre and Zengerle (2004)]. Microfluidics research is developing more convenient devices by modernizing existing sample transport and detection systems with new technologies that can perform at higher efficiencies. The platform for miniaturization starts with the basic microfluidic chip which consists of a network of microchannels connecting a series of fluid reservoirs. An example of a simple microfluidic chip, with a cross configuration, is illustrated in Figure 1.1. Various components located in the chip are used to perform a specific task, such as mixing, reacting, sample separating, or heating. Integrating one or more microfluidic elements with miniaturized sensors, on-chip analysis tools, and automated control units is referred to as a lab-on-a-chip device or micro total analysis system (μTAS).

It is possible to achieve unprecedented levels of mass and heat transfer control and improved analysis sensitivity by reducing the size of the structures transporting biomaterials to the scale of the sample. Reducing the characteristic length scale changes the time scale, resulting in drastic reductions

in mixing, reaction, and processing times for many operations. Faster diagnosis allows higher sample throughput and quicker medical intervention. Also, different physical behaviour at the microscale permits multiple methods for driving fluids or manipulating particles: pressure forces, electric fields, magnetic fields, capillary forces, centrifugal forces, and optical forces. Pressure forces and electric fields are two commonly used pumping methods in the application of microfluidics.

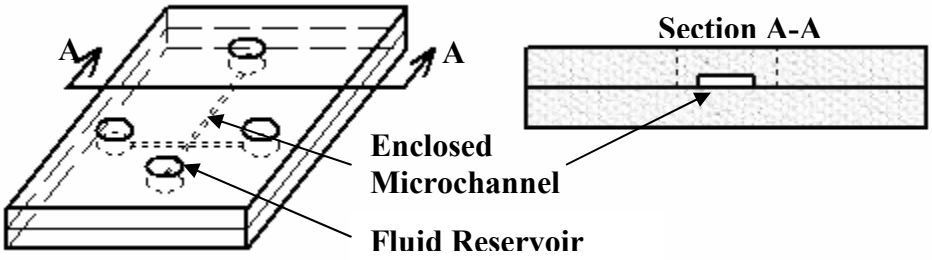

Figure 1.1 Schematic of a microfluidic chip with a cross-microchannel configuration.

In addition to the miniaturization of the fluid transport network, replacing expensive and large optical detection systems with small solid state optics minimizes the size and weight of the entire system and enables portability of the devices. Portable operation facilitates point-of-care diagnostics, which is important for applications such as the detection of bacteria in food samples or the discovery of biological warfare materials.

The modification of conventional lithographic methods of silicon micromachining for fast, cost effective, and less stringent fabrication of microfluidic chips was a key development [Xia and Whitesides (1998)]. The ability to rapidly fabricate disposable, biocompatible devices has facilitated the experimental studies that have been improving the functionality and complexity of lab-on-a-chip devices for the last 10 years.

The cell cytometer is the device most commonly used to characterize cell populations by single cell analysis methods and can be combined with a sorting component, fluorescence-activated cell sorter (FACS), to enrich selected subpopulations [Herzenberg et al. (2002)]. This system can analyze multiple physical properties of individual cells and determine levels of intracellular components, such as proteins, DNA, and RNA. The FACS is a complex system with multiple laser light sources and fluid handling mechanisms; most units require specially trained individuals to operate.

Research in microfluidic cell cytometry systems has demonstrated the ability to perform cell characterization and several micro fluorescence-activated cell sorters (μFACS) have been fabricated

and tested. Reports indicate potential in the development of μFACS devices and full integration into lab-on-a-chip devices. The use of a cell sorting element will be critical in many lab-on-a-chip devices, where cell detection or population enrichment is required prior to analysis.

This area of research is still relatively young and there are opportunities to advance the collective knowledge of microfluidic phenomena and improve the efficiency, reliability, and the capacity for miniaturization through experimental and numerical studies.

1.2 Justification of Research

Several variations of microfluidic cell sorters, implementing different sorting mechanisms, have been designed and fabricated [Fu et al. (1999), Takahashi et al. (2004), Wang et al. (2005)]. The choice of the sorting style depends on the specific application. Certain cells have characteristics that enable the use of unconventional techniques, such as magnetic fields, to achieve cell enrichment. The most common sorting technique is fluidic switching, where the path of the sample stream is directed into the desired channel for collection. Successful operation of such chips has been reported, however, there are a few concerns to be further addressed. First, the evaluation of the microfluidic chip designs has not been thoroughly described. Second, the electrokinetic cell sorter designs are not optimized for flow control or miniaturization. Higher efficiencies in cell enrichment can still be achieved by improvements to the function, speed, and accuracy of the sorting mechanisms, sensitivity of the cell detection, and controlling functions. A reduction in the required applied potential is important to achieve handheld operation; analyses of the various fluid components can provide means to accomplish this goal. There are also opportunities to improve the reliability and robustness of the chips.

Preliminary evaluations of the design components can be performed by using numerical models and simulations that predict the applied electric field which influences the flow field, the flow field of the bulk liquid and the sample, and the concentration field of the sample. These simulations provide guidelines for the operating conditions required to achieve the correct cell transport. The selected chip designs, based on the numerical analyses, can be investigated by experimental methods. Fluorescence-based flow visualization gives insight into the flow fields generated in the microchannels. Using fluorescent microparticles during cell sorter operation provides quantitative results of the performance and the limitations of the system. Experiments are essential in the iterative design process because many factors that influence microfluidic chip operation are difficult to

represent in numerical simulations. Implementing measures to minimize these uncertainties is a major challenge facing lab-on-a-chip developments.

With an effective microfluidic cell sorter design, an optical detection system can be integrated and fully autonomous operation of the device can be accomplished. Further miniaturization of the system components will allow incorporation into a lab-on-a-chip device or operation as a separate stand-alone unit.

1.3 Objectives of Thesis

The objective of this work is to design a microfluidic chip capable of dynamic sorting of bio-particles that can be applied towards the development of a fully autonomous lab-on-a-chip system. The primary fluidic components evaluated are the sample focusing cross-junction and the fluidic switching network for particle collection. Additional elements are implemented to minimize flow anomalies that occur during operation, such as induced pressure effects and disruptions from channel blockages. The criteria for design selection are based on improving the adaptability of the systems to hand-held operation and maximizing performance. Both experimental and numerical methods are used to compare design variations and improve upon designs reported in literature.

A system for fluorescence microscopy is developed and setup to characterize the flow field and monitor the sorting capability of the testing devices. Electrical force is employed as the driving mechanism for sample and buffer solution transport. Several generations of chip designs are fabricated using the in-house soft-lithography process and a custom glass chip, fabricated by wet chemical etching, was purchased (Micralyne, Alberta). The use of a commercial computational fluid dynamics (CFD) package, COMSOL Multiphysics, and custom models provide information to assist the development of the microfluidic chips.

The goals of this thesis are as follows:

1. Apply microfluidic theory to design a preliminary cell sorting device capable of counting, separating, and collecting various microparticles.
2. Conduct an iterative design process based on experimental and numerical analyses for various chip configurations.

3. Develop a model to determine the location of the focusing streamline, which separates the sample fluid and the focusing sheath fluids, from experimental cross-flow intensity profiles.
4. Investigate the effect of the focuser configuration and the sheath and sample channel widths on the focused sample stream width using a combination of experimental and numerical results.
5. Perform dynamic cell sorting to investigate the performance of various chip designs. Evaluate the designs and identify the final operating capabilities of each microfluidic cell sorting chip.
6. Present a proposed final design incorporating features selected based on the evaluation criteria.

An overview of the fundamental microfluidic concepts and their application to bio-analytical devices is presented in Chapter 2. The benefits of miniaturization of existing systems and the results of changing the characteristic scales are discussed. Key transport equations for electroosmotic flow are introduced along with electrophoretic effects of charged samples and the concentration field equations. The significance of cell cytometry and FACS systems is established and the major components of these devices are summarized. A review of the experimental and numerical developments in μFACS devices is presented. The review focuses on the three major components of fluidic switching microfluidic cell sorters: sample focusing, particle detection and analysis, and cell sorting.

In Chapter 3, the experimental setup designed for this project is described. Fluorescence flow visualization and the monitoring of cell sorting operation are performed on a fluorescence microscopy system.

In Chapter 4, the characteristics of the microfluidic system and the numerical models for simulating the momentum and mass transport are discussed. This includes the determination of electroosmotic mobility values for the working fluids using the current monitoring method and electrophoretic mobility of particles by individual tracking methods. The source of and influence of pressure differences are discussed. Lastly, circuit equivalency models for the potential field and flow field are developed and the COMSOL Multiphysics numerical models are described for solving the potential field, velocity field, and concentration field.

In Chapter 5, details of the chip design process are presented. A brief summary of the fabrication details of the two types of chips and the different attributes of each is included. The problems and solutions encountered during the design iteration are described and the key chip designs are introduced.

Chapters 6 and 7 define the criteria used to evaluate the focusing and sorting components of the chip, respectively. The numerical and experimental results are presented and conclusions are made regarding the recommended design of each component. Chapter 6 also features a model developed to determine the separating streamline between sheath and sample flows from experimental concentration profiles.

The final recommended design is described in Chapter 8. The various components incorporated in the design are summarized and the expected performance values, based on previous experimental results and predicted improvements, are presented.

In Chapter 9, a summary of this work is presented and recommendations for future developments are outlined. These recommendations pertain to further miniaturization of the chip and the next stages of experimentation.

Chapter 2

Literature Review

2.1 Introduction

Developing lab-on-a-chip systems for the purpose of miniaturization of bio-analysis and chemical synthesis devices requires a wide range of knowledge and understanding involving multiple disciplines: biology, chemical engineering, mechanical engineering, and electrical engineering. One of the major responsibilities of the mechanical engineer is the design and optimization of the components that constitute the system. Familiarity of the transport processes that occur at the microscale is necessary to design microfluidic chips that control the sample activity. Various benefits are encountered with the physical laws applied at the microscale, which differ significantly from macroscale behaviour. In addition to the advantages of transport processes, practical characteristics of lab-on-a-chip systems have provided significant motivation for further research and developments in this technology.

This chapter provides the background information necessary to understand the concepts involved in designing an electrokinetic driven microfluidic chip to perform a specific function; in this case cell sorting. The benefits of miniaturization of bio-medical devices are introduced. The basics of electrokinetic flow are discussed and the primary relationships and equations are provided. The function and major components of conventional cell cytometry and fluorescence-activated cell sorter systems are detailed. Finally, a summary of the numerical and experimental studies conducted in the development of microfluidic cell cytometry and cell sorting devices is presented.

2.2 Microfluidics for Biomedical Applications

Significant time is invested in numerous research fields to reduce the size of complex systems to reap benefits such as decreased material and space requirements, more efficient fabrication processes, lower costs, greater functionality, and any other advantages specific to the technology. While not every technology is suitable for miniaturization, the rapid progress achieved in reducing the scale in

the microelectronic and MEMS industries has created the opportunity to apply similar techniques to biological processing devices.

Many of the systems used for analyzing biological samples are large benchtop systems that incorporate a variety of sensors, laser light sources, complex fluid handling equipment, environment control systems, and bio-analysis tools. The cost of such equipment is usually high and the duration of performing multiple tests is relatively long. By reducing the size of the fluid networks to the microscale, where one or more dimension is 1 μm to 100 μm, the length scale of the channel becomes comparable to the size of the materials to be analyzed. This provides potential for improved sensitivity of the system, drastic reduction in the time scales of diffusion and reaction, and high throughput by means of parallelization [Dittrich and Manz (2006), Stone et al. (2004), Huh et al. (2005)].

Several advantages justify the replacement of large chemical synthesis and bio-analysis systems with lab-on-a-chip or micro total analysis systems. The size reduction of the overall system can permit handheld, portable operation. The volume of sample or reagents required for operation is decreased significantly. In circumstances where access to the sample is limited, forensic studies for example, volumetric savings may be critical. Cost and ease of manufacturing is improved by using microlithographic processes made popular in the microelectronics industry. Microscale systems also differ from macroscale in the dramatically increased surface to volume ratio [Ho and Tai (1998)]. This condition enables unprecedented levels of control of heat and mass transfer. Alternative methods of driving flow become viable in microfluidics; one popular technique is electroosmotic flow.

The development of lab-on-a-chip devices is currently in a transition from concept to application. There are opportunities to improve functions at the design level of many of the primary components. The microfluidic chip can achieve higher performance efficiencies and savings in the required operating power, whether it uses applied potentials or pressure sources. Issues of device contamination, flow anomalies, blockages, and altered surface properties are relevant and need to be investigated further. Despite the difficulties encountered and the industry's infancy, several lab-on-a-chip systems have been developed and are sold commercially. The GeneXpert, a DNA extraction and polymerase chain reaction (PCR) amplification system, developed by California-based Cepheid extracts DNA and RNA from blood samples or microbial spores for amplification and analysis. The reduced processing time for this device is 96-fold that of conventional systems [Clayton (2005)]. The BioMEMS-768 developed by GenoMEMS, the benchtop Experion assay system from BioRad

Laboratories, Agilent Technologies' 2100 BioAnalyzer, and Caliper Life Sciences' LabChip 90 device perform electrophoretic separation of protein, DNA, or RNA. The CytoChip, by CelTor Biosystems, is a drug analysis platform that simulates a precise biological environment. Invitrogen developed the PathAlert system which allows detection of infectious agents using PCR and analysis techniques. This device can be used to detect plague, anthrax, small pox, or tularemia pathogens. Benefits from the application of microfluidics are expected in pharmaceutical research, drug delivery systems, and biological engineering research in addition to the diagnostic and analysis devices described above [Fitzgerald (2002), Clayton (2005)]. Several reviews have been published that outline the major developments and applications for lab-on-a-chip technologies: Reyes et al. (2002), Vilkner et al. (2004), Erickson and Li (2004), Andersson and Van den Berg (2003), and Li (2006).

Fabrication of microfluidic chips applies lithography techniques established in microelectronics manufacturing [Elliot (1986)]. The standard photo-lithography method provides high resolution channel networks etched in silicon or glass which can be directly bonded to another silicon or glass layer to form an enclosed chip. Photo-lithography also can produce positive relief structures that function as a mould for soft polymer replication. Both types of micromachining are performed by exposing a thin layer of photo-sensitive material, called photoresist, on the silicon or glass substrate through a patterned photomask and developing the soluble portions of the photoresist coating. The remaining photoresist acts as a mask during the etching process. As a quicker and more cost effective alternative, the recently developed soft-lithography method allows the creation of a similar positive relief mould without the stringent clean room conditions [Xia and Whitesides (1998), McDonald et al. (2000)]. The primary difference is that no etching is required due to the use of the patterned photoresist as the relief structures. In the casting process, a liquid elastomer mixture is poured on the chip mould and cured to solidify the replica. The solid replica containing the channel features is then reversibly or irreversibly bonded to a substrate of glass, silicon, or a similar elastomer. The soft-lithography process is discussed further in Chapter 5.

Poly (dimethylsiloxane) (PDMS) is a common replicating material due to its transparent optical properties, bio-compatibility, ability to transfer sub-micron features, gas permeability, and elastomeric mechanical properties that provide flexible, watertight interconnects [Li (2006), Rolland et al. (2004), Quake and Scherer (2000)]. The main disadvantages of using PDMS, compared to glass or silicone, is the instability of surface properties over time [Ren et al. (2001), Choi and Yang

(2003)], hydrophobic surface characteristics in its untreated state, and typically lower fluid mobility values.

2.3 Microscale Transport Phenomena

Reducing the length scale of fluid systems has important effects on momentum, energy, and mass transport. A brief description of the flow in microsystems and the relevant relationships are described here; for full details refer to the fluid mechanics and transport phenomena texts from White (1999) and Bird et al. (1960), respectively. Texts available for microfluidic fundamentals and electrokinetic flow include Hunter (1981), Masliyah (1994), Li (2004), and Tabeling (2005).

The Reynolds number, Re, for most microfluidic applications is less than 1 and simplified forms of the Navier-Stokes equation are substantiated; Stokes' flow conditions are often satisfied. The characteristics of the strictly laminar flow regime alter the design process for microfluidic components, in particular micro-reactors and micro-mixers. Scaling down the size creates a surface force dominating environment. Surface forces, such as capillary and electrostatic forces, scale to the first or second order of the characteristic length while body forces, gravity and magnetic forces, scale to the third power [Ho and Tai (1998)]. According to the same principle, diffusion time and velocity time scale to the second power and first power of the length, respectively. The Peclet number (Pe) scales approximately to the first power; however, it isn't uncommon for a wide range of Pe values to be encountered in microfluidics, making generalizations about the relative advection and diffusion properties difficult.

Four principal methods are used for generating flow in microfluidic systems: 1. pressure force, 2. electroosmotic force, 3. centrifugal force, and 4. capillary force. Pressure driven flow is very common; the flow characteristics are well reported and predictable in the laminar regime. The fluid pumping is accomplished by external high-precision syringe pumps or by on-chip peristaltic [Fu et al. (2002)] or micro-pneumatic pumping [Yang et al. (2006)] techniques. Centrifugal force is rarely incorporated as the primary microfluidic flow technique due to the requirement for high-speed rotation. The Gyrolab microlaboratory developed by Gyros is an example of a device using this mechanism for the analysis of proteins. Capillary forces become very significant at the microscale and can rapidly propel fluids through networks with appropriate hydrophilic surface conditions. Passive valves have been developed by patterning hydrophobic sections in an otherwise hydrophilic network [Feng et al. (2003)], but capillary action is difficult to harness for continuous flow operation.

Electroosmotic flow is a promising technique that takes advantage of a potential distribution in the region near the channel walls that reacts to an applied electric field. Justification for the choice of electroosmotic flow for this study is provided in Section 2.3.1. The remainder of this section focuses on this technique and the electrokinetic effects on the sample and working fluids.

Hunter (1981) details the process of surface charge generation when an electrolyte solution is in contact with a dielectric material. This charge attracts counter-ions and repels co-ions in the solution resulting in an uneven ionic distribution near solid-liquid interfaces. The distribution is referred to as the electrical double layer (EDL) and consists of a region of immobile counter-ions, called the Stern or compact layer, and a diffuse layer where the ions can move. The potential generated at the shear plane between the Stern and diffuse layers is called the zeta potential, ζ. A diagram of the non-uniform ion distribution and the electrostatic potential in the EDL can be seen in Figure 2.1(a) and Figure 2.1(b), respectively.

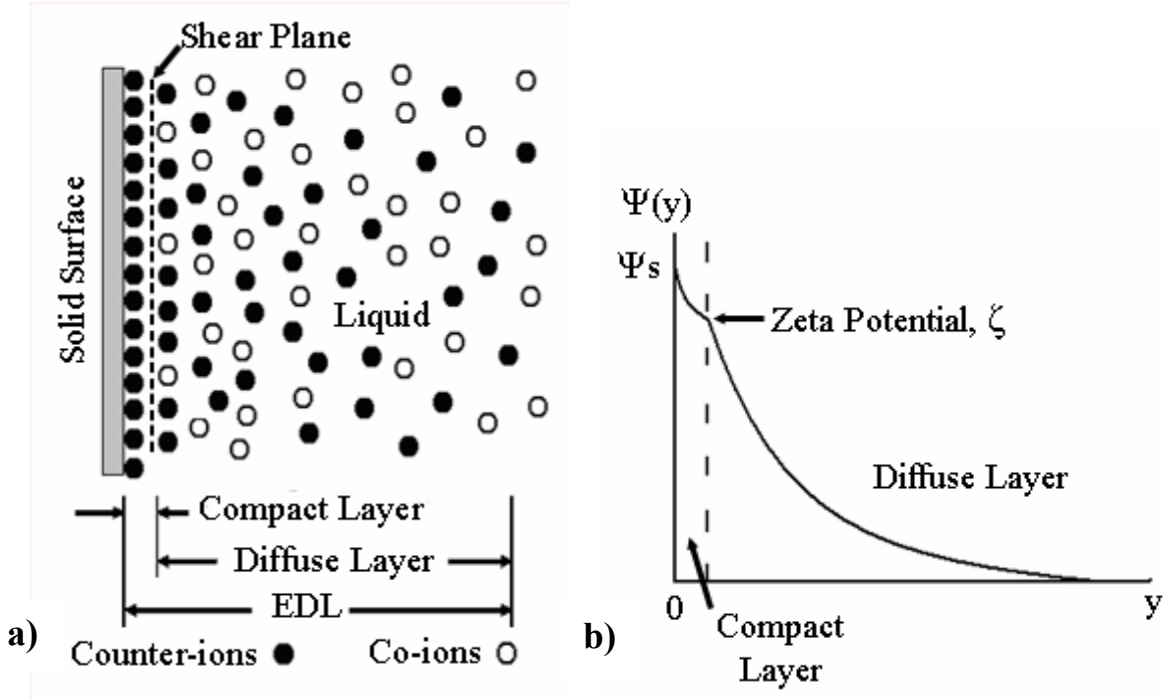

Figure 2.1 Schematic of phenomena occurring in the electric double layer (EDL): a) the non-uniform ion distribution in the EDL and b) the potential distribution in the EDL.

The zeta potential depends on the fluid-solid interaction; typical electrokinetic potentials for glass in contact with an aqueous electrolyte range from -32 mV to -180 mV [Davies and Rideal (1963)]. A

50 mM sodium (bi-)carbonate buffer solution in contact with glass or PDMS produces a negative charge on the order of -80 mV. An estimate of the characteristic length of the EDL is determined by the expression for the Debye-Huckel parameter λ_D:

$$\lambda_D = \sqrt{\left(\frac{D\varepsilon}{\sigma}\right)} \qquad \textbf{(2.1)}$$

where σ is the electrical conductivity, ε is the dielectric permittivity ($\varepsilon = \varepsilon_r \varepsilon_0$, where ε_r is the dielectric constant of the solution and the permittivity of a vacuum ε_0 = 8.854 x 10^{-12} C/Vm), and D is the diffusion coefficient of the ions in the double layer. For a simple 100 mM buffer solution (valence = 1:1) in contact with glass, the order of the EDL is approximately 10 nm. The Debye length increases as the concentration of the electrolyte is reduced; water has a characteristic EDL thickness of 300 nm. The EDL thickness for most buffer solutions in microchannels greater than 10 μm can be considered negligible.

2.3.1 Electroosmotic Flow

The Navier-Stokes and continuity equations govern the flow field [Bird et al. (1960)]. The Navier-Stokes equation for electrokinetic flow of an incompressible, Newtonian fluid with constant viscosity and the continuity equation are

$$\rho\left[\frac{\partial \vec{u}}{\partial t} + \left(\vec{u}\cdot\vec{\nabla}\right)\vec{u}\right] = -\vec{\nabla}p + \mu\vec{\nabla}^2\vec{u} + \rho_e\vec{E} \qquad \textbf{(2.2)}$$

$$\vec{\nabla}\cdot\vec{u} = 0 \qquad \textbf{(2.3)}$$

where ρ is the mass density, p is the pressure, $\vec{u}$ is the fluid velocity vector, μ is the viscosity, ρ_e is the net charge density, and $\vec{E}$ is the electric field vector defined by the potential field:

$$\vec{\nabla}\cdot\left(\sigma\vec{\nabla}\phi\right) = 0 \qquad \textbf{(2.4)}$$

$$E_x = -\frac{\partial\phi}{\partial x}, E_y = -\frac{\partial\phi}{\partial y}, E_z = -\frac{\partial\phi}{\partial z} \qquad \textbf{(2.5)}$$

where σ is the fluid electrical conductivity, ϕ is the applied potential field, and E_x, E_y, and E_z are the electric field strength in the x, y, and z directions, respectively. The conductivity may vary in the chip for applications where multiple fluids are present; however, for this project all the fluids are assumed to have the same conductivity. The last term of Equation 2.2 accounts for the electroosmotic

effect. The net charge density can be related to the electric potential caused by the surface charge with the Poisson equation for a fluid with constant permittivity:

$$\vec{\nabla}^2\psi = -\frac{\rho_e}{\varepsilon} \tag{2.6}$$

where ψ is the electrostatic potential and ε is the fluid permittivity. The ionic concentration of the i^{th} species in the EDL can be acquired by the Boltzmann distribution:

$$n_i = n_{i\infty} \exp\left(-\frac{z_i e \psi}{k_b T_{abs}}\right) \tag{2.7}$$

where $n_{i\infty}$ is the bulk ionic concentration of the i^{th} species, z_i is the ion valence, e is a proton charge (e = 1.602 x 10^{-19} C), k_b = 1.381 x 10^{-23} m^2 kg/s^2K is the Boltzmann constant, and T_{abs} is the absolute temperature. The net charge density is found by applying the Boltzmann distribution:

$$\rho_e = e\sum_i z_i n_{i\infty} \exp\left(-\frac{z_i e \psi}{k_b T_{abs}}\right) \tag{2.8}$$

Electroosmotic flow is achieved by applying an electric field in the longitudinal direction of the channel, causing the excess counter-ions in the EDL to be repulsed or attracted depending on the sign of the zeta potential. The ions in the diffuse layer are free to move in the direction of the Coulomb force and the remaining fluid is dragged along due to viscous forces. A schematic of this process is illustrated in Figure 2.2. Since the time required to achieve fully developed flow in the microscale is on the order of milliseconds the transient term is dropped. The convective term for microchannel flow is eliminated because the inertial forces are considered negligible compared to the viscous forces for Reynolds numbers on the order of 0.1. These simplifications applied to Equation 2.2 provide the Stokes' approximation:

$$0 = -\vec{\nabla}p + \mu\vec{\nabla}^2\vec{u} + \rho_e\vec{E} \tag{2.9}$$

Considering the scenario where flow in the x-direction is occurring between two plates, separated in the z-direction, Equation 2.9 can be simplified to [Tabeling (2005)]

$$0 = -\frac{\partial p}{\partial x} + \mu\frac{\partial^2 u}{\partial z^2} - \varepsilon E_x \frac{d^2\psi}{dz^2} \tag{2.10}$$

In the absence of a pressure gradient, Equation 2.10 can be integrated and appropriate boundary conditions applied. At the edge of the EDL both the potential gradient and the velocity gradient are

zero. At the wall the potential is equal to the zeta potential and the velocity is zero. The resulting equation is [Tabeling (2005)]

$$u(z) = \frac{\varepsilon E_x}{\mu}(\psi - \zeta) \qquad \textbf{(2.11)}$$

where ζ is the zeta potential formed at the liquid-solid interface. For most microfluidic applications, ψ is zero outside the EDL and we get an expression for the velocity, u_{eof}, called the Helmholtz-Smoluchowski velocity:

$$u_{eof} = -\left(\frac{\varepsilon\zeta}{\mu}\right)E_x \qquad \textbf{(2.12)}$$

The direction of the electroosmotic flow for negative ζ values is towards the cathode. Considering the small size of the EDL compared to the channel, we can generally assume a slip wall condition that provides a plug flow phenomena for purely electroosmotic flow. The Helmholtz-Smoluchowski velocity can be used to define the electroosmotic mobility μ_{eof}:

$$u_{eof} = \mu_{eof} E_x \qquad \textbf{(2.13)}$$

It is clear from this relationship that electroosmotic flow is proportional to the electric field. Defining the electric field by controlling the voltages at specific locations generates precise flow without the use of moving parts.

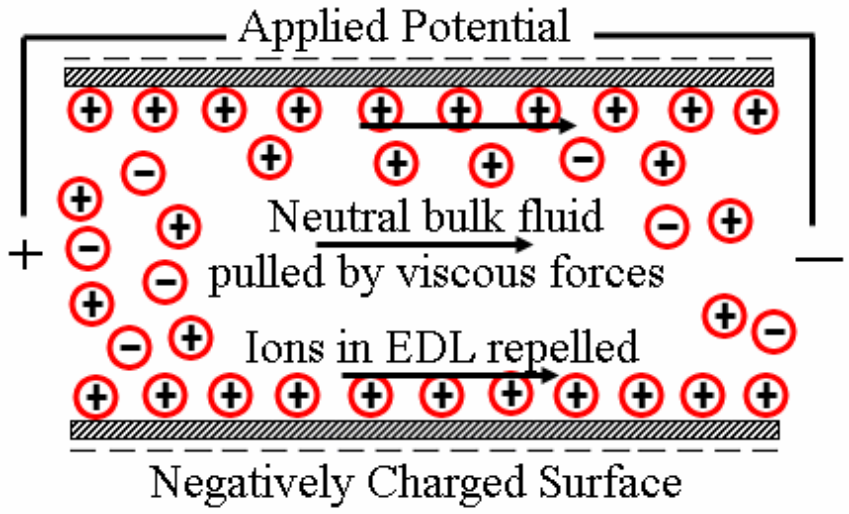

Figure 2.2 Schematic of the electroosmotic flow mechanism. Excess counter-ions at the charged surface are repelled by the applied electric field and drag the bulk fluid by viscous forces. A plug-like velocity profile is achieved for small EDLs.

Electroosmotic flow has several advantages over pressure driven flow that make it attractive for lab-on-a-chip applications. The plug-like velocity minimizes sample dispersion [Paul et al. (1998)] and reduces the velocity variation of samples transported in the fluid medium compared to pressure driven flow, which has a dependence on transverse location. Platinum electrodes placed in the fluid reservoirs or patterned electrodes on the microfluidic chip substrate are used to generate the electric field; therefore, precise flow can be achieved with limited obtrusiveness. Patterned and embedded electrodes are becoming popular to assist miniaturization and allow elaborate electric fields to be achieved. The applied potentials can be varied at high frequencies to meet requirements for devices using dielectrophoresis or high speed flow switching. The system required for pressure driven flow in complex chips is often large and, in the absence of active valve components, has a low frequency response. Devices that incorporate electrophoresis as a separation method for detection of various solutions or particles can simultaneously use electroosmotic flow to transport the bulk materials. Adaptation of portable, battery-based power supplies for capillary electrophoresis has been demonstrated to achieve voltages in excess of 1 kV for prolonged operation [Jackson et al. (2003), Garcia et al. (2003)]. These high-voltage power supplies can be used in a wide range of microfluidic applications.

However, studies providing evidence to the contrary have demonstrated a higher sensitivity for electroosmotic flow than pressure driven flow. Electroosmotic flow is proportional to the charge generated at the electrolyte-solid interface. Surface properties have been found to vary over time for PDMS and poly (methylmethacrylate) elastomer chips [Ren et al. (2001)] and absorption or adherence of samples and particles [Ghosal (2002), Li and Harrison (1997), McClain et al. (2001)] can create regions of heterogeneous surface potentials.

Depending on the geometry and size of the chip, the magnitude of the applied potentials can reach a few thousand volts to achieve adequate flow. Increasing the electric field produces a higher electroosmotic velocity and a higher potential sample throughput; however, the electric field is limited in many cases to prevent destruction of the biological samples. Cell membranes undergo electroporation above a characteristic threshold electric field [Chang et al. (1992)]. This process causes pores to form in the membrane through which materials can pass. Typically, high intensity pulsed electric fields are used to temporarily breach the cell membrane for insertion of materials into the cell. The optimal pulse duration, number of pulses, and electric field conditions for electroporation differ for each type of cell. An example for *E. coli* (strain pUC18) is one pulse of

7 kV/cm for 20 ms [Chang et al. (1992)]. If the cell is exposed to sufficiently high electric field levels for a prolonged period of time the cytoplasm will rapidly leak from the cell and cause the cells to die. Electric field values of 400 V/cm have been observed to cause electroporation of mammalian cells [Wang and Lu (2006)].

A consequence of applying a strong electric field in the fluid is the generation of heat in a process called Joule heating. Xuan et al. (2004) investigated the Joule heating effect experimentally and developed a model to predict temperature fields in a glass capillary. It was found that the fluid temperature increased significantly under high electric fields, nearly 45 °C for a 15 kV/m electric field. The resulting changes in the conductivity and viscosity caused a net increase of the mobility. The influence of joule heating on the system depends heavily on the surface to volume ratio. In small channels this ratio is high and effective conduction of the excess heat is achieved without severe changes in temperature. As the effective diameter of the channel increases, the surface to volume ratio decreases and Joule heating becomes an issue. Obviously the materials that constitute the chip affect the heat conduction and influence the temperatures generated. PDMS has a lower thermal conductivity (k ~ 0.18 W/mK) than glass and acts as an insulating material. Likewise, a capillary suspended in a still air environment (k_{air} ~ 0.025 W/mK) has very poor thermal heat transfer. In the study by Xuan et al. (2004), the cross-sectional area of the suspended capillary is 25 times that of the channels designed in this work, therefore has a more pronounced temperature effect.

Bello (1996) reported that long-term electrophoresis or electroosmosis operation can significantly change the pH levels in the reservoirs containing the anode and cathode. Electrolysis of the buffer solution occurs at the electrodes, causing an excess of negative ions and lower pH at the anode and excess positive ions and higher pH at the cathode. The pH changes affect the conductivity of the solutions and the mobility. The magnitude of this effect depends on several factors: initial electrolyte solution, applied voltage, volume of the reservoirs, size of the channels, and the electroosmotic flow. It was observed that a KCl buffer solution could vary by ±4.4 pH , but $Na_2B_4O_7$ had a ΔpH of ±0.10. By periodic replenishment of the buffer solutions in the reservoirs and an informed choice of buffer solution, the influence of electrolysis in generating pH gradients can be minimized.

2.3.2 Particle Electrophoresis

A charged particle situated in an electrolyte solution will generate an electric double layer analogous to the electrolyte-solid interface at the channel walls. The Debye-Huckel length λ_D is calculated with the same equation (Equation 2.1):

$$\lambda_D = \sqrt{\left(\frac{D\varepsilon}{\sigma}\right)} \tag{2.14}$$

where σ is the electrical conductivity, ε is the dielectric permittivity, and D is the diffusion coefficient of the ions in the double layer. The size of the particle relative to the EDL thickness influences the method of analysis in determining the mobility of the particle [Tabeling (2005)]. If the particle, such as an ion or small strand of protein, is small compared to the EDL we can consider a point charge with the electrophoretic mobility as follows:

$$\mu_{ep} = \frac{q}{6\pi R_p \mu} \tag{2.15}$$

where q is the charge, R_p is the radius of the particle, and μ is the viscosity of the fluid. If the particle is large, for example a blood cell or large DNA strand, the double layer creates a thin surrounding coating of counter-ions similar to the channel wall. An electric field causes the particle to move relative to the fluid. In this case, the mobility is

$$\mu_{ep} = \frac{2\varepsilon\zeta}{3\mu} f_1(\kappa a) \tag{2.16}$$

where ε is the liquid permittivity, ζ is the zeta potential of the particle, and $f_1(\kappa a)$ is a correction factor that depends on the particle shape and the size of the particle relative to its Debye-Huckel length, defined by the parameter κa. Several correction factors for a sphere and other shapes can be found in Hunter (1981). As κa approaches infinite, the case of the EDL length being insignificant to the size of the particle, $f_1(\kappa a)$ approaches 1.5 for a sphere and estimated mobility μ_{ep} becomes,

$$\mu_{ep} \approx \frac{\varepsilon\zeta}{\mu} \tag{2.17}$$

The zeta potential for a particle is usually not known initially and experimental methods are used to estimate the mobility and the corresponding zeta potential. In a bulk electrolyte solution under an

applied electric field in the axial direction, the observed velocity of the particle is a sum of the electroosmotic velocity of the fluid u_{eof} and the electrophoretic velocity component u_{ep} :

$$u_{obs} = u_{eof} + u_{ep} \tag{2.18}$$

The electrophoretic mobility μ_{ep} is defined by the velocity and known electric field strength:

$$\mu_{ep} = \frac{u_{ep}}{E_x} \tag{2.19}$$

This value is useful for applications that require electrophoretic separation of particles or solutions as a means of detection [Harrison et al. (1992), Armstrong (2002)].

2.3.3 Concentration Field

The concentration field affects the transport and dispersion of samples in microfluidic devices; therefore, determining the mass transport of the sample due to diffusion and electrophoretic motion is important in many applications. Also, fluorescent dyes used in flow visualization techniques are often charged, causing them to migrate relative to the bulk flow. The governing equation for the concentration field of the i^{th} species, considering both ordinary and forced diffusion, electrophoretic motion, and reactive generation of the sample fluid, is as follows [Masliyah (1994)]:

$$\frac{\partial c_i}{\partial t} + \vec{u} \cdot \left(\vec{\nabla} c_i\right) = D_i \vec{\nabla}^2 c_i - \frac{D_i z_i e}{k_b T_{abs}} \vec{\nabla} \cdot \left(c_i \vec{E}\right) + R_i \tag{2.20}$$

where c_i is the molar concentration of species *i*, $\vec{u}$ is the velocity vector, D_i is the diffusion coefficient of the i^{th} species, z_i is the valence of the i^{th} species, *e* is the magnitude of charge of an electron or proton, k_b is the Boltzmann constant, T_{abs} is the absolute fluid temperature, $\vec{E}$ is the electric field vector, and R_i is the volumetric rate of generation of the i^{th} species by reaction. The term on the right hand side with the electric field dependence is the source of electrophoretic motion of a charged sample or dye species. Neglecting the gravitational forces, only two forces exist for a charged particle in a stationary liquid under an applied electrical field: the drag force and the electromigration force. The balance between the drag force and the electrical migration force allows the electromigration term to be expressed as a velocity, such as

$$\vec{u}_{ep\_i} = \mu_{ep\_i} \vec{E} = \frac{D_i z_i e}{k_b T_{abs}} \vec{E} \tag{2.21}$$

where $\vec{u}_{ep\_i}$ is the electrophoretic velocity vector and μ_{ep_i} is the electrophoretic mobility. A negatively charged species will migrate towards the anode under an applied electrical field. Based on the above assumptions, the species conservation equation is often reduced to

$$\frac{\partial c_i}{\partial t} + \left(\vec{u} + \vec{u}_{ep\_i}\right) \cdot \vec{\nabla} c_i = D_i \vec{\nabla}^2 c_i \qquad \textbf{(2.22)}$$

The fully developed, 1-D form of Equation 2.22 with no species reaction and no pressure gradients can be rearranged for a charged species under a constant applied electric field, E_x, in the x-axis:

$$\frac{\partial c_i}{\partial t} + \left(u_{eof} + u_{ep\_i}\right)\left(\frac{\partial c_i}{\partial x}\right) = D_i \frac{\partial^2 c_i}{\partial x^2} \qquad \textbf{(2.23)}$$

where u_{eof} is the electroosmotic velocity component of species *i* and u_{ep_i} is the x-component of the electrophoretic velocity:

$$u_{ep\_i} = \mu_{ep\_i} E_x \qquad \textbf{(2.24)}$$

The vector sum of the bracketed velocities in the second terms of Equation 2.23 can be considered the same observed velocity, u_{obs}, outlined in Equation 2.18. For a 1-D field,

$$\left(u_{eof} + u_{ep\_i}\right) = u_{obs} \qquad \textbf{(2.25)}$$

In microfluidics the time scale for diffusion is drastically reduced compared to macroscale flows; however, a wide range of Peclet numbers is realized and the effect of diffusion varies from application to application. For the characteristic devices tested in this and similar studies, diffusion and electrophoretic transport of the dyes are significant.

2.4 Cell Sorting Devices

Information about a given cell population can be gained using a variety of cell control, detection, and analysis methods. Furthermore, distinct characteristics of subpopulations can be gathered by analyzing each individual cell from a population, as opposed to averaging the parameters of an entire population. Characterization of the individual cells and intracellular contents is useful for the study of many processes where details of cell behaviour and function provide understanding of biological practices and assist in optimization. This function enables far more flexibility in cell diagnostics. For example, the detection and analysis of a particular cell is used in oncology for the diagnosis of chromosomal defects and cancers, such as leukemia, lymphoma, and breast cancer [Rieseberg et al.

(2001)]. Pharmacology, drug discovery, and the effects of drugs on bioparticles can be investigated using cellular analysis [Andersson and Van den Berg (2003)]. Rapid detection of bacteria, such as *E. coli*, in food or water sources has importance as food transported illnesses and outbreaks are seemingly common [Yamaguchi et al. (2003)]. Also, genetics research, environmental monitoring, and immunology, such as the analysis of blood samples and bone marrow samples, benefit from the ability to characterize subpopulations from a larger cellular matrix [Huh et al. (2005)].

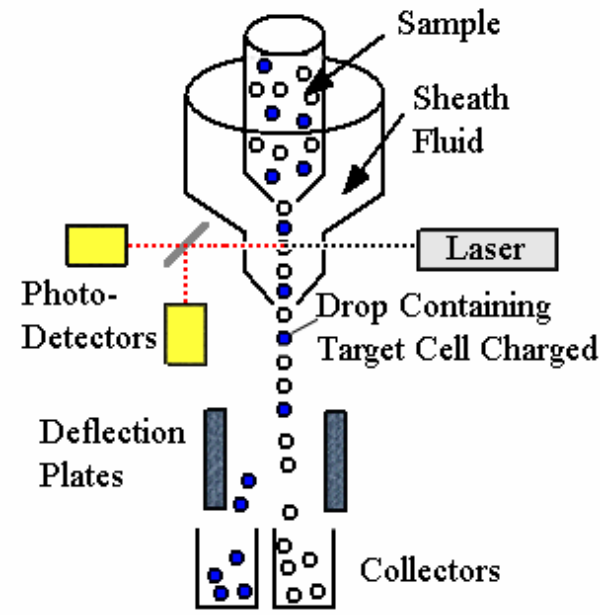

Figure 2.3 Schematic of a conventional FACS droplet sorter. Detection is performed on individual cells in a focused stream. Formed at the nozzle, droplets containing target cells are charged upon exiting the nozzle and deflected by charged plates into a collector.

A common detection instrument used to perform characterization of particles is the cell cytometer [Recktenwald and Radbruch (1998), Shapiro (2003), Melamed et al. (1990)]. These systems incorporate a series of laser light sources and light sensing units that capture information about the cells transported through the detection region as a suspension in a liquid stream. The schematic of a droplet cell cytometry unit is shown in Figure 2.3. This system employs a sheath fluid that hydrodynamically focuses the cell suspension. The particles contained within the sheath fluid pass through a specific location where the cells can be uniformly illuminated by focused laser beams. Derived from the light scattering and fluorescent emissions, some cell cytometers can detect up to 12 fluorescent colours and have the capability to determine the size of particles, granularity of the cytoplasm, cell shape, membrane potential, intracellular pH, and cell viability. Cell cytometers can

also quantify the intracellular levels of DNA, RNA, proteins, lipids, antigens, enzyme activity, and surface receptors [Rieseberg et al. (2001)]. This analysis can be performed at frequencies up to 25 kHz.

There are many applications where characterization of the morphological features of a cell population is not sufficient and further processing must be conducted on an enriched subpopulation. Enriched samples can be cultivated, implemented in other biological applications, or directly transported to additional processes such as cell lysing for the analysis of DNA, RNA, or proteins and the amplification of DNA using PCR. The separation of desired cells from undesired cells is a common challenge. Extraction of viable cells from unviable or undesired cells has been extended to the enrichment of motile sperm [Cho et al. (2003)], recovery of viable *E. coli* bacteria [Fu et al. (2002)], isolation of stem cells from bone marrow cells [Melamed et al. (1990)], and dielectric separation of malignant cancerous cells [Kanagasabapathi et al. (2005)]. Cases of extremely rare target cells require enrichment to make analysis more practical. In the electrophysiological analysis of breast cancer cells, the number of target circulating tumor cells (CTCs) is 1 or 2 per 10 billion blood cells, therefore vast removal of red blood cells is required before the CTCs could be quantified [Han et al. (2006)].

To achieve enrichment of a target cell population, a mechanism is required that can distinguish the desired cells and subsequently perform an action to increase the density in the final sample. A fluorescence-activated cell sorter (FACS) combines sorting capabilities with flow cytometry. These systems have the benefit that they can select cells using multiple pieces of information gained from cell cytometry. The most common FACS technique is the droplet sorting method, shown in Figure 2.3. Once the focused sample stream passes through the laser detection region it forms small droplets by means of periodic disturbance from a nozzle. The droplets, some of which contain a single cell and others nothing, are charged immediately after formation if they are expected to be carrying a target cell. The droplets fall towards a waste collector and the charged particles are deflected by electrostatic plates into a target collection reservoir for recovery. The rate of sorting can reach values of 10 000 cells per second. To account for errors, multiple droplets are directed for each positive detection; therefore, the yield may be sacrificed at high frequencies. This method is successful due to the selection capabilities for collection, but drawbacks include the high cost, complexity of the system and operation, large size, and the large quantity of sample required.

By applying microfluidic theory to cell cytometry and FACS systems, there is potential to create portable units with small sample requirements, significantly lower cost, and improved control of heat and mass transfer that perform similar functions [Huh et al. (2005), Yang et al. (2006)]. Microfluidic cell cytometry and cell sorting devices can be integrated much easier with lab-on-a-chip devices than conventional benchtop systems. The microfluidic cell sorter is expected to play a large role in the progression of lab-on-a-chip technologies because information of the cell population and sample enrichment is required for many biological processes.

Miniaturization of cell sorting devices requires a reduction in the scale of the fluid network, the optical detection equipment, and the auxiliary components (power supplies and control unit). As the length scales of the fluid channels are diminished, additional methods for driving flow and cellular transport become viable. Hydrodynamic [Yang et al. (2006), Kruger et al. (2002), Struder et al. (2004)] and electrokinetic [Li and Harrison (1997), Fu et al. (1999), Xuan and Li (2005)] systems, or a combination of the two [Dittrich and Schwille (2003), Johann and Renaud (2004)], are commonly used for bulk fluid transport, while electrophoretic [McClain et al. (2001), Takahashi et al. (2004), Wu et al. (2004)], dielectrophoretic [Hu et al. (2005), Bhatt et al. (2005), Huang et al. (2002)], gravitational [Yao et al. (2004)], optical [Wang et al. (2005)], and magnetophoretic [Han et al. (2006), Pekas et al. (2005)] forcing methods have all been used individually for the purpose of transporting or directing particles. This flexibility provides opportunities for microfluidic systems in a wide variety of automated sorting applications.

Replacing the complicated and bulky optical detection systems of traditional flow cytometers with smaller solid-state optics significantly reduces the overall size and cost of the system. For example, the laser light sources in cytometry units used for fluorescence excitation and light scattering are being substituted by new technologies. High-power light-emitting diodes (LEDs) are being incorporated into microsystems as a cheap and potentially disposable alternative that can be mounted directly on the chip [Kuo et al. (2004), Miyaki et al. (2005)]. On the detection side, chip-mounted photodiodes have been used to replace photo-multiplier tubes (PMTs) for signal acquisition [Kamei et al. (2003), Jorgensen et al. (2003), Chabinyc et al. (2001)]. Bulk optics, mirrors and lenses, are being replaced by the use of fibre optics and on-chip waveguide structures. Implementing these components furthers miniaturization, but partially at the expense of detection power and versatility compared to a cell cytometer system with three lasers.

The design and function of microfluidic cell sorters can vary considerably to meet the task requirements. The scope of this project was primarily concerned with microfluidic systems that function similar to conventional enclosed FACS systems and therefore the remainder of this review will focus on this type of sorting device. A schematic of a typical microfluidic cell sorting chip, based on the FACS model with fluidic switching, is shown in Figure 2.4. The major components of this design are the focusing region, the detection zone, and the sorting region. By means of a sheath fluid, the focusing junction is used to control the dispensing of the particles and align them for detection at a downstream location. At the point of detection an incident light source will illuminate the sample and the scattered light and fluorescence emission will be detected by photo-sensitive devices. Once a particular target cell is detected, the path of the particle is controlled for collection at the flow switching junction by manipulating the bulk or carrier fluid.

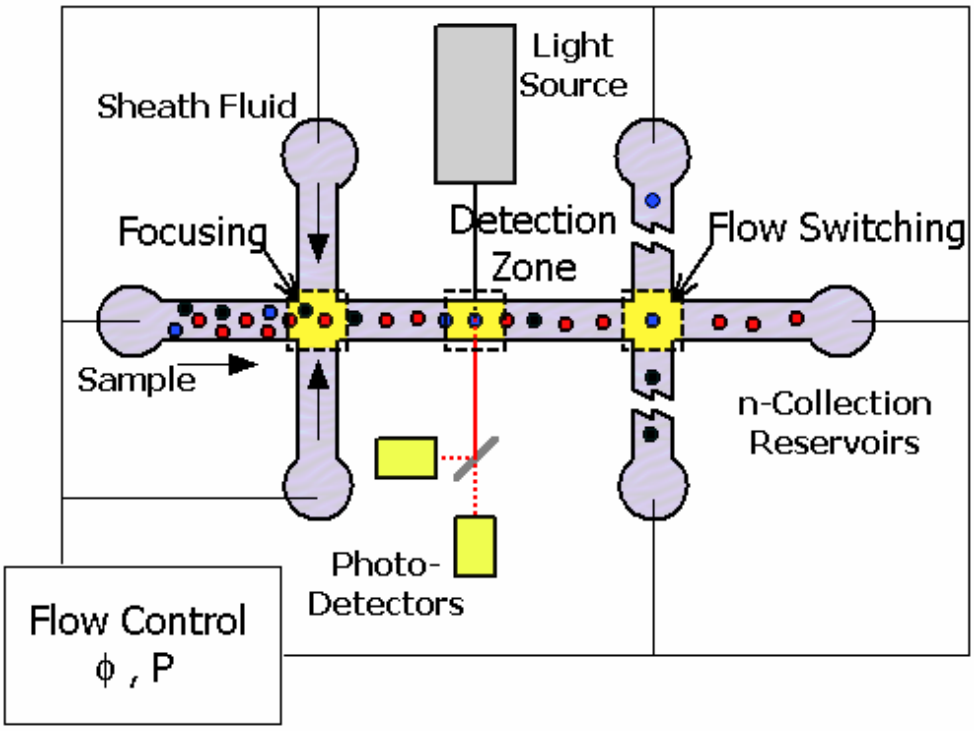

Figure 2.4 Schematic of a typical fluidic switching microfluidic cell sorter. The key regions are indicated: focusing junction, detection zone, and flow switching junction. External pressure or electrical systems are used to control the flow.

2.4.1 Samples for Cell Sorting

In reviews of microfluidic developments for cellular analysis, Andersson and Van den Berg (2003) and Yi et al. (2006) summarize the use of cell cytometers and cell sorters for the detection of many different cell types: *E. coli* and other bacteria cells, yeast cells, nerve cells, rat leukemia cells, red blood cells, white blood cells, cardiac myocyte, sperm, mammalian cells, human breast cancer cells [Kanagasabapathi et al. (2005)], and human lung cancer cells [Yang et al. (2006)]. This work will primarily focus on the sorting of bacteria cells, such as *E. coli*, but can be adapted for a variety of cells.

Operating these systems with live cells requires consideration of the individual cell properties. The wide range of cell properties encountered presents a challenge in designing cell sorting devices. There is a large size differential for the cells listed above. Bacteria cells diameters generally range from 1-10 μm and plant and animal cells from 10-100 μm. This affects the size of the channels in the design and the parameters for controlling the flow. Some cells have a tendency to adhere to channel walls [Ghosal (2002), McClain et al. (2001)] and require the microchannels to be rinsed with chemical agents prior to experiments. Electrophoretic motion of charged particles must be accounted for when using electrokinetic driven flow; biological particles frequently possess a negative charge of varying strength. Deviations from a spherical shape can cause changes in particle motion due to unbalanced electric forces or drag forces. Maintaining an environment for viable cells to survive is also a challenge. Appropriate buffer solutions must be used and measures need to be taken to ensure safe operation; for example, limiting the electric field strength to avoid cell electroporation or controlling the sample temperature to sustain cell viability.

Fluorescent microspheres are frequently employed in preliminary studies and experiments as an alternative to the cultivation, fluorescent labeling, and operational difficulties of using live cells. These spheres are available in a variety of sizes and fluorescent characteristics to mimic the cells they represent and to work in different laser excitation ranges. The use of microspheres alleviates some of the issues encountered with real cells, such as a narrow variation in size and charge, bright fluorescence emission, and insensitivity to electric fields. Testing the devices with real cells is required to ensure suitable operation, but the microparticle suspensions can reduce the effort, cost, and time spent during the initial stages of experiments.

2.4.2 Sample Focusing

Function

Focusing of the sample, in conventional and microfluidic cell cytometry, is performed by pinching the particle suspension flow with sheath fluid to reduce the width of the stream transporting the cells. The sheath fluid is supplied on either side of the sample and encapsulates the sample stream in the transverse direction and restricts the lateral position of the particle. The sample continues downstream to the detection region, where a focused light source will illuminate the particle for analysis. To ensure particles are reduced to a single stream for maximum detection sensitivity, the focused stream width should be comparable in size to the particles being analyzed [Schrum et al. (1999), Huh et al. (2002)]. If the focused stream width is too large, multiple cells will pass through the detection region simultaneously, which will cause errors in the data and will make it very difficult to distinguish different cells. Also, particles with insufficient spacing will be difficult to isolate during separation and will reduce the yield of the device. The width of the focused stream depends on the ratio of sheath flow to sample flow and is controlled by adjusting the relative flow rates. Characteristic of microsystems, the flow is laminar and a well defined dividing streamline is established between the sample and sheath fluids. Mixing between the streams is minimized and diffusion dominates transverse mass transport. This is particularly true for chips comprised of homogeneous materials, glass-glass for instance. Using electroosmotic flow with non-uniform hybrid chips, for example PDMS-glass, can cause additional dispersion effects [Devasenathipathy and Santiago (2002)].

2-D sample focusing can be accomplished with two sheath streams, one on each side, and 3-D focusing is achieved with four sheath streams, one on each side and top and bottom. Microfluidic devices are normally fabricated in a planar process and 2-D focusing is used in the majority of studies; however, as fabrication capabilities improve, the ability to construct more complex three dimensional chips is growing. 3-D focusing has the advantage that the sample is entrained in both transverse directions and the location of the cells is restrained to a smaller volume, which can provide better detection. Planar focusing does not restrict the location of the particles in the vertical axis and can lead to higher variance in signal acquisition. The differences between 2-D and 3-D focusing have been investigated numerically [Chung et al. (2003)] and experimentally [Miyake et al. (1997)]. 2-D focusing is used in this thesis.

Several types of fluids have been used for sheath flow in microfluidic focusing. The combination of sample and sheath fluids fall under two categories: 1. liquid-liquid or liquid-gas multi-phase

focusing or 2. liquid-liquid single-phase focusing [Lee et al. (2006)]. In the multi-phase liquid-liquid scenario, the relevant characteristics of the sheath fluid differ from the sample fluid. This could include density, viscosity, conductivity, electroosmotic mobility, and permittivity. The effects of changing the viscosity in a liquid-liquid multi-phase flow were investigated numerically for hydrodynamic focusing by Chung et al. (2003), who determined that decreasing the sheath viscosity provided better focusing, i.e. narrower focused sample width. Adjusting the mobility of the sheath fluid in electroosmotic flow has a similar effect to viscosity in pressure driven systems. The flow of a sheath fluid with a higher mobility will be greater under a constant applied electric field and therefore the focused width will also be reduced. Air was used as the sheath fluid in a study by Huh et al. (2002) to reduce the constant pumping requirements and large fluid volume of liquid sheath flows. They were able to achieve stream widths as thin as 15 μm and successfully detect microbeads and C2C12 myoblast cells. The liquid-air two-phase focusing is restricted to hydrodynamic driven flow and makes it difficult to integrate sorting functions. Single-phase focusing uses the same solution for the bulk sample and sheath fluids and the properties are assumed consistent in all channels.

As an alternative to using sheath flows, Fu et al. (1999, 2002) demonstrated a similar function by narrowing the sample channel to a size, 3 x 4 μm cross-section, comparable to the particle. Altendorf et al. (1997) employed a V-groove channel with appropriate dimensions to allow blood cells to be transported single-file, eliminating the need for focusing. Some complexity of the system is eliminated in these chips, but channels with such small dimensions become susceptible to blockages by larger particles or cell adhesion.

Of the primary flow driving mechanisms, hydrodynamic [Yang et al. (2006), Chung et al. (2003), Lee et al. (2001)] and electrokinetic [McClain et al. (2001), Xuan and Li (2005), Jacobson and Ramsey (1997)] systems are used extensively for sample focusing. The results of both methods are comparable. In hydrodynamic focusing the aspect ratio of the outlet channel affects the streamwise velocity profile, which influences the focused stream width. As the height of the channel and the aspect ratio ($\varepsilon_c = height/width$) approach zero, the planar velocity profile becomes plug-like and the degree of focusing will match the electrokinetic driven case, where slip conditions at the wall are generally assumed [Lee et al. (2006)]. Each method has advantages that may help the selection for a particular application. For example, pressure driven flow does not generate the same potentially harmful environment as electrokinetic flow and the velocities can be increased significantly without destruction of the cells [Huh et al. (2005)]. Pressure systems require moving parts such as pumps and

valves, whereas electrokinetic flow only requires submersed electrodes to generate an electric field. Electrophoretic effects may complicate particle control when using electrokinetic flow for transport of highly charged particles. Under certain conditions the electrophoretic mobility of the particles may be larger than the electroosmotic mobility of the electrolyte and the particle will move in the opposite direction of the bulk flow. These are tradeoffs that must be evaluated in the design of a microfluidic cell sorting device.

Application

Evaluation of focusing can be achieved by considering the reduction of the sample stream with the least amount of required power. In practice, a minimum level of focusing is required to properly dispense the sample, but savings in applied potential or pressure will assist in adaptation to a handheld device. Determining the location of the dividing streamline of the sample and sheath fluids provides an accurate parameter to compare designs. In numerical models, diffusion can be neglected and a step concentration profile is achieved, illustrated in Figure 2.5(a). In experiments, fluorescent dye solutions are used in the sample stream to visualize the flow field and the intensity of the fluorescence represents the concentration of the dye. Due to diffusion and electrophoretic effects, in the case of a charged species, the dye moves in the transverse direction causing a more widely distributed profile, shown in Figure 2.5(b).

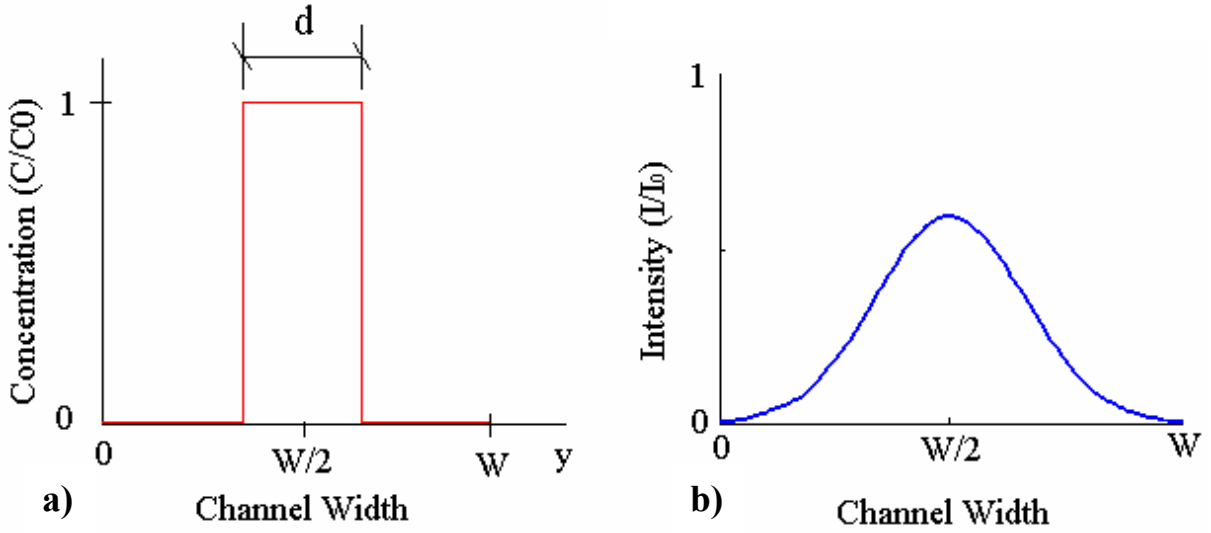

Figure 2.5 Transverse concentration profiles after focusing: a) ideal step concentration for zero diffusion and zero electrophoretic migration and b) intensity profile taken from experimental image, with finite diffusion and electrophoretic migration.

Estimating the dividing streamline from the experimental data has not been addressed in previous studies. As an alternative, the full-width at half-maximum (FWHM) values are commonly reported [Jacobson and Ramsey (1997)]. The FWHM value is the width of the sample profile that corresponds to the locations where the concentration is half of the maximum profile concentration. Another method is to find the rising and falling inflection points of the profile curve. These values do not represent the true focused stream width. Many studies plot experimental and numerical results, but do not divulge how the focusing width is quantified from experimental data.

Various geometries of the focusing junction have been fabricated and tested. Streamlined designs are not critical because of the characteristically low Reynolds number, such that no recirculation regions are encountered. The geometry does affect the local electric field and pressure field for electrokinetic and hydrodynamic focusing, respectively. If the applied potentials or pressures are constant and the fluid remains the same, the biggest influence in focusing is the relative dimensions of the sample, sheath, and outlet channels [Lee et al. (2006), Yang et al. (2005)].

The simplest focusing design is a cross, shown in Figure 2.6(a), where the focusing sheath fluid channels are perpendicular to the sample channel and the main channel where detection is performed. This configuration is common due to its simplicity, off-the-shelf availability, and ease of modeling. Numerical models were developed for 2-D hydrodynamic focusing in a cross configuration by Lee et al. (2006) and 2-D electrokinetic focusing by Yang et al. (2005) and Xuan and Li (2005). These studies propose theoretical models that predict the width of the focused sample stream. The assumptions associated with these models will be described in greater detail in Chapter 6. Applying mass conservation of the sample and the entire fluid system with constant fluid properties it becomes clear that the focused stream width depends on the ratio of flow from the sheath and sample streams, but is independent of the magnitude of the flow rate. The flow rates in pressure driven flow are a function of the respective channel dimensions (width and height), pressure gradient, and viscosity. In electroosmotic flow, the electric field and inlet and outlet channel dimensions determine the flow rates and resulting focused stream width. The data is presented as d / W_{outlet}, the focused stream width d relative to the outlet channel width W_{outlet}, as a function of the focusing potential, $\phi_{foc} = \phi_{sheath} / \phi_{sample}$, or ratio of flow rates, Q_{sheath} / Q_{sample}, for electrokinetic and hydrodynamic focusing, respectively. In both cases the focused stream width decreases with increasing relative sheath flow.

All of the models predict values that agree well with experimental results, but there are limitations in the electrokinetic models that restrict their widespread usage. Yang et al. (2005) used a 1-D electric field approximation to generate their mathematical model. This approximation does not incorporate changes in cross-sectional area to calculate the electrical resistance of a channel. Although the derivation of the flow model accommodates different channel widths, the 1-D electric field derivation provides accurate results only in the case of identical channel dimensions for each stream. The model by Xuan and Li (2005) also suffers from the uniform channel dimension restriction. The physical limits of these models occur when the focused stream is the same size as the outlet channel and when the focused stream width becomes zero. According to these boundary cases, it should be possible to achieve a wide range of sample stream widths for a given design.

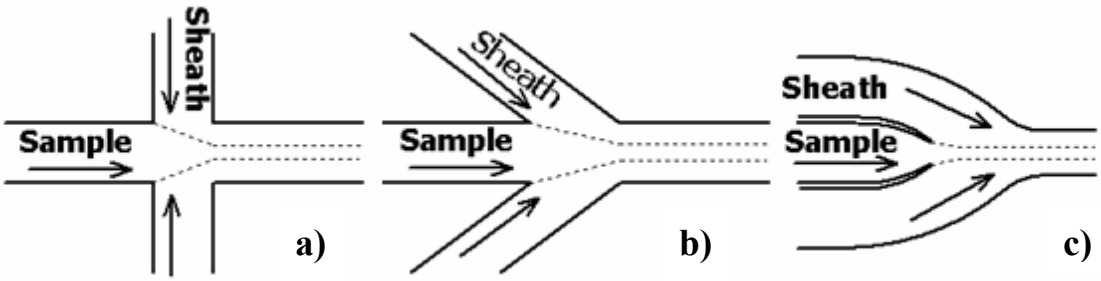

Figure 2.6 Three common focusing configurations: a) perpendicular sheath flow focuser, b) angled sheath flow focuser, and c) double nozzle style focuser.

Additional studies using numerical simulations on cross-microchip focusing were performed by Ermakov et al. (1998), Ren et al. (2003), Lin et al. (2002), and Fu et al. (2004). The experimental and numerical results obtained in these studies are qualitatively and quantitatively similar. The results of the numerical models indicate that the ratio of the sheath channel width to the sample channel width influences the focused stream width; however, this parameter is not directly addressed. All of the reported cross-microchip geometries had uniform cross-sections. Adjusting the relative cross-sectional areas of these channels may provide more efficient focusing.

Another design, shown in Figure 2.6(b), has angled sheath inlet streams. Chung et al. (2003) developed a 2-D and 3-D hydrodynamic model for this geometry, where the 3-D configuration employs sheath and outlet channels with larger depths than the sample channel. This study does look at the influence of the relative widths of the sheath channels to sample channel. It was demonstrated that increasing this ratio reduces the focused stream width. The angled focusing stream design is

relatively common in microfluidic cell sorter designs [Kruger et al. (2002), Dittrich and Schwille (2003), Tung et al. (2004)].

Lee et al. (2001) present a hydrodynamic focusing model for a double nozzle style configuration, similar to the schematic in Figure 2.6(c). The focused stream widths are provided for varying relative flow rates of the sheath and sample streams. The curves appear very similar to the perpendicular focuser geometry, indicating a limited influence of shape on the degree of focusing. Lee et al. (2003) used the same configuration for testing a microfluidic flow cytometer.

The designs demonstrated in literature achieved levels of focusing adequate to control the dispensing of fluorescent dye, microspheres, or live cells. However, there is room for design improvements to minimize the required power for operation and a need for better techniques to analyze experimental profile data. These concerns will be addressed in Chapter 6.

2.4.3 Cell Detection and Characterization

The cellular analysis in a conventional cell cytometer characterizes a wide variety of physical parameters, levels of intracellular components, and fluorescence behaviour. Of course, quantification of any property requires that the specific trait is discernable and the system has the ability to resolve this feature. To obtain the cellular information, a series of incident laser light sources are focused on the path of the particles using bulk optics components and the fluorescence emission and scattered light from multiple angles are detected with several light sensing elements. The light signal data is correlated with known relationships and assembled for statistical analysis. Systems with cell sorting capabilities also use this data to identify target cell subpopulations to be collected for sample enrichment. Positive cell detection providing the position of the particle and the velocity can be obtained by dual detection methods or by estimating the signal peak duration. The timing for optimal sorting can be calculated using this information.

This same process is applied to microfluidic cell cytometry and μFACS systems that use fluidic switching mechanisms. Unconventional separation methods do not necessarily use the same detection strategy; some sorting techniques are applied to discrete sample volumes prior to detection [Han et al. (2006)], while others use passive separation techniques [Cho et al. (2003)] that differ from the continuous operation cell cytometer model. Lasers are often used in research studies for fluorescence detection, but they are not practical for lab-on-a-chip devices due to the large size and weight, high cost, high power requirements, and potential hazard. The development of alternative devices for

illumination and sensing is an active area of research. Also, the bulk optics components have been replaced with fibre optics systems and on-chip waveguide structures.

For target cells to be detected and sorted, parameters such as the size of the particles can be determined by light scattering and absorption measurement techniques, but this information alone is not always sufficient to distinguish target cells. Several different particles may be similar in size making size discrimination difficult. The preferred method is to use selective fluorescence labeling of the cells of interest. Considerable advances in this technology have enabled the individual detection of many types of cells and intracellular components.

The ability to accurately characterize and detect cells also depends on parameters such as the transit time in the detection zone and particle spacing. Dittrich and Schwille (2003) investigated the effect of transit time for signal integration and found that too long a transit time, relative to the integration time of detection unit, reduces the definition of the signal and makes it difficult to identify target cells. Very short transit times may not provide enough intensity to differentiate from the noise of the system. They reported an optimal transit time of 6 ms for a 15 μm detection region, equivalent to a frequency of 160 Hz. Wang et al. (2004) observed peak signal widths to be approximately 10 ms and estimated that a maximum frequency of 50-65 Hz could be achieved with clearly distinguishable peaks. These detection limitations have direct implications for the overall throughput of μFACS systems.

This section provides a brief description of the use of fluorescence staining for cell cytometry and the common detection systems that have been implemented in microfluidic systems. The integration of an optical detection system was not achieved during the time of this study, but the design of the chip was conducted to accommodate optical components.

2.4.3.1 Fluorescence Staining

Fluorescence is used to illuminate a desired region of fluid or material from the surrounding medium. Each type of fluorophore, a fluorescent molecule, has a characteristic range of excitation frequencies at which they are excited to a higher level of energy upon exposure. At this excited S_2 state, some energy is lost due to vibration and the molecule rapidly moves into to the lower energy S_1 state. At this time the molecule returns to its initial ground state and releases a photon. Due to the energy losses, the emitted light spectrum emission is at a longer wavelength (lower frequency) than the

excitation spectrum. This difference in peak frequencies is called the Stokes shift, illustrated in Figure 2.7, and the time delay is called the emission time delay.

The Stokes' shift behaviour of the fluorophore is exploited to filter out the incident light and observe only the emission light. Common fluorescence microscopy applications use an excitation filter (band-pass) to generate a band of frequencies for excitation of the fluorescent materials, a dichroic mirror (cut-on) to eliminate the majority of the incident excitation light, and an emission filter (band-pass or long pass) to eliminate stray light signal and the remaining incident light.

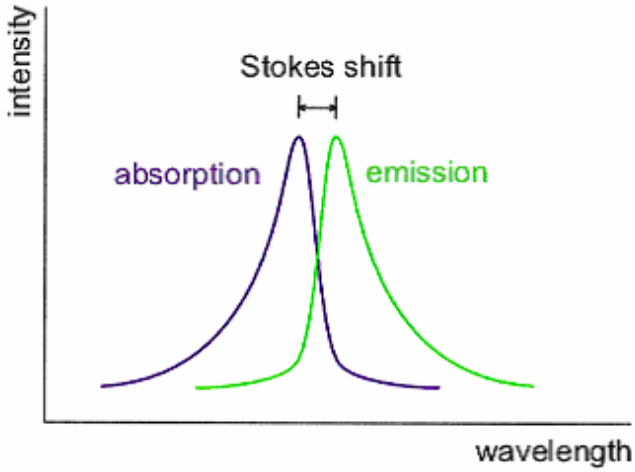

Figure 2.7 Illustration of the absorption and emission spectra for a fluorescent material. The peak intensities are separated by the Stokes' shift.

The use of fluorescence labeling of specific microorganisms using biological reagents is a crucial for many analysis tools, such as assay measurements of populations and detection for sorting systems. The review by Veal et al. (2000) summarizes the developments and applications of staining cells for real-time monitoring with cell cytometry. The choice of a fluorescence reagent depends on the characteristics that are being investigated; fluorescent dyes are available that stain biological materials and activity. Phylogenetic labeling involves probes that bind to specific nucleic acid sequences. Immunological labeling uses antibodies that bind to a particular molecular site, an epitope, that is exclusively present on all target cells. Fluorescent labeling dyes are available that respond in intracellular enzyme activity. The detection of viable cells, used commonly for bacteria and yeast, can be accomplished using dyes that only stain cells with breached membranes, cells that are respiring, or

cells that possess membrane potentials [Veal et al. (2000)]. For more information about the particular stains used in cytometry, refer to the texts by Shapiro (2003) and Melamed et al. (1990).

Many of the fluorescence reagents used in cytometry and sorting are excitable in the blue fluorescence range (~ 488 nm) provided by an argon-ion or a blue semi-conducting laser. Dittrich and Schwille (2003) conducted studies to detect *E. coli* cells that had been labeled with the R-phycoerythrin fluorescent protein, which acts as a cell surface antigen. Fu et al. (1999) also distinguished *E. coli* that expressed green fluorescent protein from non-fluorescing *E. coli*. An argon-ion laser source was used in both studies. Wang and Lu (2006) used a membrane impermeable nucleic acid stain, SYTOX, to investigate the electroporation effects on Chinese hamster ovary (CHO-K1) cells. This stain has green fluorescence characteristics and is reported to increase in intensity greater than 500-fold upon binding with nucleic acids. Wang et al. (2005) sorted HeLa cells that expressed a fused-histone green fluorescent protein, excited with a blue semi-conducting laser source. Han et al. (2006) used a cell permeable nucleic acid dye, SYTO 13, to stain MDA-MB-321 breast cancer cell lines.

The application of cell staining requires knowledge of the biological and chemical processes that are present in microorganism and access to appropriate facilities for handling the cells and the fluorescent reagents. Staining can sometimes be performed on-chip, but often requires pre-processing of the samples. Many studies are thus performed with fluorescence microspheres used to represent the fluorescently stained cells. The chosen microspheres should exhibit similar fluorescent properties.

2.4.3.2 Detection Systems

Designing and implementing optical components into a miniaturized system for biological analysis is still in a developmental stage. Reduction in size and cost is necessary, but challenges arise in trying to maintain the same capabilities and system sensitivity of conventional devices. There is potential for efficient detection due to the high levels of particle transport control and the ability to incorporate optics very close to the sample. Detailed information on the advances in micro-analysis optical detection systems is presented in reviews by Verpoorte (2003), Mogensen et al. (2004a), Dittrich and Manz (2005) and Erickson and Li (2004). A key development is the progress of LEDs and solid-state lasers, which provide an alternative to larger lasers, and micro avalanche photo diodes (μAPDs), which can potentially replace photo-multiplier tubes and photodiode sensors. The smaller light source

and detection components can be mounted directly onto the chip to reduce losses and minimize the size of the system.

The basic components of a detection system for μFACS devices are the light sources for fluorescence illumination, light transporting optics, filters, photo-sensitive detectors, and data acquisition system with signal analysis and controlling functions. While LEDs [Kuo et al. (2004), Miyaki et al. (2005)] and μAPDs [Kamei et al. (2003), Jorgensen et al. (2003), Chabinyc et al. (2001)] have been implemented in individual studies, the majority of research performed in μFACS still uses laser sources and fluorescence microscopy for operation and observation. Epi-illumination microscopy is mainly used to monitor the operation and to carry out detailed recording; however, Takahashi et al. (2004) developed a system to perform real-time microscopy imaging, signal analysis, and cell sorting. The potential benefit of this system is the high resolution imaging capabilities.

Detection using laser light sources requires optical elements to transport the light to the chip and additional elements to transport the emission signal from the chip to the photo-sensor. Optical fibres are commonly used to alleviate alignment issues involved with bulk optics. Integration of the fibre for sample illumination has been accomplished by two principal methods: 1. embedded optical fibres in the chip and 2. optical waveguide structures, coupled to the fibre, are fabricated in the chip.

Lin and Lee (2003) and Fu et al. (2004) inserted optical fibres into guide channels located on the chip which aligned the end of the fibre to the fluid channel. The two fibres, one for excitation light one for emission light, are located on opposite sides of the fluid channel. Fluorescence emission, although possible, was not detected in either of these studies; rather, the absorption of the illumination light when a particle passed the region caused a decrease in signal intensity. This method is called extinction detection, which can be used to measure the size of a particle and cell viability.

Waveguides, coupled with the optical fibre transmitting the illumination light, can transmit light in a microfluidic chip to and from a sample similar to an embedded fibre. The use of polymer waveguides has been presented by Lee et al. (2003), Mogensen et al. (2003), and Wang et al. (2004). The planar optical waveguides were fabricated from SU-8 photoresist because of its high optical transmittance, high index of refraction, and low cost compared to waveguides made from silicate glass, which has been employed in electrokinetic separation devices [Mogensen et al. (2004b)]. Wang et al. (2004) incorporated several waveguides for detection at various angles to provide a more thorough analysis. They were able to measure forward light scattering, extinction signal, and large

angle scattering with their chip design. It was not employed by Wang et al. (2004), but one of the advantages of planar waveguides over embedded fibres is that the signals can be split and merged on-chip, enabling the use of multiple detection zones. Disadvantages of waveguides include the loss encountered in the coupling between the fibre and waveguide and the additional steps required during chip fabrication.

To maximize the illumination signal that reaches the particle, integration of 2-D optical components has been introduced in microfluidic chip design. Wang et al. (2004) used a planar lens in the channel to focus the incident light on the particles. A similar lens was used by Camou et al. (2003) at the end of fibre insertion channel to counteract the diverging light from the fibre.

The detection of fluorescence requires the use of a filter to eliminate the incident signal to isolate the emitted light from the fluorophores. A combination of a dichroic filter and band-pass filter, or just a band-pass filter, is commonly used for this purpose. The filters do not require a significant amount of space and therefore are easily integrated into microfluidic systems.

Data acquisition of the detected light signals is generally performed with a computer that subsequently performs a peak detection analysis on the signal. A control system responds to a positive detection notice and initiates the mechanism for particle collection. The trigger of this collection event depends on the criteria for a given target cell. In the simplest threshold analysis case, a positive detection occurs when the signal reaches a pre-determined level. Signal filtering and processing can improve the signal-to-noise ratio and provide more accurate and sensitive detection [Tung et al. (2004)].

2.4.4 Cell Sorting by Fluidic Switching

Principles

Conventional FACS systems that employ the droplet sorting technique are categorized as an open sorter system. The droplets are formed in an open air environment which is susceptible to outside contamination and is potentially dangerous for sorting biohazardous materials. The slower but simpler alternative is the enclosed sorter, which generally has a lower cost and provides full containment of samples to avoid material transfer in and out of the system. Microfluidic cell sorters fall nearly exclusively in the category of enclosed sorters.

Trade-offs are encountered in cell sorting between sorting rate, purity of the collected sample, and the percentage of target cells that are collected. Three different sorting modes are used to cater to specific requirements: 1. enrichment, 2. single cell, and 3. exclusion [Recktenwald and Radbruch (1998)]. An illustration of their operating principles is shown in Figure 2.8. The enrichment mode collects all events that provide positive target cell detection, regardless of the presence of an unwanted cell. This mode collects the highest number of target cells, but as the frequency of particles increase the presence of an unwanted cell is more probable and the purity of the collected sample decreases. The single cell mode collects only when a single target cell is detected in a sorting event, therefore rejects all events where more than one cell is present. High purity is achieved with this method, but its rejection criterion is the most stringent. Primary use of single cell mode occurs when a known number of target cells are to be captured with high purity. The exclusion method collects all events with a target cell unless an unwanted cell is present. This provides high purity similar to the single cell sorting, but is more efficient because it captures sorting events with multiple target cells present. In the case of a low initial concentration of target cells, such as rare cell sorting conditions with 1:100 or 1:100,000 cell fractions, the exclusion and single cell modes essentially become the same function.

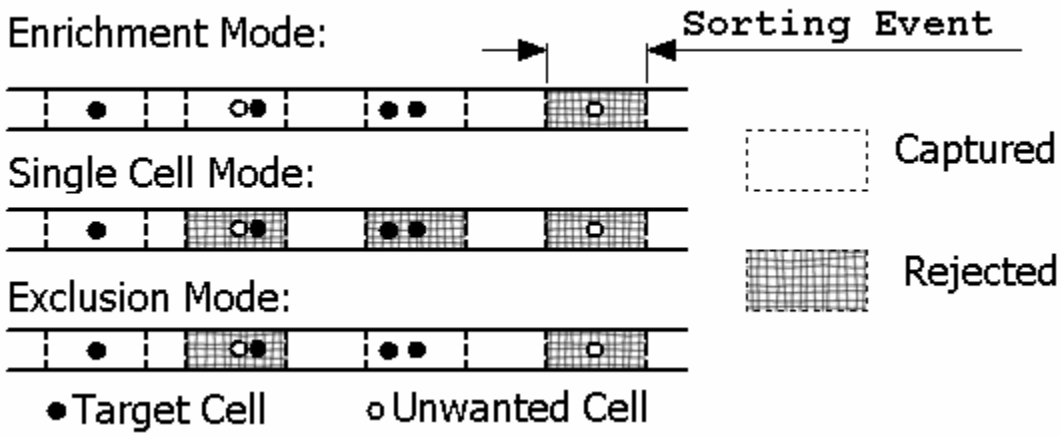

Figure 2.8 The operating principles of the three modes for target cell capture: 1. enrichment mode, 2. single cell mode, and 3. exclusion mode. A sorting event indicates the volume captured during a single sorting activation.

The purity of the collected subpopulation is an important parameter of cell sorting. In the single cell and exclusion modes, a well tuned and functioning system can achieve purity close to 100%. Achieving such a high level of purity requires the ability to detect all of the unwanted cells and reject

sorting events where undesired cells are present. Microfluidic sorting systems solely using fluorescence may not be able to detect non-fluorescent particles and would require simultaneous acquisition of multiple signals, such as extinction signal in addition to fluorescence, to operate in single cell or exclusion modes. The purity of enrichment sorting depends on the probability that an unwanted cell is present in the sorting event. The probability, P, that no other particle besides the target cell is present can be determined using Poisson statistics [Recktenwald and Radbruch (1998)]:

$$P = e^{-(1-s)rT} \quad \textbf{(2.26)}$$

where s is the fraction of the subpopulation that is to be sorted, r is the particle throughput rate in cells/s, and T is the time required to perform a sorting event. P is also the purity of the enriched sample using the enrichment sorting mode. From Equation 2.26 it is clear that increasing the throughput r and the time of a sorting event T increases the chance of an unwanted particle will be collected and a decrease in purity will be observed.

The efficiency can be evaluated similarly. Efficiency is defined as the fraction of target cells collected from the total number of target cells detected. This quantity differs from the yield of a cell sorter, which is the fraction of detected target cells that are actually recovered. Ideally the enrichment mode will have an efficiency of 100%, while the single cell and exclusion modes reject target cells and have the following efficiencies [Recktenwald and Radbruch (1998)]:

Single Cell Mode: $E = e^{-rT}$ **(2.27)**

Exclusion Mode: $E = e^{-(1-s)rT}$ **(2.28)**

While these two sorting modes have very high purity, the efficiency is sacrificed. Figure 2.9 shows efficiency of the exclusion mode with varying particle throughput and initial target cell fraction.

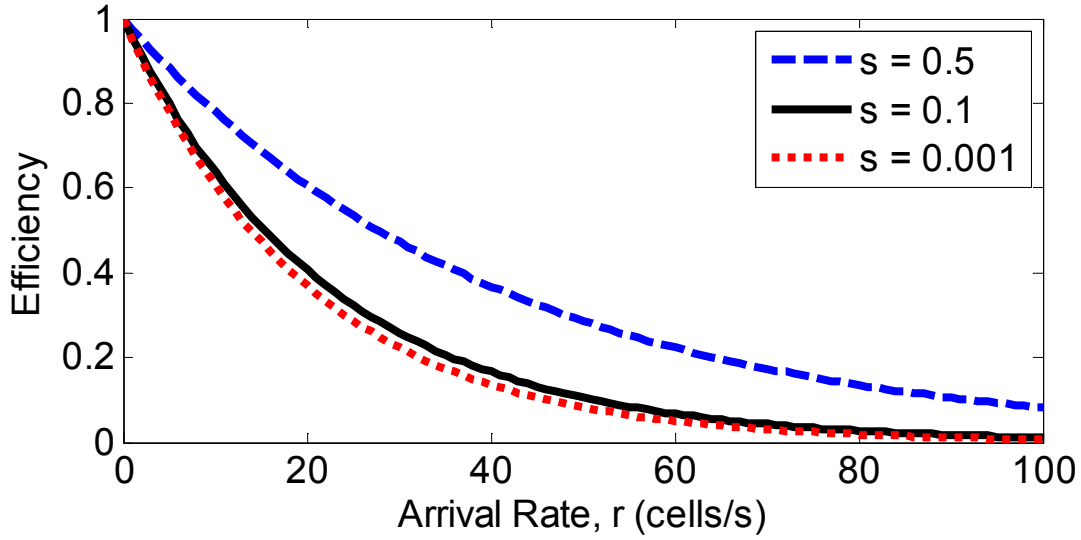

Figure 2.9 Sorting efficiency of the exclusion sorting mode versus cell arrival rate. Three target cell fractions are plotted: s = 0.5, s = 0.1, and s = 0.001. The sorting interval time $T = 50$ ms.

Multiplying the efficiency of the sorting mode by the rate of arrival of the target cell, we can determine the rate of sorting R [Recktenwald and Radbruch (1998)]:

Single Cell Mode: $R = (sr)e^{-rT}$ **(2.29)**

Exclusion Mode: $R = (sr)e^{-(1-s)rT}$ **(2.30)**

The optimal rate of a target cell arrival depends on the time required for sorting. The maximum sort rate for single cell and exclusion sorting is [Recktenwald and Radbruch (1998)]

$$R_{\max} = \frac{sr}{e} \qquad \textbf{(2.31)}$$

For enrichment mode, the maximum rates of sorting and cell arrival are

$$R_{\max} = \frac{1}{T} \qquad \textbf{(2.32)}$$

$$r_{\max} = \frac{1}{sT} \qquad \textbf{(2.33)}$$

Application

Various methods of directing cells have been implemented in microfluidic cell sorting devices and many designs have been tested, but there is no clearly superior technique that will be universally adopted in future developments. The capabilities and limitations of noteworthy cell sorting studies are summarized here.

Takahashi et al. (2004) designed a cell-sorter that uses a cross-flow electric field to deflect the path of cells. The chip is composed of two hydrodynamically driven laminar streams that join, but remain parallel, for a short region at their midpoints and resembles the letter 'X'. Agar gel electrodes are used at the junction to pass electric current and create a local electric field across the channel. During operation, unwanted particles are directed across the dividing streamline into the waste stream by applying the electric field. Target cells remain in the initial laminar flow by disconnecting the applied potential when they are present in the separating region. 100% accuracy of collection is reported by applying a potential of 6 V, however, the throughput of the system, concentration of the target particles, and time required for particles to pass through the separation zone are not reported. Also, the principle used here relies on a prescribed charge of the waste particles to achieve electrophoretic motion. This notion severely limits the application of this device. Selective electrophoretic directing of target particles may be a more reliable technique.

The development of magnetic tagging capabilities enables the use of magnetic fields for controlling particle motion. Pekas et al. (2005) integrated this function into a microchip by embedding metal lines close to the fluid channels and supplying a current. They were able to direct fluorescent super-paramagnetic beads into one of two collection channels with an efficiency of 85% during static sorting (not actively switching between paths). Dynamic sorting was not demonstrated. Less than ideal efficiency was attributed to insufficient charge of certain particles.

The use of optical forces for controlling living cells was reported by Askin et al. (1987). This method of optically deflecting particles in a continuous operation cell sorter has been presented by Wang et al. (2005). A high-power infrared laser directed the hydrodynamically focused particles from a default waste channel to the collection channel. The values reported indicate effective operation of this system to detect fluorescently labeled HeLa cells and sort them from unlabeled cells. A throughput of 20-100 cells/s was achieved for target cells fractions of 0.01, 0.1, and 0.5. The purity of the collected sample ranged from 0.83 to 0.99 and the collection efficiency exceeded 85% for all

tests, excluding the highest cell throughput run (106 cells/s). A major downfall to this system is the requirement of a high power IR laser, which is difficult to incorporate into lab-on-a-chip devices.

Electroporation of a cell creates open pores in the membrane and is used to allow penetration of materials into cells that would otherwise be impermeable. Applying a high electric field for an elongated period of time will result in death of the cells. Bakker Schut et al. (1990) applied this principle to selectively electroporate cells in a full size enclosed flow cytometer. Field strengths on the order of 1 x 10^6 V/m were pulsed for 10 μs to kill the unwanted cells. While this method could achieve greater than 99% purity at rates up to 1000 cells/s, the resulting sample still required additional separation techniques, such as centrifugation, to isolate the living cells. Wang and Lu (2006) performed non-fatal electroporation on mammalian cells in a microfluidic chip by simply creating a constriction in the channel through which the particles must pass. Combining the ideas of these two studies has potential for the development of a microfluidic selective electroporation cell sorter.

Minimizing the activation time for sorting of desired particles can lead to higher throughput and higher purity of the collected sample. Chen et al. (2006) proposed a fluid directing switching method that incorporated rapid bubble formation to create displacement fluid jets. The fast response (5 μs) of the 20 μm x 20 μm microheater used to create bubbles makes high speed particle throughput possible. Dynamic sorting was not demonstrated and limitations were not quantified. The creation of a recirculation zone in the separation region when the bubbles collapse may reduce the potential sorting rates. Also, the fabrication process with integrated heaters is more involved than basic microfluidic chips.

Hydrodynamic and electrokinetic flow switching sorting techniques have been used most widely for μFACS systems. Fu et al. (2004), using electrokinetic flow, and Kruger et al. (2002), using hydrodynamic flow, demonstrated the ability to collect to samples in various channels, but do not report performance values for dynamic sorting. Using an electroosmotic cell sorter, Fu et al. 1999) achieved 30-fold enrichment and 20% recovery of viable *E. coli* cells at 10 cells/s. In a later study of a similar design, Fu et al. (2002) used hydrodynamic flow and pneumatic valves to sort *E. coli*. They demonstrated a number of test sequences with varying parameters. Two such results achieved 48% recovery and 7-fold enrichment for a sample with 0.04 initial fraction at 1.3 cells/s and 21% recovery and 89-fold enrichment for a sample with 0.001 initial fraction and a throughput of 26 cells/s. The recovery efficiency appears to decrease with increased particle frequency and the enrichment of the

collected sample was much improved for rare target cell conditions; these values agree with theoretical predictions of cell sorting.

The fully operational microfabricated sorting system by Yang et al. (2006) uses pneumatic micro-valves, with a 15 Hz response limit, to direct the desired cells for collection. The cell throughput is 2 cells/s with a reported 2% sorting error. The external driving mechanisms in pressure driven systems usually do not have the required response for high speed flow switching, therefore the use of active valves is necessary. These valves are commonly constructed with 3D fabrication techniques. The extra complexity is avoided with electrokinetic flow switching.

The configuration of the switching/collection region is an aspect of the design that has not been thoroughly addressed in literature. Successful sorting has been accomplished with a variety of chips, but better understanding of individual features is important. One of the main inconsistencies is the use of directing streams that act to deflect the particle during the separation process. The use of additional streams has potential to provide better control of electric and pressure fields within a chip. Several reported designs include this element, while others do not. Dittrich and Schwille (2003) used perpendicular flow to deflect the particles slightly in the direction of desired collection to improve the likelihood it would be captured by the correct channel. Johann and Renaud (2004) use similar flows to prevent backflow pressure from reversing the particle motion away from the desired reservoir. Whether the value of these arguments justifies the use of additional channels, which increase the overall complexity of the system, is a question that is addressed in Chapter 7.

The number of collection channels also varies by design. Traditional systems have a waste reservoir and a collection reservoir for the target cells, but this can be expanded to multiple collection reservoirs for multiple target cells. Two collecting streams are used in the majority of studies. A handful of designs include three collecting streams, but the effectiveness of this system relies on the simultaneous detection of multiple target cells.

In all of the fluidic switching studies, the potential throughput of particles is much less than the 10 000 cells/s capabilities of conventional FACS systems. Rates approaching the reported limitations imposed by the detection system have been demonstrated. Considering microfluidic systems can take advantage of parallelization, overall processing can still be improved significantly. There is opportunity to achieve higher efficiency of the sorting mechanism by investigating the components of the switching design.

2.5 Conclusion

The use of microfluidic technology for the miniaturization of bio-analytical devices has been successfully demonstrated and commercialized for a variety of processes. There are several benefits of reducing the scale of the system, which include better control of transport properties, reduced cost, portability, and higher efficiency of operation. Cell cytometry and FACS devices show potential for similar adaptation to lab-on-a-chip systems. Furthermore, characterization and enrichment of cell subpopulations is often a prerequisite for biological analysis techniques.

Several studies have reported microfluidic cell cytometers and μFACS systems that are capable of detecting fluorescently labeled target cells and sorting them to a desired collection reservoir. Hydrodynamic and electrokinetic flow systems are commonly used for bulk flow transport and several methods of cell directing have been employed. Investigations of cell sorting chips generally use large pressure or electrical sources, fluorescence microscopy, or laser light sources which are not practical for handheld operation; therefore, full miniaturization of these units still faces several challenges.

A wide variety of designs have been attempted, but detailed evaluation of specific design components has not been thoroughly reported. In particular, improvements to the focusing junction and sorting regions can reduce the required power for operation and improve the efficiency of sorting. Also, the current methods of estimating the focused stream width from experimental focusing data do not directly address the location of the dividing streamlines between the sample and sheath fluids, which is the true measure of focusing.

Chapter 3

Experimental Setup and Procedures

The major components of the experimental setup used in this work were acquired for the purpose of visualizing fluorescent samples in various lab-on-a-chip devices at the Microfluidics and Biochip Laboratory. These include the fluorescence microscope, charge coupled device (CCD) imaging system, and high voltage power sequencer. The remaining items in the experimental apparatus were designed and implemented specifically to perform tests on microfluidic cell sorter chips. In this chapter, details of the experimental system are presented and the procedures followed in this work are described.

3.1 Methodology

Fluorescence flow visualization was used to investigate flow behaviour of dye and particle samples inside the microfluidic chips. The experimental method for testing the devices is relatively straight-forward; however, attention to details is important to avoid contamination and to generate repeatable results. First of all, the chips, consisting of a network of fluid microchannels connecting fluid reservoirs, were fabricated using the soft-lithography method, with the exception of the Micralyne glass chip. The PDMS and glass chips were filled with de-ionized (DI) water and sealed for storage until use.

The glass chip required a cleaning rinse of acid, base, and water prior to use in experiments to ensure residual materials from previous days were removed. Since the PDMS chips were single use, this step was not necessary. The reservoirs of both chips were then filled with the electrolyte buffer solution and the entire chip was purged of the initial contents using electroosmotic flow. Electroosmotic flow was induced by supplying an electric field via applied potentials in the reservoirs. After purging with buffer solution, the chip was ready for experiments.

The dye sample or particle solution was placed in the chip's sample reservoir and the level of the buffer solutions were replenished, if necessary. The voltage distribution was controlled with the software accompanying the power sequencer to achieve sample focusing and dynamic cell sorting. Focusing studies were performed with fluorescent dye under various operating conditions; single

images were acquired with the microscope CCD camera image acquisition system. Fluorescent particles undergoing focusing were recorded as a series of high-speed images. Investigation of the dynamic flow switching operation was performed by real-time monitoring and recording of images. The data for focusing and particle collection was analyzed and used to evaluate the designs

3.2 Working Solutions and Samples

The solutions chosen for this study are commonly used in biological sample processing and fluorescence flow visualization. The basic properties of these fluids are present in literature.

3.2.1 Buffer Solution

Buffer solutions are employed in bio-analytical processes primarily because of the ability to attain a well-defined pH level by choosing the chemical compounds and the concentration. The solutions can maintain this pH level under moderately varying environmental conditions. The electrolysis of water that occurs under electroosmotic flow operation can alter the solution pH during long operating times [Bello (1996)], but this effect can be minimized by using certain buffer solutions. This is extremely important when the biological samples are sensitive to the surrounding pH and require a constant level. For microfluidic applications, the surface charge present at the solid-liquid interface is dependent on the pH; therefore, the electroosmotic mobility of the fluid also varies with pH.

The working aqueous buffer solution for these experiments is sodium (bi-)carbonate. 7.96×10^{-3} mol of sodium carbonate and 0.68×10^{-3} mol of sodium bicarbonate were added to 200 millilitres of de-ionized water to create a 50 mM solution concentration with pH = 9.0 [Sinton (2003)]. The properties of the solution are similar to water: density, ρ = 998 kg/m^3, viscosity, μ = 0.001 Ns/m^2, and thermal conductivity, k = 0.6 W/mK. These values are used for modeling the buffer solution.

3.2.2 Fluorescent Dye

Fluorescent dye is used in flow visualization as a means of effectively imaging specific regions of flow that are difficult to observe with brightfield illumination and direct monitoring methods. Choosing how the dyes are implemented in the fluid system is important to the overall effectiveness of the fluorescent visualization methods.

The fluorescent dye was placed in the sample reservoir and used to visualize sample focusing. The dye used in this study is standard reference fluorescein (Molecular Probes, Oregon) diluted in 50 mM

sodium (bi-)carbonate buffer to a concentration of 100 μM. Fluorescein has a peak excitation frequency of 490 nm and a peak emission frequency of 513 nm. The absorption and emission spectra are shown in Figure 3.1.

The concentration of the dye solution is low enough that fluid properties are assumed to be the same as the electrolyte buffer. The diffusion coefficient of fluorescein at this concentration has been reported to be 4.37 x 10^{-10} m^2/s and the dye is anionic [Sinton (2003)].

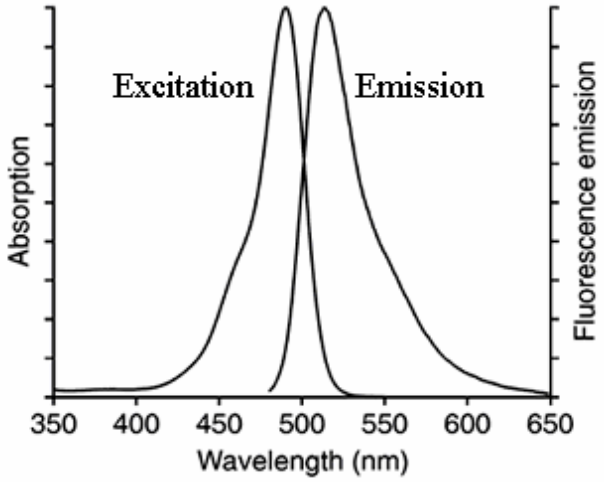

Figure 3.1 Excitation and emission spectra for fluorescein dye at pH = 9.0.

3.2.3 Fluorescent Particles

Staining cells with fluorescence is a conventional method for detection in cell cytometry process, such as counting and sorting. Proper staining allows for optical differentiation of cells of interest in matrix or multi-cell solutions. Applying this technique requires the capability to cultivate live cells or to handle biological mixtures and detailed knowledge of staining processes. Since the laboratory equipment necessary to accomplish these tasks was unavailable at this time of this thesis, an alternative testing sample was required; fluorescent microspheres were substituted for the stained cells.

Three separate microparticle solutions were used during the course of the experiments. The first set contains particles with a nominal diameter of 4.0 μm (Molecular Probes, Oregon). The beads are made from a polystyrene latex material with a sulfate modified surface and they are filled with a fluorescent dye mixture. The concentration of the stock particle solution is 2% or 5.7 x 10^8 particles/ml, but was diluted to 0.05% for experiments. Properties of the particles are not well

reported, but the sulfate modified surface groups are believed to produce a negatively charged surface. The peak excitation and emission wavelengths for the yellow-green particles are 505 nm and 515 nm, respectively. The second set purchased from Polysciences, Inc. (Pennsylvania) consists of microspheres with a nominal diameter of 1.0 μm and are reported to be neutral or slightly negatively charged [Eckenrode et al. (2005)]. The stock solution has a concentration of 2.5% or 4.55 x 10^{10} particles/ml. A diluted sample concentration of 0.025% was used in experiments. The 1.0 μm particles are also yellow-green fluorescent and have peak emission and excitation wavelengths at 441 nm and 486 nm, respectively. The third microparticle solution has spheres with a nominal diameter of 3.8 μm and was supplied in a 0.005% aqueous solution, approximately 1 x 10^{7} particles/ml (Bangs Laboratories, Inc., Indiana). These particles contain a combination of dyes and can be excited with any light in the range of 365 nm-650 nm.

For dynamic sorting operation, a mixture of the 3.8 μm and 4.0 μm microsphere suspensions was created. Various concentrations of each particle were used in the suspensions. The most commonly used mixture consisted of 0.004% and 0.04% solids for the 3.8 μm and 4.0 μm microspheres, respectively. Since the stock solution of the 3.8 μm particles was already sufficiently diluted, it was necessary to replace the stock fluid, water, with the buffer used in the experiments. This was accomplished by allowing the particles to settle at the bottom of a PCR tube, at which point the majority of the fluid was extracted and replaced by a similar quantity of buffer solution. As a result, the suspension concentrations described are estimates of the true concentration. The observed initial particle fractions were calculated for each test run and were found to vary from 0.1 to 0.5 for the 3.8 μm particles. The initial fraction values are reported with the experimental results in Chapter 7.

3.2.4 Cleaning Solutions for Glass Microfluidic Chip

To eliminate contaminants from settling in the Micralyne glass microfluidic chip, a rinse of acid, base, and de-ionized water was performed before and after the experiments. The acid and base solutions used in this procedure were 1 M hydrofluoric acid and 1 M sodium hydroxide, respectively.

3.2.5 Preparation of Solutions

The aqueous sodium (bi-)carbonate buffer, hydrofluoric acid, and sodium hydroxide solutions were prepared in 250 ml batches at the desired concentration and stored at 2-5 ˚C. Prior to experiments the solutions were temporarily stored in 0.5 ml PCR tubes. The fluorescein solution was diluted from the

stock concentration to the experimental concentration with sodium (bi-)carbonate buffer. The fluorescent dye and microparticles were stored at 2-5 ˚C in 0.5 ml PCR tubes. All solutions, except the microsphere suspension, were filtered using a 0.2 μm pore size syringe filter before the experiments.

3.3 Microfluidic Chips

In this study two distinct types of chips were tested. The first chip design was constructed from etched glass, while all subsequent designs were fabricated in a polymer material bonded to a glass slide.

3.3.1 Fabrication

The first chip was designed before renovations to the Microfluidics and Biochip Laboratory facilities had been finished; therefore, fabrication from an outside resource was required. A set of 5 identical chips were purchased from Micralyne Inc. that comprised of an etched channel network enclosed by two glass layers. The fabrication process and the chip characteristics are discussed further in Sections 5.2.1 and 5.2.2, respectively.

To fabricate all other testing chips, the soft-lithography method was used. The processing steps of the soft-lithography, as applied to this project, are briefly described in Section 5.3.1. Full details of the recipes used in the fabrication of the testing devices are included in Appendix A.

3.3.2 Preparation for Experiments

The glass chip from Micralyne was re-useable and the PDMS chips were one time experimental devices. Both required preparation before experiments were conducted. The glass chip was cleaned using a rinsing process of 15 minutes of 1 M hydrofluoric acid, 15 minutes of 1 M sodium hydroxide, and 15 minutes of buffer solution. The fluids were drawn through the channel by friction fitting a trimmed pipette tip into one reservoir and creating a vacuum pressure by extending the plunger of a 10 ml syringe. The fluid levels in the remaining reservoirs were maintained to prevent air bubbles from entering the channels, as bubbles cause unpredictable flow behaviour during experiments. The rinsing time lengths were chosen conservatively to ensure the previous solution had been replaced. Also, rinsing was carried out from both ends of the chip to thoroughly purge each channel.

Before running the experiments, an electroosmotic flow purging rinse is completed with the buffer solution. This drives out any fluids that may be remaining in the channels. The duration of the rinse is usually five minutes.

To prevent the microfluidic chips from drying and contaminants from solidifying during storage, all chips were filled with de-ionized water and sealed with a polyfilm wrap. The DI water saturation was performed after the acid and base rinse for the glass chip and immediately after O_2 plasma treating for the PDMS chips. Failure to fill the channels with an aqueous solution shortly after plasma treating allows the surface properties to revert back to the non-ideal hydrophobic state.

3.3.3 Chip Mounting Platforms

Two separate mounting devices were constructed to handle the two sizes of chips used in these experiments. The mounts, shown in Figure 3.2, included holders for the platinum electrodes, which were placed in the fluid reservoirs, and electrical connections for the high voltage power sequencer. The electrodes for the glass chip holder were fixed on the mount and required manual positioning in the reservoirs prior to each experiment. The repeatability of placement of the electrodes was low, introducing a small source of error. Also, frequent bending of the electrodes caused them to break and require frequent replacing. In the PDMS chip mount, a two piece mounting unit was machined such that the entire electrode assembly could be lifted from the chip holding bracket. This helped improve repeatability in placement of the electrodes. The electrodes were moveable along the length of the chip and additional flexibility was achieved, without sacrificing the quality of the platinum wire, by using a copper insert that bolts to the mount. The copper inserts, visible in Figure 3.2(b), were also interchangeable. The versatility of this mount proved very valuable due to the number of designs tested and the varying reservoir locations.

The designs were also developed with the requirement of optical access from the top for microscopy. The working distance of the objectives limited the distance from the chip that the electrodes or other components could extend.

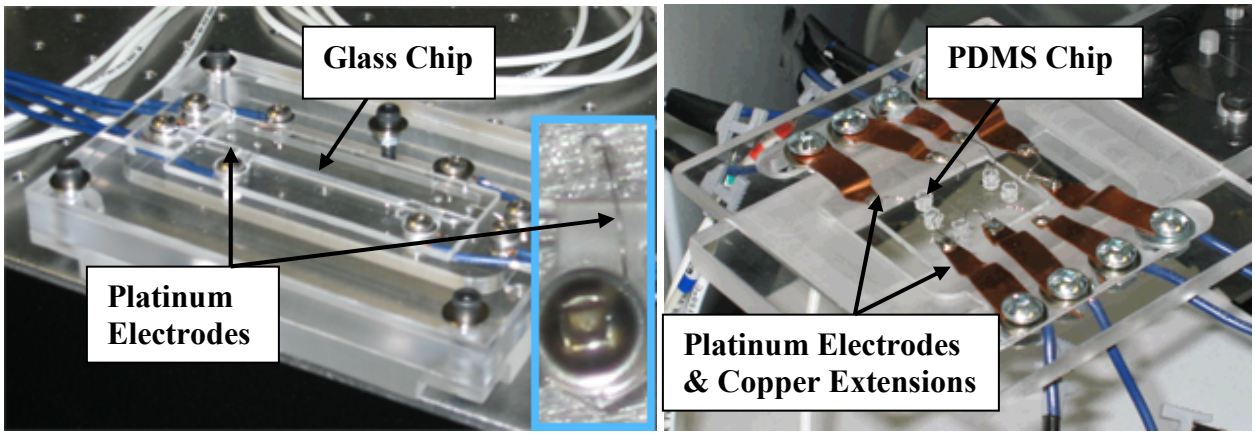

Figure 3.2 Chip mounting units with electrical connections for a) the glass chip and b) the PDMS chips.

3.4 Sample Visualization – Fluorescence Microscopy

Fluorescent visualization methods were used in these experiments to characterize the flow of particles and sample solutions. This was performed with a fluorescent microscope and CCD imaging system.

The fluorescence microscopy was completed on two separate systems. The microscope used in nearly all the dye and particle flow experiments is the Olympus BX-51M metallurgical fluorescence, reflected light, upright microscope (Figure 3.3). The major components of the system include the dual lamp housings (Hg arc lamp and Halogen lamp) with corresponding mirror housing, optical illuminator and filter mount, objectives, filter cubes, and CCD camera with acquisition computer. The latter three items are discussed in greater detail below. The specifications of the system were chosen expressly for microfluidic visualization according to the initial equipment budget.

The second fluorescence microscope, which was used for pressure evaluation studies and measurements of the fabricated chips, is the Olympus GX-71 reflected light, inverted microscope. The components of this system are similar to the BX-51M microscope with the primary differences being inverted observation and an additional number of objectives.

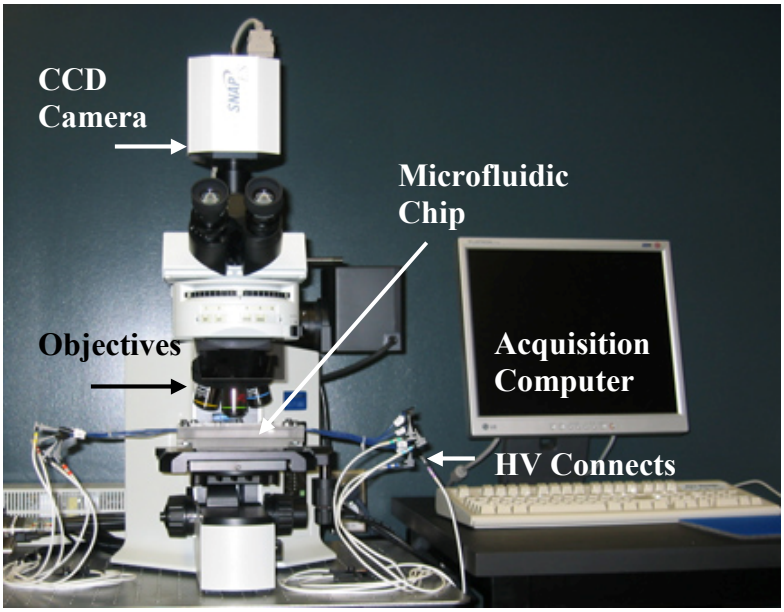

Figure 3.3 Fluorescence microscopy system for flow visualization. The system consists of an Olympus BX-51M microscope, CCD camera, and image acquisition computer.

3.4.1 Objectives

Choosing objectives is important due to the sensitive nature of fluorescence microscopy. The inherent low light levels place an emphasis on maximizing the light that is captured. This is achieved with a high numerical aperture (NA), which is defined by,

$$NA = n \sin \theta \qquad \textbf{(3.1)}$$

where n is the index of refraction of the surrounding medium (air or immersion fluid) and θ is the half-cone angle of the light that is acquired by the objective. Increasing the NA has a positive effect on the ability to perform fluorescence visualization, i.e. better spatial resolution, more sensitive light detection, and shallower depth of field. Trade-offs exist with high NA objectives. The distance between the objective and the sample, called the working distance, is shorter and often require the use of immersion fluids.

The channels that contain the samples were encased by a 1 mm thick glass microscope slide on one side and PDMS on the other, which ranges in thickness from 1- 7 mm. These dimensions presented a minimum limit on the working distance. The upright microscope required observations be made through the PDMS layer and enough space provided to allow the electrodes to have access to the reservoirs without contacting the metal objective housing.

Three objectives were chosen for the BX-51M microscope and five for the GX-71 microscope. The specifications are detailed in Table 3.1. All of the objectives can be used for fluorescence, brightfield, and darkfield lighting methods.

Table 3.1 Objective specifications for BX-51M and GX-71 fluorescence microscopes.

Objectives BX-51M:	**UMPlanFl-BD 10x**	**UMPlanFl-BD 20x**	**LMPlanFl-BD 50x**		
Magnification	10x	20x	50x		
NA	0.3	0.4	0.5		
Working Distance (mm)	6.5	3	10.6		
Objectives GX-71:	**UMPlanFl-BD 5x**	**UMPlanFl-BD 10x**	**UMPlanFl-BD 20x**	**LMPlanFl-BD 50x**	**LMPlanFl-BD 100x**
Magnification	5x	10x	20x	50x	100x
NA	0.15	0.3	0.46	0.5	0.8
Working Distance (mm)	12	6.5	3	10.6	3.3

The magnification of the objective reduces the amount of light gathered by an epi-illumination microscope; therefore it is important to limit the magnification to values that are necessary to perform the tasks. The 10x and 20x objectives on the BX-51M system were used for the majority of glass chip experiments and the PDMS chip testing was done virtually exclusively with the 10x objective. The 10x objective has a NA of 0.30 and a working distance of 6.5 mm and the specifications of the 20x objective are 0.40 and 3.0 mm for the NA and working distance, respectively.

3.4.2 Sample Excitation/Emission/Filtering

Mercury arc lamps are the light source for fluorescence imaging in both microscopes. The BX-51M and GX-71 microscopes are fitted with 100 W Hg lamps. Filter cubes were used to generate a solitary band of excitation light that corresponds to the excitation and emission spectra of the dye samples. The filter cubes consist of an excitation band pass filter, a long pass dichroic mirror, and an emission long pass filter. The BSWM Olympus filter cube was used for fluorescein dye and the 1.0 μm and 4.0 μm microspheres. This filter unit has the following wavelength characteristics: BP450-480 nm excitation, DM500 nm Dichroic mirror, and BA515 nm long pass emission. The GSWM filter cube with BP510-550 nm excitation, LP570 nm Dichroic mirror, and BA590 nm long pass emission was used with the 3.8 μm microspheres. The nominal values of the filter cube components represent the wavelengths at which half transmission occurs.

3.4.3 CCD Imaging

The CCD camera was used to record high speed images during microscopy visualization. The key specifications for a CCD camera include the frame grabbing rate, the spatial resolution, the sensitivity, and the scan recording technique. High frame rates are desirable to capture sequences and perform particle tracking. The monochrome CCD camera used in this work (Photometrics CoolSNAP ES) can acquire images at 10 frames per second in full-scale and full-depth operating conditions. The merging of neighboring pixels, called binning, allows up to 50 frames per second at full-depth. The CCD sensor has 6.45 x 6.45 μm pixels with an imaging area of 8.77 x 6.6 mm and a 12 bit image depth to quantify both low and high level signals in the same image. The camera has high quantum efficiency which allows sensitive observation of low light experiments. The CCD uses a progressive scan imaging process. This method acquires signals from all pixels sequentially during one scan. This differs from interlaced scanning which scans only the odd pixels or only the even pixels during each scan. Progressive scanning eliminates flickering that can occur with interlaced scans and provides better resolution.

The camera is mounted to the BX-51M microscope with a 1.0x magnification c-mount adapter. The approximate field of view corresponding to the 10x, 20x, and 50x objectives are 880 x 660 μm, 440 x 330 μm, and 180 x 130 μm, respectively. Calibrations were performed for each objective using images of a micrometer scale.

A similar camera (Q-Imaging Retiga EXi Mono) was used in visualization with the GX-71 microscope. This camera acquires images at 12 bit depth with pixels of the same size. The frame rate and scanning method are the same as the CoolSNAP ES. A 0.5x c-mount provides a wider field of view than the BX-51M system. Calibrations were completed for all of the objectives using the same micrometer scale procedure.

Image Pro-Plus is the software used with both systems to capture the images and perform post-image processing. Intensity line profiling, particle tracking, data filtering, image level adjusting, and spatial measuring were commonly executed in Image Pro-Plus. For acquisition, the program is very flexible and has several manual and automatic adjustment features.

3.5 Flow Control

Electroosmotic flow in the experiments was achieved by applying a voltage distribution to generate an electric field. A high-voltage (HV) power sequencer was implemented for this task.

3.5.1 HV Power Sequencer

The Labsmith HVS448-3000 power sequencer has eight independent channels, each capable of supplying a maximum of 3000 V. This enables as many as eight reservoirs to be designed in the fluidic chip for controlling the particle transport. The corresponding Sequence software allows the channel levels to be changed manually in real-time or programmed for more complex sequences. The ability to adjust the voltages easily and simultaneously was necessary to perform focusing and cell sorting studies. Modules have been developed to control the HV sequencer from LabVIEW to implement control systems for setting the voltage distributions. Current and voltage monitoring during experiments provided authentication of the applied potential field and helped in the discovery of system irregularities, which generally indicated disconnected electrodes or the presence of bubbles in the channels.

3.5.2 Flow Switching

One of the major advantages of using electroosmotic flow is the ability to switch flow directions without complicated pressure systems and valves. This can be accomplished by changing the electric field in the channels in the sorting region. Experimentally, the voltages that achieved the desired flow were determined by manually adjusting the levels. The number of reservoirs for flow switching depended on the chip designs and ranged from two to five reservoirs. Two or three cell collection channels were present for each design, requiring two or three possible voltage combinations. Each combination was programmed as a ‘step’ function in the HV power sequencer to allow simultaneous switching of the applied potentials.

Three operating techniques were implemented to evaluate the flow control and perform flow switching for particle collection. Examples of voltage traces of each method for a binary collection system (2 collection reservoirs) are plotted in Figure 3.4. The first was a timing function programmed to alternate between steps at pre-determined intervals. The time interval for each combination could be set individually. This method was used to investigate general switching capabilities of the system and the designs. Secondly, the manual step selection technique provided flow to a specified reservoir

until a different flow path was selected, at which point the new potentials were set and the system would await the next order. Thirdly, the power sequencer operated in a default mode indefinitely until the alternate step was selected and activated for a specified duration. Once the switching time was reached, the distribution returned to the default setting. This manual 'pulse' sorting method was used with real-time observation of the samples containing two different particles in order to imitate fully autonomous operation.

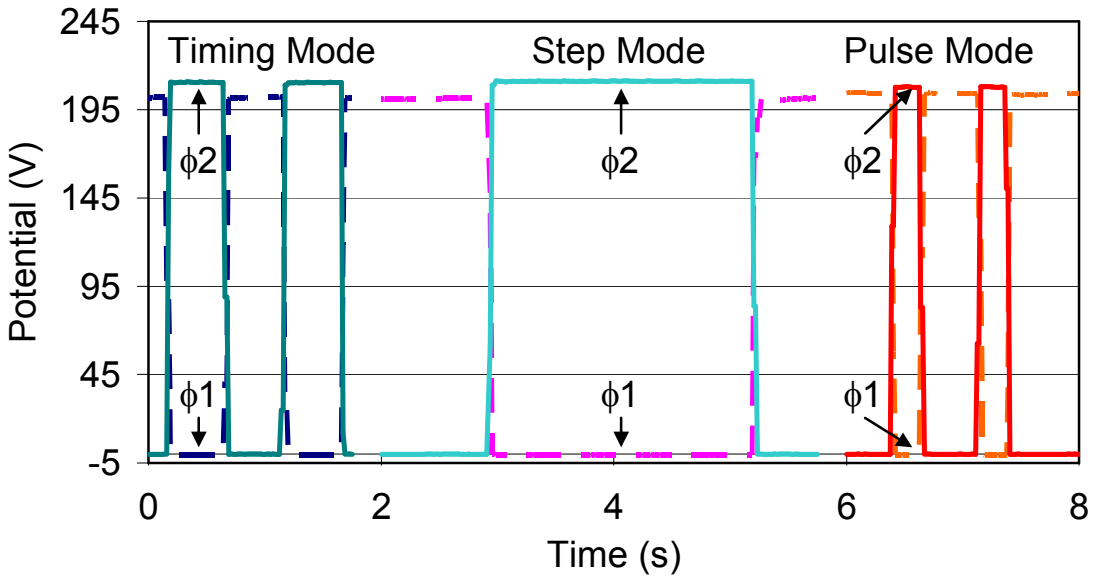

Figure 3.4 Two-channel voltage traces for three modes of flow switching. From 0-2 seconds the voltages switch every 500 ms (Timing Mode). From 2-6 seconds the switching is performed by manual choosing the step switch (Step Mode). From 6-8 seconds the manual pulse mode is operated twice with 250 ms durations (Pulse Mode).

The response of the power sequencer in high-speed switching provided a limitation to the maximum throughput of particles. To reach a steady state voltage, 30-40 ms was required. A trace of high speed channel switching is shown in Figure 3.5 for 100 ms intervals. The pulsing method of sorting, in manual and automated switching, require switching times that exceed 50 ms to account for the power sequencer response. The suggested switching time durations for the tested designs under regular operating conditions are discussed further in Chapter 7.

During switching of the separation voltages, attempts were made to maintain a constant potential at the flow switching junction to minimize the effect on sample focusing. The focusing voltages for each design were held constant throughout the flow switching experiments.

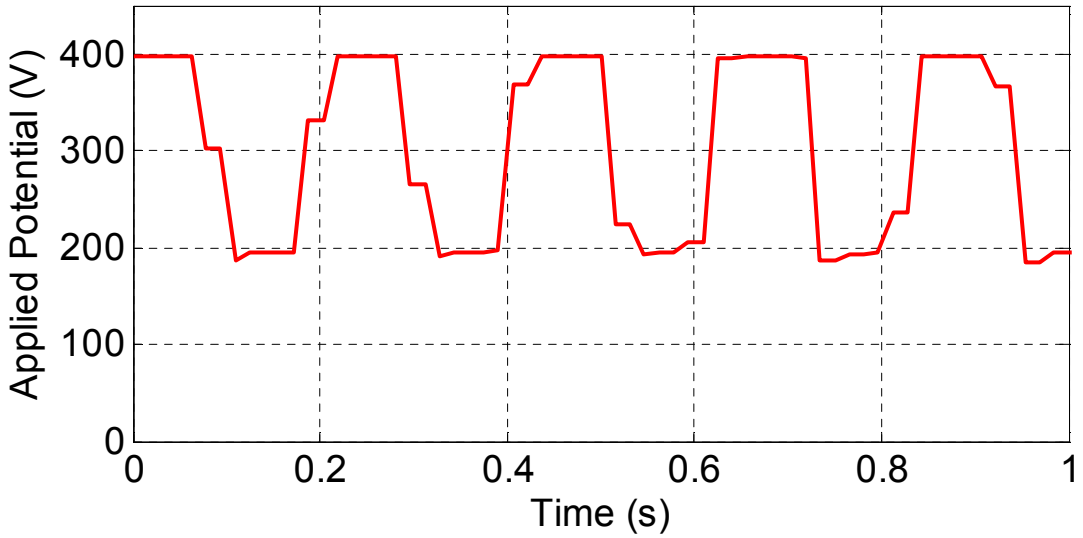

Figure 3.5 Switching response of high voltage power sequencer at 100 ms intervals.

3.6 Safety Measures

During the course of this work precautions were taken to ensure safe operation with the high voltage power sequencer and proper handling of hazardous materials used in the chip fabrication process.

3.6.1 Electrical Safety

The application of high voltages is required to achieve electroosmotic flow. For the microfluidic chips tested in this study, potentials up to 2000 V were applied. Voltages of this magnitude have the ability to cause physical harm. Fortunately, electroosmotic flow is a low-current application with typical maximum current values ranging from 100 μA to 1000 μA. Physical sensitivity to current begins at approximately 0.2 mA with a startle reaction threshold at 0.5 mA [Greenwald (1991)]. At 10 mA paralysis of afflicted muscles can occur, providing a much more dangerous scenario. Asphyxia, the contraction of chest muscles that interfere with breathing, can occur at 35 mA and 50 mA is sufficient for shocks longer than two seconds to disrupt proper functioning of the heart [Greenwald (1991)]. The power sequencer has a built in current limit that was set to 6.5 mA and was rarely exceeded during experimentation.

Additional measures were taken to reduce the risk of electric shocks. The power supplies were grounded to a nearby receptacle. Electrical connections were covered with electrical tape wherever

possible. Efficient space was incorporated into the design of the chip/electrode mount to prevent the microscope objectives from touching the platinum electrodes.

3.6.2 Chemical Handling

Several chemicals employed in the chip fabrication are potentially hazardous to the health of the user. The most dangerous chemicals and materials are the SU-8 developer PGMEA, SU-8 photoresist, acetone, PDMS releasing agent (TCMS), PDMS grafting agent (HEMA), sulfuric acid, and sodium hydroxide. Safety measures were followed as described in their respective material safety data sheets. The precautions included wearing goggles, respiratory devices, gloves, and lab coats when necessary.

Chapter 4

Experimental and Numerical Analysis of the Microfluidic System

The process of using experimental and numerical analyses for design evaluation requires an understanding of the behaviour and characteristics of the system. In microfluidics, effective control of transport properties depends on the working fluid and how it responds under the applied conditions. These attributes can frequently be determined by methods supplemental to the main experimental procedure. This chapter addresses several important parameters of the experimental system: fluid properties, fluid electroosmotic mobility, particle electrophoretic mobility, and pressure influences. Knowledge of the relevant physical parameters allows the use of numerical methods to assist in further understanding of the function of the chip. A variety of models and simulation techniques are available to engineers; the numerical analysis methods used for the design of the cell sorting chip are outlined in this chapter.

4.1 Experimental System Characteristics

The foundation of this project is the precise control of particle transport using an electric field; therefore, knowing the physical and electrokinetic parameters of the fluids and sample particles is necessary. Certain values, such as the physical properties, are either well documented in literature, supplied by the manufacturer, or are commonly assumed, but others are specific to the procedure and need to be investigated. A method of determining the average electroosmotic mobility of various fluids was adapted from literature and the results are presented in this section for fluid-solid combinations relevant to this study. Also, particle tracking measurements are used to determine the approximate electrophoretic mobility of the 3.8 μm and 4.0 μm particles and velocity variations in the populations. The source of on-chip pressure differences and their influence on the flow are discussed.

4.1.1 Physical Properties of Fluids and Particles

The primary working fluid is 50 mM sodium (bi-)carbonate buffer solution. The concentration is sufficiently low that the physical properties of water are assumed: density, ρ = 998 kg/m^3, viscosity,

μ = 0.001 Ns/m^2, and thermal conductivity, k = 0.6 W/mK. The 50 mM sodium (bi-)carbonate electrolyte is reported to have a pH = 9.0 and an electrical conductivity, which is highly dependent on pH, of 0.20 S/m [Sinton (2003)]. The dielectric constant ε_r of water is 80 at 20 °C.

The fluorescent dye sample, fluorescein, was mixed in the buffer at a concentration of 100 μM. The dye solution at this low concentration was assumed to be unchanged from the buffer with the same physical properties. The diffusion of the fluorescein dye was determined by matching concentration profiles obtained by numerical simulation to experimental concentration profiles. The diffusion coefficient D_i = 4.6 x 10^{-10} m²/s was found to provide the best correlation, which is close to the reported value of 4.37 x 10^{-10} m²/s by Sinton (2003). Applying the Nernst-Einstein relationship we can calculate the electrophoretic mobility by,

$$\mu_{ep} = \frac{D_i z_i e}{k_b T_{abs}} \qquad \textbf{(4.1)}$$

where z_i is the valence of the species, e = 1.602 x 10^{-19} C is the magnitude of a proton or electron charge, k_b = 1.381 x 10^{-23} m^2 kg/s^{2}K is the Boltzmann constant, and T_{abs} is the temperature. Fluorescein has a valence z_i = -2 and a corresponding electrophoretic mobility μ_{ep} = -3.58 x 10^{-8} m^2/Vs.

The properties of the microspheres are not well documented. Companies that manufacture fluorescent particles for flow cytometry and similar applications rarely provide more than the size, fluorescent properties, and suspension concentration. All the microspheres are made from polystyrene latex, which has a density ρ = 1.05 g/ml. During storage the particles tend to separate and collect at the bottom of the container, but an ideal suspension is assumed for the duration of the experiments. The 1.0 μm microspheres have a coefficient of variation of 3% and the 3.8 μm microspheres vary in diameter from 3.61 μm to 3.99 μm. These variations cause a non-uniform distribution of charge and mobility in the particle population, which is addressed later in this chapter along with an estimation of the electrophoretic mobility.

4.1.2 Electroosmotic Mobility Measurements – Current Monitoring Method

Direct methods of measuring electroosmotic velocity, such as micro particle image velocimetry (μPIV), require the use of specialized equipment not widely available. As an alternative, the current monitoring method was proposed by Ren et al. (2002) to determine the average electroosmotic

mobility of a solution. The basic procedure is to apply an electric field along the length of a straight microchannel filled with the solution to be tested. The reservoirs on each end are initially full of the same solution. The reservoir containing the anode is siphoned dry of the buffer solution and replaced by a slightly diluted solution of the same buffer. Dilution to 95% of the initial buffer concentration is suggested to maintain a similar mobility. The diluted buffer proceeds to replace the initial solution from the channel at a constant rate. The current draw from the power supply is proportional to the conductivity of the fluid in the channel. The average conductivity changes due to displacement with the lower conductivity fluid and the current drops accordingly. By recording the current throughout this process we can estimate the time required for displacement of the initial buffer. An example of a current measurement is shown in Figure 4.1, where a linear regression was performed to help determine the start and end times of the purging. It should be noted that the electrical connection is broken when the buffer is drawn from the reservoir and the current drops to the baseline level.

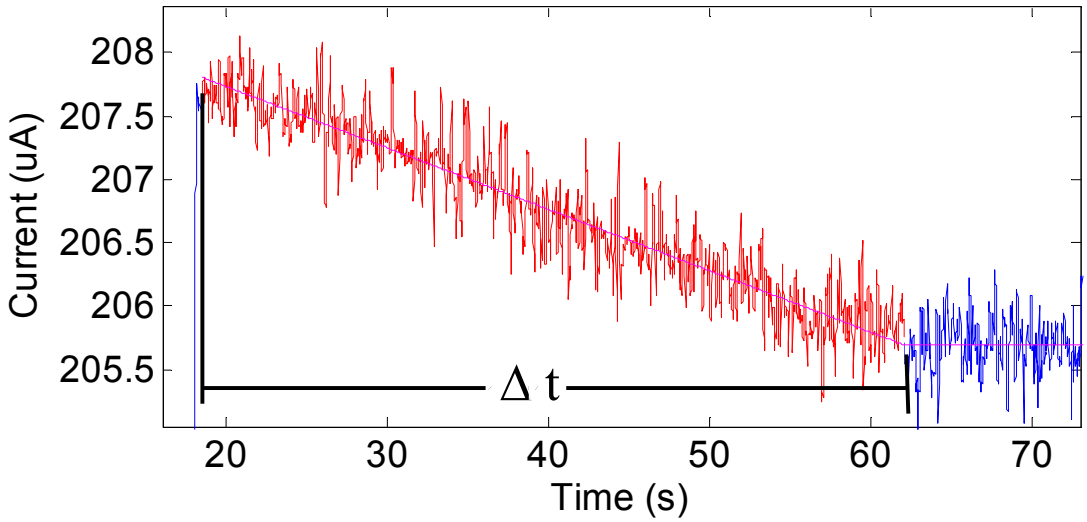

Figure 4.1 Current measurements during displacement of 50 mM sodium (bi-)carbonate solution with a 45 mM sodium (bi-)carbonate solution in a PDMS-glass chip.

Knowing the time duration, Δt, and the length of the channel, $L_{channel}$, we can calculate the average velocity:

$$\bar{u}_{ave} = \frac{L_{channel}}{\Delta t} \qquad \textbf{(4.2)}$$

Equating this average velocity to the Helmholtz-Smoluchowski velocity u_{eof} gives,

$$u_{eof} = \bar{u}_{ave} = -\frac{\varepsilon_r \varepsilon_0 \zeta}{\mu} E_x \qquad \textbf{(4.3)}$$

where ζ is the zeta potential formed at the liquid-solid interface, ε_r is the dielectric constant of the fluid, ε_0 is the permittivity of a vacuum, μ is the viscosity of the fluid, and E_x is the electric field applied along the length of the channel. From the average velocity we can determine the electroosmotic mobility μ_{eof} of the solution and the zeta potential ζ :

$$\mu_{eof} = \frac{\bar{u}_{ave}}{E_x} \qquad \textbf{(4.4)}$$

$$\zeta = -\frac{\mu \cdot \mu_{eof}}{\varepsilon_r \varepsilon_0} \qquad \textbf{(4.5)}$$

It can be seen from Figure 4.1 that resolving the time required for the solution to be purged is not an exact process. To reduce the uncertainties, tests were always performed three times and the average values were documented. Except for the occasional outlying point, the Δt values for a test set were generally within 3% of each other. This level of uncertainty is acceptable and below the expected errors of the system.

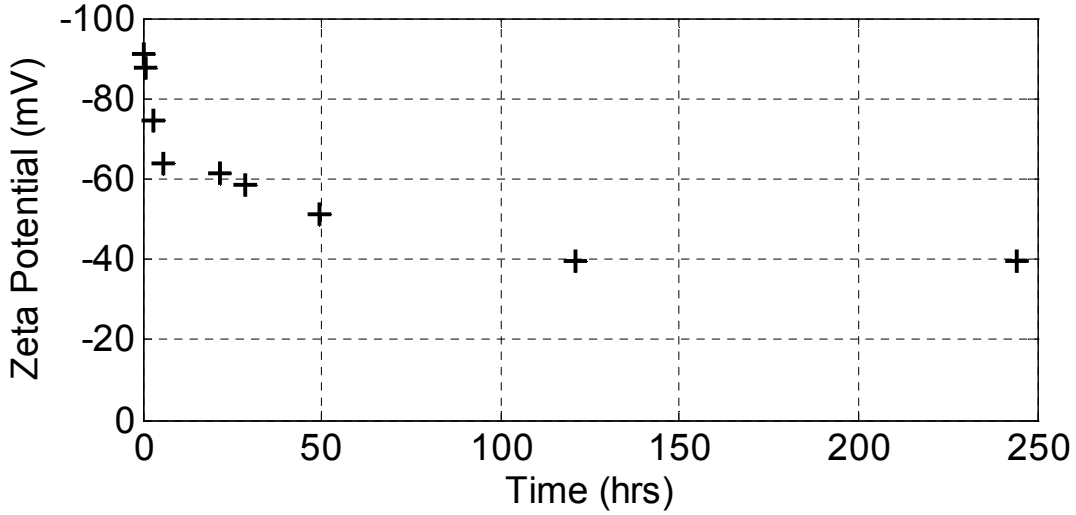

Figure 4.2 Aging characteristics of a PDMS-glass chip. The amplitude of the zeta potential is observed to decrease over time.

This method was used to estimate the mobility of 50 mM sodium (bi-)carbonate buffer in a PDMS-glass chip and a PDMS-PDMS chip. In this process the mobility and zeta potential of PDMS were observed to vary substantially over time. Investigated on a single chip, the zeta potential

decreased significantly with time after the O_2 plasma treatment and bonding, shown in Figure 4.2. Although the use of the same chip for repeated testing may have additional influences, there is a clear trend that agrees with reported findings [Choi and Yang (2003)]. The most drastic change in mobility occurs in the first 12 hours after bonding, therefore it was attempted to perform experiments on chips that were bonded at least 24 hours prior. At this stage, a sufficiently high mobility is maintained and the PDMS exhibits greater stability. Tests performed with PDMS-glass chips of similar age show representative mobility and zeta potential values of 4.9×10^{-8} m^2/Vs and -69 mV, respectively.

PDMS channels are reported to have a lower zeta potential for electrolytes than glass channels. Sinton (2003) reported an average electroosmotic mobility μ_{eof} = 5.7×10^{-8} m^2/Vs and a corresponding zeta potential of -80 mV for 50 mM sodium (bi-)carbonate in a glass channel. The non-uniform zeta potential in hybrid chips creates a non-uniform velocity profile and reduces the validity of 2-D analyses. Spehar et al. (2003) demonstrated a mobility difference of 20% between PDMS-PDMS and PDMS-glass chips with a trapezoidal channel (68 μm wide across top, 41 μm wide across the bottom, and 19 μm deep). The mobility and zeta potential values obtained from the current monitoring method for a PDMS-PDMS channel were 5.9×10^{-8} m^2/Vs and -83 mV, respectively. The reason that these values are higher than the PDMS-glass channel is unclear. Many factors influence the results; however, the small data set for PDMS-PDMS chips may not be truly representative of the material characteristics.

Other factors that influence the mobility of the fluid are the ionic strength and the pH level. The mobility of the electrolyte increases drastically as it reaches very low concentrations. The mobility is stable at pH levels above 6, but decreases below this level to near zero mobility at pH = 4 and below [Spehar et al. (2003)]. This relationship is relevant for long experimental run times where the buffer has been demonstrated to change due to evaporation and electrolysis [Bello (1996)]. The direct effects relating to the experiments performed in this study has not been determined.

4.1.3 Particle Tracking Measurements

Particle observation, imaging, and analyses by fluorescence microscopy were used for two major purposes: seeded particles provided information about the flow, similar to PIV methods, and particles were monitored in real-time for dynamic sorting of cell subpopulations. Particle tracking methods were performed on series of images to determine several parameters of the particle motion, such as position, velocity, and acceleration. Automated tracking was used for low density particle

distributions where the particles do not overlap; otherwise manual tracking was performed by selecting the location of each particle in successive images. An example of particle tracking is shown in Figure 4.3.

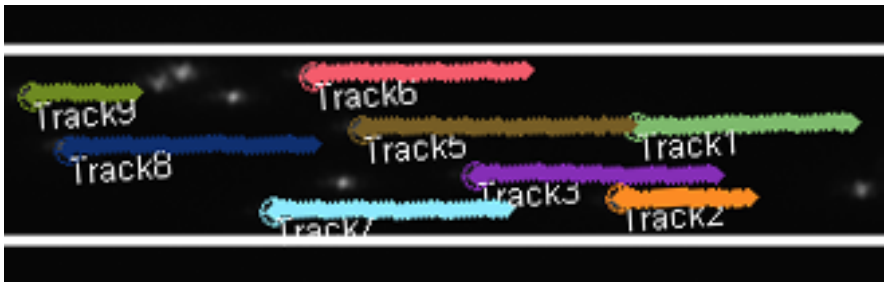

Figure 4.3 Example of particle tracking measurements in microchannel flow.

Measuring the velocity of the particles implies the velocity of the fluid in the absence of additional forces acting on the particles. To determine the validity of this assumption, a length and time-scale analysis is conducted. The force balance for the particle acceleration and the drag force and the drag coefficient C_d are as follows:

$$V_p \rho_p \frac{Dv_p}{Dt} = \rho C_d \frac{\pi \cdot {d_p}^2}{4} \frac{{v_f}^2}{2} \tag{4.6}$$

$$C_d = \frac{k_d}{\mathrm{Re}_d} \tag{4.7}$$

where V_p is the particle volume, ρ_p is the density of the particle, v_p is the particle velocity, ρ is the fluid density, d_p is the diameter of the particle, v_f is the relative velocity of the particle in the bulk fluid ($v_f = V_\infty - v_p$), k_d = 24 for low Re drag on a sphere [White (1999)], and Re_d is the Reynolds number of the sphere in the bulk fluid. Substituting Equations 4.7 and into Equation 4.6 gives,

$$\frac{Dv_p}{Dt} = \frac{3\mu\pi \cdot d_p}{\rho_p V_p}\left(V_\infty - v_p\right) \tag{4.8}$$

where μ is the fluid viscosity. The time constant τ is

$$\tau = \frac{\rho_p V_p}{3\mu\pi \cdot d_p} \tag{4.9}$$

and the corresponding length scale ℓ_τ is

$$\ell_\tau = \tau \cdot V_\infty \qquad \textbf{(4.10)}$$

For the 4.0 μm microspheres (ρ_p = 1050 kg/m^3, d_p = 4.0 x 10^{-6} m) in water (ρ = 1000 kg/m^3, μ = 0.001 kgm²/s) with a bulk velocity of 1 mm/s the time-scale τ = 9.3 x 10^{-7} s and the length scale ℓ_τ = 9.3 x 10^{-10} m. Based on these values, the particles represent the fluid velocity in the absence of additional forces acting on the spheres.

Under electroosmotic driven flow, the velocity of a charged particle is the combination of the electroosmotic velocity of the fluid and the electrophoretic velocity of the particle. The electrophoretic mobility of the particles can be estimated from the observed mobility if μ_{eof} of the fluid is known. Particle tracking is used to determine the observed velocity and calculate the resulting mobility values.

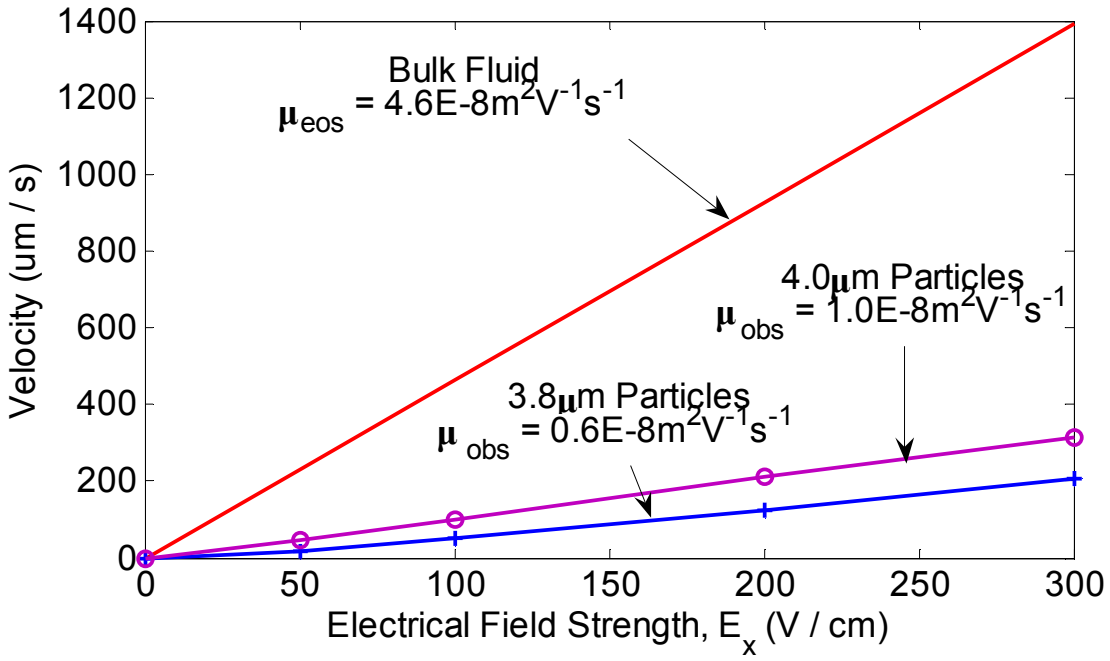

Figure 4.4 The velocity of bulk fluid (50 mM sodium (bi-)carbonate) and 3.8 μm and 4.0 μm particles under an applied electric field. The mobility of the fluid is 4.6 x 10^{-8} m^2/Vs, while the particles exhibit mobility values of 0.65 x 10^{-8} m^2/Vs and 1.04 x 10^{-8} m^2/Vs for the 3.8 μm and 4.0 μm spheres, respectively.

Experiments were conducted to observe the electrokinetic flow of particles in a straight channel under a range of electric field values. The mobility of the buffer solution in the same chip was found to be 4.6 x 10^{-8} m^2/Vs using the current monitoring technique. The comparison between this value and the observed mobility of the 3.8 μm and 4.0 μm particles is shown in Figure 4.4. The electrophoretic

mobility values for the 3.8 μm and 4.0 μm particles are estimated to be -3.95 x 10^{-8} m^2/Vs and -3.56 x 10^{-8} m^2/Vs, respectively. This indicates a strong negative charge on both particles, as the electrophoretic effects almost fully counteract the electroosmotic flow of the buffer.

Variations in the size and charge of the microspheres affect the velocity under an applied electric field. Quantifying the distribution of the velocities among the particles is important for timing mechanisms in automated flow switching and optimization of the design of the chip. The velocity distribution was found by tracking several particles for each flow condition. The distribution immediately after applying an electric field to a fresh particle suspension was observed to be extremely wide (Figure 4.5(a)). This is attributed to a number of positively charged particles, which have a velocity greater than the bulk flow, and the negatively charged particles that constitute the majority of the population. The concentration of positive particles is depleted after a few minutes of running time and the distribution of the particles becomes much narrower, shown in Figure 4.5(b).

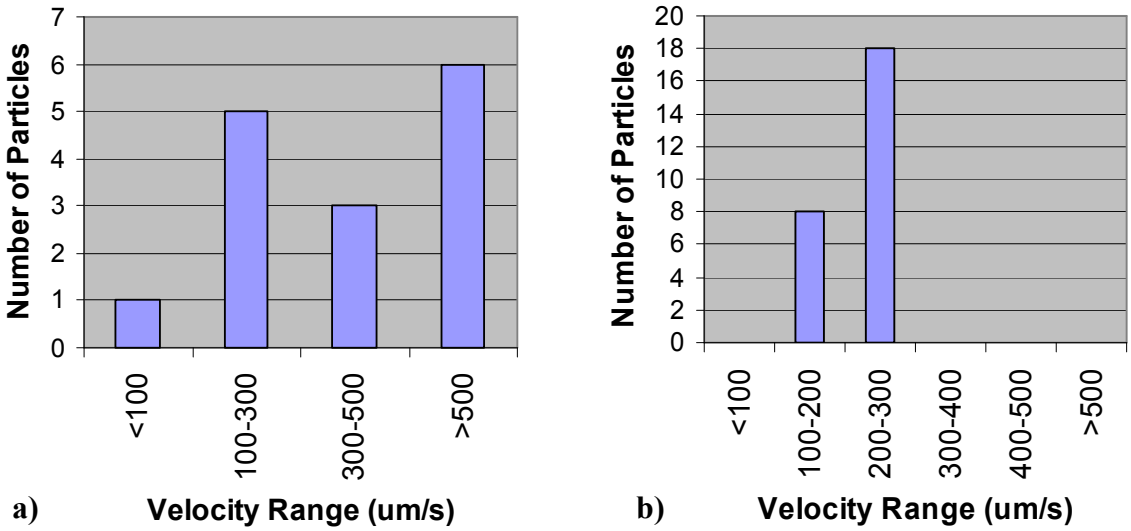

Figure 4.5 Velocity distributions of 4.0 μm particles under an applied electric field. a) The distribution immediately after applying an electric strength E = 50 V/cm. b) The distribution after several minutes of operation at electric strength E = 200 V/cm. The narrower distribution in b) is attributed to the depletion of positive particles.

4.1.4 Pressure Effects in Microfluidic Systems

The uniform velocity profile is one of the main advantages to using electroosmotic flow in microsystems. Introducing a simultaneous pressure field causes deviation from this characteristic. Crabtree et al. (2001) addressed several sources of pressure differences that can be encountered

during normal operation. The unpredictable pressure field determined by these mechanisms alters the flow field and may have severe consequences for the performance of a microfluidic device. Crabtree et al. (2001) observed conditions where the pressure driven flow was on the same order as the electroosmotic flow.

The volumetric flow rate Q in a channel can be calculated by the equation [Beebe et al. (2002)],

$$Q = \frac{|\Delta P| w h^3}{12 \mu L} \left[1 - \frac{h}{w} \left(\frac{192}{\pi^5} \sum_{n=1,3,5}^{\infty} \frac{1}{n^5} \tanh\left(\frac{n \pi w}{2h} \right) \right) \right] \quad \textbf{(4.11)}$$

where ΔP is the pressure difference, w is the channel width, h is the channel height ($w > h$), μ is the fluid viscosity, and L is the channel length. This form of the flow equation is required for low aspect ratio channels ($h \approx w$); flow in high aspect ratio channels ($w >> h$) can be determined by the simplified form,

$$Q = \frac{|\Delta P| w h^3}{12 \mu L} \quad \textbf{(4.12)}$$

The largest contribution of pressure differences arises due to surface tension effects acting at the reservoirs. Laplace pressure is generated at a curved meniscus and balances the surface tension force, which forms at the liquid-air interface. The Laplace pressure ΔP_L for a spherical meniscus is

$$\Delta P_L = \frac{2\gamma}{r_m} \quad \textbf{(4.13)}$$

where γ is the surface tension value for the liquid-air interface and r_m is the radius of the meniscus. The actual shape of the meniscus is a dynamic phenomenon that depends on a number of parameters, such as the location of the electrode, and is generally not a true hemisphere. An estimate of the radius of curvature is related to the radius of the reservoir, $R_{reservoir}$, and the contact angle, θ_{ca}, of the fluid-solid interface:

$$r_m = \frac{R_{reservoir}}{\cos \theta_{ca}} \quad \textbf{(4.14)}$$

If the menisci formed in reservoirs connected by a fluid channel have different radii, then a pressure difference is formed and flow results. This effect is illustrated in the schematic shown in Figure 4.6. The meniscus acts as a flexible membrane and the direction of the Laplace force on the fluid is determined by the displacement to achieve a meniscus of zero radius.

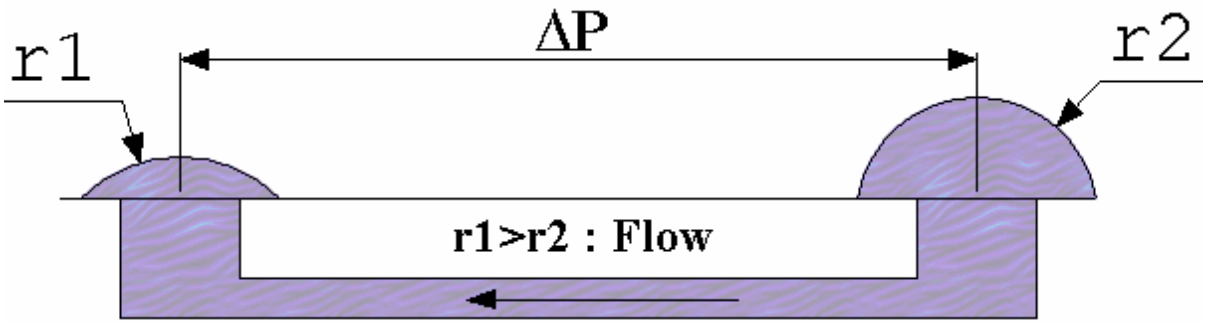

Figure 4.6 Schematic of one mechanism for pressure driven flow in microchannels. Connected fluid reservoirs with different radii cause Laplace pressure differences that result in flow.

Walker and Beebe (2002) employed Laplace pressure to induce pumping in a microchannel. Using Equation 4.13, the magnitude of the pressure generated for water (γ = 72.8 mN/m) forming a hemispherical meniscus in a reservoir with a radius of 1 mm is 146 Pa. The resulting flow of water through a 50 mm long channel of square cross-section with 50 μm sides produces a linear flow rate $\overline{u}_{Laplace}$ = 257 μm/s. Electroosmotic flow of 50 mM sodium (bi-)carbonate buffer in a glass channel (ζ = -80 mV) of the same dimensions generates a velocity u_{eof} = 560 μm/s for an electric field of 100 V/cm. In practice, the radius of each meniscus is relatively similar and the effective Laplace generated force is reduced, but this phenomenon has potential for very noticeable effects on the flow.

Differences in reservoir levels generate hydrostatic pressure forces. Initial height differences and the transport of a fluid from one reservoir to another are the primary causes of this inequality. According to Equation 4.11, the flow of water through the same channel used in the example of Laplace pressure effects (50 mm long channel of square cross-section with 50 μm sides) due to 1 mm of hydrostatic head produces a linear flow rate $\overline{u}_{hyd}$ = 18 μm/s. Compared to $\overline{u}_{Laplace}$ = 257 μm/s and u_{eof} = 560 μm/s, the influence of hydrostatic pressure is confirmed to be minimal unless large reservoirs are used to generate substantial height variations or unusual volumes of fluid are being transported.

The volume of fluid transferring from one reservoir to another reservoir during experiments is generally very small relative to the volume of the reservoir. A transient model was developed to investigate the effects of pressure and volumetric transport. Mass conservation was applied in the reservoirs and a force balance was performed on the channel flow. Full details of the model can be found in Appendix B. The linear flow rate for simultaneous electroosmotic flow and hydrostatic pressure, as described above, is shown for a 10 minute period in Figure 4.7. The 1 mm difference in

fluid levels generates flow in the same direction as the electroosmotic flow. A decrease of 5 μm/s is estimated by the model. For long experimental run times this effect can become significant.

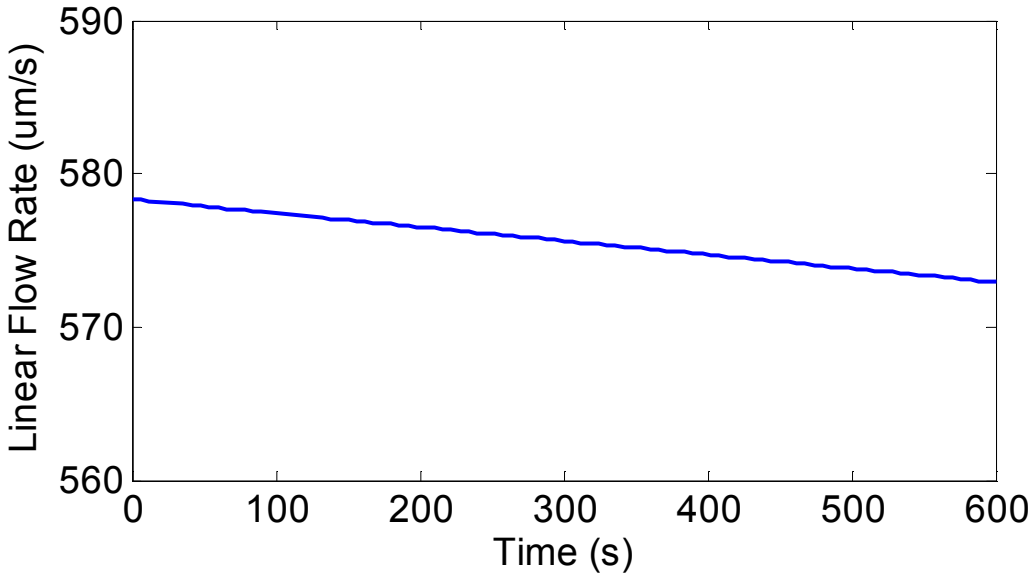

Figure 4.7 Transient linear flow rate for simultaneous electroosmotic flow and pressure-driven flow resulting from a 1 mm hydrostatic head difference between reservoirs. The channel is 50mm long channel with a square cross-section of 50 μm sides. The electroosmotic velocity is specified as u_{eof} = 560 μm/s.

Particle tracking was performed under large hydrostatic pressure differences to confirm the effect of pressure on the bulk flow. Two large reservoirs connected by a 50 mm long straight channel with 40 μm x 50 μm cross section were unevenly filled with a fluorescent particle suspension. For each test, the average velocity of several particles was found by tracking. The maximum particle velocity, which generally occurred in the centre of the channel as expected, was chosen as the characteristic parameter of the flow. The velocities were plotted for the estimated hydrostatic pressure, determined by measuring the fluid levels. Figure 4.8 shows the experimental results and the linear flow rate calculated for the channel using Equation 4.11. The maximum velocity is expected to be greater than the linear flow rate, but Laplace pressure effects were not completely eliminated and they may have reduced the overall flow. Regardless, the effects of pressure are demonstrated to be significant.

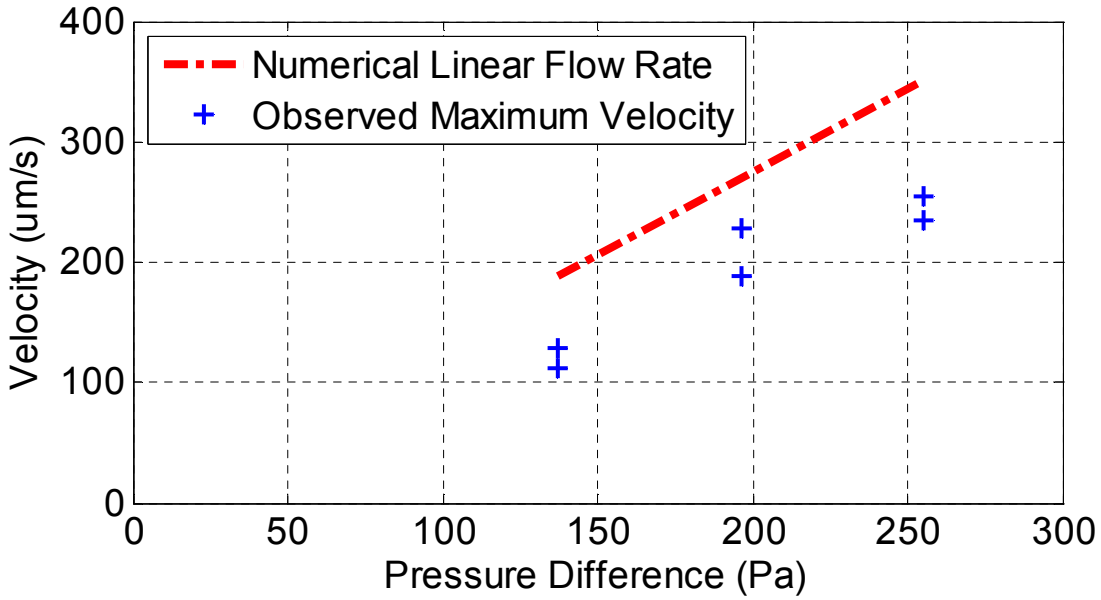

Figure 4.8 Observed particle velocities under hydrostatic pressure and the expected linear flow rate calculated using Equation 4.11.

Fletcher et al. (2001) attempted to reduce the impact of unintended pressure flows by implementing hydrodynamic resistance elements into their microfluidic T-channel. Each channel had a short constriction section where one of the cross-sectional dimensions was reduced. The constriction had a depth of 2.4 μm while the main channels were 24μm deep. Writing the flow rate as the current equivalency,

$$Q = \frac{|\Delta P|}{R_{hyd}} \tag{4.15}$$

the hydrodynamic resistance of the channel R_{hyd} can be estimated from Equation 4.11:

$$R_{hyd} = \frac{12\mu L}{wh^3}\left[1 - \frac{h}{w}\left(\frac{192}{\pi^5}\sum_{n=1,3,5}^{\infty}\frac{1}{n^5}\tanh\left(\frac{n\pi w}{2h}\right)\right)\right]^{-1} \tag{4.16}$$

From Equation 4.16 it is clear that a reduction in the height, or the characteristic (smallest) dimension of the channel, increases the hydrodynamic resistance to the third power for high aspect ratio channels. Therefore, for two channels of equivalent length and width, reducing the height from 24 μm to 2.4 μm improves the resistance to pressure flow by 1000-fold. The results of a series of numerical simulations, presented in Figure 4.9, show a significant improvement in reducing the flow by

implementing a planar resistance element. Two cases were investigated on a straight channel, 100 µm wide and 50 mm long, with a depth that was varied from test to test. A pressure difference of 1000 Pa was applied along a channel with no constrictions and a channel where a 1250 µm long constriction of 10 µm width was integrated in the channel. The large pressure difference was used to exaggerate the results and the constriction width was chosen as a conservative value easily obtained in fabrication. Further reduction of the size or lengthening of the constriction will improve its effectiveness as a hydrodynamic resistance element.

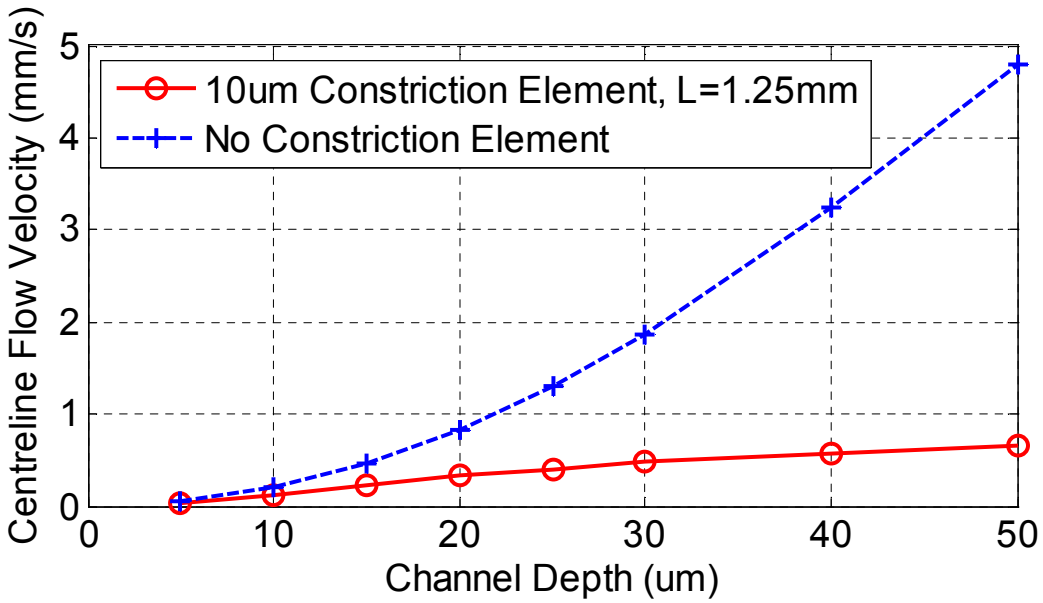

Figure 4.9 Channel centerline velocity with and without hydrodynamic resistance elements. A significant reduction in velocity is observed with a constriction. The values were obtained from a numerical simulation with 1000 Pa applied along a 100 µm wide, 50 mm long channel with a 1250 µm long constriction on one channel.

4.2 Numerical Analysis Methods

Strictly using experimental and analytical methods in the chip design process is time consuming and can limit the range of conditions investigated due to constraints on the testing equipment. Numerical simulations allow multiple parameters of a design or system to be explored relatively quickly. The cost of performing these analyses depends on the type of simulation being performed. Models based on a simplified physical system can often be developed that provide satisfactory results for extremely low computational cost. Due to the simplifications of these models, the accuracy and detail of the results are generally lower than simulations performed with full commercial or custom CFD

packages. The strategy of the numerical analysis is determined by the requirements of the project. In this work, a combination of 1-D circuit equivalency models for the electric and flow fields and 2-D numerical simulations for electric, velocity, and concentration fields were employed. The essential details of these methods are described here. The circuit equivalency derivation is carried out in greater depth in Appendix C for the chip design example used in the following sections.

4.2.1 Electric field and Flow Field Circuit Equivalency Models

1-D circuit equivalency models have been demonstrated to solve linear electric and flow fields for microfluidic chips and provide values that compare well with full numerical models [Qiao and Aluru (2002)]. These compact models lose accuracy in regions of 2-D or 3-D non-uniformities, such as junctions or expansions, and are limited to relatively simple geometries where the channel length is much greater than the channel width, $L >> w$. The major assumptions are as follows: 1-D (uniform velocity and electric potential), steady state, fully developed flow, constant conductivity (potential field), and constant density (flow field).

An example of the chip layout for a 5-reservoir design (1 sample reservoir, 2 focusing reservoirs, and 2 collection reservoirs) is shown in Figure 4.10(a). The potentials and pressures are applied at the reservoirs and each channel has a characteristic resistance value. The equivalent resistance network is illustrated in Figure 4.10(b). One of the primary disadvantages of this method is the need for a unique derivation for each different chip configuration, depending on the number of reservoirs and number of junctions.

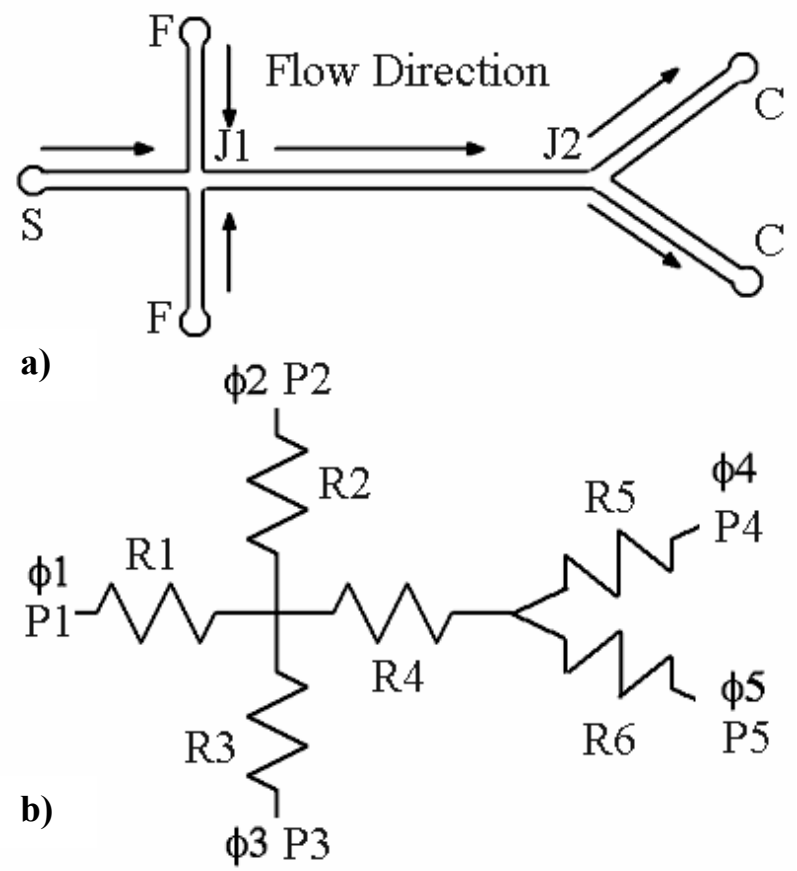

Figure 4.10 Schematic of a) a 5-reservoir chip and the direction of the flow and b) the equivalent resistance network for solving the 1-D potential field and the 1-D flow field.

4.2.1.1 Potential Field

The potential field can be solved for a fluid with constant conductivity by the Laplace equation,

$$\vec{\nabla}^2\phi = 0 \qquad \textbf{(4.17)}$$

where ϕ is the electric potential. The simplified model assumes a linear drop in potential along the channel length and electrical insulation boundaries at the wall. The potential drop ΔV is related to the resistance of the channel, R_V, according to Ohm's law,

$$\Delta V = IR_V \qquad \textbf{(4.18)}$$

where I is the electric current passing through the channel. The applied potentials at the reservoirs are known and the electrical resistance of each channel is related to the cross-sectional area A_c and channel length L. The resistance, R_V, for a channel with uniform conductivity σ is

$$R_V = \frac{L}{\sigma A_c} \tag{4.19}$$

In a rectangular channel $A_c = h \cdot w$, where h is the channel height and w is the channel width.

Applying Kirchoff's law at each node, the potentials at the junctions can be found by solving the system of equations. The electric field strength in each channel is easily calculated once the junction potentials are known. An example of the potential field calculated for the 5-reservoir chip geometry is shown in Figure 4.11. The applied potentials at reservoirs 1 through 5 are ϕ = [500, 500, 500, 100, 0] V, respectively, the channels 1 through 6 have lengths L = [0.01, 0.01, 0.01, 0.01, 0.005, 0.005] m, respectively, and the channel cross-section was 50 μm x 25 μm.

This model can be extended to include multiple resistance elements for each channel. This would be required to solve the electric field of multiple-level chips or channels with varying cross-sectional area.

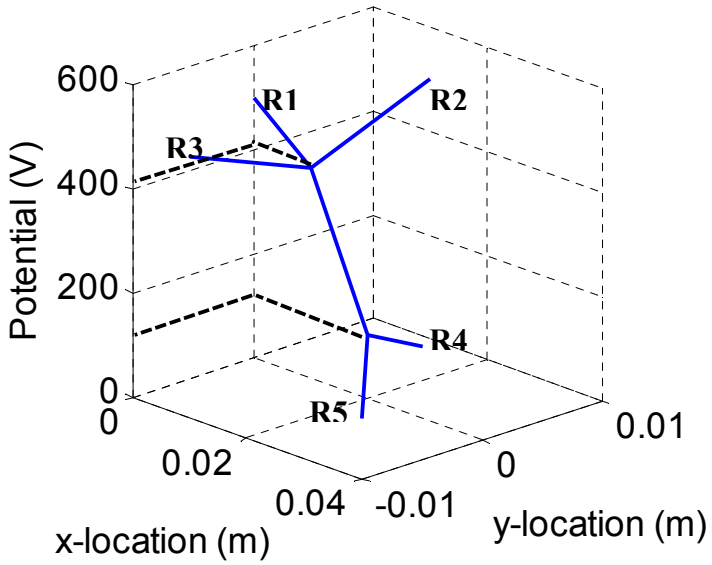

Figure 4.11 Potential field for the 5-reservoir chip design solved using the circuit equivalency model. The applied potential at reservoirs 1-5 are ϕ = [500, 500, 500, 100, 0] V, respectively, the channel lengths for channels 1-6 are L = [0.01, 0.01, 0.01, 0.01, 0.005, 0.005] m, respectively, the channel width w = 50 μm, and the channel height h = 25 μm.

4.2.1.2 Flow Field

The steady, incompressible flow field in microchannels is governed by the Stokes' equation and mass conservation:

$$0 = -\vec{\nabla}p + \mu\vec{\nabla}^2\vec{u} + \rho_e\vec{E} \quad \textbf{(4.20)}$$

$$\vec{\nabla}\cdot\vec{u} = 0 \quad \textbf{(4.21)}$$

The contributions from pressure driven flow and electroosmotic flow are evaluated individually. The Helmholtz-Smoluchowski equation for electroosmotic velocity is applied as a slip condition at the wall, with resulting flow rate Q_{eof},

$$u_{slip} = -\frac{\varepsilon\zeta}{\mu}E_x \quad \textbf{(4.22)}$$

$$Q_{eof} = u_{slip}hw \quad \textbf{(4.23)}$$

The pressure component Q_p can be determined by Ohm's law for the flow field:

$$Q_p = \frac{|\Delta P|}{R_{hyd}} \quad \textbf{(4.24)}$$

where ΔP is the pressure difference along the channel and the hydrodynamic resistance R_{hyd} is calculated from Equation 4.16:

$$R_{hyd} = \frac{12\mu L}{wh^3}\left[1 - \frac{h}{w}\left(\frac{192}{\pi^5}\sum_{n=1,3,5}^{\infty}\frac{1}{n^5}\tanh\left(\frac{n\pi w}{2h}\right)\right)\right]^{-1} \quad \textbf{(4.25)}$$

The overall flow rate Q, where $Q = Q_{eof} + Q_p$, becomes

$$Q = u_{slip}hw - \frac{\Delta P w h^3}{12\mu L}\left[1 - \frac{h}{w}\left(\frac{192}{\pi^5}\sum_{n=1,3,5}^{\infty}\frac{1}{n^5}\tanh\left(\frac{n\pi w}{2h}\right)\right)\right] \quad \textbf{(4.26)}$$

The negative sign on the pressure term indicates that a decrease in pressure along the channel will result in a positive flow rate. It should be noted that the hydrodynamic resistance calculation requires *w* to be greater than *h*. If this is not the case, then the terms must be switched because the characteristic length must be the term raised to the third power.

Applying Kirchoff's law at each junction similar to the electric field provides the pressure field, which is used to calculate the resulting flow field. The pressure field is shown in Figure 4.12 for the same 5-reservoir chip with 100 Pa applied at reservoir 1. The combined pressure flow and electroosmotic flow (μ_{eof} = 5.5 x 10^{-8} m²/s) produce linear flow rates $\bar{u}$ = [0.78, 0.43, 0.43, 1.64, 0.27, 1.37] mm/s for channels 1 through 6, respectively.

Like the electric field model, multiple resistance elements for each channel can be implemented, but the accuracy of the pressure field would likely become less accurate.

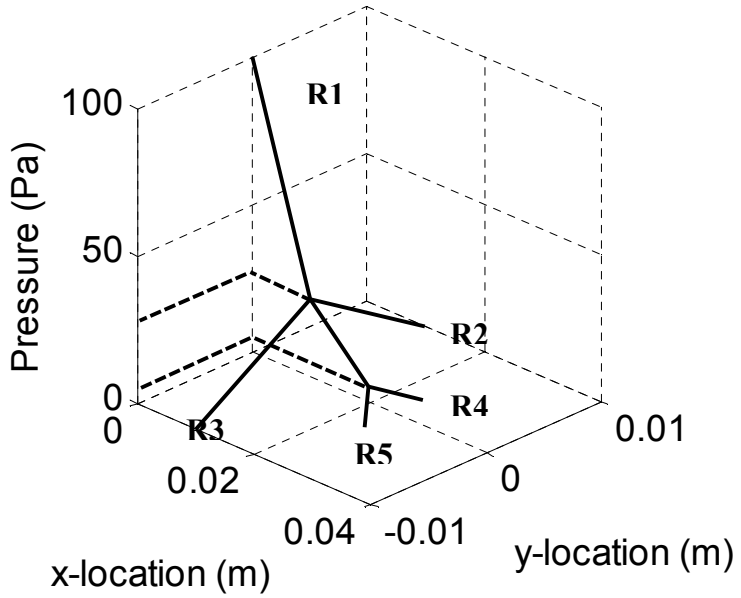

Figure 4.12 Pressure field for the 5-reservoir chip design solved using the circuit equivalency model. The applied pressures at reservoirs 1-5 are P = [100, 0, 0, 0, 0] Pa, respectively, the channel lengths for channels 1-6 are L = [0.01, 0.01, 0.01, 0.01, 0.005, 0.005] m, respectively, the channel width w = 50 μm, and the channel height h = 25 μm.

4.2.2 FEMLAB Numerical Models

A more thorough investigation of the physical parameters can be accomplished with a more detailed numerical simulation. COMSOL Multiphysics 3.2, formerly FEMLAB, was the primary modeling and simulation software package used to evaluate the chip design. COMSOL Multiphysics is a finite-element modeling program that has 2-D and 3-D capabilities. There are many built-in modules to solve momentum, energy, and mass transport for specific applications. The MEMS module and Microfluidics models are particularly useful for the analysis of flow phenomena inside a chip. The electric field, velocity field, and concentration field were solved for the numerical models applied in this project.

The majority of the simulations were 2-D, steady state models. Transient focusing models were used infrequently to observe the transport of the sample from the sample reservoir. A 3-D shallow depth-approximation was used for 2-D modeling of pressure-driven flow to simulate the

hydrodynamic resistance effect of the depth. All other simulations are 2-D, steady flow problems. The fluids are assumed incompressible (constant density) and they have a uniform conductivity. The temperature field is assumed to be constant (20 °C) and iso-thermal.

A triangular, unstructured grid mesh is applied to the domain with the automatic meshing function in Multiphysics. The number of elements is controlled by adjusting the maximum element size for the various subdomains, element growth rate, and the resolution of geometry factor. A higher density mesh is applied in regions of the chip deemed of high importance, such as the focusing junction and the cell separation region.

The stationary linear direct solver UMFPACK was used to solve the model. To reduce the required memory during solving, the modules were solved individually in sequence: potential field, velocity field, then concentration field. This was possible because neither the velocity field nor the concentration field influence the potential field and the flow field can be solved independent of the concentration field.

The governing equations, boundary conditions, and subdomain settings for each of the three models are provided in the following subsections.

4.2.2.1 Potential Field

The DC conductive media model was used to solve the potential field. The governing equation for this model is the potential equation:

$$\vec{\nabla} \cdot \left(\sigma \vec{\nabla} \phi \right) = 0 \qquad \textbf{(4.27)}$$

where σ is the electrical conductivity and ϕ is the potential. The assumption of constant conductivity reduces Equation 4.27 to the Laplace equation.

The wall boundary condition for the potential field is electrical insulation. The applied potentials are specified at the inlets and outlets of the chip. Any interior boundaries have a continuity condition. For the 50 mM sodium (bi-)carbonate buffer used in this work, the conductivity is 0.20 S/m.

4.2.2.2 Velocity Field

The Stokes' flow model was used for the low Reynolds number flow in microchannels. The advantage of this model is that a linear solver can be used, which reduces the required memory. Also, there is an electroosmotic velocity boundary condition included in the model. The Stokes'

approximation, Equation 4.20, and the continuity equation, Equation 4.21, are the governing equations for the velocity field.

Normal flow/pressure boundary conditions are applied at the inlet and outlets of the chip. For purely electroosmotic conditions, all the pressures are set to zero. Otherwise, the pressure is specified and solved using the shallow-depth approximation function. The electroosmotic boundary condition is applied at the wall with either the mobility of the fluid or the zeta potential selected to define the slip velocity. The electric field values are defined by the potential field solution. Interior boundaries have a neutral boundary condition. The constants associated with the flow field are the density (ρ = 1000 kg/m³), viscosity (μ = 0.001 Ns/m^2), and the volume force ($\vec{F}$ = 0).

4.2.2.3 Concentration Field

The concentration field was solved using the Electrokinetic Flow model. The governing equation is

$$\frac{\partial c_i}{\partial t} + \vec{u} \cdot \left(\vec{\nabla} c_i\right) = D_i \vec{\nabla}^2 c_i - \frac{D_i z_i e}{k_b T_{abs}} \vec{\nabla} \cdot \left(c_i \vec{E}\right) + R_i \qquad \textbf{(4.28)}$$

where c_i is the molar concentration of species *i*, $\vec{u}$ is the velocity vector, D_i is the diffusion coefficient of the i^{th} species, z_i is the valence of the i^{th} species, *e* is the magnitude of charge for an electron or proton, k_b is the Boltzmann constant, T_{abs} is the fluid temperature, $\vec{E}$ is the electric field vector, and R_i is the volumetric rate of generation of the i^{th} species by reaction.

The boundary conditions for this model are the known sample concentration at the inlet from the sample channel, zero concentration from the focusing reservoirs, and insulating walls. The use of a strong boundary condition (c_i = 0 M), instead of a gradient condition, on the focusing channel inlets is justified by the function of typical sample focusing. In addition, because of the well defined flow direction in the sample and sheath flows, the concentration domain can be shortened and artificial boundaries are usually placed closer to the focusing junction. Interior boundaries have a continuity condition.

The reaction rate for all of the simulations was zero. The diffusion coefficient, electrophoretic mobility, and charge of the species are constants: D_i = 4.6 x 10^{-10} m^2/s, μ_{ep} = -3.58 x 10^{-8} m^2/Vs, and *z* = -2. The x- and y-velocity components are defined by the velocity field solution and the potential field, which causes electrophoretic transport, is the solution obtained with the DC Conductive Media model.

4.2.3 Comparison of Circuit Model and COMSOL Multiphysics Results

The results of the circuit equivalency model are reported to be similar to more detailed simulations for simple, 2-D chip configurations. The linear flow rates in each inlet and outlet channel and the pressure and potentials at the junctions, determined by the Multiphysics and circuit equivalency models, are compared to determine the approximate accuracy of the simplified circuit model. The chip and operating conditions are the same as for the circuit equivalency model example. The design is a 5-reservoir chip (Figure 4.10) with channels lengths L = [0.01, 0.01, 0.01, 0.01, 0.005, 0.005] m for channels 1 through 6, respectively. The channel dimensions are w = 50 μm and h = 25 μm. The applied potentials at reservoirs 1 through 5 are ϕ = [500, 500, 500, 100, 0] V, respectively, and the applied pressures at reservoirs 1 through 5 are P = [100, 0, 0, 0, 0] Pa, respectively. The electroosmotic mobility of the fluid was set at μ_{eof} = 5.5 x 10^{-8} m^2/s.

The linear flow rates at each inlet and outlet were found to agree within 2% of each other. The predicted pressures and potentials at the junctions had differences of less than 0.2%. Typically the largest discrepancies occur at the junctions where the domain becomes less one-dimensional. In Figure 4.13, the pressure and potential distributions near the focusing junction are plotted for a 1 mm section along the channel. It is clear from these results that the compact circuit model can predict the potential field and pressure field with acceptable accuracy.

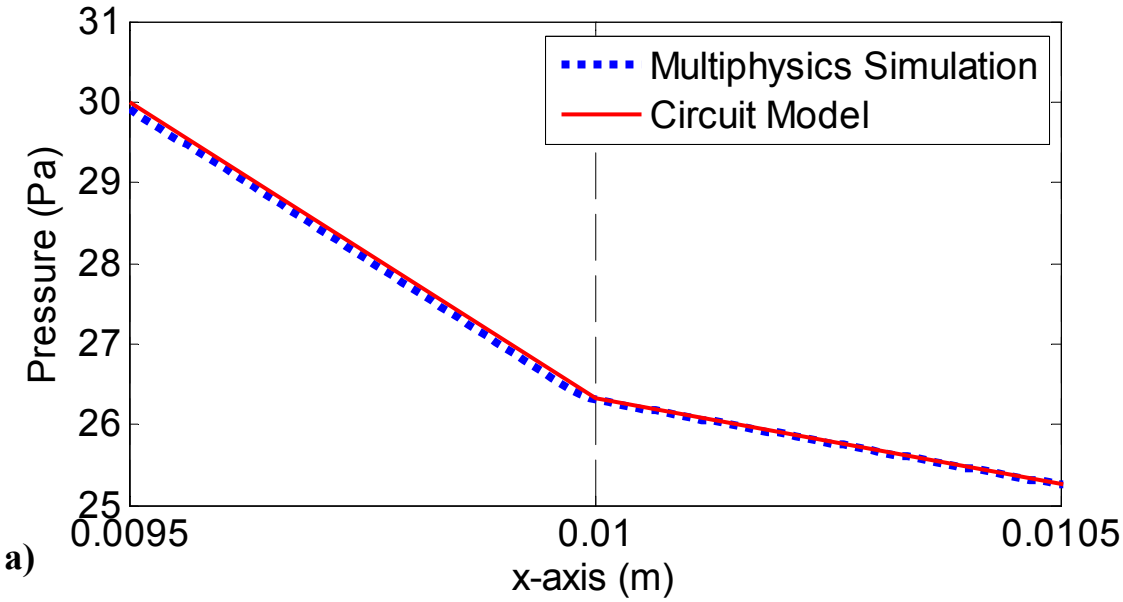

a)

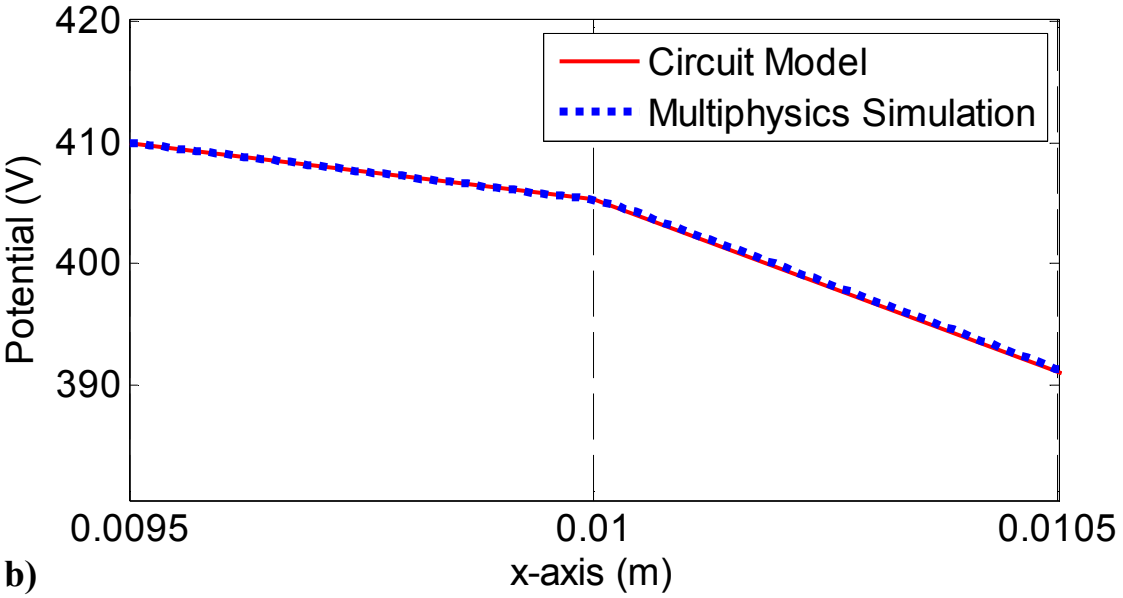

b)

Figure 4.13 Comparison of the circuit model and COMSOL Multiphysics 2-D simulation in the region near the focusing junction of the 5-reservoir chip design. The distributions were taken for a 1 mm section along the length of the channel. The centre of the junction is located at x = 0.01 m. a) The pressure field with applied pressures P = [100, 0, 0, 0, 0] Pa at reservoirs 1-5, respectively. b) The potential field for applied potentials ϕ = [500, 500, 500, 100, 0] V at reservoirs 1-5, respectively.

Chapter 5

Microfluidic Chip for Cell Sorting

In this chapter, the microfluidic cell sorter chip design process is described. The performance requirements for the different elements of the design are presented. The two types of chips, glass and PDMS, used during this project are described and the fabrication processes are briefly outlined. The various chip designs considered and tested are introduced. Several issues encountered during the iterative design process and the implemented solutions are presented. The operational designs achieved at the end of the iteration process were used for more extensive testing; these results are presented in Chapters 6 and 7.

5.1 Chip Design Elements – Performance Requirements

The design process for any device requires the identification of minimum performance requirements. These guidelines are determined by the intended application of the device. This project has separated the functional elements of the microfluidic cell sorting chip into four categories: sample focusing element, sample detection element, fluidic switching element for cell sorting, and the general flow elements. The performance requirements are presented here; detailed evaluation criteria for selecting the focusing element and sorting configuration are presented in Chapters 6 and 7, respectively.

5.1.1 Sample Focusing Element

The main function of the focusing component is to control the dispensing of the individual cells in the main detection channel. The rate of particles dispensing depends on the level of focusing, which can be adjusted by varying the relative flow rates of the sheath fluid and sample streams. Individual control of each flow is therefore required for precise operation.

The width of the focused sample stream must be similar in size to the cells to achieve the single-file particle transport required for detection. The focusing mechanism must reduce the stream width to approximately 4 μm, the diameter of the fluorescent microspheres and the size of common yeast and bacteria cells.

The transverse location of the focused sample stream must be predictable to enable optimization of the illumination light and the particle detection. Two-dimensional focusing is necessary for this project.

5.1.2 Sample Detection Element

The integrated detection system was not developed during the course of this study, but it does affect the design of the chip. Optical access to the channel requires adequate space to accommodate the use of embedded optical fibres or polymer waveguide structures. This feature becomes more challenging in the design of chips with parallel sorting systems; a single sorter was considered in this work. The detection zone must be located close enough to the focusing junction that the particles are still in the desired transverse coordinate. Also, the distance from the detection zone to the sorting junction is important for efficient operation of the chip. A calculated time delay, using an estimated particle velocity, determines when flow switching occurs after target cell detection. Ideally, the distance between the detection point and sorting junction is minimized to limit the effect of any downstream velocity variations; however, a minimum distance is required to allow time for signal analysis and activation of the flow switching. Optimization of the detection channel length requires knowledge of the detection system response time.

5.1.3 Cell Sorting Element

The fluidic switching mechanism requires the ability to direct cells to any of the desired paths. Under normal operating conditions, the motion of the particles in any of the collection streams should not reverse direction. High speed switching between the different paths is necessary for dynamic sorting. The duration of the switching must be less than 1 second to achieve modest sorting rates, but much faster operation is desired.

A minimum of two collection reservoirs are required; one reservoir is for waste flow and one is for target cell collection. Conventional FACS systems have two sorting paths. Designs with additional paths provide potential for more complex sorting routines and multiple target cells.

5.1.4 General Flow Elements

The microfluidic chip must be capable of reliable and repeatable operation. The effect of uncertainties encountered during normal conditions should be reduced to manageable levels; additional elements

may be required to limit flow anomalies. The system must be able to control individual channel flow rates throughout the chip. Ideally, the control of various flow parameters will be automated using information from the detection system. Reductions in the power consumption and system complexity are highly valued in the design of microfluidic chips for lab-on-a-chip devices.

5.2 Chip I: Micralyne Glass Chip

At the outset of this work, the soft-lithography fabrication system in the Microfluidics and Biochip Laboratory had not been implemented. The fabrication of the first fluid chip was completed by Alberta-based Micralyne, Inc. The per-unit cost of fully customized chip fabrication is high for small batch runs; therefore, the Protolyne glass chip prototyping technology was used to reduce the cost. The Protolyne technique employs a common template for small run orders that can be fabricated in bulk.

The template used in this technology limits the design of the chip. The major constraints that pertain to this work are the fixed 20 μm channel depth, fixed reservoir locations and size (2 mm diameter), size of the chip (95 mm x 16 mm), minimum mask line width (10 μm = 50 μm channel width), and post-etch feature spacing (100 μm).

5.2.1 Fabrication Details

The detailed fabrication process for the glass chip can be obtained from Micralyne, Inc. Essentially, the chip design was constructed using the L-Edit program, from which Micralyne printed a photomask of the design features. The photomask is used to selectively block regions of a thin layer of photo-sensitive material coating the glass substrate from exposure to UV light. Changes in the chemistry of the photoresist material occur in the exposed areas. The unchanged material is developed away from the substrate leaving an exposed pattern on the glass slide. An isotropic, wet chemical etch is used to create the fluid channels with a depth of 20 μm. The etched glass slide is then fusion bonded to a similar glass slide that contains the pre-machined fluid reservoirs. A photograph of the Micralyne chip filled with a dark ink is shown in Figure 5.1. The coin is used as a size reference.

Figure 5.1 Micralyne microfluidic chip filled with dark ink to enhance the channels.

5.2.2 Chip Characteristics

Isotropic etching generates a D-shaped channel cross-section in the glass slide. A schematic of this cross-section is shown in Figure 5.2. The non-rectangular cross-section causes an intensity drop-off near the edges during fluorescence dye visualization. Additional adjustment of the data is required to normalize the concentration based on the intensity profile of a channel filled with dye solution. This process contributes to the experimental error. Also, simulating the flow with a 2-D numerical model has reduced accuracy.

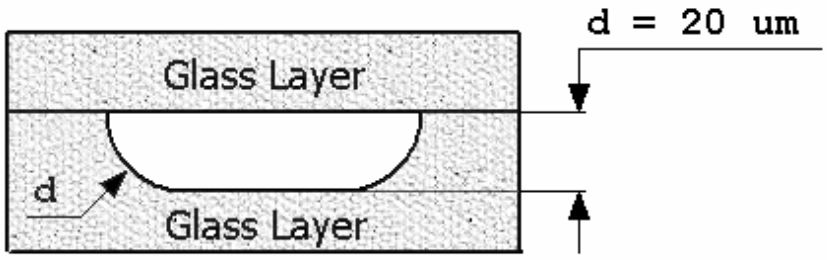

Figure 5.2 Schematic of an isotropically etched glass channel cross-section. The etch depth is denoted by *d*.

The mobility of fluids in a glass-glass chip is generally higher than PDMS chips and tends to be more stable. These characteristics are beneficial for the chip performance.

The reservoirs of the Protolyne template are quite small, 2 mm in diameter, which makes it difficult to fill during experiments without supplying too much fluid. Excess fluid forms droplets on the top of the glass chip and contributes to Laplace generated pressure gradients.

5.3 Chip Series II: PDMS Chips

The development of the in-house soft-lithography chip fabrication system was crucial to the design process of this work. This technique allows much faster prototyping than standard photo-lithography techniques and Micralyne custom chip fabrication. A chip can be completed in less than one day with soft-lithography, provided the photomask had previously been printed; whereas, the chips from Micralyne took approximately five months from design to delivery. More designs can be rapidly investigated with soft-lithography for a fraction of the cost of glass chips. This accelerates the iteration process.

There are design limitations for chips fabricated by soft-lithography. The designs must be transferred to a photomask, similar to the glass chip fabrication process. Chrome masks are common and have a high level of precision. These masks are expensive and time consuming to make. The popular alternative is transparency photomasks. The designs are printed on a transparent sheet with an extremely high resolution printer or photoplotter. Photomasks for this study were printed at resolutions of 10 000 dots per inch (DPI), 20 000 DPI, and 40 000 DPI. The recommended minimum feature sizes are 25 μm, 12.5 μm, and 8 μm for 10 000 DPI, 20 000 DPI, and 40 000 DPI, respectively; however, 5 μm features were successfully printed at 20 000 and 40 000 DPI resolutions. The transparency material used for photomasks has imperfections, mainly bubbles formed during manufacturing, which can affect the quality of the channel structures if the exposure process is not optimized. The transparency masks are also more easily damaged than chrome masks.

The chips were initially restricted to a single planar fabrication level. This required all elements of the design to be at the same depth. Improvements to our fabrication process and a better understanding of the system have enabled the fabrication of multiple level chips. Greater design flexibility and better chip performance is possible with 3-D capabilities. The last two design iterations described in this chapter utilize multi-layer fabrication.

5.3.1 Fabrication Details

The basic principles of the soft-lithography process, as it is applied in this work, are described here. The main steps are illustrated in Figure 5.3. The full fabrication recipe is documented in Appendix A.

The first step is to coat a thin layer of negative SU-8 photoresist onto a pre-cleaned glass microscope slide. This is accomplished by dispensing a small amount of the SU-8 onto the slide and

spinning the slide at a set speed. The rate of spinning determines the thickness of the coated photoresist and the depth of the fluid channels. A heat treatment process called the soft-bake is then used to drive off the solvent in the photoresist to help solidify the layer.

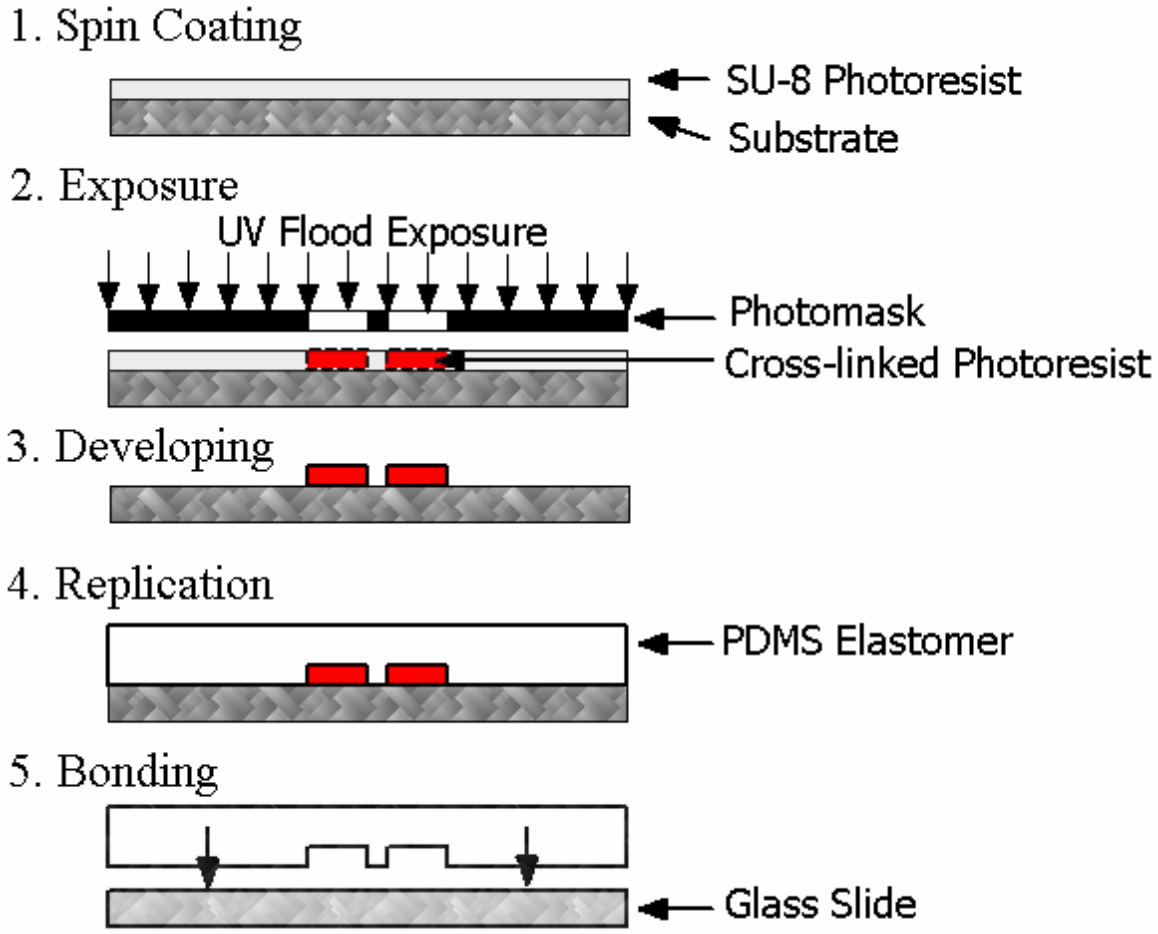

Figure 5.3 Steps of the soft-lithography process: 1. spin coating, 2. UV exposure, 3. photoresist developing, 4. mould replication, and 5. chip bonding.

Next, the coated slide is placed in the mask aligner unit and is covered by the photomask. Vacuum pressure forces the mask in close contact to the photoresist layer. To achieve a positive relief structure of the channel network, the design features are transparent on an otherwise opaque photomask. A flood UV exposure source illuminates the chip assembly and light is transmitted through the transparent regions of the photomask into the photo-sensitive SU-8 layer. The exposed SU-8 undergoes a change in chemistry and becomes fully hardened or 'cross-linked' during a subsequent heat treatment called the post exposure bake (PEB). It should be noted here that multiple layer

fabrication repeats steps 1 through 3 from Figure 5.3 for each layer. A different photomask must be used for each level and they must be aligned to ensure proper fluid connections are established.

The development step removes the unexposed SU-8 material from the substrate leaving only the positive relief structures. This is completed in a chemical bath that dissolves uncross-linked SU-8. The chip mould, referred to as the master, is ready for replication.

Replication of a single master can be performed multiple times; the exact number depends on the rigidity of the master and the complexity of the design. Chip replication is achieved by pouring a liquid PDMS elastomer mixture on the master and curing the material in an oven. The cured PDMS layer has a consistency of a flexible rubber and is removed from the master. The channel network is imprinted in the removed PDMS layer. The surface of the PDMS and the bonding substrate, glass or PDMS, are treated with O_2 plasma to favourably modify the surface properties and promote bonding of the two layers. The two layers are placed in contact, forming the enclosed channel network. A finished PDMS-glass chip can be seen in Figure 5.4.

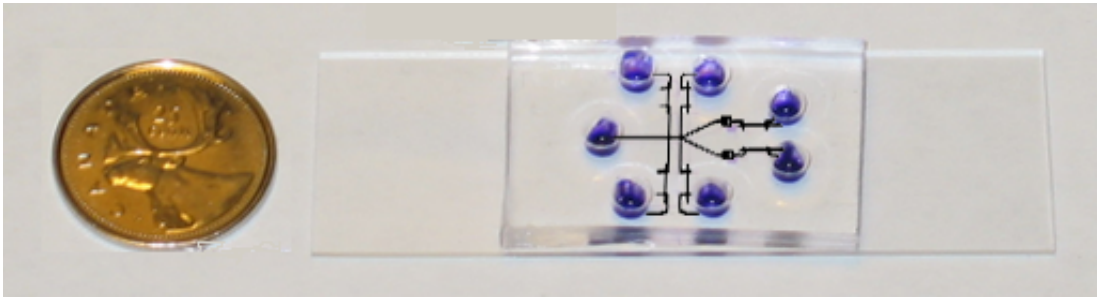

Figure 5.4 PDMS-glass microfluidic chip filled with digitally enhanced channels.

5.3.2 Chip Characteristics

The channel features fabricated by the soft-lithography process have a rectangular cross-section, although, slight sloping of the side wall has been encountered. This characteristic is commonly reported in literature. The master feature dimensions are regularly larger than the size of the photomask features. The structure is usually between 1 and 2 μm in excess on each side. There is also some variation in channel depth due to non-uniformities of the spun SU-8 coating. This value is difficult to quantify. Measurements of the depth are often taken at a few locations around the chip and they tend to be within a few microns. Chip depth is assumed uniform for the purpose of modeling.

Imperfections of the photomask get replicated as poor surface properties of the master at lower exposure doses. This can be avoided by properly calibrating the required exposure. Critical imperfections of the mask, such as large scratches, can cause the chip to be unusable.

Many of the steps in the fabrication process are sensitive and can cause defects in the final master. Spin coating is particularly critical, as contamination particles or inadequately cleaned slides often produce crevasses or divots. Multiple fabrication attempts are commonly required before acquiring a useable master. Fortunately, several chips can be fabricated in parallel.

The fluid reservoirs are created with a leather punch tool that shears the cylindrical reservoir in the PDMS layer. Compression of the PDMS during punching results in a slight hour-glass shape. Locating the reservoirs is difficult to control precisely, which adds to the chip-to-chip variability.

It has been established that aging of the PDMS changes the surface properties and the electroosmotic mobility of fluids. The experiments for a particular chip must be planned according to the aging characteristics. Waiting too long to test the chip has additional consequences. The PDMS has been observed to become cloudy after a long period of storage. Visualization of dyes and particles becomes difficult with these clouded chips. The reason for this change in optical properties is not fully understood, but is attributed to the absorption of fluids.

5.4 Chip Designs and Iteration Process

Testing and evaluation of several iterations of the microfluidic chip designs was required to achieve repeated, successful operation. Each step provided a greater understanding of the behaviour of the system and the influences of various parameters, which were previously unknown. Modifications to the sample focusing and cell sorting configurations were implemented throughout the process. Also, changes to the chip layout and the incorporation of additional fluid components were conducted to improve the performance of the system. Characteristic designs from each iteration are presented in this section; justification is provided for design changes.

Print A

The design of the initial Micralyne glass chip, Design A-1 (‘A’ is used to designate the order of the mask print and ‘1’ is the design identifier), was based on the enclosed fluidic switching cell sorter model and microfluidic cell sorter devices reported in literature. The layout of this design and exploded views of the focusing junction and sorting configuration are shown in Figure 5.5. The letters

at the reservoirs designate the purpose of each channel: S is the sample channel, F is a sheath fluid focusing channel, D is a directing stream channel, and C is a collection channel.

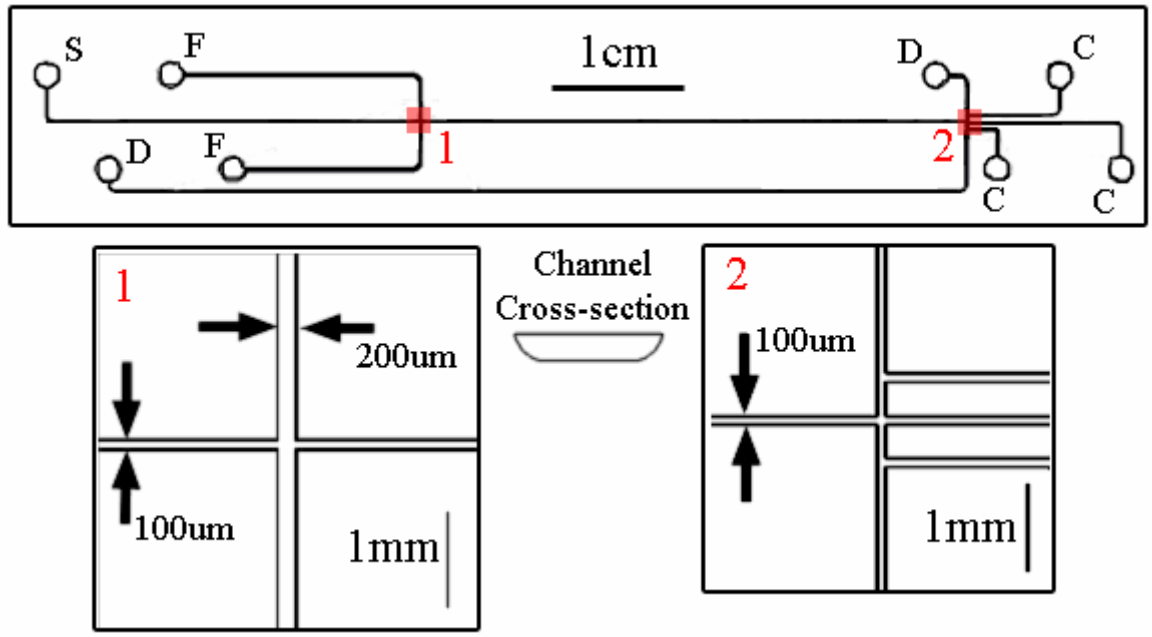

Figure 5.5 Layout of chip A-1 (Micralyne Glass Chip). The letters at the reservoirs designate the function of each channel: S is the sample channel, F is a focusing sheath fluid channel, D is a directing stream channel, and C is a collection channel. The numbers on the chip layout diagram, 1 and 2, indicate the location of the inset images.

Several key features of Design A-1 were chosen according to the results of preliminary numerical simulations. The width of the focusing sheath channels were designed to be twice as large as the sample channel. This was found to provide a reduced focused stream width compared to uniform channel widths for a prescribed focusing potential ϕ_{foc}, defined by $\phi_{foc} = \phi_{sheath} / \phi_{sample}$. This relationship is discussed in detail in Chapter 6. The sorting configuration consisted of three collection reservoirs; one channel is a waste line and the other two are target cell paths. Directing streams were included to assist with control of the flow field in the sorting region.

Performing experiments on chip A-1 established a baseline from which improvements were developed. Many of the problems encountered with this design stemmed from the limitations defined by using the Protolyne template. The overall size of the chip and spacing of the reservoirs required long channels and unnecessarily high voltages. Reducing the size of the system allows lower operating potentials and is encouraged in the development of micro-devices. From a functional

standpoint, the length of the detection channel, located between the focusing and sorting junctions, was much too long and the particles arrived at the sorting junction in random transverse locations. This partially defeats the purpose of focusing the sample. The channels were also too wide to effectively control the dispensing of the sample particles.

The asymmetry of the design caused difficulties in controlling the flow experimentally. Determining the proper potential combinations to define the particle path for three operating conditions was time consuming and rather ineffective. Flow uncertainties existing in the system contributed to the inability to perform dynamic sorting. Pressure effects were observed to influence the flow. During fluids replenishing, a droplet of solution would form on the glass slide due to the small size of the reservoirs. Differences in the radii of these droplets caused Laplace pressure driven flow. The placement of the electrodes in the reservoirs was also a variable that affected the flow field. The development of a chip holder with repeatable electrode positioning would eliminate this problem.

Particles directed for collection in either the top or bottom streams spend a short period of time in the perpendicular channels between the initial sorting junction and the collection channels, which are located a small distance up the directing channels. The purpose of the directing streams is to help direct the particles and to eliminate back flow from the collection streams; however, in this short channel length the directing flows do not eliminate path reversal. Minimizing this length cuts down on the time a particle spends in this sensitive flow region.

Print B

The first set of designs printed on a transparency photomask, Print B, implemented many of the findings from the Micralyne chip experiments. The lengths of the channels were drastically reduced; the approximate distance from the sample reservoir to collection reservoir was shortened from 8 cm to 1.5 cm. The width of the sample channel was 50 μm, compared to 100 μm in Design A-1. The designs were all symmetric to simplify flow control. The distance from the focusing junction to the sorting region was shortened; values ranged from 0.2 mm to 2 mm for the different designs. Design B-1, shown in Figure 5.6, incorporates these changes with a similar focusing and sorting configuration. It can be seen that the distance of the perpendicular channel between the sorting junction and collecting channels was shortened. There was potential for further reduction of this length, but fabrication capabilities were initially unknown.

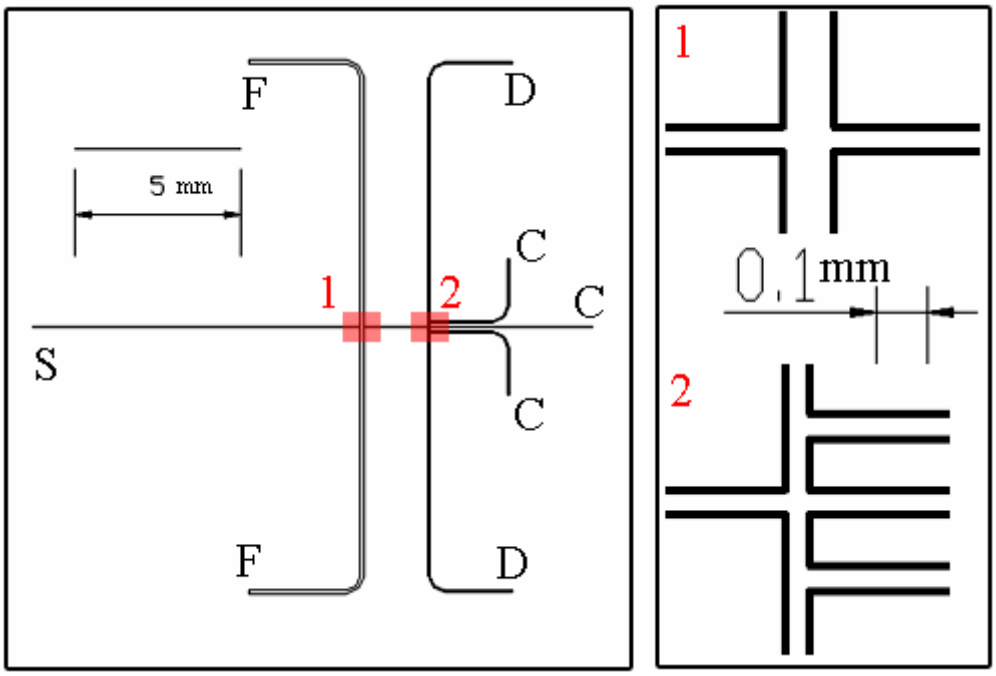

Figure 5.6 Layout of Design B-1. S is the sample channel, F is a focusing fluid channel, D is a directing stream channel, and C is a collection channel.

Variations in the configuration of the focusing and sorting regions were considered. Focusing crosses with different ratios of sheath channel width to sample channel width, $\eta = W_{sheath} / W_{sample}$, were fabrication to investigate the effect of the channel sizes on focusing. The three focusing channel width ratios considered, $\eta = 1$, $\eta = 2$, and $\eta = 3$, are shown in Figure 5.7. Design B-2 is similar to Design B-1, but has a reduction in the channel widths in the focusing and sorting region, illustrated in Figure 5.8. The fluid velocity in the narrower channels is greater than in Design B-1 for the same potential distribution, but otherwise functioned comparably.

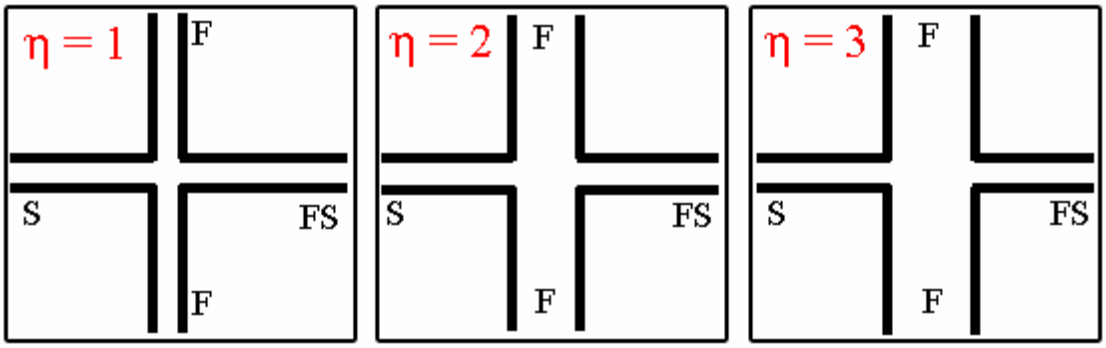

Figure 5.7 Focusing configurations from Print B with $\eta = 1$, $\eta = 2$, and $\eta = 3$. S is the sample channel, F is a focusing fluid channel, and FS is the focused sample channel.

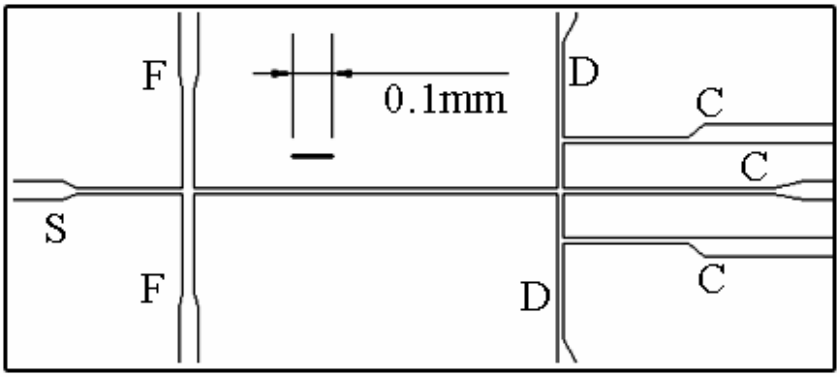

Figure 5.8 Focusing and sorting configurations of Design B-2. S is the sample channel, F is a focusing fluid channel, D is a directing stream channel, and C is a collection channel.

Focusing and particle collection was performed with the new designs; however, repeatable results were not achieved because of the difficulties in controlling the flow. The channels were fabricated deeper than chip A-1 to prevent adherence of the particles to the bottom of the channels. This increase in depth and the reduction of length critically reduced the hydrodynamic resistance of the system and pressure had a major influence on the flow field. Measures were taken to reduce the Laplace pressure effects in the reservoirs, but this alone was not satisfactory.

Experiments did demonstrate that shortening the length of the detection channel improves the positioning of the particle for sorting. An appropriate length was found to lie somewhere between the 0.2 mm and 2 mm tested in this run.

Print C

The next mask print, Print C, had similar designs to Print B with modifications to reduce the pressure effects. The channels were lengthened and the chips were fabricated shallower (15 and 25 μm depths) than the previous chips (40 μm depth). These actions helped significantly, but did not fully eliminate the pressure influence. Additional design alterations to Design B-1 included further reduction of the channel length between the sorting junction and the collecting channels. Design C-1, the updated version of Design B-1, is shown in Figure 5.9.

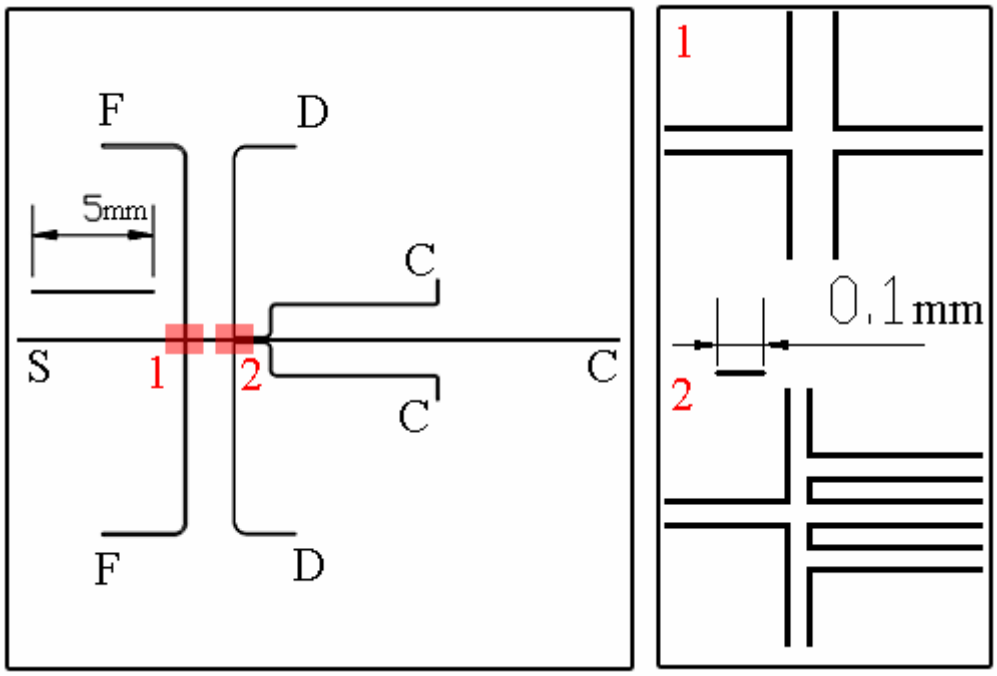

Figure 5.9 Layout of Design C-1. S is the sample channel, F is a focusing fluid channel, D is a directing stream channel, and C is a collection channel.

Several different sorting configurations from Print C were tested. Four such designs are shown in Figure 5.10. Design C-2 had modified directing channels to prevent accidental flow of particles into the directing streams. Design C-3 employed angled collection channels at the switching junction. Design C-4 was a two-collection channel version of Design C-3. Design C-5 had three collection streams, but the use of the directing streams was eliminated.

Instability of the applied potential was observed for 7- and 8-reservoir systems during the testing of these chips. The high voltage power sequencer used in the experiments to control the electroosmotic flow has eight independently controlled channels, but has difficulties to maintain voltages when a channel is drawing a slight sink current. This condition arises in many of the switching potential settings and can critically affect the ability to test the design. An example of an unstable voltage trace is shown in Figure 5.11 for a design with three collection potentials. Two of the signals are relatively stable (ϕ_7 and ϕ_8), while the third (ϕ_6) fluctuates wildly between the specified 50 V setting and 0 V. As a result, effective collecting of particles in 8-reservoir systems with 3 collecting streams was difficult. In particular, collecting the particles to the middle channel without drawing particles from the other two collection streams required very precise flow control.

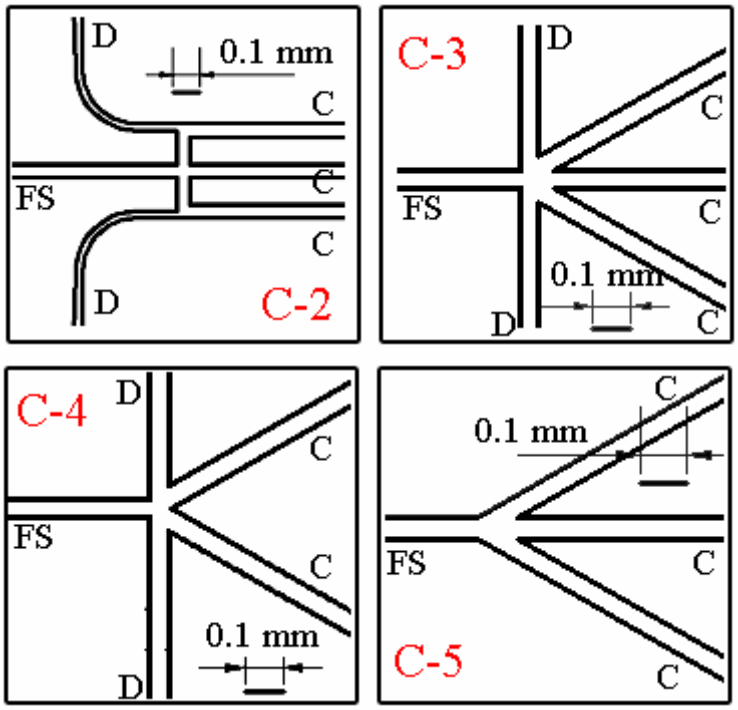

Figure 5.10 Layout of various sorting configurations in Print C. From left to right, top to bottom: Design C-2 (3 collecting (C), 2 directing (D)), Design C-3 (3 collecting (C), 2 directing (D)), Design C-4 (2 collecting (C), 2 directing (D)), and Design C-5 (3 collecting (C), 0 directing). FS is the channel with the focused sample.

Designs C-4 and C-5 were found to be the most successful for particle collection. For both designs, the directing paths were alternated using the timed switching mechanism and the majority of the particles were properly directed. Design C-5 suffered from the same demanding level of control to capture the particles in the middle stream as several of the other designs. The inclusion of a third collection stream was not a necessity for the function of the device and the added complexity was found to be a detriment to the overall performance of the chip. Configurations with two collection channels were selected for further investigation.

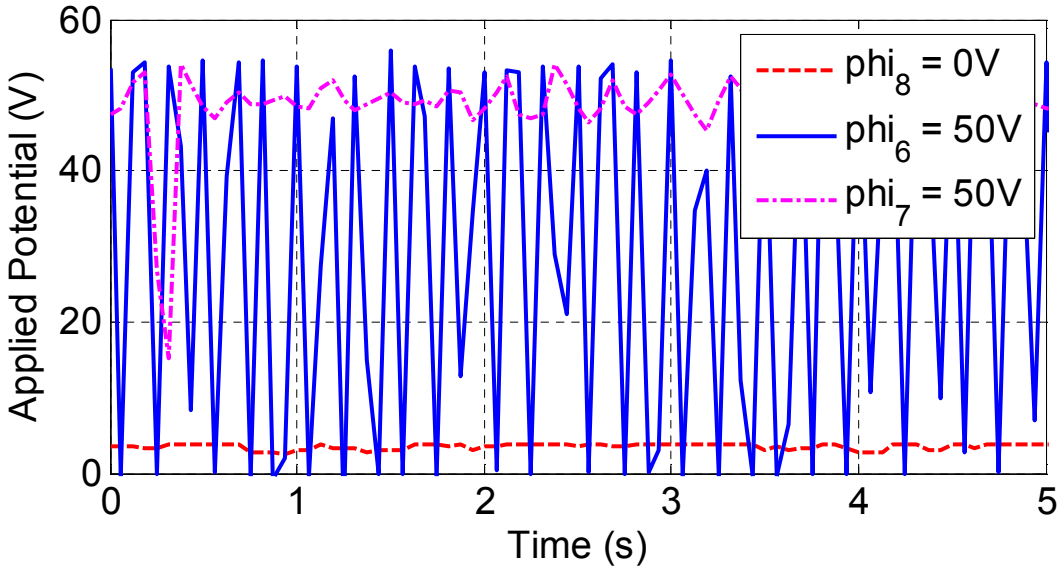

Figure 5.11 Voltage traces of applied potentials in the three collection reservoirs. Reservoir 6 (ϕ_6 = 50 V) is exhibiting voltage instability (solid line).

Print D

The use of hydrodynamic constriction elements in the chip design was investigated in Print D. Planar constrictions were fabricated in straight channel designs to evaluate the effective reduction in pressure driven flow. Four different styles of constriction sections were considered, illustrated in Figure 5.12. The capability of the fabrication system had not been fully characterized at this stage; therefore, test sections were prepared to determine the minimum feature size and maximum length of the constriction that could reliably be fabricated. Short lengths of constrictions were supported by larger channel sections and multiple constrictions were used in series. 5 μm wide constrictions were achieved repeatedly at lengths of 125 μm for the serpentine type of constriction, shown in the top right portion of Figure 5.12. The thin structures on the master were still rather fragile and the number of chips that could be replicated from a single master was limited.

Flow caused by a hydrostatic pressure difference was reduced nearly 3-fold by implementing a 10 μm wide constriction with a total length of 1 mm in a 40 mm long channel. Creating a narrower constriction, according to the fabrication limitations, can decrease the pressure flow more than 24-fold. Also, the hydrodynamic resistance is proportionally increased by the number of constriction elements. This reduction in the cross-sectional area requires higher applied electrical potentials due to the higher electrical resistance of the channels; a consequence unfavourable for miniaturization.

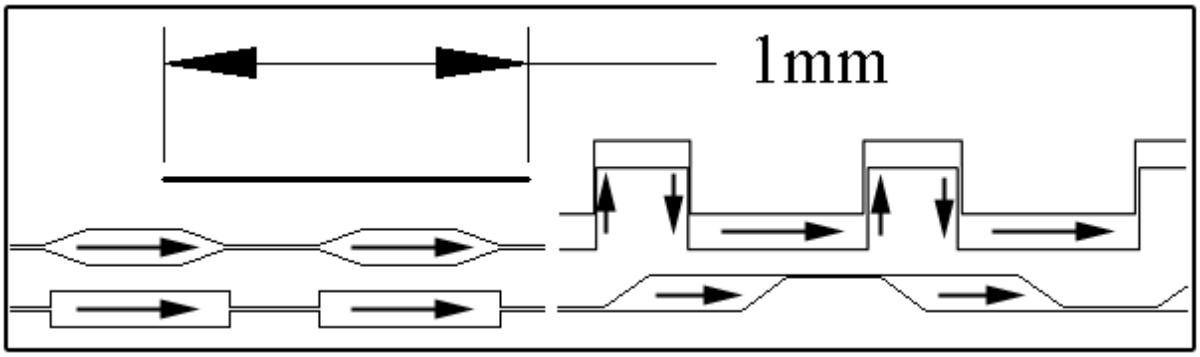

Figure 5.12 Four types of hydrodynamic resistance elements tested from Print D.

Print E

At the time of Print E, the development of a multi-layer fabrication process was accomplished. An example of a multilayer hydrodynamic resistance is illustrated in Figure 5.13. The base layer of photoresist is coated to 5 μm and the constriction element is exposed. Another layer of photoresist is coated to the desired depth of the chip (25 μm) and the rest of the channel structures are exposed. The hydrodynamic resistance elements constructed by this method tend to be much more robust and slightly narrower constrictions can be achieved. The elements can be longer than those of the planar designs. However, the fabrication process is more complicated and there is a lower success rate with multi-layer soft-lithography.

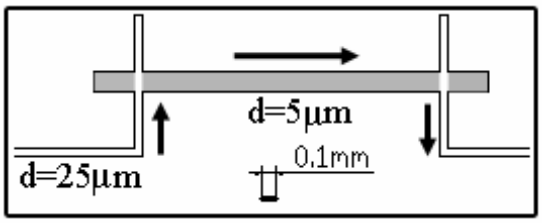

Figure 5.13 Typical two-layer hydrodynamic resistance element.

Testing the multi-layer constriction under hydrostatic pressure forces indicated an additional 2.5-fold reduction from the planar constriction element fabricated in Print D. Also, a large Laplace pressure was generated during a focusing experiment by creating a hemispherical meniscus with excess fluid in one of the sheath fluid reservoirs. In previous chips this would have critically disrupted the flow field, but the deflection of the focused sample was minimal with the resistance element. Greater increases in the hydrodynamic resistance of this constriction can be achieved by lengthening the channel and decreasing the width, which was chosen conservatively to provide a large interface

between the main channel structures and the constriction structure. Ideally, the cross-sectional area of the constriction and the regular fluid channels will be similar to maintain a uniform electric field.

The drawback to implementing narrow constrictions in every channel is that the chip becomes more susceptible to flow blockages. The 4.0 μm microspheres were observed to collect at the entrance to the channel constriction. Noticeable effects on the flow velocity occurred when enough particles had accumulated in the channel. To prevent the particles from reaching the constriction the use of large chambers to collect the particles was investigated. Two mechanisms were employed to stop the particles. Firstly, the decrease in velocity due to the reduction in electric field promotes adherence of the particles to the bottom of the chamber. The seeding of particles would also provide a convenient method to image and quantify the sorting of various subpopulations over long term operation. The second technique is the placement of obstacles and a filter element in the chamber. Several types of obstacles and filter sizes were tested on three sizes of chambers. Two types of obstacles and a close up view of a filter design are shown in Figure 5.14. Experiments revealed that the chambers were not large enough to effectively seed the particles. Many did adhere to the bottom of the chamber, but others were transported through the chamber and accumulated at the constriction. The obstacles did not assist in the capture of the particles and the filter element had too large of a spacing to stop the 4.0 μm spheres. The limitations of the mask print and fabrication process make direct filtering of small cells nearly impossible.

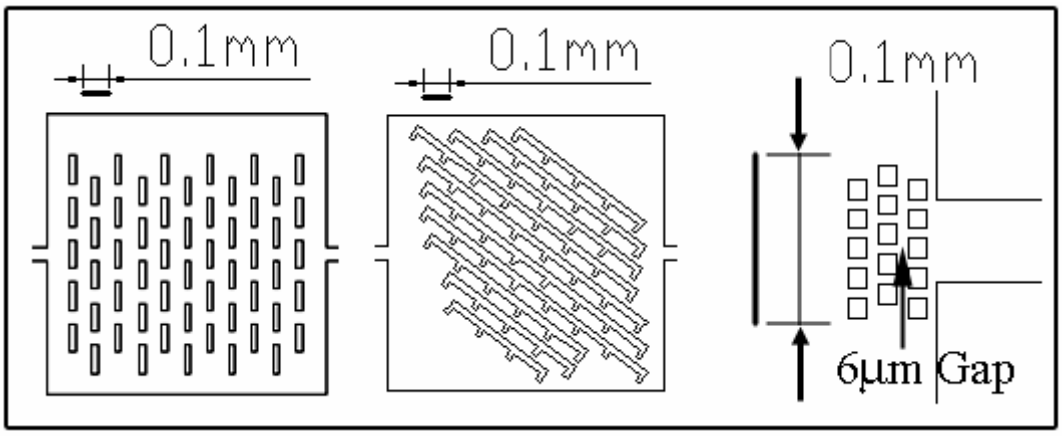

Figure 5.14 Cell capture chambers with two types of obstacles (left and centre) and a chamber with a staggered column filter on the chamber exit (right).

The full-chip designs for this mask print incorporated the particle chambers and the hydrodynamic resistance elements. The resistance elements were placed on all channels except the sample channel, which would be prone to rapid accumulation of cells. Two main configurations were designed with

slight component variations. The first design (E-1), shown in Figure 5.15, has two angled collection channels and two directing streams. Design E-1a and Design E-1b have focusing channel width ratios of $\eta = 2$ and $\eta = 3$, respectively. Designs E-1a and E-1b were printed with two-level constrictions and serpentine-type planar constrictions; however, only the former will be discussed further. Figure 5.15 shows the version with two-level constrictions. Design E-2 also has two directing streams and two collection channels, which are located a short distance up the directing channel. Similar to Design E-1, Design E-2 was printed with $\eta = 2$ (Design E-2a) and $\eta = 3$ (Design E-2b). Design E-2b is shown in Figure 5.16.

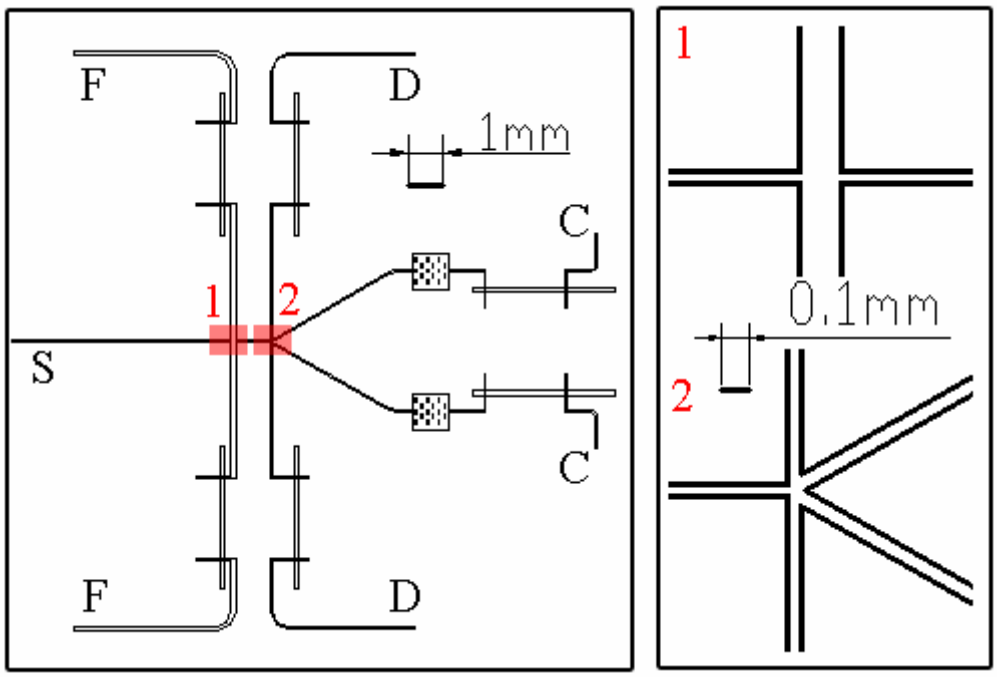

Figure 5.15 Layout of Design E-1b. S is the sample channel, F is a focusing fluid channel, D is a directing stream channel, and C is a collection channel.

Designs E-1b and E-2b were tested using the manual pulse switching method. Repeatable operation was demonstrated with greater success than any previous chips. The improvement in flow control is largely attributed to the reduction in the pressure effects. More detailed evaluations of the designs, in particular Design E-2b, are included in Chapter 7.

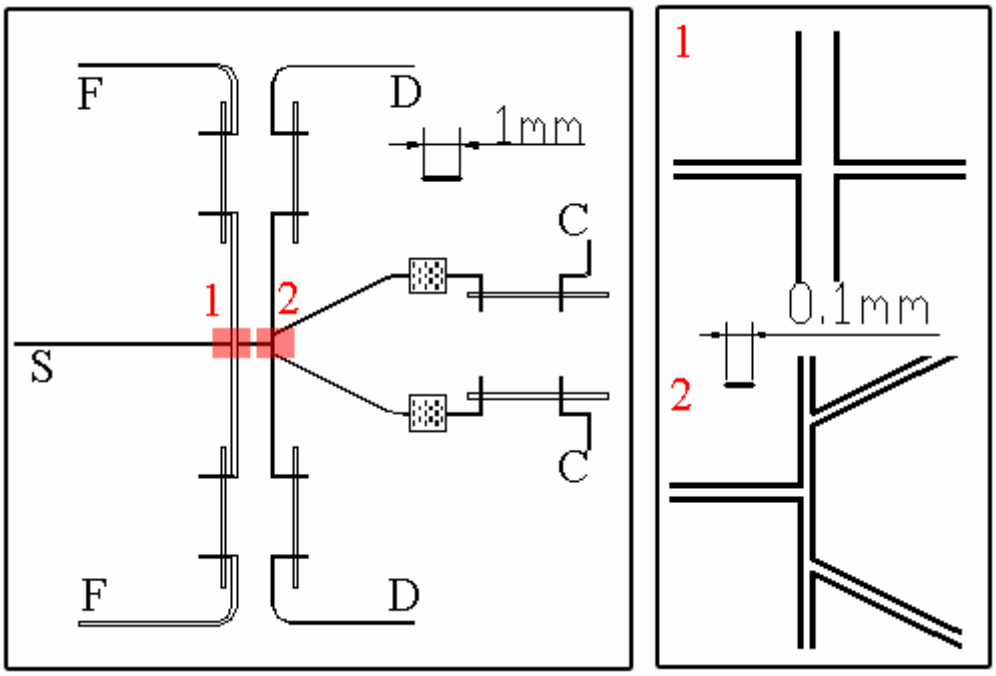

Figure 5.16 Layout of Design E-2b. S is the sample channel, F is a focusing fluid channel, D is a directing stream channel, and C is a collection channel.

Print F

Minor modification were made for the final mask print, Print F. The sample channel length was increased to provide a greater resistance to the pressure from the sample reservoir. Larger chambers were designed to slow down the particle to further promote adhesion to the chip, thus preventing blocking of the constrictions and allowing easy counting of particle concentrations in the respective collection streams. The majority of the particles were observed to adhere to the chip surface in the large chambers, but enough particles accumulate at the constriction after approximately one hour of continuous operation to reduce the flow through the channel. In the target cell collection chamber, fluorescence imaging using two filters could distinguish the two types of particles, allowing automated counting methods to be used. An example of a set of images that illuminates the different particle species is shown in Figure 5.17. This was not the principal method used to quantify the cell sorting performance because not all of the particles seeded in the chamber and there were times during operation when the flow was not monitored.

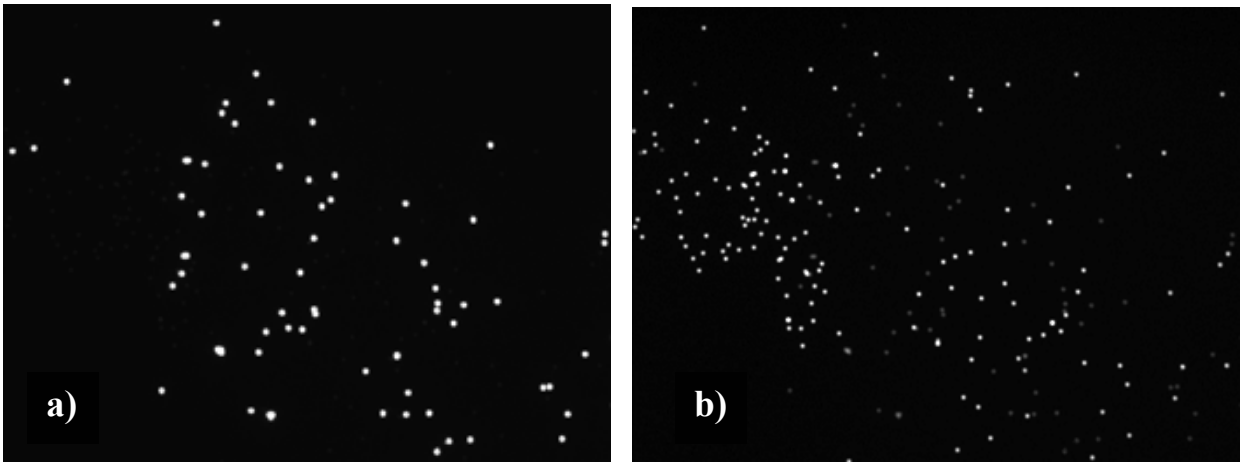

Figure 5.17 Images of seeded particles in target cell stream chamber, from the same location. a) Image taken with blue excitation. The non-target cells are the illuminated. b) Image taken with green excitation. Target cells are the brighter particles. An automated counting technique could be used to quantify the cell percentages.

Four designs were printed in this run. Designs F-1 and F-2 are extensions of Design E-1b. Design F-1, shown in Figure 5.18, merely incorporates the larger chamber and longer sample channel, while F-2, shown in Figure 5.19, is a simplified version without the directing streams. Designs F-3 and F-4 employ directing streams at an upstream location to divert the particles prior to sorting. F-3 and F-4 can be seen in Figures 5.20 and 5.21, respectively. The focusing channel width ratio is $\eta = 3$ for all four designs. The results and evaluation of dynamic sorting with these chips are presented in Chapter 7. Recommended modifications for the final chip design are described in Chapter 8.

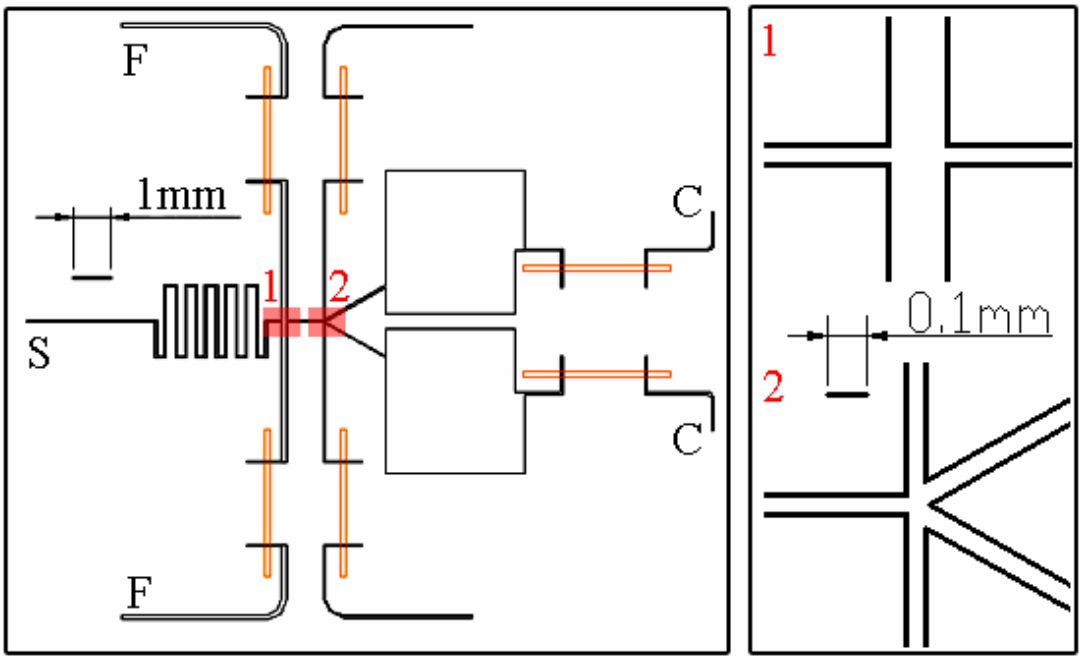

Figure 5.18 Layout of Design F-1. S is the sample channel, F is a focusing fluid channel, D is a directing stream channel, and C is a collection channel.

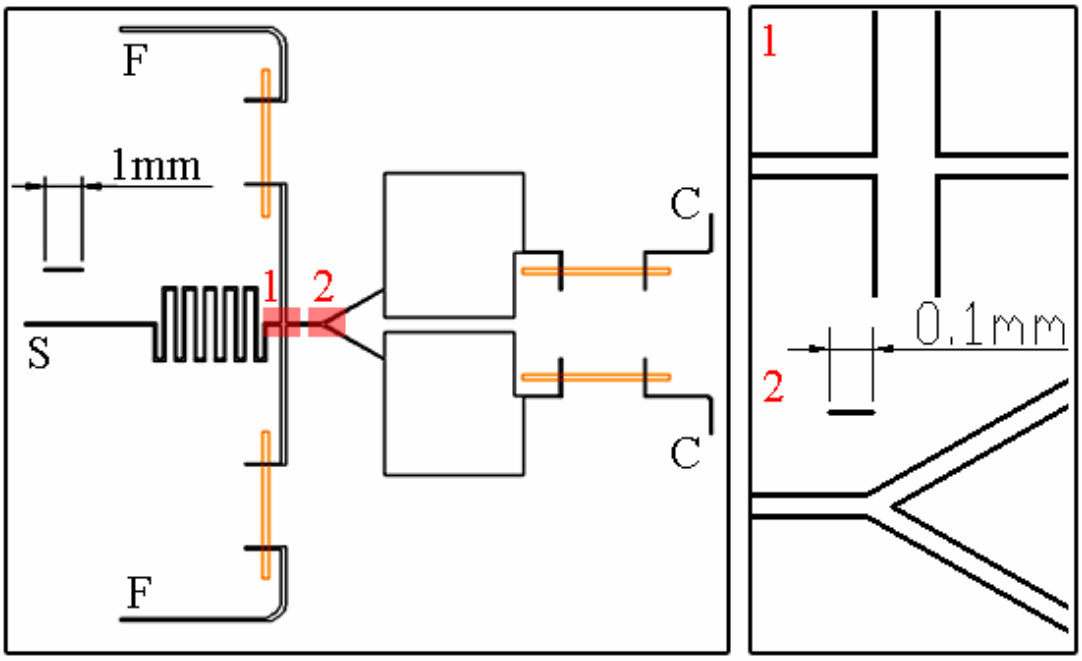

Figure 5.19 Layout of Design F-2. S is the sample channel, F is a focusing fluid channel, and C is a collection channel.

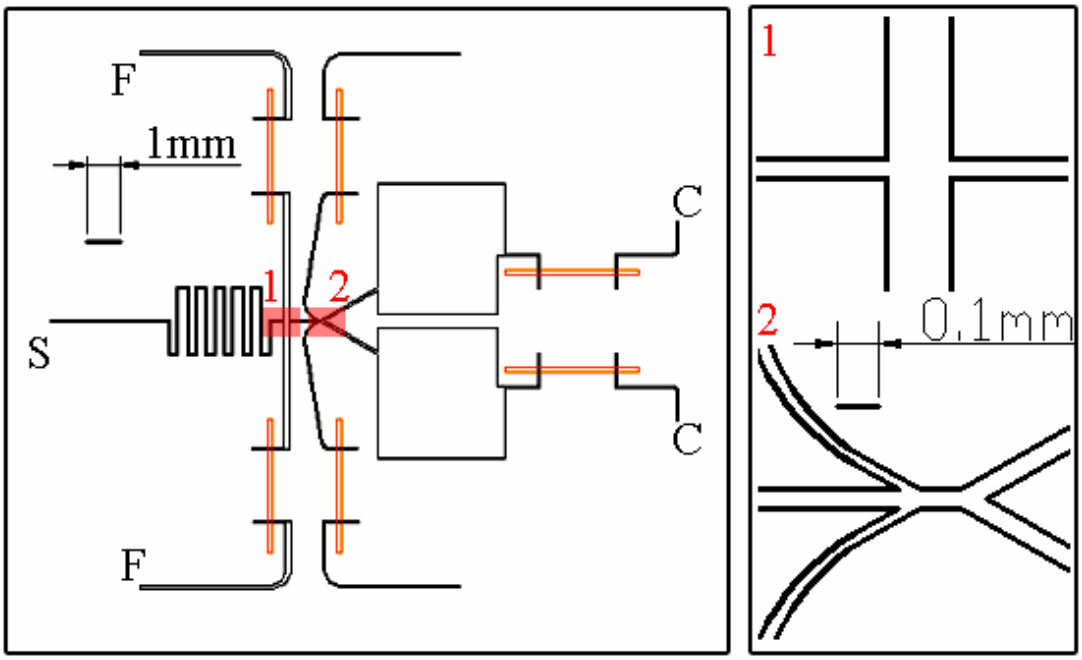

Figure 5.20 Layout of Design F-3. S is the sample channel, F is a focusing fluid channel, D is a directing stream channel, and C is a collection channel.

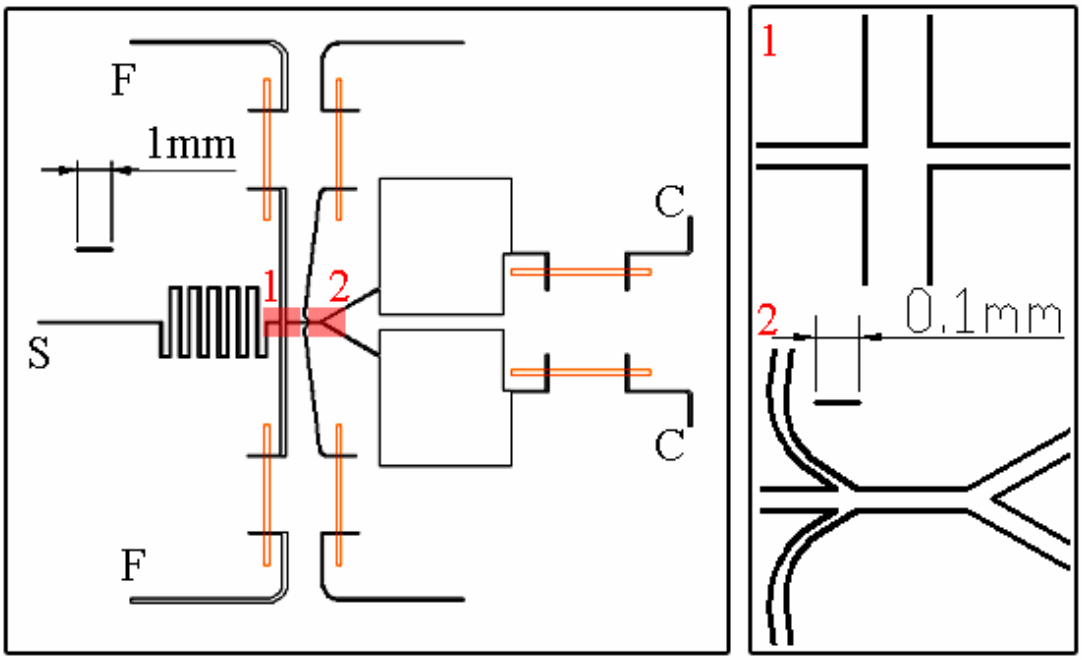

Figure 5.21 Layout of Design F-4. S is the sample channel, F is a focusing fluid channel, D is a directing stream channel, and C is a collection channel.

Chapter 6

Sample Focusing Evaluation

Sample focusing is a critical element of the microfluidic cell sorter. The purpose and function of focusing have been described earlier in this work (Chapter 2 and Chapter 5). This chapter presents the criteria used to evaluate the different focusing configurations, the compact numerical model used for estimating the focused stream width, the Gaussian model for the analysis of experimental focusing data, and the experimental and numerical results of the sample focusing study. Finally, the selected focusing component based on this evaluation is presented.

6.1 Criteria for Design Evaluation

Several factors determine the effectiveness of the component for sample focusing. Virtually any design can reach the physical limit where the sample flow is entirely pinched off; therefore, it is possible to achieve the required focused stream width for channels of any size. Producing focused stream widths comparable to the cell size becomes impractical for large channels because the velocity in the sample channel will be extremely low. Under these conditions the cells may be more inclined to adhere to the channel and small variations in the flow field may result in back flow of the sample. It is preferred that the channel sizes be sufficiently small that the correct focused width is achieved with reasonable sample velocities. The channel, on the other hand, cannot be too small that it becomes susceptible to blockages.

To assist device miniaturization, the required power for focusing should be minimized. The design that achieves the best focusing for a given combination of applied potentials is desired. This criterion has a large influence on the choice of the sample focusing element.

The ease of fabrication for a given focusing configuration is considered. The design must be fabricated using the soft-lithography method, where robustness is valuable to maximize the chip output from a single master. Also, a layout that is simple to model has the benefit of lower computational costs. Commercial packages are easily adapted to various geometries, but custom models may encourage the use of a particular coordinate system for simplicity.

6.2 Numerical Model – Determination of Focused Stream Width

A compact model to estimate the width, *d*, of the focused stream is useful to investigate various parameters involved in sample focusing. Such a model was developed for electrokinetic focusing in a uniform width, cross-microchannel by Yang et al. (2005). This model is adapted for this study to consider non-uniform widths of the sheath, sample, and outlet channels. The model assumes steady, 2-D flow and uniform velocity profiles in each of the channels. The diffusion and mixing of the sample and sheath fluids are neglected such that the calculated width represents the dividing streamline between the two fluids. The domain, shown in Figure 6.1, is symmetric about the x-axis with the same applied potential at both focusing reservoirs ($\phi_2 = \phi_3$ and $L_2 = L_3$). The fluids are assumed identical in each channel and have a constant density and conductivity.

Applying mass conservation about the sample fluid entering at inlet section 1 and exiting at outlet section 4 provides,

$$\bar{v}_1 \frac{W_1}{2} = \bar{v}_f \frac{d}{2} \tag{6.1}$$

where $\bar{v}_1$ is the average velocity at inlet 1, W_1 is the width of the sample channel, $\bar{v}_f$ is the average velocity of the focused sample stream, and *d* is the focused stream width. Mass conservation of the entire system gives,

$$\bar{v}_4 \frac{W_4}{2} = \bar{v}_1 \frac{W_1}{2} + \bar{v}_2 W_2 \tag{6.2}$$

where $\bar{v}_4$ is the average velocity at outlet 4, W_4 is the width of the outlet channel, $\bar{v}_2$ is the sheath fluid average velocity at section 2, and W_2 is the width of the sheath fluid channel. This model assumes that the flow at outlet section 4 is fully developed, where $\bar{v}_f = \bar{v}_4$. Substituting Equation 6.1 into Equation 6.2 gives,

$$\frac{d}{W_4} = \frac{1}{2\left(\frac{\bar{v}_2}{\bar{v}_1}\frac{W_2}{W_1}\right) + 1} \tag{6.3}$$

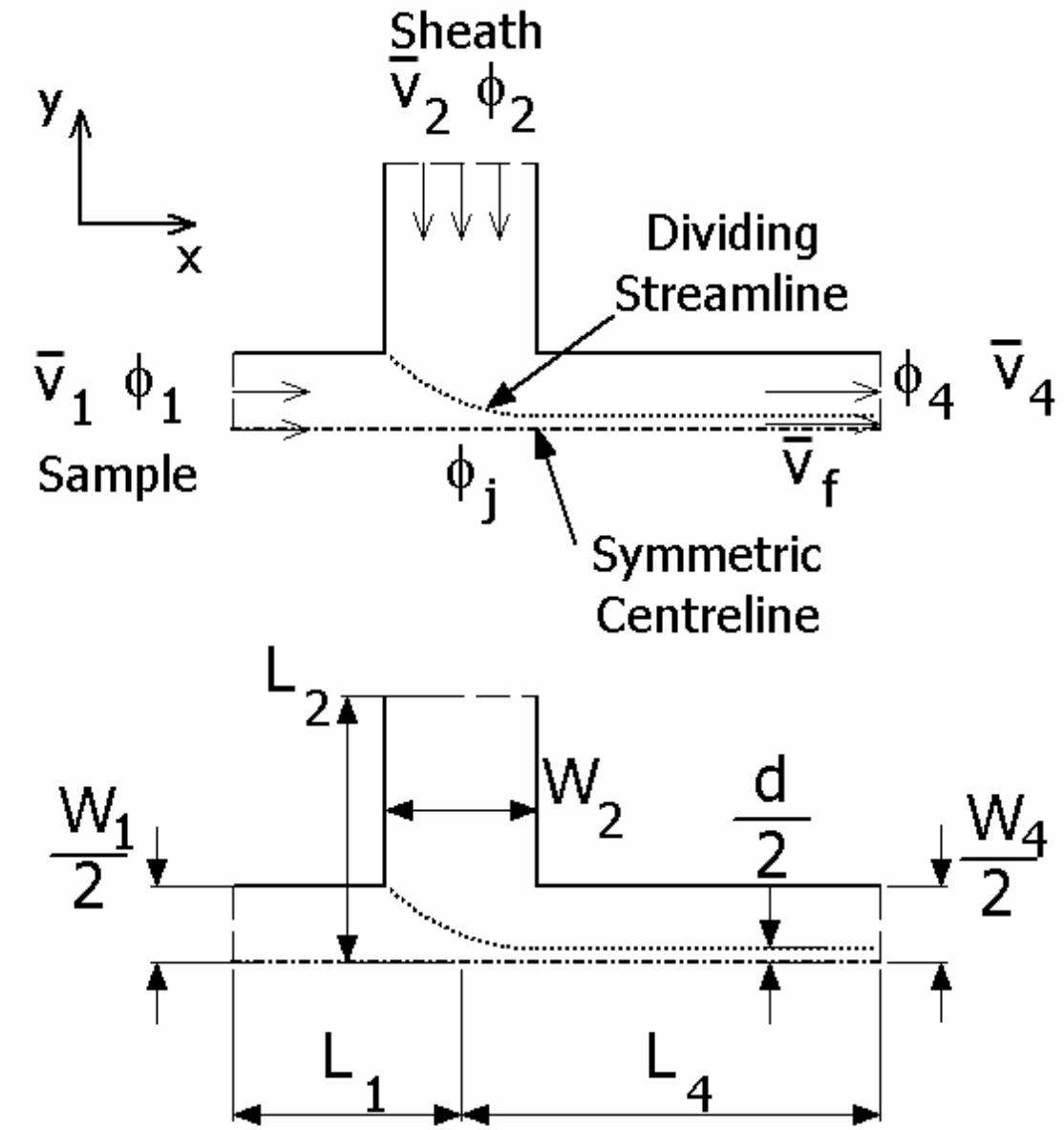

Figure 6.1 Focusing cross-microchannel domain for compact focusing model.

The velocities of the sheath and sample fluids must be known to evaluate *d* from Equation 6.3. An estimate of these velocities can be calculated using the Helmholtz-Smoluchowski velocity, from Equation 2.12. Assuming that the fluids have a constant permittivity and there exists a uniform surface charge, ζ, throughout the entire chip, then the electric fields are directly proportional to the flow rates. The potentials are assumed to drop linearly in the channels because the channel lengths are

must greater than the widths. Replacing the velocity terms in Equation 6.3 with the linear electric field, we get the following expression:

$$\frac{d}{W_4} = \frac{1}{2\left(\frac{\phi_2 - \phi_j}{\phi_1 - \phi_j}\frac{L_1}{L_2}\frac{W_2}{W_1}\right)+1} \qquad \textbf{(6.4)}$$

where ϕ_j is resulting potential at the junction, ϕ_1 and ϕ_2 are the applied potentials at reservoirs 1 and 2, and L_1 and L_2 are the lengths of channels 1 and 2, respectively. The one remaining unknown parameter is the potential at the focusing junction. This can be estimated by applying Kirchoff's law at the junction. This process has been described for the circuit equivalence model in Section 4.2.1. The circuit equivalency model for the potential field was directly incorporated into this focusing model.

The limiting cases of this model occur when the sample flow becomes zero and d / W_4 = 0 and when the sheath flow becomes zero and d / W_4 = 1. In the first case, the focusing potential ratio ϕ_{foc} is

$$\phi_{foc} = \frac{\phi_2}{\phi_1} = 1 + \frac{1}{2}\frac{L_2}{L_4}\frac{W_4}{W_2} \qquad \textbf{(6.5)}$$

where reservoir 4 is grounded (ϕ_4 = 0) and L_4 is the length of the outlet channel. The focusing potential ratio for the second limiting case is

$$\phi_{foc} = \frac{\phi_2}{\phi_1} = \frac{1}{\left(1 + \frac{W_4}{W_1}\frac{L_1}{L_4}\right)} \qquad \textbf{(6.6)}$$

The values predicted with the compact focusing model correlate well with the COMSOL Multiphysics 2-D numerical simulations. The normalized focused stream widths, d / W_4, estimated by the compact focusing model and Multiphysics simulations versus ϕ_{foc} are shown in Figure 6.2 for a focusing element consisting of a cross with uniform channel widths and the following lengths: L_1 = 0.01 m, L_2 = 0.008 m, L_3 = 0.008 m, and L_4 = 0.016 m.

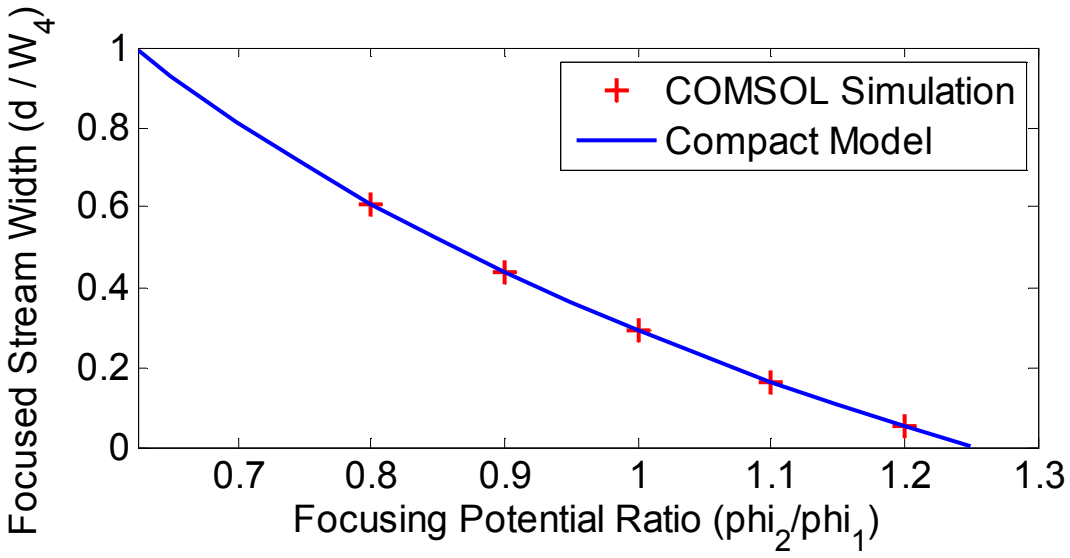

Figure 6.2 Comparison of the focused stream width estimated with the compact focusing model (line) and COMSOL Multiphysics numerical simulations (crosses).

6.3 Gaussian Model – Experimental Determination of Focusing Streamline

In a 2-D focusing analysis, the dividing streamline between the sheath and sample fluids defines the focused stream width. Experimentally, dye is injected into the sample stream to allow fluorescence visualization. Challenges arise in determining the location of the streamlines because diffusion of the dye occurs across this boundary, resulting in a dye intensity profile that does not directly reveal the dividing streamlines, as illustrated in Figure 6.3. The common method to estimate the focused stream width from experimental data is the full-width at half-maximum (FWHM) approach. The FWHM corresponds to the distance between locations where the intensity or concentration is half of the maximum intensity of the profile. This is only an estimate of the true focusing parameter. The diffusion of the sample in the transverse direction affects the profile width; therefore this technique has a dependence on the sample and sheath fluids and the location at which the profile is taken. The method presented here fits a Gaussian curve to the data and provides a more accurate estimate of the distance between the dividing streamlines.

For this analysis, many of the assumptions are the same as the focusing model discussed previously: 2-D steady flow, constant density, and uniform velocity profiles. Three cases of sample diffusion are encountered when applying mass conservation, depicted in Figure 6.3, to the sample undergoing focusing. The first case occurs when there is no diffusion of the sample. The dividing

streamline encapsulates the sample and the step concentration profile at the outlet, section 4, is shown in Figure 6.4(a). The sample mass balance is

$$\dot{m}_1 c_1 = \dot{m}_1 c_4^{\max} \tag{6.7}$$

$$c_1 = c_4^{\max} \tag{6.8}$$

where $\dot{m}_1$ is the mass flow at inlet section 1, c_1 is the concentration of the sample at inlet section 1, and $c_4^{\max}$ is the maximum concentration at outlet section 4. The value of *d* can be found directly from the experimental concentration profile in this scenario.

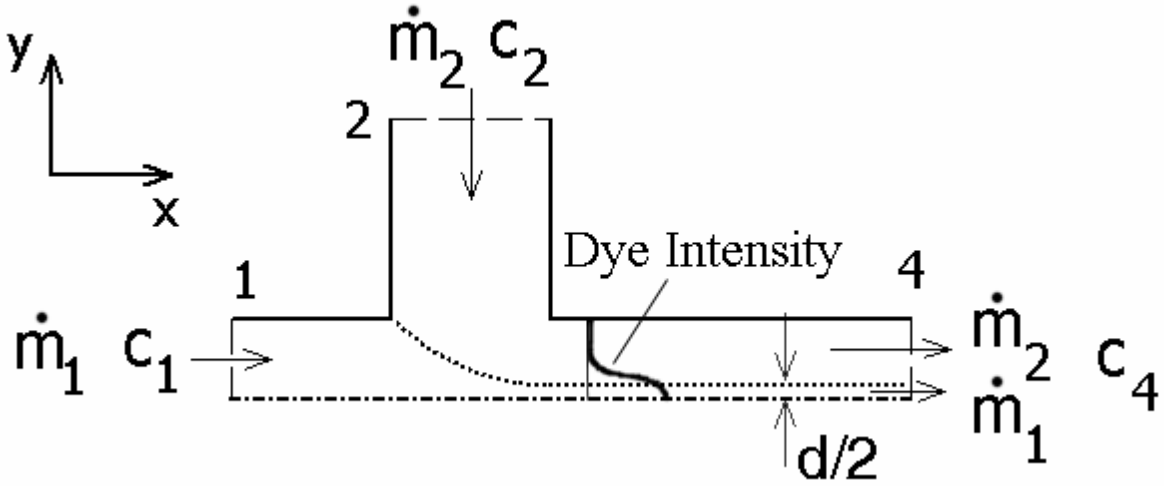

Figure 6.3 Mass balance of sample undergoing focusing in cross-microchannel.

The second case involves infinite diffusivity of the sample, resulting in a uniform concentration profile across outlet section 4. The profile is illustrated in Figure 6.4(b). The mass balance on the sample gives,

$$\dot{m}_1 c_1 = (\dot{m}_1 + \dot{m}_2) c_4^{\max} \tag{6.9}$$

$$\frac{c_4^{\max}}{c_1} = \frac{1}{2\left(\frac{\bar{v}_2}{\bar{v}_1}\frac{W_2}{W_1}\right)+1} \tag{6.10}$$

where $\dot{m}_2$ is the mass flow of the sheath fluid, $\bar{v}_1$ is the average velocity at inlet section 1, W_1 is the width of the sample channel, $\bar{v}_2$ is the average velocity at inlet section 2, and W_2 is the width of the sheath channel. The right hand side of Equation 6.10 is the same as Equation 6.3. Equating these, we find that the focused stream width, *d*, can be determined by the concentration values:

$$\frac{d}{W_4} = \frac{c_4^{\max}}{c_1} \tag{6.11}$$

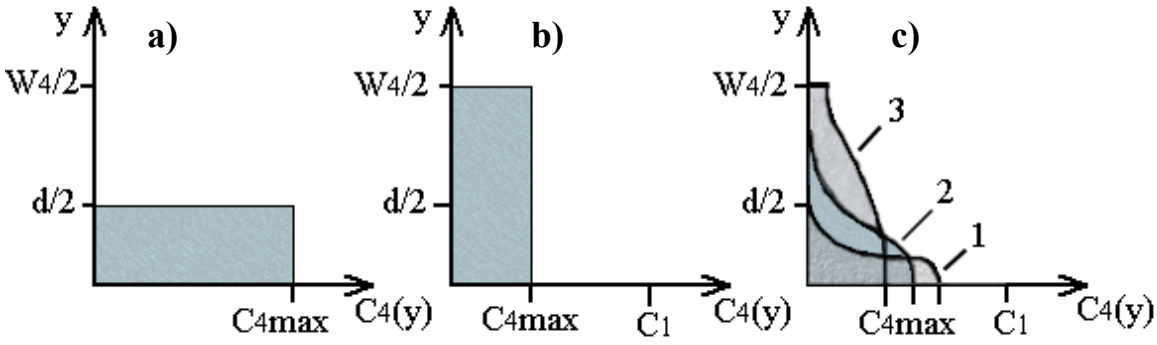

Figure 6.4 Concentration profiles downstream of focusing junction for three diffusion conditions: a) zero diffusion, b) infinite diffusion, and c) finite diffusion. In case c), the concentration profile changes with the downstream location; indicated by lines 1, 2, and 3.

The final scenario, encountered in experiments, consists of a finite diffusivity of the sample fluid in the transverse direction. The concentration is non-uniform in the y-direction and the profile varies along the x-axis. Three profiles at various x-locations are illustrated in Figure 6.4(c). Profile 1 occurs at the location where the focused stream is narrowest, Profile 2 occurs a short distance downstream, and Profile 3 is taken further downstream where a non-zero concentration exists at the wall. Profile 2 is assumed to fit a Gaussian curve and has the concentration,

$$c_4(y) \approx c_4^{\max} \exp\left(\frac{-y^2}{2\sigma^2}\right) \tag{6.12}$$

where the y-axis is defined from the channel centreline and σ is the standard deviation of the curve, a measure of sample dispersion. The mass conservation of the sample gives,

$$\dot{m}_1 c_1 = c_4^{\max} \int_0^{\left(W_4/2\right)} \exp\left(\frac{-y^2}{2\sigma^2}\right) \cdot \rho \bar{v}_4 \, dy \tag{6.13}$$

where $\bar{v}_4$ is the average velocity at outlet section 4 and ρ is the fluid density. By substituting the fluid mass balance, Equation 6.2, into Equation 6.13 and integrating, the focused stream width becomes,

$$\frac{d}{W_4} = \frac{c_4^{\max}}{c_1}\left(\frac{W_1}{W_4}\right)\left(\frac{2\sqrt{2}\sigma}{W_1}\right)\left(\frac{\sqrt{\pi}}{2}\right)erf\left(\frac{W_4}{2\sqrt{2}\sigma}\right) \qquad \textbf{(6.14)}$$

The use of this Gaussian model to estimate the width between dividing streamlines from experimental data requires that the profile of the fluorescence intensity fits well to the Gaussian curve. Deviations from the Gaussian shape will generate errors in determining the stream width. It was observed that the profiles taken a short distance downstream from the minimum focused stream width, 50-150 μm downstream for fluorescein, produce a very good fit. An example of a fitted curve is plotted in Figure 6.5.

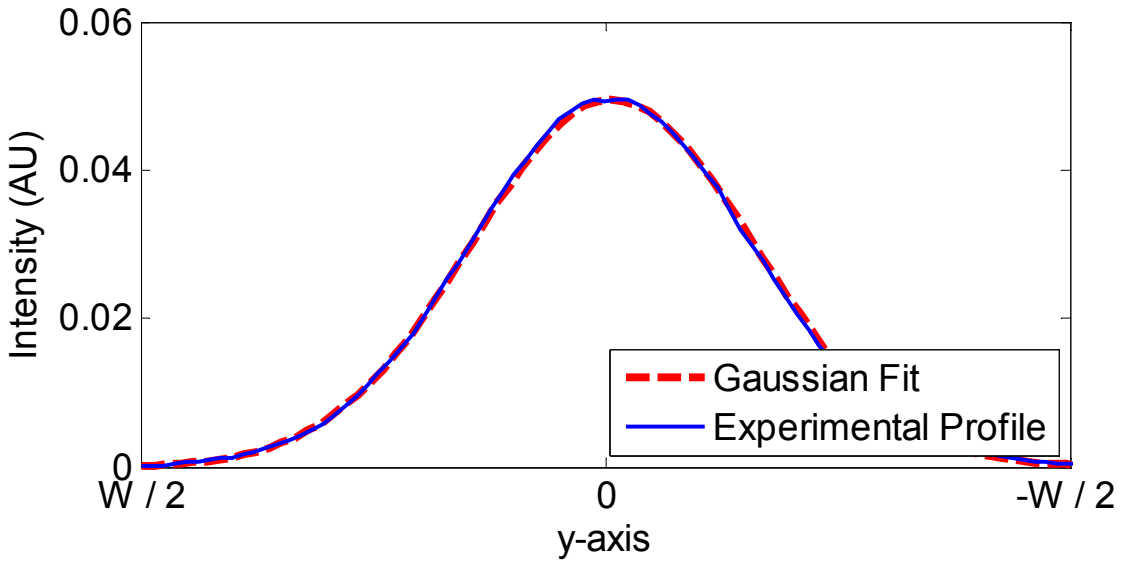

Figure 6.5 Experimental intensity profile fitted with a Gaussian curve.

The benefit of this method is that it is independent of the properties of the sample, while the FWHM method is not. To confirm this aspect of the model, several simulations with varying physical parameters were performed using COMSOL Multiphysics and the concentration profiles were analyzed with the Gaussian model. The diffusion coefficient of dye sample was varied from 3.0×10^{-10} m^2/s to 1.0×10^{-9} m^2/s with no change in the focused stream width (Figure 6.6(a)). Furthermore, the stream width determined with the Gaussian model agrees well with the values obtained from the Multiphysics numerical simulation and the compact focusing model. The values from the Gaussian model are consistently about 1% lower than the numerical predictions. This level accuracy is acceptable due to high level of errors encountered during experimentation.

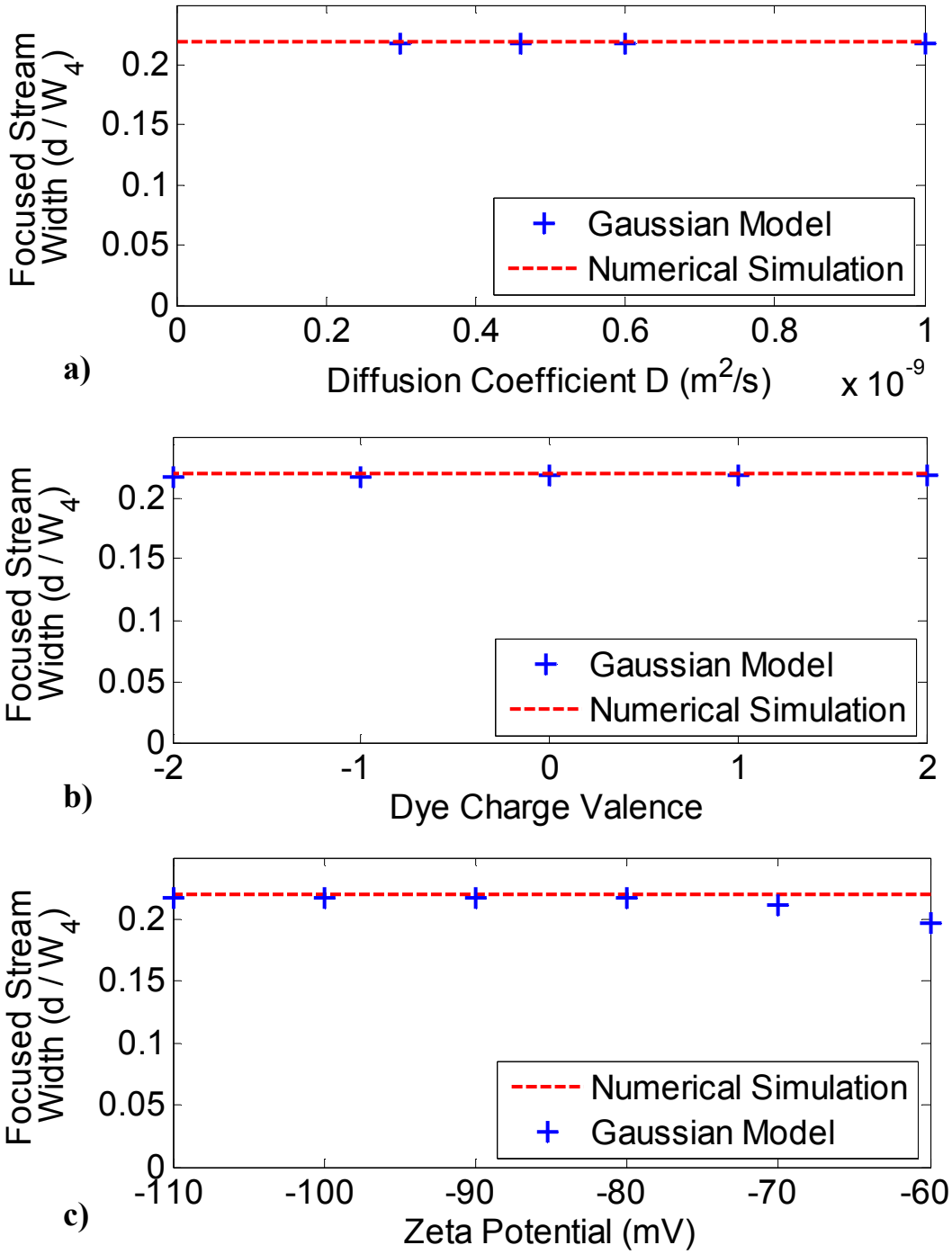

Figure 6.6 Comparison of estimated focused stream widths obtained directly from COMSOL Multiphysics numerical simulations and from the Gaussian model analysis of numerical concentration profiles. The effect of several parameters were investigated, these include: a) the diffusion coefficient of the dye, b) the charge of the dye, and c) the mobility of the fluid.

The effects of the charge of the dye (Figure 6.6(b)) and the mobility of the fluid (Figure 6.6(c)) were observed to be negligible, as expected. There is a reduction in the Gaussian determined focused stream width as the amplitude of the zeta potential decreases, but this is attributed to poor fitting of the data to the Gaussian distribution. This emphasizes the importance of obtaining a profile that approximates the Gaussian shape.

A similar comparison was performed between the compact focusing model and experimental data fitted with the Gaussian model. Figure 6.7 shows three test runs with various buffer concentrations, which have different electroosmotic mobility. The Gaussian model results correlate well to values predicted with the focusing model. There is some deviation between the three experimental results; however, the differences are smaller than the estimated experimental uncertainty of these particular cross-microchannels. The FWHM method, applied to the same 50 mM buffer experimental data, significantly over exaggerates the width of the focused stream. This is caused by diffusion and electrophoretic dispersion of the dye in the transverse direction. Also, the shape of the curve differs from both the compact model and the Gaussian model. The Gaussian fitting model is therefore a valuable tool in analyzing experimental focusing data.

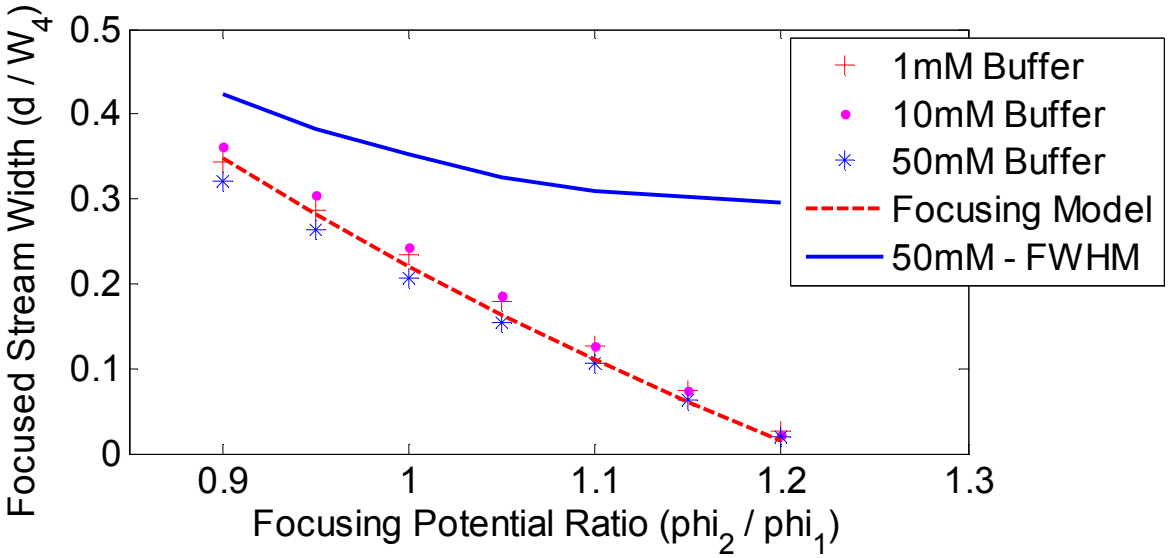

Figure 6.7 Focused stream widths for various concentrations of sodium (bi-)carbonate buffer solution (1 mM, 10 mM, and 50 mM) obtained from experimental data (points) and numerical simulations (dashed line). The focused stream widths obtained using the FWHM method (solid line) are plotted for the 50 mM buffer solution data. The cross-microchannel had a channel width ratio $\eta = 2$ with a 50 μm wide sample channel and channel lengths $L_1 = 0.01$ m, $L_2 = 0.011$ m, $L_3 = 0.011$ m, and $L_4 = 0.013$ m.

6.4 Effects of Junction Design on Focusing

The performance of different configurations of the focusing element was investigated numerically. The design of the junction does not have the same influence as it might for high Reynolds number applications, but slight variations in the focusing ability were observed. Figure 6.8 shows concentration plots obtained from Multiphysics simulations for three geometries under the same operating conditions: ϕ_1 = 1000 V, ϕ_2 = 1000 V, ϕ_3 = 1000 V, ϕ_4 = 0 V, L_1 = 0.01 m, L_2 = 0.008 m, L_3 = 0.008 m, L_4 = 0.016 m, D_i = 4.6 x 10^{-10} m^2/s, z = 0, and ζ = -80 mV.

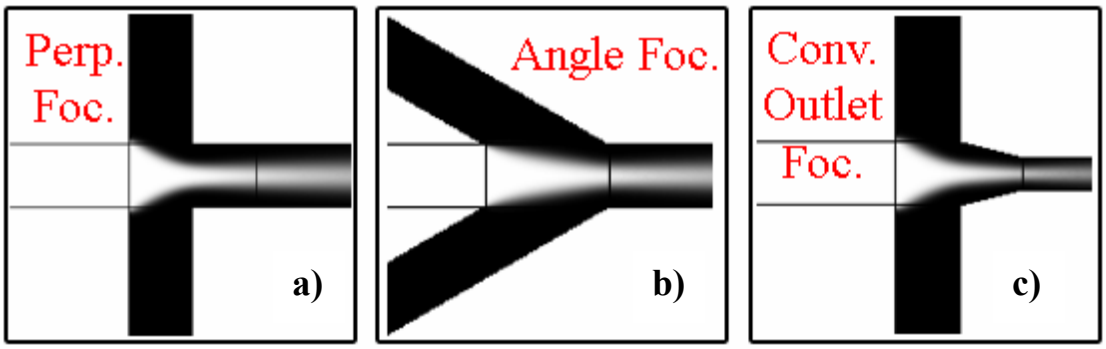

Figure 6.8 Concentration plots for three focusing configurations obtained from numerical simulations: a) perpendicular focuser, b) angled focuser, and c) converging outlet focuser.

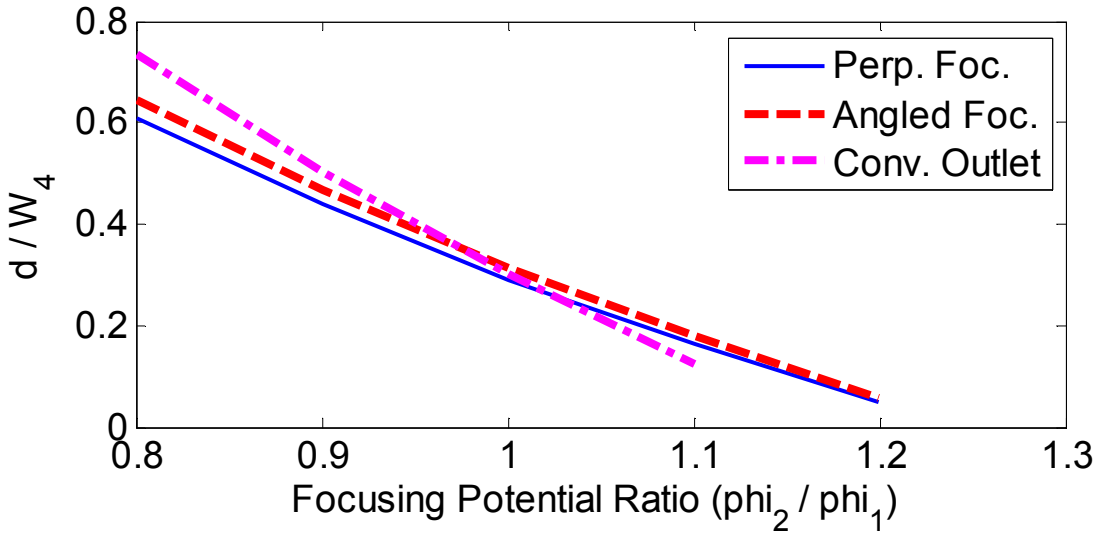

Figure 6.9 Focused stream widths for three focusing configurations obtained from numerical simulations: perpendicular focuser, angled focuser, and converging outlet focuser.

The perpendicular focuser design, the angled focuser design, and the converging outlet channel design produce similar concentration plots and focused stream widths. Values of d / W_4 are plotted in Figure 6.9 for varying ϕ_{foc}. The perpendicular focuser exhibits a slightly better performance than the angled focuser. This is likely attributed to the shorter length for flow pinching in the perpendicular focuser than the angled focuser, which has an elongated focusing length. The converging outlet channel focuser appears to have a different slope than the two other designs. Changes to the electrical resistance network, by reducing the outlet channel width, alter the electric field and therefore the focusing behaviour is different. When a constriction of the same width and length is placed on each of the channels in the cross-microchannel, then similar results to the perpendicular focuser design are achieved. The disadvantage of using constrictions near the focusing element is that the local velocity is increased, but the velocity in the wide channel sections will be reduced compared to the uniform width design. This is an undesirable characteristic for the sample channel because adherence of the cells to the chip is more likely.

The influence of the ratio of sheath channel width to sample channel width, $\eta = W_2 / W_1$, was also considered. Under a constant ϕ_{foc}, changes to η alter the electric field and cause a change in the electroosmotic flow field. Experiments were performed on cross-microchannels with $\eta = 1$, $\eta = 2$, and $\eta = 3$. A comparison of the focusing of the three designs is shown in Figure 6.10. The length of the focusing zone appears proportional to the width of the sheath channel. Also, the width of the focused stream, *d*, is smallest in the $\eta = 3$ design for the same ϕ_{foc}. In each case, the Multiphysics numerical simulations show good agreement to the experimental concentration plots, despite relatively high experimental uncertainty observed with these cross-microchannels.

The Gaussian model was used to determine the width of the focused stream from the experimental data. The resulting d / W_4 values for the three η values are shown in Figure 6.11 as a function of ϕ_{foc}. Predicted values from the compact focusing model are plotted with the dashed lines. It is clear that for a given potential ratio, the design with $\eta = 3$ provides a greater level of focusing. The improvement in focusing from $\eta = 1$ to $\eta = 2$ is more drastic than $\eta = 2$ to $\eta = 3$. This relationship is illustrated in Figure 6.12. As η increases, d / W_4 approaches a steady value. A trade-off is encountered between a savings in the applied potentials and a practical channel width ratio. If η is too large, predictable sample dispensing may become difficult; however, no irregularities were observed at $\eta = 3$.

a)

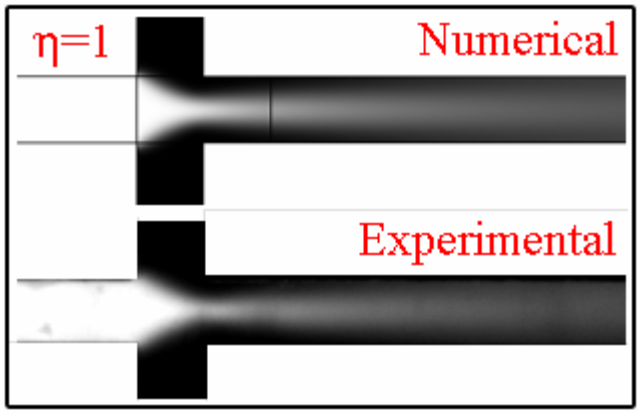

b)

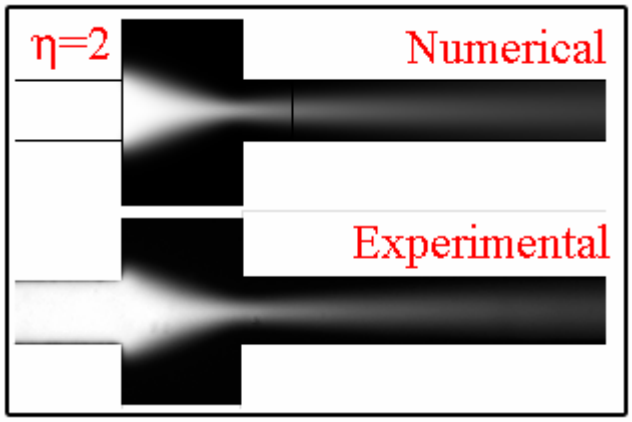

c)

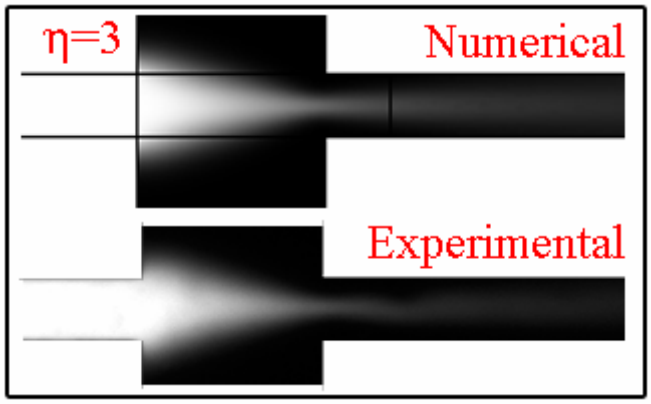

Figure 6.10 Concentration plots for a) $\eta = 1$, b) $\eta = 2$, and c) $\eta = 3$ obtained from numerical simulations and experiments with fluorescein dye. The applied potentials at reservoirs 1-4 are ϕ = [1000, 1000, 1000, 0] V, respectively, the length of the channels 1-4 are L = [0.01, 0.008, 0.008, 0.016] m, respectively, the diffusion is assumed $D_i = 4.6 \times 10^{-10}$ m^2/s, dye valence z = -2, and zeta potential ζ = -80 mV.

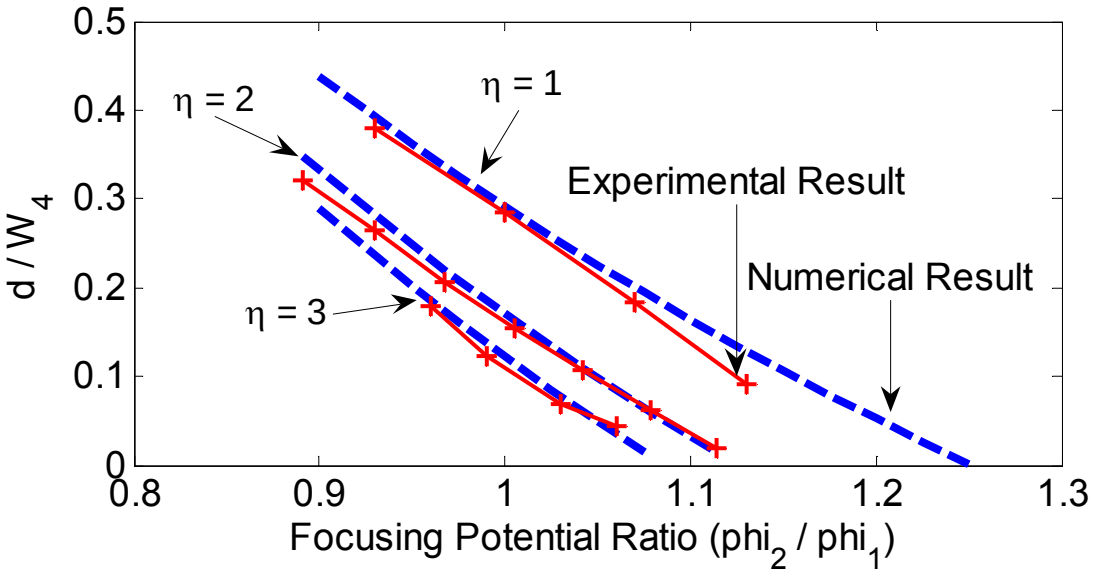

Figure 6.11 Comparison of numerical and experimental focused stream width results versus focusing potential for $\eta = 1$, $\eta = 2$, and $\eta = 3$.

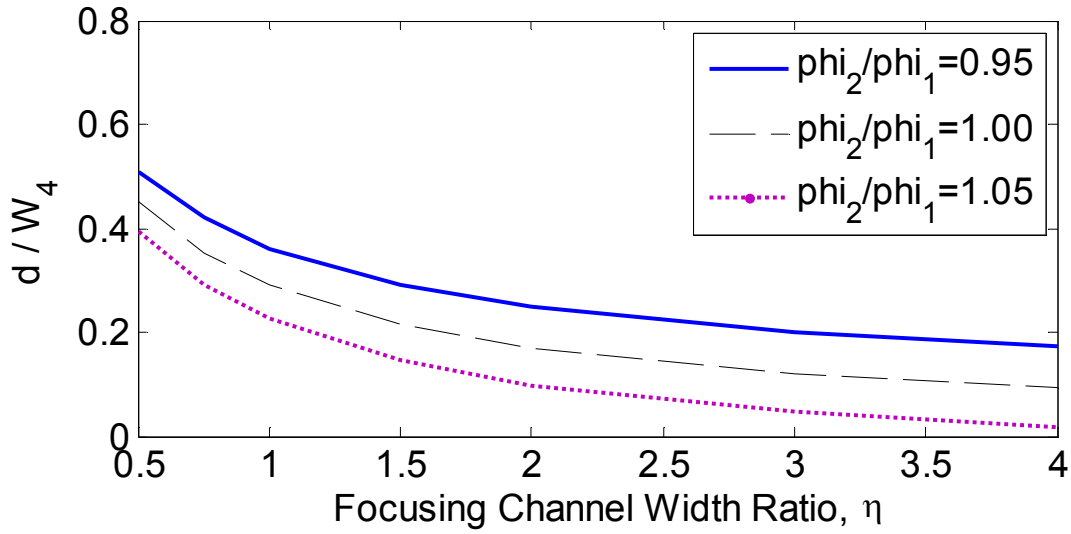

Figure 6.12 Predicted focused stream widths versus focusing channel width ratio η. Three values of ϕ_{foc} are illustrated: $\phi_{foc} = 0.95$, $\phi_{foc} = 1.00$, and $\phi_{foc} = 1.05$.

Dispensing the 3.8 μm and 4.0 μm diameter fluorescent microspheres was successfully achieved with all the designs tested, except for the glass chip, which was too large to fully control dispensing. Similarly, controlling the 1.0 μm diameter microspheres proved more difficult due to the size of the channels used in this work. The channel size should be approximately 5-10 times the size of the cells to be focused. This range is chosen based on results from Figure 6.11 to prevent operation where

$d / W_4 < 0.1$. Below this value the sample velocity is very low and may promote cell adhesion on the channel surfaces.

An example of particle focusing is shown as a series of images in Figure 6.13, where the time between images is approximately 550 ms. The particles are aligned in the outlet channel after focusing and space is provided for individual detection downstream. Particles 5 and 6, initially attached, were separated in the focusing process.

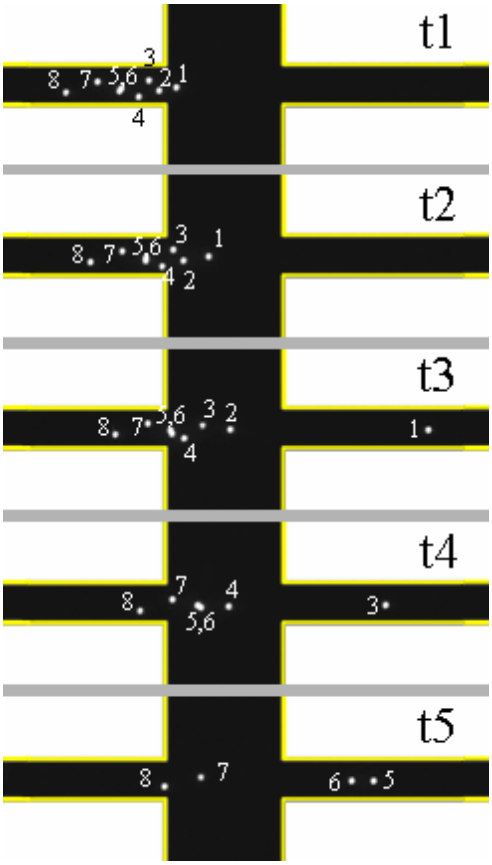

Figure 6.13 Time sequential images of particle focusing. The 4.0 μm microspheres are focused in Chip F-1 ($\eta = 3$). The elapsed time between images is 550 ms.

For several tests, the transverse location of the particles after focusing was determined by particle tracking. The distribution of particle location variance is plotted in Figure 6.14. The maximum variation from the average location is 2.6 μm in a 50 μm wide outlet channel. This observed consistency should enable adequate sample detection.

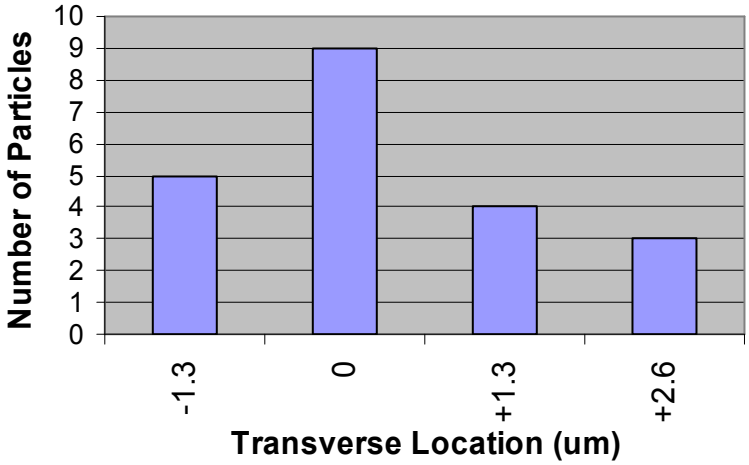

Figure 6.14 Distribution of particle position in the transverse direction after focusing.

The designs tested for dynamic cell sorting had focusing width ratios $\eta = 2$ and $\eta = 3$. Both designs had similar performance, but the applied potentials were lower for the design with $\eta = 3$. The typical operating voltages for the designs can be found in Appendix D. Adjustments were occasionally required during experiments to control the particle throughput. The concentration of the particle suspension often decreased after a long run-time and a higher sample flow was necessary to maintain the particle frequency.

6.5 Selected Focusing Component

The perpendicular design configuration was selected for the focusing element due to the simplicity of design and slightly better performance than the angled focuser design. The study of the effect of non-uniform channel widths indicated a 66% and 100% decrease in the focused stream width can be achieved with $\eta = 2$ and $\eta = 3$, respectively. Further reductions are possible with higher η values, however, such designs may be impractical. No observed performance anomalies were encountered for the focuser design with $\eta = 3$. Based on the plots of d / W_4 versus ϕ_{foc}, the width of the sample and outlet channels should optimally be 5-10 times the size of the cells intended for focusing. For the 4.0 μm and 3.8 μm microspheres, the width of the recommended sample channel is 30 μm.

Chapter 7

Cell Sorting Evaluation

The purpose of the microfluidic chip developed in this work is to separate target cells from a non-homogeneous suspension. The dynamic sorting performance values of the prospective fluidic sorting designs introduced in Chapter 5 are presented in this chapter. Experimental and numerical results are analyzed and the most effective sorting design is selected, based on the evaluation criteria. The selected component is implemented in the final recommended chip design described in Chapter 8.

7.1 Criteria for Design Evaluation

Three critical parameters are used to evaluate the performance of a cell sorting device: the sorting efficiency, the purity of the enriched sample, and the maximum particle throughput. The efficiency of the sorting routine measures the ratio of successfully sorted target cells to the total number of target cells detected. The efficiency depends on the sorting mode (enrichment, single cell, or exclusion), operating conditions (cell arrival rate, target cell fraction, and switching time duration), and the ability of the system to collect a desired sorting event. Comparisons between the efficiencies of the designs are possible by operating under similar conditions. Selecting the design with the highest efficiency is preferable.

The purity, or final cell fraction, of the enriched sample is also dependent on the sorting mode, rate of cell arrival, switching time duration, and target cell fraction. Achieving the highest possible level of purity is desired. While the design does not directly factor into the purity, as it does with the efficiency, the time required to undergo a switching event is influenced by the design. The design that provides effective sorting with the shortest pulse duration will generally provide the purest sample. This places importance on minimizing the switching time duration.

The application and usefulness of a cell sorting unit is in part determined by the maximum particle throughput. Conventional droplet-style FACS systems can achieve rates up to 10 000 cells/s and microfluidic cell sorters using fluidic switching mechanisms are generally on the order of 1-100 cells/s. Maximizing the sample throughput allows faster processing and the analysis of larger sample volumes, therefore is beneficial. The optimal lengths of switching for the designs were determined

according to the sorting efficiency and sample purity at various sorting durations. These values were compared between the designs.

Uncertainties that result from pressure differences and chip-to-chip variations can cause flow anomalies that affect the ability to sort particles. Robustness of the sorting mechanism under various conditions was investigated by numerical and experimental methods. The design that accurately directs the cells under adverse conditions is favoured.

The simplicity of the design is important for miniaturization and mass production. The number of fluid reservoirs and channels was taken into account in selecting the design component.

7.2 Sorting Capability of Chip Designs

Flow Control

Numerical simulations were performed for the various chip designs to determine the electric field strengths and fluid velocities throughout the chip. Examples of the electric field and velocity field are shown in Figure 7.1(a) and Figure 7.1(b), respectively, for Design F-1 under typical operating conditions. The operating conditions for this and the other tested designs are listed in Appendix D. The electric and velocity fields were observed to be very similar for designs with minor variations and do not provide much support for further evaluation. Instead, these results were more useful for finding appropriate operating conditions; for example, to avoid electroporation of live cells during operation, the values of the electric field must be kept below the threshold level of the cell. The 400 V/cm electric field strength reported to cause electroporation in mammalian cells was used as a guideline [Wang and Lu (2006)]. The typical fluid velocity in the detection channel was approximately 2 mm/s, while the cell velocities were on the order of 0.5 mm/s.

Determining the flow paths for cell sorting is critical to understanding and predicting the behaviour of a particular design. Numerical velocity streamline plots indicate the course of the particles and flow in the control streams. The streamlines that provide the most information are the ones that separate the sample from the sheath fluid, follow the walls in the main detection channel, and extend from the directing channels. The entrapped sample should follow the centerline streamline for symmetric focusing conditions; therefore, this streamline must be directed into the desired collection channel. The streamlines at the edge of the detection channel provide boundaries for the particle motion. The velocity streamline plot for Design F-1 is shown in Figure 7.1(c).

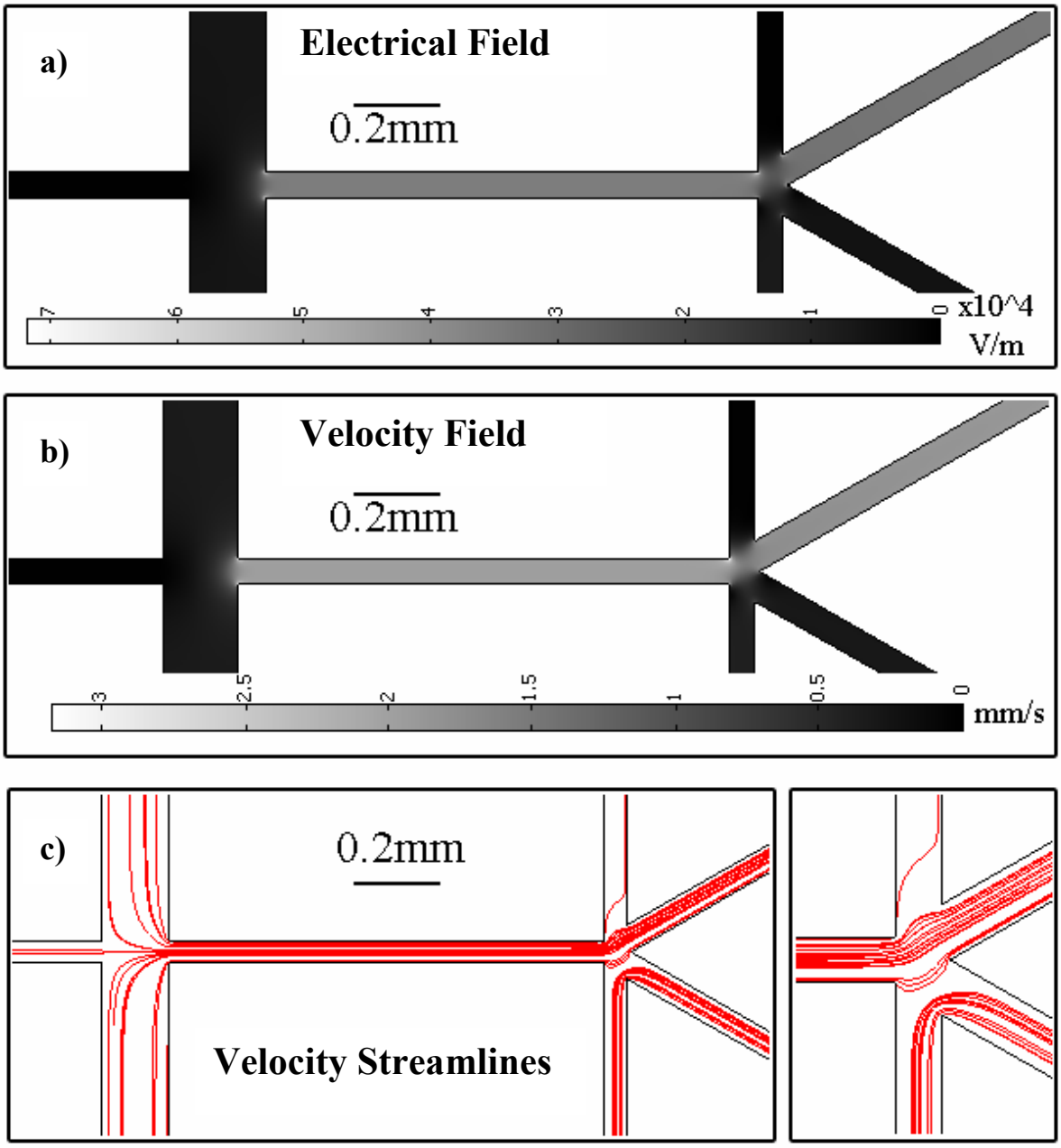

Figure 7.1 Numerical simulation results for Design F-1: a) electric field strength, b) velocity field, and c) velocity streamline plot. See Appendix D for voltages.

Preventing particles from reversing directions in the inactive collection stream requires flow towards the reservoir to be maintained. This is generally accomplished by two methods. Firstly, directing streams ensure that there is continuous flow to all of the collection reservoirs. This provision of directing streams is illustrated for Design F-1 in Figure 7.1(c). All the flow from the detection

channel is directed into the upper collection channel. The lower directing stream helps deflect the particle and provides continuous flow to the lower collecting stream. Secondly, a small amount of flow leaks from the detection channel and enters the inactive collection channel. This is achieved by precisely controlling the applied potential at the inactive collection stream reservoir. Design F-2 employs this technique because it does not have directing streams. Figure 7.2 illustrates the leakage flow mode.

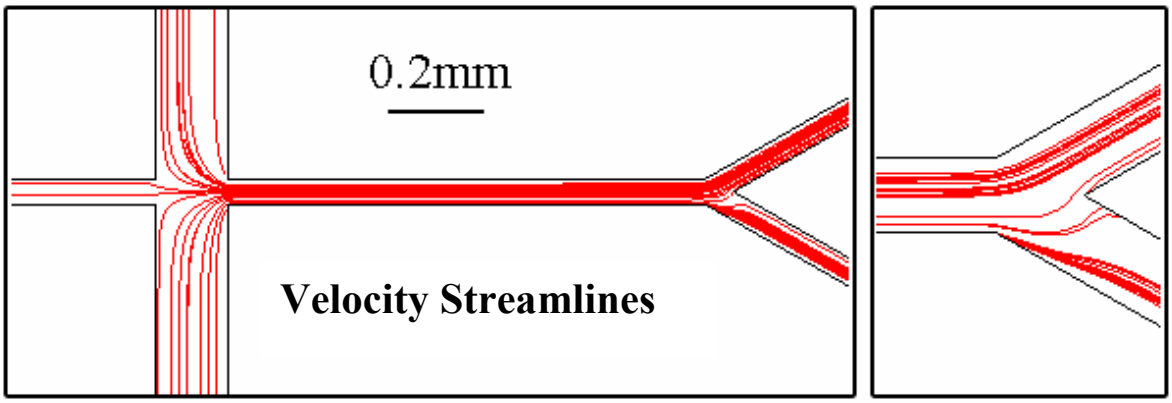

Figure 7.2 Velocity streamline plot for Design F-2 obtained by numerical simulation. See Appendix D for operating voltages.

The downside to operating with leakage flow is the observed sensitivity to the arrival location of the cell. If the cell travels along the streamline that enters the inactive collection stream, the particle will be sorted incorrectly. During regular tests, the arrival locations of the cells were relatively consistent; therefore, experiments were performed using asymmetric focusing potentials to deliver particles near the wall of the detection channel opposite the collection side. Many of the particles were accurately collected with Design F-2, but a significant portion entered the wrong channel. Flow anomalies from outside influences could cause similar conditions to be encountered. The simplicity of Design F-2 is an asset for system miniaturization because it has fewer applied potentials to control; however, eliminating the need for leakage flow with directing streams removes some flow sensitivity. Design F-1 accurately directed the vast majority of the particles with the asymmetric focusing conditions.

Designs F-3 and F-4 have directing channels located upstream of the sorting junction to direct the particle prior to separation. The streamline plots are shown in Figures 7.3 and 7.4 for Designs F-3 and F-4, respectively. The directing channels are located closer to the junction for Design F-3 and they appear to provide better flow deflection than Design F-4, for the same applied potentials. The

directing flow for these designs eliminates the need for leakage flow, and should be less sensitive to particle location than Design F-2.

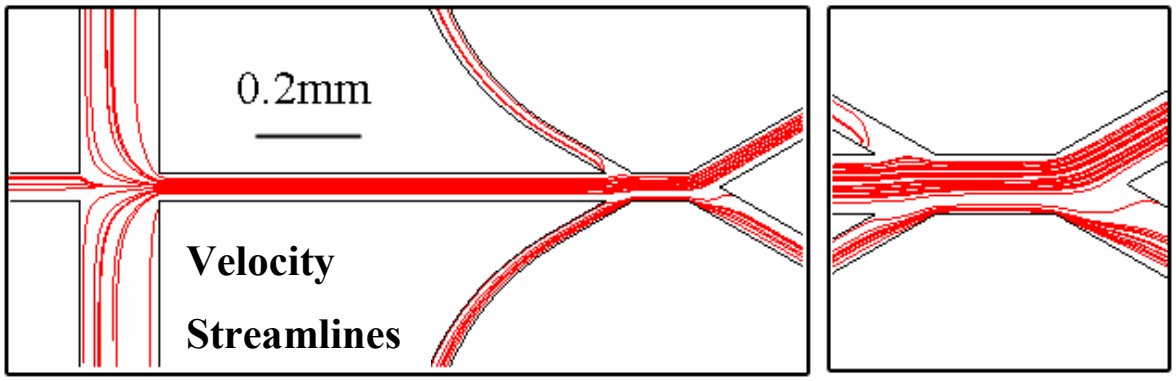

Figure 7.3 Velocity streamline plot for Design F-3 obtained by numerical simulation. See Appendix D for operating voltages.

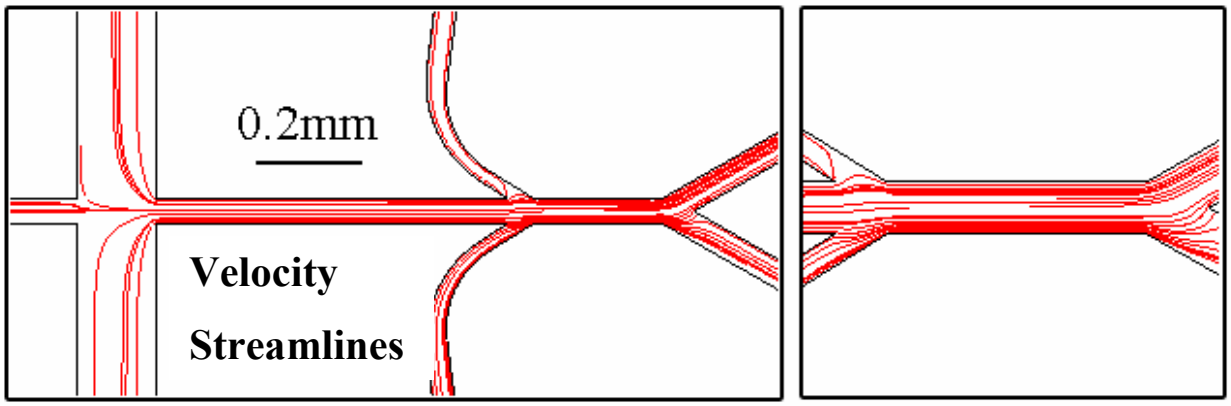

Figure 7.4 Velocity streamline plot for Design F-4 obtained by numerical simulation. See Appendix D for operating voltages.

Design E-2b has similar characteristics to the initial design, A-1; the collection channels are located a short distance up the directing stream channels. Indicated by the streamline plot, Figure 7.5, the vertical channel section between the sorting junction and the collection channel is susceptible to backflow. Small changes in the flow field can cause particle reversal and sorting errors. The directing streams provide continuous flow to the reservoirs once the particles reach the collection channel. Also, it was observed that the particles react to the sorting T-junction a short distance upstream, which may cause the particles to deflect and enter the wrong channel during high speed flow switching. The advantage of this design is that flow directing is easy to control with the use of binary junctions.

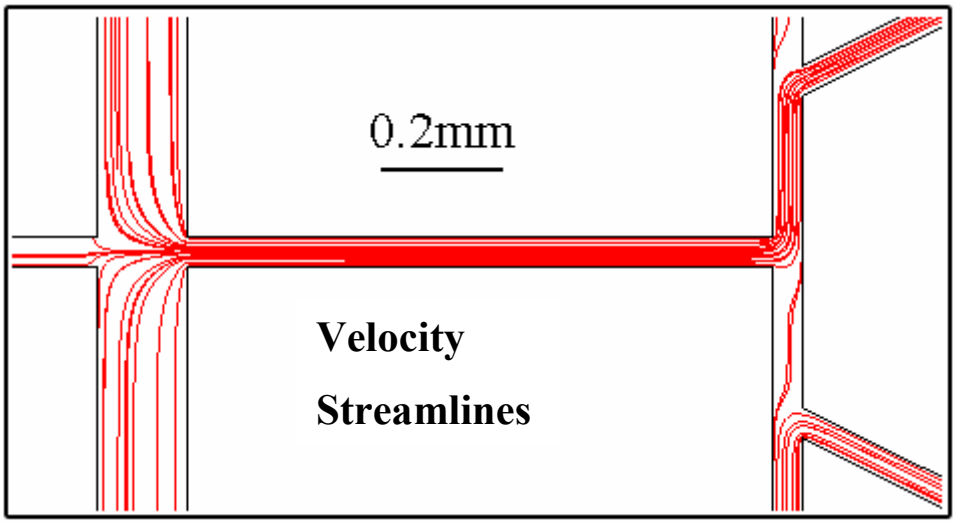

Figure 7.5 Velocity streamline plot for Design E-2b obtained by numerical simulation. See Appendix D for operating voltages.

Dynamic Sorting

Dynamic sorting of a cellular suspension containing two types of fluorescent microspheres was performed to characterize and evaluate the chip designs. A manual pulse flow switching technique was used for real-time operation, which simulates fully automated sorting. The basic procedure is illustrated in Figure 7.6. The two particles, 3.8 μm and 4.0 μm microspheres, have different fluorescent characteristics and emit different intensities using a green filter cube; the signals are shown as inset images in the figure. The brighter 3.8 μm particles were the target cells for all of the experiments. The cell sorter runs in a default path mode, collecting to the top channel, until a target cell (particle A) is observed in the detection region (at t2). After a short time delay, the target particle is near the sorting junction and enters the flow switching region (at t3), defined by the volume collected during a sorting event. Using the control software, the potential distribution is switched from the default 'waste' path to the collection path for a short duration *T* (from t3 to t4). The target particle is collected to the desired channel during this time. The flow automatically returns to the default state to capture the unwanted cells (particle B). This process is repeated for every target cell detected. The mode of sorting using this method is limited to enrichment mode, where all target particles are selected for sorting. Single cell and exclusion modes may be possible with an automated detection and signal analysis system.

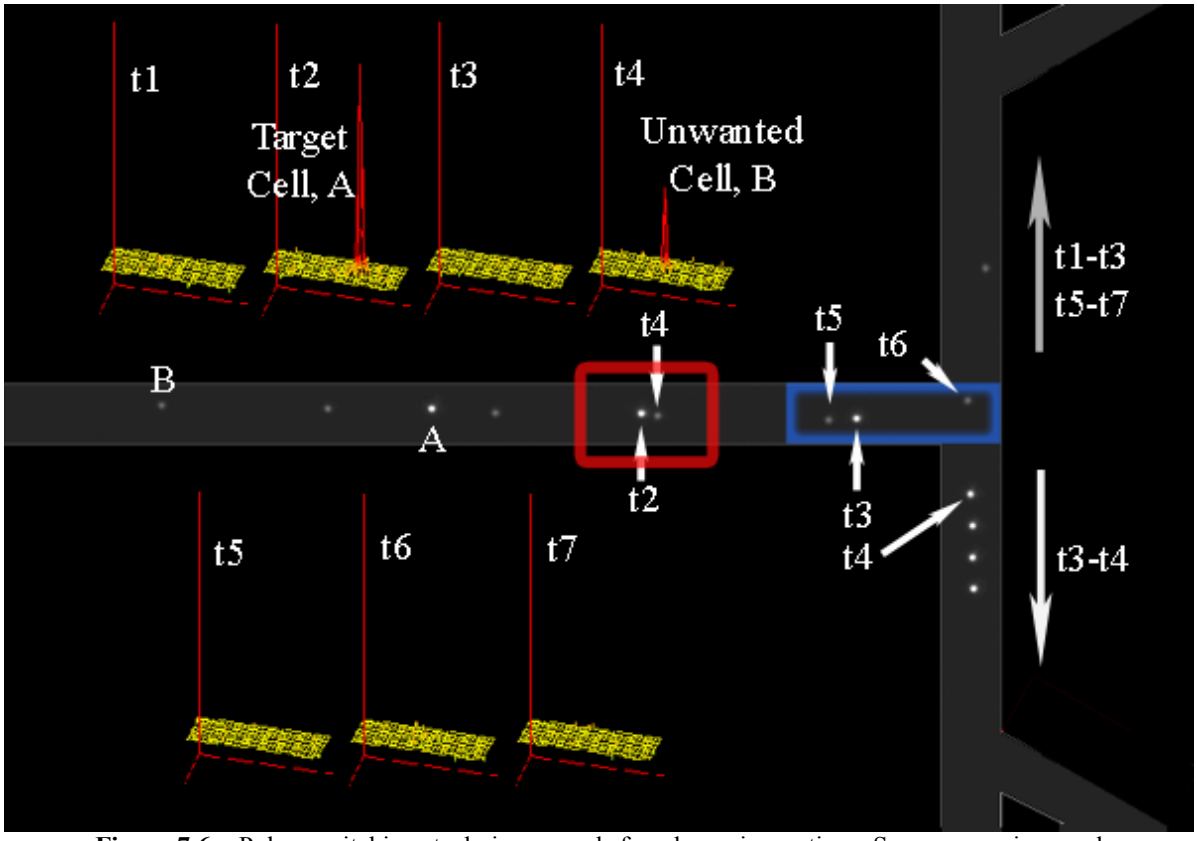

Figure 7.6 Pulse switching technique used for dynamic sorting. Seven superimposed images of two particles (target cell A and waste cell B) illustrate the two directions of collection. Particle A reaches the detection zone at time t2, where the fluorescence signal of the particle is detected (signal plot shown in inset image t2). After a short period of time (at t3), particle A reaches the switching region and the potentials are manually switched from the default 'waste' path to the collection path for a short duration (t3-t4). The cell is collected during this pulse, and afterwards the system returns to the default path where it awaits future activation. Particle B reaches the detection zone at t4 (weaker signal detected) and the switching region at t5. It is directed to the default path of sorter.

High speed image sequences recorded during operation are used to count the cells and determine the sorting performance for each test run. An example of the initial and final cell fractions of the target cell and unwanted cell for a series of tests is shown in Figures 7.7(a) and 7.7(b), respectively. For this test set, the initial target cell fraction ranged from approximately 0.2-0.4 and the final enriched fraction was greater than 0.8 for all the tests, except two. The final cell fraction of the unwanted cell was greater than 0.9 in all tests. Significant improvement in the cell fraction was achieved for both cells; however, the enrichment of the target cell is the primary interest of this project.

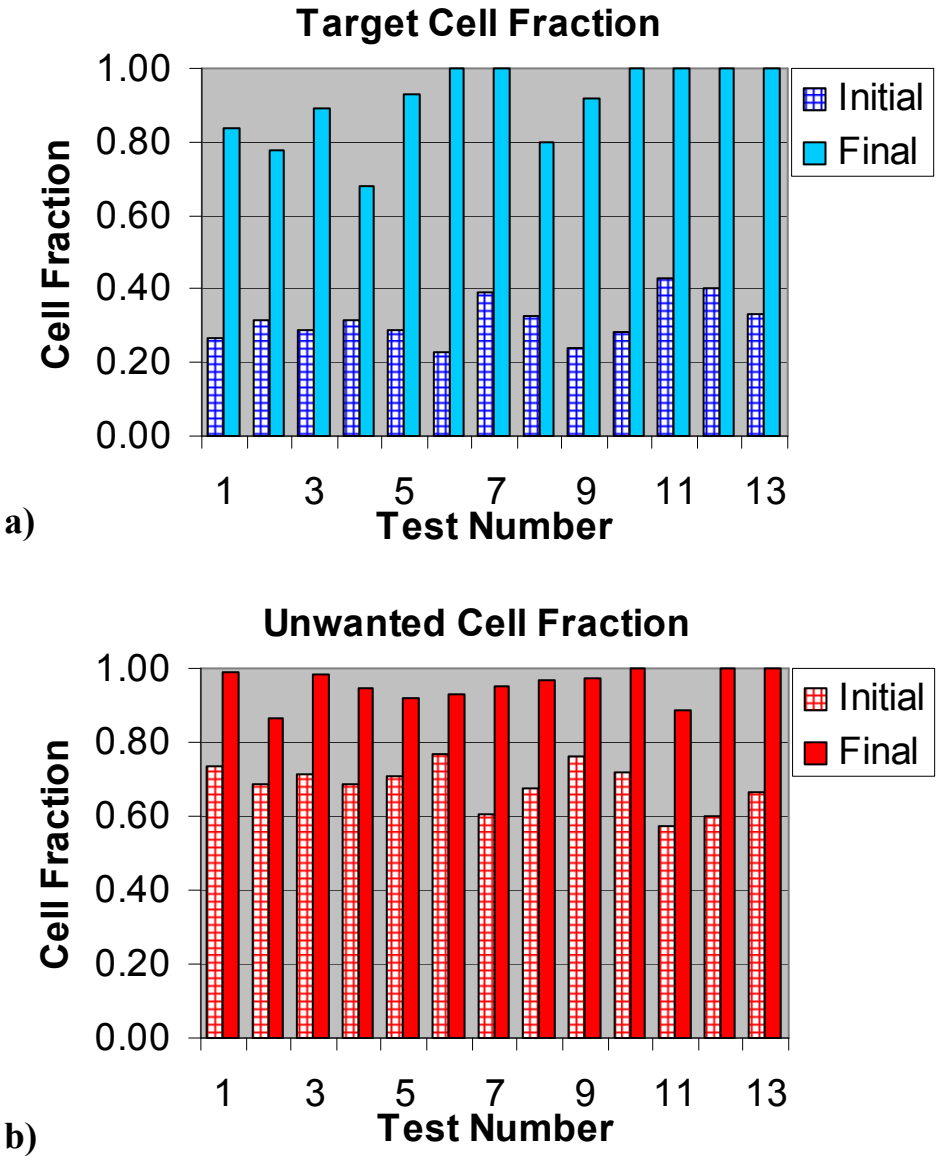

Figure 7.7 Cell fraction data for a set of experiments performed on chip Design F-2: a) the target cell fraction before and after sorting and b) the unwanted cell fraction before and after cell sorting.

The time duration for sorting was investigated for each design by running multiple tests with different pulse lengths. Agreeing with cell sorting theory, a trade-off between the sorting efficiency and the enriched sample purity was observed. The efficiency increases with a longer pulse, Figure 7.8(a), and the sample purity decreases with longer pulse durations, Figure 7.8(b). Too short of a pulse does not provide adequate time for the cell to be directed into the desired channel, while too

long a pulse increases the probability of an unwanted cell being captured along with a target cell. The optimal pulse time required to achieve high purity and high capture efficiency was selected for comparison of the designs. The sorting duration for Designs E-2, F-1, F-2, F-3, and F-4 are shown in Figure 7.9. Designs F-1 and F-2 clearly have the fastest sorting capability, with pulse times less than 250 ms. The speed of Designs F-3 and F-4 suffered because upstream particle deflection was most effective when activated prior to the sorting activation. With the experimental system, this entire sequence would run for each triggered event and could not be re-activated until completion. The duration was therefore longer than Designs F-1 and F-2. Design F-4 exhibited the longest required pulse because the directing streams were located further upstream. Design E-2b required a longer pulse to ensure the particle traveled far enough into the collection stream that it did not reverse paths.

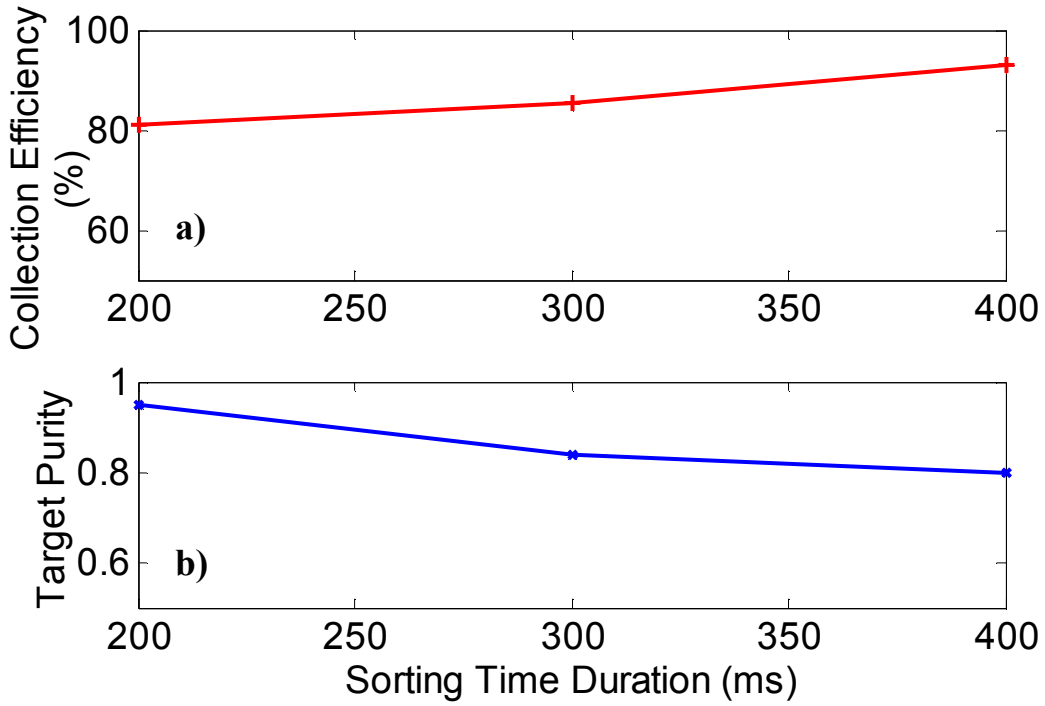

Figure 7.8 Experimental sorting data for Design F-2: a) the collection efficiency versus the sorting time duration and b) the target cell purity after sorting versus the sorting time duration.

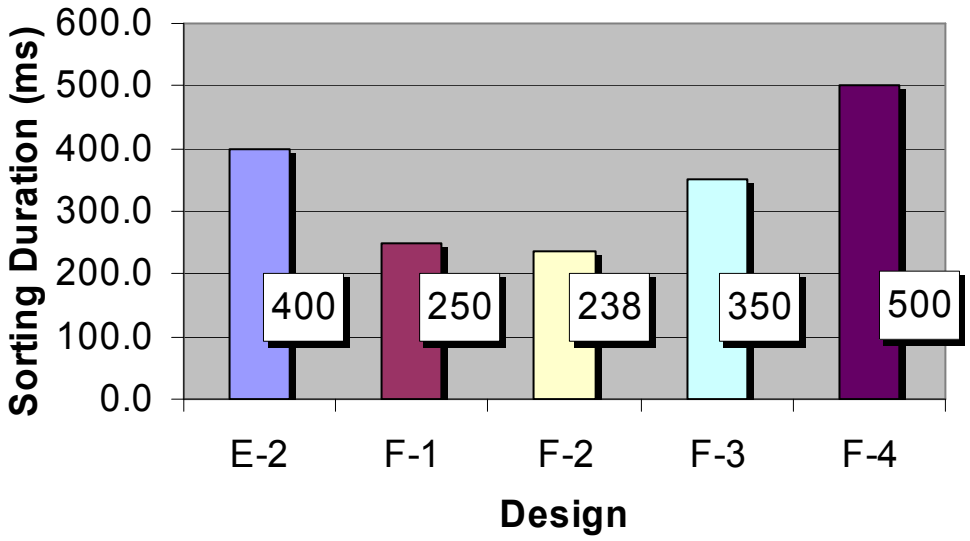

Figure 7.9 The optimal sorting time duration *T* determined from experiments.

The predicted maximum cell throughput for various target cell fractions, calculated with the optimal pulse time of each design, are shown in Figure 7.10. Rates up to 40 cells/s can be achieved for cell fraction $s = 0.1$. The difficulty associated with increasing the cell arrival rate is that the purity of the enriched sample decreases. Experimental results are plotted against theoretical values for a high cell fraction ($s = 0.29$) in Figure 7.11(a) and a rare cell condition ($s = 0.01$) in Figure 7.11(b). A rapid drop-off of purity was observed at modest cell arrival rates.

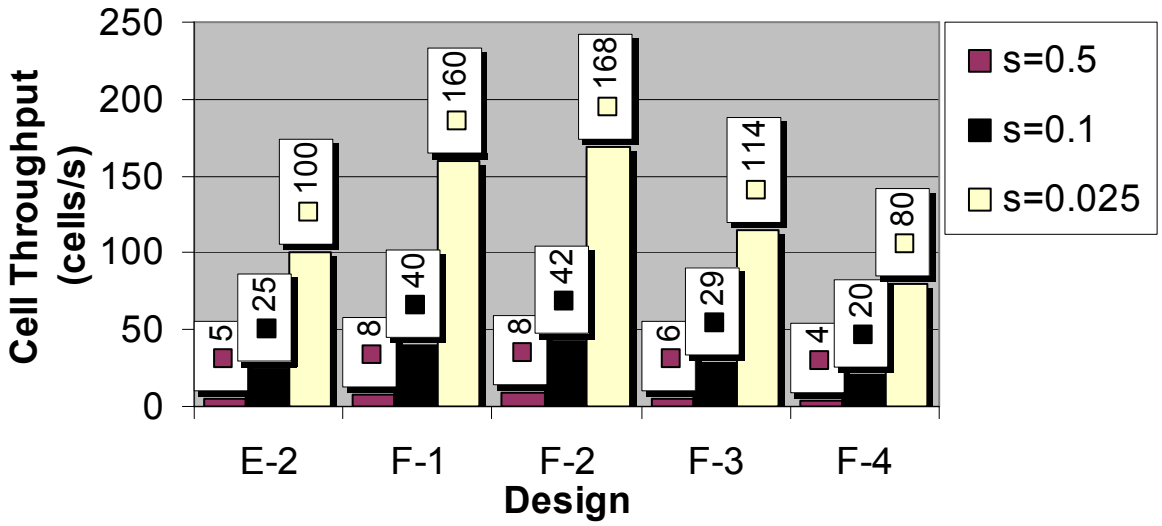

Figure 7.10 The predicted maximum cell throughput calculated from the optimal *T* values for various target cell fractions: $s = 0.5$, $s = 0.1$, and $s = 0.025$.

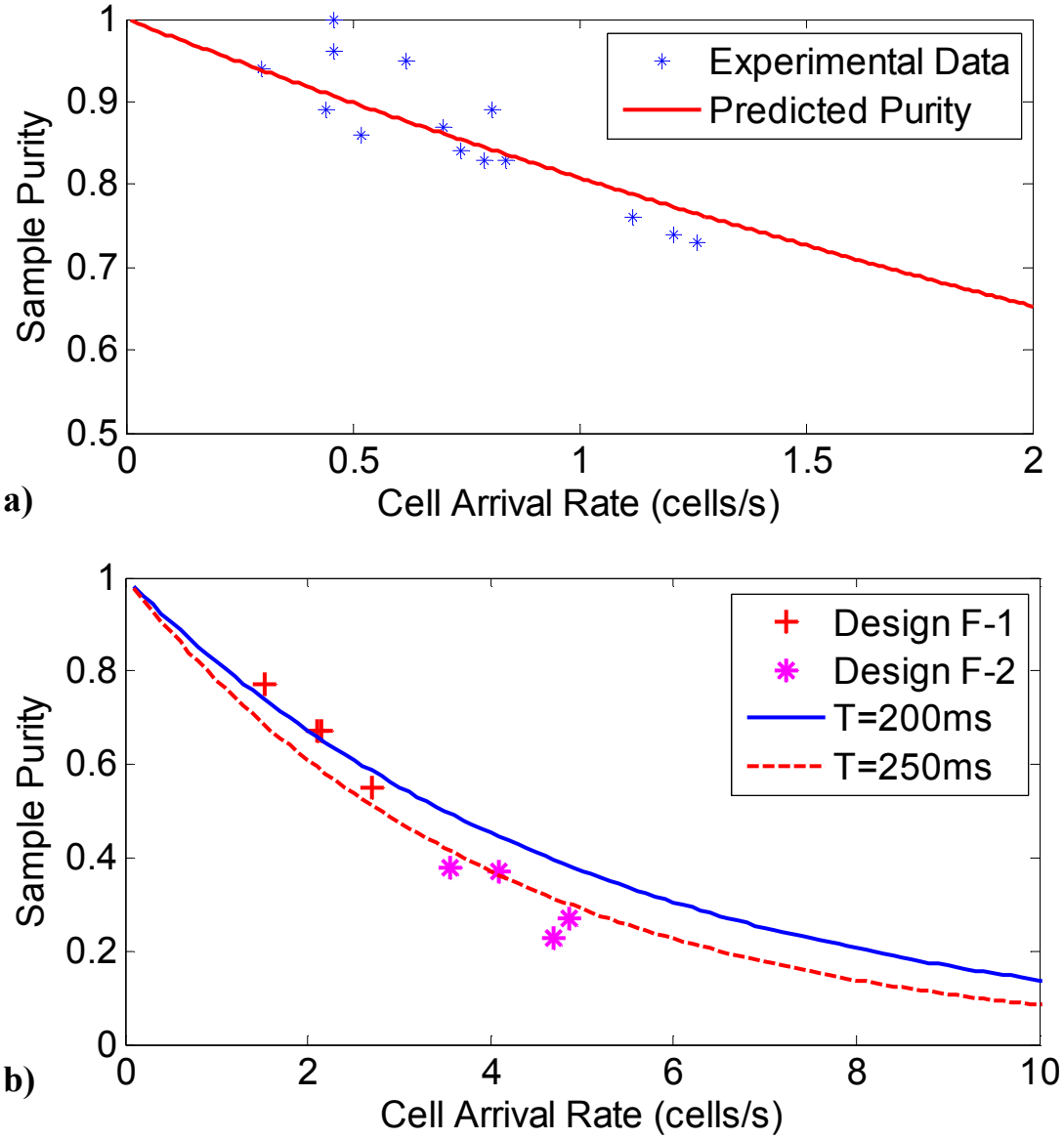

Figure 7.11 Experimental and predicted sample purity data with varying cell arrival rates. a) The results for high target cell fraction conditions: s = 0.29, T = 300 ms, in enrichment mode. b) The purity for rare cell conditions: s = 0.01, T = 200 and 250 ms, in enrichment mode.

The sample purity can be improved by reducing the sorting time. It was observed in experiments that increasing the velocity of the particles reduced the time duration required for capture. A simple analysis shows that reducing the sorting time T from 250 ms to 50 ms for a rare cell solution at r = 10 cells/s can improve the purity nearly 7.5-fold. Higher velocities can be achieved by increasing the electric field, reducing the buffer concentration, or improving the channel surface properties to

increase mobility. Manual detection of particles at higher velocities was too difficult to perform reliable experiments, but automated operation can take advantage of these findings.

The sorting efficiency at the optimal sorting duration is shown in Figure 7.12. The values are averages from multiple tests under similar operating conditions to moderate performance inconsistencies. The efficiencies range from 75.5% for Design E-2b to 91.5% for Design F-1. Design F-2 is second best at 90%. Many of the target cells collected incorrectly were due to mistiming of the manual pulse switching, resulting in reduced efficiency values. Automated detection and flow control systems should increase the sorting efficiency.

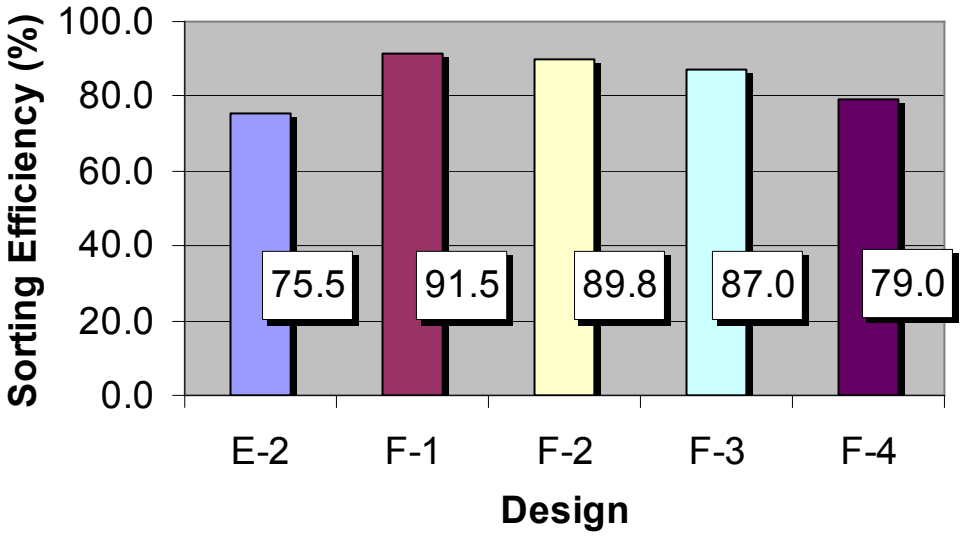

Figure 7.12 The sorting efficiency achieved at optimal *T* values for the designs tested.

The purity values of the enriched sample after sorting are illustrated in Figure 7.13 for the same averaged experimental results. Cell arrival rates for these tests were around 0.5 cells/s. The minimum purity achieved for these conditions was 0.86 with Design F-4. Designs E-2b and F-1 demonstrated the highest purity with a 0.90 target cell fraction. The enrichment for this range of tests varied between 3.5- and 6-fold. Under rare target cell conditions, approximately 1% of the total particles, 60-fold and 25-fold enrichment were achieved for Designs F-1 and F-2, respectively.

The sorting results for the different designs are summarized in Table 7.1. The values are averages from multiple test runs with a cell throughput around 0.5 cells/s.

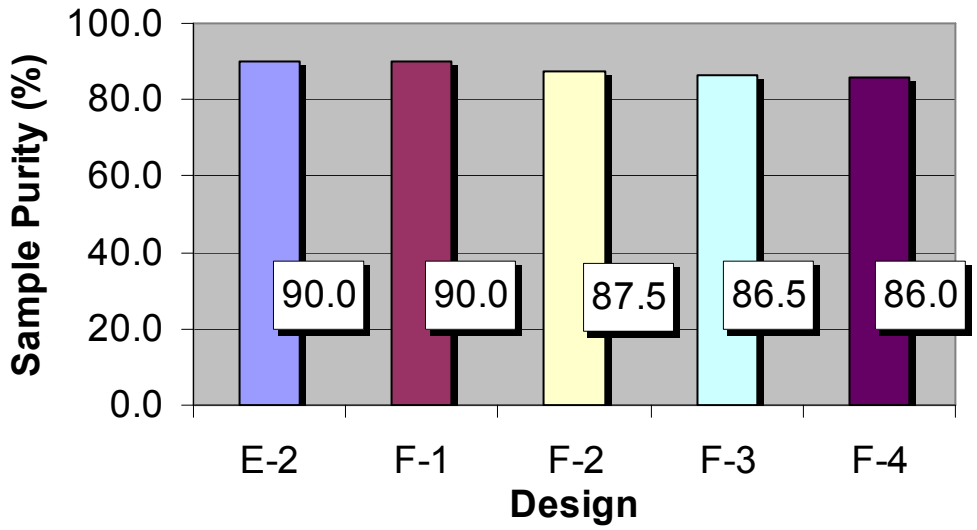

Figure 7.13 The enriched sample purity achieved at optimal *T* values for the designs tested.

Table 7.1 Sorting performance values for the cell sorter designs tested.

Design	Sorting Time (ms)	Sorting Efficiency (%)	Enrichment	Sample Purity (%)	Max Cell Rate, s=0.5	Max Cell Rate, s=0.1	Max Cell Rate, s=0.025
E-2b	400.0	75.5	3.6	90.0	5	25	100
F-1	250.0	91.5	3.9	90.0	8	40	160
F-2	237.5	89.8	5.3	87.5	8	42	168
F-3	350.0	87.0	6.0	86.5	6	29	114
F-4	500.0	79.0	3.6	86.0	4	20	80

7.3 Selected Sorting Configuration

Based on the sorting performance, Designs F-1 and F-2 provide the highest efficiency and sample purity with the shortest sorting time. These two designs have the potential for the highest cell throughput. The use of directing streams was demonstrated to improve performance by preventing backflow of particles and by reducing the sensitivity of particle location on sorting; design F-1 captured a higher percentage of particles offset by asymmetric focusing than Design F-2. Despite the added complexity that exists with directing streams, more robust operation is expected. Design F-1 is selected as the sorting configuration for the proposed design detailed in Chapter 8.

Chapter 8

Final Cell Sorter Design

Elements of the microfluidic chip demonstrated to provide the best performance were implemented into a final cell sorter design. This chapter presents the proposed chip design and summarizes the individual components. Estimated performance quantities are described based on the experimental results of the previous designs. Also, the limitations and uncertainties of the system are presented as they affect the chip operation.

8.1 Microfluidic Chip Design

The experimental and numerical investigation of the cell sorter chip designs provided valuable information about the function and influence of various parameters. Evaluation criteria described in Chapters 6 and 7 were used to select the individual components. The design with the selected elements and modifications is shown in Figure 8.1. The optimized adaptations of the focusing junction for sample dispensing, cell sorting configuration, and additional elements for flow control and reliability are discussed in greater detail in the following sections.

8.1.1 Sample Focusing Element

It was demonstrated that a focusing junction with perpendicular sheath channels allows efficient cell dispensing for detection and sorting. Furthermore, increasing the width of the sheath channels decreased the required potentials to achieve sufficient focusing conditions, as discussed in Chapter 6. The focusing channel width ratio is $\eta = 3$ for the selected design, shown in Figure 8.2. The size of the sample channel is determined by the cell size; a width 5-10 times the cell diameter is favourable. The width of the sample channel is 30 μm for this device to sort cells ranging from 2-5 μm in length, such as yeast or bacteria.

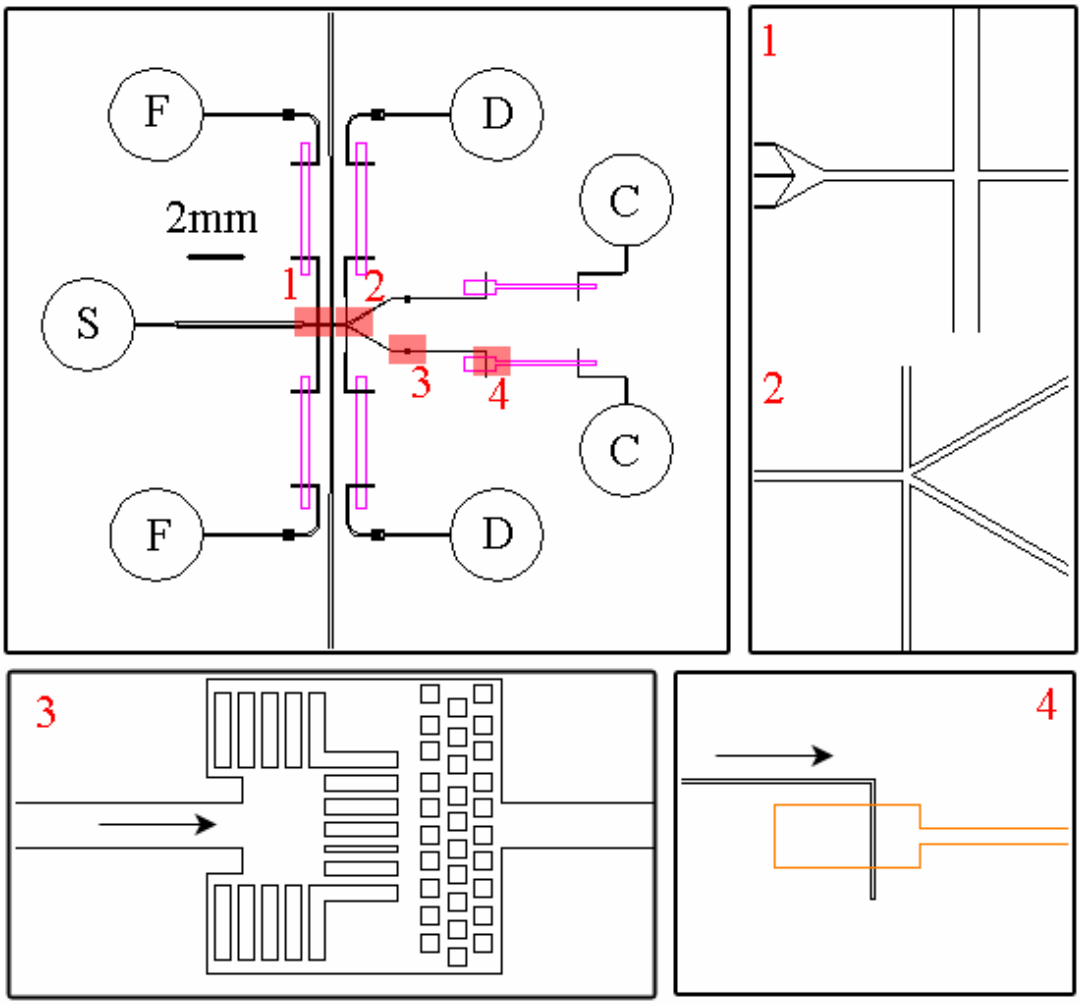

Figure 8.1 Final proposed design layout. S is the sample channel, F is a focusing fluid channel, D is a directing stream channel, and C is a collection channel.

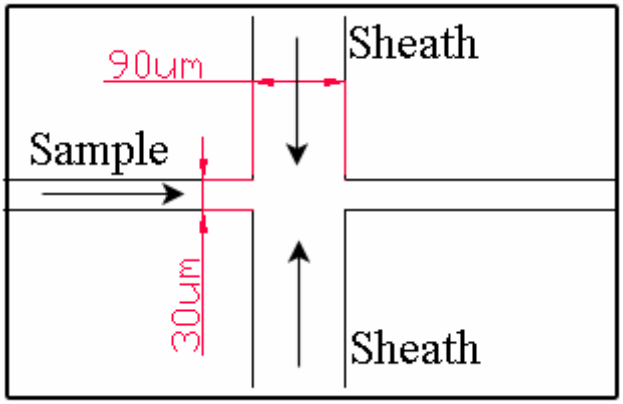

Figure 8.2 Focusing junction configuration and dimensions for the proposed final design.

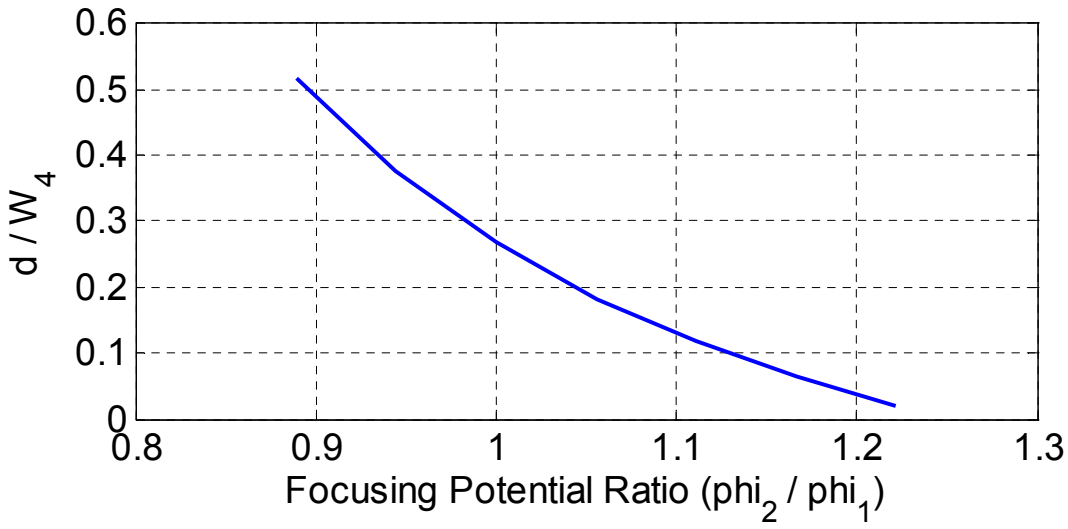

Figure 8.3 Predicted focused stream width versus the focusing potential ratio ϕ_{foc}.

The focused stream widths for a range of ϕ_{foc} values ($\phi_{foc} = \phi_{sheath} / \phi_{sample}$) are plotted in Figure 8.3. According to these predicted values, the potential ratio should be ϕ_{foc} = 1.07 to achieve adequate focusing of a 4 μm cell. A velocity streamline and concentration plot under these conditions is shown in Figure 8.4.

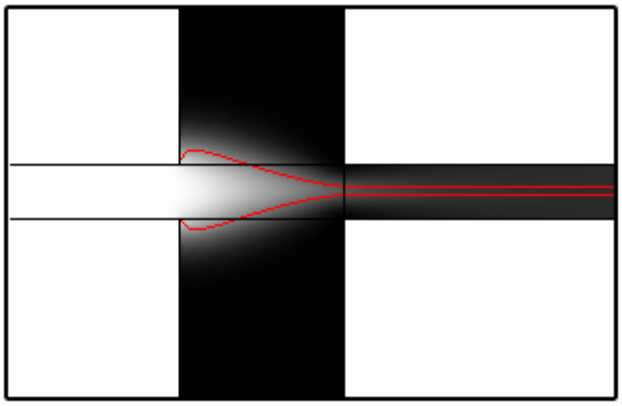

Figure 8.4 Numerical simulation velocity streamline and concentration plot for sample focusing. The focusing potential ratio ϕ_{foc} = 1.07 for this simulation. The diffusion is assumed D_i = 4.6 x 10^{-10} m^2/s, dye valence z = -2, and zeta potential ζ = -80 mV

8.1.2 Cell Sorting Element

Design F-1 exhibited the best sorting performance of the designs considered in this work. The key attributes of Design F-1 were included in the final design. A close up image of the sorting configuration is shown in Figure 8.5. There are two angled collection channels and two directing streams, which are perpendicular to the detection channel and are used to assist in deflecting the cell to the correct stream and to prevent path reversal. The widths of the channels have been reduced to 30 μm in order to match the sample channel and reduce the fluid volume of a sorting event. The directing stream channels have sections with larger widths to reduce the electrical resistance of the channel and the corresponding required applied potentials. The recommended operating voltages for this region are as follows: ϕ_{D1} = 340 V, ϕ_{D2} = 410 V, ϕ_{C1} = 0 V, and ϕ_{C2} = 250 V. A streamline plot for these conditions can be seen in Figure 8.6.

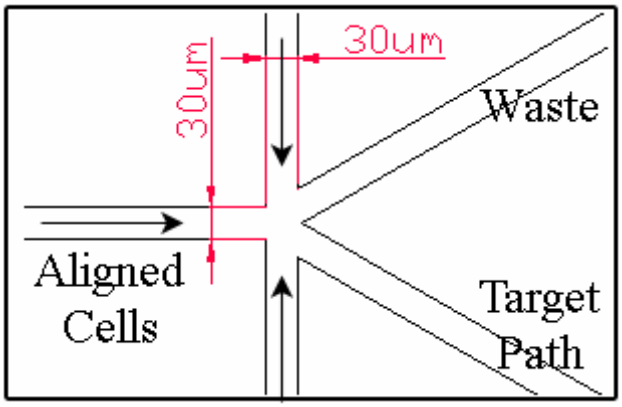

Figure 8.5 Sorting configuration and dimensions for the proposed final design.

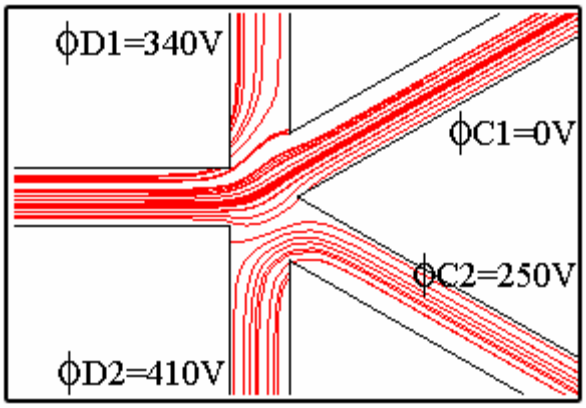

Figure 8.6 Streamline plot for the sorting region obtained by Multiphysics simulation. The applied potentials are ϕ = [340, 410, 0, 250] V for D_1, D_2, C_1, and C_2, respectively.

8.1.3 General Flow Elements

Design elements to improve the overall functionality and reliability of the cell sorter chip were investigated during this study. The primary issues encountered during testing were pressure differences causing unpredictable flow behaviour and flow blockages after long running times.

Hydrodynamic Resistances

Hydrodynamic resistance sections, created using two-layer fabrication, proved effective at reducing the level of pressure driven flow. The resistance channel is a shallow depth region connecting full-depth channels, shown in Figure 8.7. Slight modifications were made to the elements previously tested. The depth of the section was increased from 5 µm to 6 µm to help allow the 4 µm cells to pass through and prevent blockages. Also, the interface between the resistance channel and main channel in the collection channels is increased to reduce the flow effects of particles that do accumulate at this location. The channels have been lengthened from 2.25 mm to 3.5 mm and the widths were designed to maintain a similar cross-sectional area as the bridged channels. The widths are 150 µm and 350 µm for the 30 µm and 90 µm channels, respectively. These elements are located on all channels, except the sample channel.

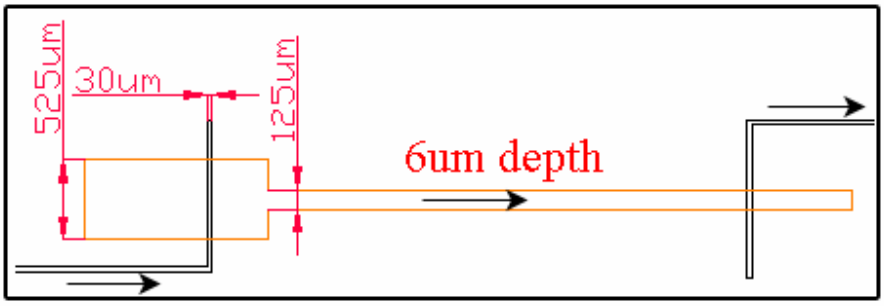

Figure 8.7 Hydrodynamic resistance element configuration and dimensions for the proposed final design.

For the sample channel, a unique element was designed. Shown in Figure 8.8, three parallel narrow channels fabricated at the same depth as the full design replace the straight length of the sample channel. The widths of these channels are 10 µm. The hydrodynamic resistance of this component is 4-fold that of a single 30 µm wide channel of the same length. This method will be less prone to blockages than a two-level resistance section and fewer cells will adhere to the channel compared to the long sample channel used in design Print F.

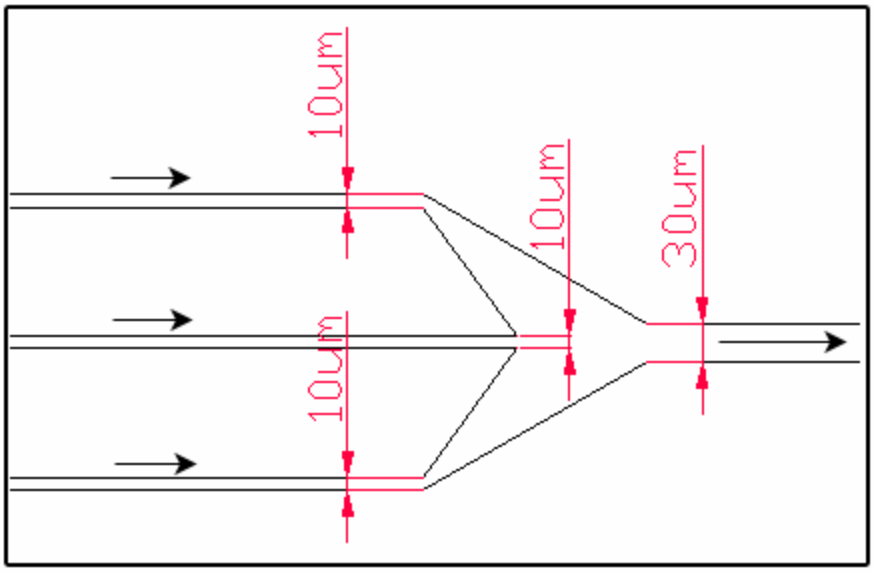

Figure 8.8 Hydrodynamic resistance element for sample channel of proposed final design.

Particle Filters

Increasing the depth of the hydrodynamic resistance channels will reduce the number of single cells that accumulate at the channel interface; however, some larger cell conglomerations and contamination particles would still be caught. Before the resistance channels, filter elements were implemented to stop the larger particles. Gaps in the filter are 6 μm, but will generally be slightly larger after fabrication. These should allow the desired cells to pass unobstructed. The filter is housed in a small chamber to provide enough surface area to not severely disrupt the flow conditions. Figure 8.9 shows the filter designs. The chambers are drastically smaller than those used in the Print F designs to lower the number of cells that seed to the chip in the low velocity regions. Larger chambers and filters were designed for the sheath fluid channels and the directing channels because particle seeding is not a concern in these streams. The dimensions of both filter sizes are shown in Figure 8.9. The filters were placed on all channels with the shallow constriction elements.

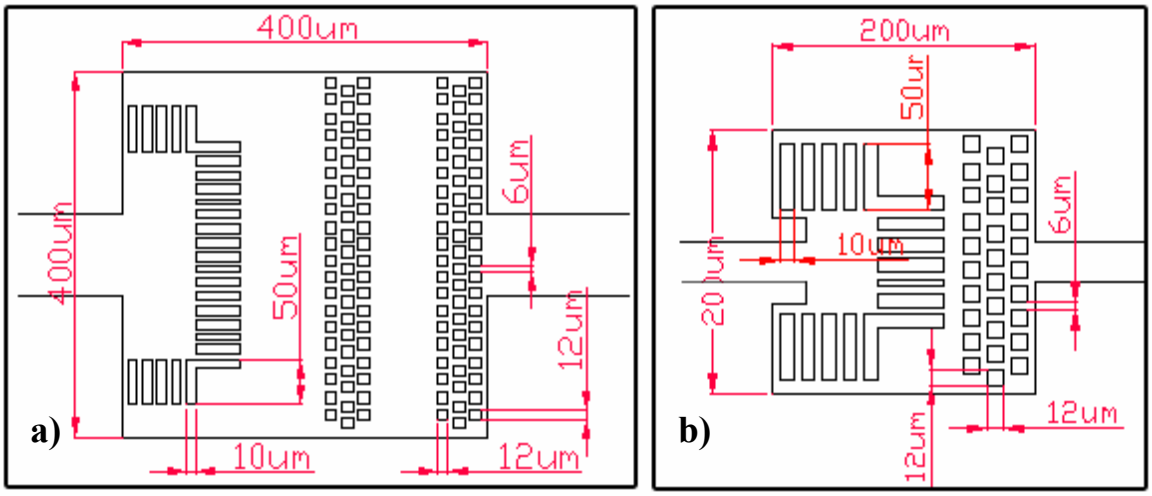

Figure 8.9 Particle filter components: a) large filter element and b) small filter element.

8.2 Overall Capability of Microfluidic Cell Sorter

The performance of the recommended cell sorter design is expected to be superior to the chips tested during this study. A summary of the estimated performance values is shown in Table 8.1. The chip has been designed for cells in the 2 μm to 5 μm range, primarily bacteria and yeast cells. The time required to capture a target cell depends on the velocity of the particle; the values range from 200 ms at lower velocities to 50 ms at high velocities. Sorting efficiency of Design F-1 was greater than 90% in manual pulse operation. This value can be improved by integration of the detection system and control algorithm for automated sorting. The predicted efficiency is 95% for this device. The purity can be determined from the cell arrival rate, target cell fraction, and sorting time duration. Values are listed for s = 0.01, cell rates r = 1 and 10 cells/s, and switching time T = 100 and 200 ms. Maximum cell arrival rates of 500 cells/s are possible for rare target cells (s = 0.01) with 200 ms switching times; however, the purity at this operating condition is too low to be practical. To achieve purity of 0.5 and 0.25 in the enriched sample, the maximum cell throughput is limited to 3.5 and 7 cells/s, respectively.

The inclusion of filter elements to prevent flow blockages should allow longer continuous run times. The previous designs with 5 μm deep hydrodynamic constrictions showed signs of flow disruption after approximately 1 hour of testing. The time limit for the new chip is difficult to predict without direct experimental results, but will be greater than 1 hour. The sample processing quantity under normal operating conditions, where the fluid velocity in the detection channel is 2 mm/s, is

approximately 15 nanolitres per minute. Operating at the maximum cell rate with 0.25 purity and 0.01 cell fraction, 25 000 and 50 000 total cells can be sorted in one hour for T = 200 ms and T = 100 ms, respectively. Additional measures taken to prevent particle seeding in the filter chambers and the sample channel should provide a higher recovery rate of the cells than previous designs.

Table 8.1 Sorting performance values predicted for the final cell sorter.

Sorting Time Duration, T	**200 ms** : 1000 μm/s > v_p > 500 μm/s **100 ms** : 2000 μm/s > v_p > 1000 μm/s **50 ms** : v_p > 2000 μm/s
Sorting Efficiency, E	**> 95 %**
Enriched Purity, $P\|_{s=0.01}$	**0.82** : r = 1 cell/s, T = 200 ms **0.14** : r = 10 cells/s, T = 200 ms **0.91** : r = 1 cell/s, T = 100 ms **0.37** : r = 10 cells/s, T = 100 ms
Maximum Target Cell Rate, $R_{\max}$	**5 cells/s** : T = 200 ms **10 cells/s** : T = 100 ms **20 cells/s** : T = 50 ms
Maximum Cell Arrival Rate, $r_{\max}\|_{T=200ms}$	**10 cells/s** : s = 0.5 **50 cells/s** : s = 0.1 **500 cells/s** : s = 0.01
Maximum Cell Arrival Rate, $r_{\max}\|_{P=0.5}$	**3.5 cells/s** : T = 200 ms, s = 0.01 **7 cells/s** : T = 100 ms, s = 0.01
Maximum Cell Arrival Rate, $r_{\max}\|_{P=0.25}$	**7 cells/s** : T = 200 ms, s = 0.01 **14 cells/s** : T = 100 ms, s = 0.01
Operating Time	**> 1 hr**
Processing Quantity, Q_{sample}	**15 nl/min** : v_f = 2 mm/s **0.9 μl/hr** : v_f = 2 mm/s
Total Sorted Cells	**25 000 cells/hr (250 target cells)** : T = 200 ms, P = 0.25, s = 0.01 **50 000 cells/hr (500 target cells)** : T = 100 ms, P = 0.25, s = 0.01
Recommended Size of Cells	**2-5 μm** : Dimensions of chip can be adapted for additional sizes

8.3 Errors and Limitations

The inherent limitations and errors of the system, which are discussed below, influenced the selection of the final design. Several factors affect the operation of the microfluidic chip and contribute to experimental error: instability of the applied potentials, unpredictable pressure differences, variations in electrode positioning and reservoir punching, channel characteristics of the fabricated chips, such as depth, width, and cross sectional profile, Joule heating, PDMS surface property changes, and the generation of pH gradients and solution changes due to evaporation and electrolysis.

It is difficult to characterize the influence of all the error sources associated with micro-scale flow without extensive direct experimentation. In this work a series of tests were conducted to determine the repeatability of fluorescent dye focusing at a single test point and to estimate the chip-to-chip uncertainty. Variations in the focused stream width were observed for the same chip over the course of ten repeated measurements. A few chips demonstrated a 30% decrease in focused stream width, while the average standard deviation of the stream width was 0.5 μm or 5% of the total stream width. The chip-to-chip variation was much greater. The deviation of the average stream widths was 2 μm or 20% with a maximum difference of nearly 50%. Pressure effects are believed to be the major contributor to this discrepancy for the cross-microchannels, which did not include hydrodynamic resistance elements. A more detailed analysis of the pressure influence was presented in Chapter 4.

Limitations of the system used in this work include the response of the high-voltage power sequencer. A time of 30-40 ms was required to reach the desired voltage during switching. This limits the overall speed of sorting as the cell throughput and cell velocity are increased. 50 ms is the recommended minimum sorting time based on this particular unit. The sizes of the cells are also constrained by the use of shallow hydrodynamic resistance sections. The proposed design is intended for particles 5 μm in diameter and smaller; larger particles will be trapped in the filter element or may accumulate at the constriction. Recovery of larger cells would require a flushing mechanism after sorting to gain access to the desired cells. Potential alternative solutions to the pressure influence can alleviate this problem.

Chapter 9

Conclusions and Recommendations

9.1 Contributions of this Thesis

The purpose of this work was to design an electrokinetically driven microfluidic chip for continuous dynamic sorting of fluorescent target cells from a non-homogeneous suspension. The miniaturization of fluorescence-activated cell sorting devices has gained momentum in recent years from research efforts looking to take advantage of the benefits accompanying microscale analysis systems. Microfluidic cell sorter designs proposed in literature have been demonstrated to collect desired cells; however, very little design evaluation has been reported. With the goal of developing an optimized design in terms of operating efficiencies and sorting capabilities, there remain opportunities for improvement of chip performance and optimization of the individual fluid components.

Several aspects of the design were investigated: the sample focusing element, the fluidic sorting configuration, and additional flow elements to improve chip functionality. A combination of experimental and numerical simulation results were used to evaluate various designs. A fluorescence microscopy experimental system was developed for monitoring and imaging fluorescent dye and microparticle samples (Chapter 3). Numerical studies were conducted with a commercial CFD package, COMSOL Multiphysics, and simplified models developed in this work (Chapter 4).

Sample focusing is necessary to control the dispensing of cells for detection and collection. The width of the focused stream is the critical parameter for reliable operation. The effect of the focuser shape was investigated using COMSOL Multiphysics simulations (Chapter 6). Differences between designs were found to be small; the perpendicular sheath channel design demonstrated slightly favourable focusing and was selected for the final design. Adjusting η, the ratio of sheath channel width to sample channel width, changed the required potentials for the desired level of focusing. This relationship was examined with a compact focusing model, adapted from a similar model reported in literature, and focusing experiments on cross-microchannels with $\eta = 1$, $\eta = 2$, and $\eta = 3$. Higher values of η provide greater savings in the applied potentials at the sheath fluid reservoirs. The value $\eta = 3$ was chosen as the optimal configuration. This feature is important for miniaturization and has

not been directly investigated or reported in literature. The appropriate size of the focuser was determined relative to the cell size and the operating conditions to achieve proper function were presented.

Experimental focusing data was analyzed using a Gaussian distribution model developed in this work to estimate the focused stream width by determining the location of the streamlines separating the sheath and sample fluids (Chapter 6). This technique is an improvement from the common full-width at half-maximum method because it is independent of the diffusion of the sample, mobility of the fluids (assuming uniformity throughout the chip), and charge of the sample. This is favourable considering the variety of samples which might be focused and the unavailability of their physical and chemical properties. The results using the FWHM technique are directly affected by these factors and do not predict the streamline location.

During the design iteration process, experiments revealed sources of irregular flow behaviour (Chapter 5). Pressure differences originating at the reservoirs were the primary influence, which made reliable operation difficult. The common and simple manipulations for reducing pressure effects were to keep the same fluid level in the reservoirs and to increase the hydrodynamic resistances by increasing the flow path. However, it is difficult to maintain the same liquid level in the reservoirs during operation and increasing the flow path requires higher applied voltages, which mitigates the advantages associated with microfluidic devices. In this thesis, hydrodynamic resistances were implemented to reduce the pressure effects. Of the resistance elements tested, two-layer shallow depth constrictions were found to be most effective. Accumulation of particles was observed for the reduced sections causing significant flow disruption during longer test runs. Filter elements to capture larger particles have been incorporated in the final design to prevent blockages (Chapter 8).

The configuration of the fluidic sorter varies widely in literature. Several designs were considered in this project (Chapter 5) and preliminary testing led to the selection of a handful of chip designs that were investigated more thoroughly (Chapter 7). Significant efforts were made to determine the effect of using a directing stream in cell sorting and to find the optimal location of the directing channels. Dynamic cell sorting was performed by real-time monitoring of a non-homogeneous suspension containing two types of fluorescent particles and manually activating the collection mechanism. This method simulates the operation of the device under automated conditions. Each design was evaluated using a number of quantities related to cell sorting: efficiency of capture, purity of the enriched sample, and cell throughput. Successful sorting was achieved for many of the designs; two in

particular, Designs F-1 and F-2, exhibited similar performance that exceeded that of the other designs. Additional experimental analyses and numerical simulation results indicated an advantage to using directing streams; hence, Design F-1 was selected for the final proposed design.

Based on the numerical and experimental investigations conducted, the selected chip components were incorporated into a final proposed chip design for dynamic sorting of fluorescently exhibiting bacteria or yeast cells ranging from 2-5 μm in diameter (Chapter 8). The predicted performance of the final design is presented using the performance of the tested designs as a reference with expected improvements.

9.2 Recommendations for Extensions of this Work

Implementing the proposed microfluidic cell sorter chip design into a lab-on-a-chip device requires further research and development. The major recommendations for continuation of this project are described here.

Experiments with Real Cells

The proposed design was not tested experimentally, which should be done to confirm the operating capabilities and to implement any changes, if necessary. Furthermore, fluorescent microspheres were used during experiments to represent cells. It is recommended to perform cell sorting with real fluorescently labeled or naturally fluorescent cells present in a non-homogeneous suspension. This will help determine if any modifications or surface treatments are required to effectively detect and sort real cells. For example, the use of a surface treatment may reduce the likelihood of cell adherence to the chip. Real cells can be used to estimate the recovery rate of the target cells by extracting and counting viable cells from the collection reservoir. Also, the effect of electric field on the cells can be investigated, which will determine the limits of operation.

Integration of Detection System

Automated cell sorting requires the integration of an illumination and fluorescence detection system. Fibre guide channels have been included in the proposed final design for embedding optical fibres, shown in Figure 9.1. The fibre on the illumination side is coupled to a laser light source and the detection fibre is coupled with a fluorescence filter and a light sensing element. Several parameters of the fibre-chip coupling need to be evaluated: the location of the fibre channels, the distance from the fibre end to the fluid channel, and whether the use of 2-D optics, such as lenses

incorporated into the chip design, will improve the detection capabilities. The signal sent to a data acquisition system from the sensing element must be analyzed and used to control the sorting mechanism. A LabVIEW program has been developed to perform peak detection and to control the HV power sequencer, but additions are required to estimate the cell velocity and to actively control the focusing parameters. The response time of the detection system will need to be characterized to optimize the sorting process.

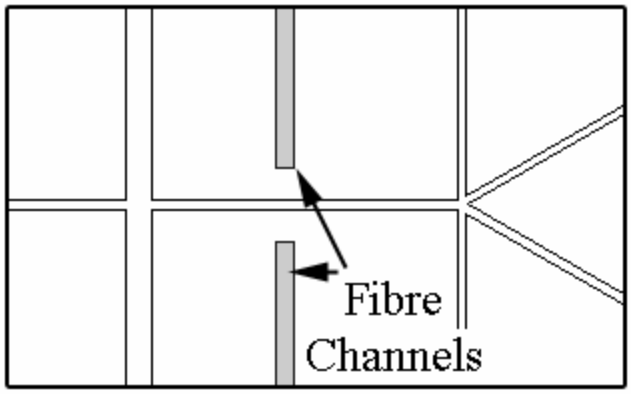

Figure 9.1 Embedded fibre channel incorporated in the proposed final design.

Improve Power Controller

Reducing the switching time *T* can improve the cell throughput and increase the overall processing capabilities. Methods to accomplish a quicker response should be investigated in conjunction with the miniaturization of the power supply. A battery operated power controller is preferable for handheld operation. The technology developed for portable capillary electrophoresis units can potentially be adapted for an electrokinetic cell sorter.

Further Miniaturization of Device

A portable platform comprised of the detection system, dynamic controller, and electrical supply is desired on which the disposable fluidic chip can be mounted. This requires miniaturization of many of the system components and integration of the various systems. To reduce the size of the optical system, the use of high power LEDs and μAPDs should be considered. The design of electrode and fluid interconnects that can be incorporated into the chip fabrication process or as external parts is required for this device. Also, the need for pre-processing elements, such as filtration or mixing, must be addressed for specific applications.

Pressure Control

The influence of pressure on the flow field was reduced in this work through hydrodynamic resistance elements. The shortfall of this method is the small dimensions that are required to attain adequate levels of resistance. Larger cells may cause flow blockages in chips with these constrictions; therefore, the application of this design is limited. The development of a more flexible method to control pressure uncertainties will allow a wider range of cells to be sorted. Ideally, the chip would simply scale to the size of the cell while maintaining similar performance capabilities.

References

Altendorf, E., Zebert, D., Holl, M., Yager, P. (1997) "Differential Blood Cell Counts Obtained Using a Microchannel Based Flow Cytometer." Transducers '97, 531-534.

Andersson, H., Van den Berg, A. (2003) "Microfluidic Devices for Cellomics: a Review." Sensors and Actuators B, 92, 315-325.

Armstrong, D.W., Girod, M., He, L., Rodriguez, M.A., Wei, W., Zheng, J., Yeung, E.S. (2002) "Mechanistic Aspects in the Generation of Apparent Ultrahigh Efficiencies for Colloidal (Microbial) Electrokinetic Separations." Analytical Chemistry, 74, 5523-5530.

Ashkin, A., Dziedzic, J.M., Yamane, T. (1987) "Optical Trapping and Manipulation of Single Cells using Infrared Laser Beams." Nature, 330, 769-771.

Bakker Schut, T.C., de Grooth, B.G., Greve, J. (1990) "A New Principle of Cell Sorting by Using Selective Electroporation in a Modified Flow Cytometer." Cytometry, 11, 659-666.

Beebe, D.J., Mensing, G.A., Walker, G.M. (2002) "Physics and Applications of Microfluidics in Biology." Annual Review of Biomedical Engineering, 4, 261-286.

Bello, M.S. (1996) "Electrolytic Modification of a Buffer during a Capillary Electrophoresis Run." Journal of Chromatography A, 744, 81-91.

Bhatt, K.H., Grego, S., Velev, O.D. (2005) "An AC Electrokinetic Technique for Collection and Concentration of Particles and Cells on Patterned Electrodes." Langmuir, 21, 6603-6612.

Bird, R.B., Stewart, W.E., Lightfoot, E.N. (1960) Transport Phenomena, John Wiley & Sons, New York, NY.

Camou, S., Fujita, H., Fujii, T. (2003) "PDMS 2D Optical Lens Integrated with Microfluidic Channels: Principle and Characterization." Lab on a Chip, 3, 40-45.

Chabinyc, M.L., Chiu, D.T., McDonald, J.C., Stroock, A.D., Christian, J.F., Karger, A.M., Whitesides, G.M. (2001) "An Integrated Fluorescence Detection System in Poly (dimethylsiloxane) for Microfluidic Applications." Analytical Chemistry, 73, 4491-4498.

Chang, D.C., Chassy, B.M., Saunders, J.A., Sowers, A.E. (1992) Guide to Electroporation and Electrofusion, Academic Press, New York, NY.

Chen, C.C, Wang, J.S., Solgaard, O. (2006) "Micromachined Bubble-Jet Cell Sorter with Multiple Operation Modes." Sensors and Actuators B, 117, 523-529.

Cho, B.S., Schuster, T.G., Zhu, X., Chang, D., Smith, G.D., Takayama, S. (2003) "Passively Driven Integrated Microfluidic System for Separation of Motile Sperm." Analytical Chemistry, 75, 1671-1675.

Choi, E.S., Yang, S.S. (2003) "Improvement of Electroosmotic Flow Characteristic in Poly (dimethylsiloxane) Channels via a Long Life Chemical Surface Modification." 7th International Conference on Miniaturized Chemical and Biochemical Analysis Systems, California, USA, October 5-9, 2003.

Chung, S., Park, S.J., Kim, J.K., Chung, C., Han, D.C., Chang, J.K. (2003) "Plastic Microchip Flow Cytometer Based on 2- and 3-Dimensional Hydrodynamic Flow Focusing." Microsystem Technologies, 9, 525-533.

Clayton, J. (2005) "Go with the Microflow." Nature Methods, 2 (8), 621-627.

Crabtree, H.J., Cheong, E.C.S., Tilroe, D.A., Backhouse, C.J. (2001) "Microchip Injection and Separation Anomalies due to Pressure Effects." Analytical Chemistry, 73, 4079-4086.

Davies, J.T., Rideal, E.K. (1963) Interfacial Phenomena, 2nd Edition, Academic Press, New York, NY.

Devasenathipathy, S., Santiago, J.G. (2002) "Particle Tracking Techniques for Electrokinetic Microchannel Flows." Analytical Chemistry, 74, 3704-3713.

Dittrich, P.S., Schwille, P. (2003) "An Integrated Microfluidic System for Reaction, High-Sensitivity Detection, and Sorting of Fluorescent Cells and Particles." Analytical Chemisty, 75, 5767-5774.

Dittrich, P.S., Manz, A. (2005) "Single-Molecule Fluorescence Detection in Microfluidic Channels – The Holy Grail in μTAS." Analytical and Bioanalytical Chemistry, 382, 1771-1782.

Dittrich, P.S., Manz, A. (2006) "Lab-on-a-Chip: Microfluidics in Drug Discovery." Nature, 5, 210-218.

Ducre, J., Zengerle, R. (2004) "FlowMap: Microfluidics Roadmap for the Life Sciences", http://www.microfluidics-roadmap.com/.

Eckenrode, H.M., Jen, S-H., Han, J., Yeh, A-G., Dai, H-L. (2005) "Adsorption of a Cationic Dye Molecule on Polystyrene Microspheres in Colloids: Effect of Surface Charge and Composition Probed by Second Harmonic Generation." Journal of Physical Chemistry B, 109, 4646-4653.

Elliot, D.J. (1986) Microlithography: Process Technology for IC Fabrication, McGraw-Hill, New York, NY.

Erickson, D., Li, D. (2004) "Integrated Microfluidic Devices." Analytica Chimica Acta, 507, 11-26.

Ermakov, S.V., Jacobson, S.C., Ramsey, J.M. (1998) "Computer Simulations of Electrokinetic Transport in Microfabricated Channel Structures." Analytical Chemistry, 70, 4494-4504.

Feng, Y., Zhou, Z., Ye, X., Xiong, J. (2003) "Passive Valves Based on Hydrophobic Microfluidics." Sensors and Actuators A, 108, 138-143.

Fitzgerald, D.A. (2002) "Riding the Microfluidic Wave." The Scientist, 16 (23), 40-45.

Fletcher, P.D.I., Haswell, S.J., Zhang, X. (2001) "Electrical Currents and Liquid Flow Rates in Micro-Reactors." Lab on a Chip, 1, 115-121.

Fu, A.Y., Spence, C., Scherer, A., Arnold, F.H., Quake, S.R. (1999) "A Microfabricated Fluorescence-Activated Cell Sorter." Nature Biotechnology, 17, 1109-1111.

Fu, A.Y., Chou, H-P., Spence, C., Arnold, F.H., Quake, S.R. (2002) "An Integrated Microfabricated Cell Sorter." Analytical Chemistry, 74, 2451-2457.

Fu, L-M., Yang, R-J., Lin, C-H., Pan, Y-J. Lee, G-B. (2004) "Electrokinetically Driven Micro Flow Cytometers with Integrated Fiber Optics for On-line Cell/Particle Detection." Analytica Chimica Acta, 507, 163-169.

Garcia, C.D., Liu., Y., Anderson, P., Henry, C.S. (2003) "Versatile 3-channel High-Voltage Power Supply for Microchip Capillary Electrophoresis." Lab on a Chip, 3, 324-328.

Ghosal, S. (2002) “Effect of Analyte Adsorption on the Electroosmotic Flow in Microfluidic Channels.” Analytical Chemistry, 74, 771-775.

Greenwald, E.K. (1991) Electrical Hazards and Accidents: Their Cause and Prevention, Van Nostrand Reinhold, New York, NY.

Han, K-H., Han, A., Frazier, A.B. (2006) “Microsystems for isolation and electrophysiological analysis of breast cancer cells from blood.” Biosensors and Bioelectronics, 21, 1907-1914.

Harrison, D.J., Manz, A., Fan, Z., Ludi, H., Widmer, H.M. (1992) “Capillary Electrophoresis and Sample Injection Systems Integrated on a Planar Glass Chip.” Analytical Chemistry, 64, 1926-1932.

Herzenberg, L.A., Parks, D., Sahaf, B., Perez, O., Roederer, M., Herzenberg, L.A. (2002) “The History and Future of the Fluorescence Activated Cell Sorter and Flow Cytometry: A View from Stanford.” Clinical Chemistry, 48, 1819-1827.

Ho, C-M., Tai, Y-C. (1998) “Micro-Electro-Mechanical-Systems (MEMS) and Fluid Flows.” Annual Review of Fluid Mechanics, 30, 579-612.

Hu, X., Bessette, P.H., Qian, J., Meinhart, C.D., Daugherty, P.S., Soh, H.T. (2005) “Marker-specific Sorting of Rare Cells using Dielectrophoresis.” Proceedings of the National Academy of Sciences of the United States of America, 102, 15757-15761.

Huang, Y., Joo, S., Duhon, M., Heller, M., Wallace, B., Xu, X. (2002) “Dielectrophoretic Cell Separation and Gene Expression Profiling on Microelectronic Chip Arrays.” Analytical Chemistry, 74, 3362-3371.

Huh, D., Tung, Y-C., Wei, H-H., Grotberg, J.B., Skerlos, S.J., Kurabayashi, K., Takayama, S. (2002) “Use of Air-liquid Two-Phase Flow in Hydrophobic Microfluidic Channels for Disposable Flow Cytometers.” Biomedical Microdevices, 4, 141-149.

Huh, D., Gu, W., Kamotani, Y., Grotberg, J.B., Takayama S. (2005) “Microfluidics for Flow Cytometric Analysis of Cells and Particles.” Physiological Measurement, 26, R73-R98.

Hunter, R.J. (1981) Zeta Potential in Colloid Science: Principles and Applications, Academic Press, New York, NY.

Jackson, D.J., Naber, J.F., Roussel Jr., T.J., Crain, M.M., Walsh, K.M., Keynton, R.S., Baldwin, R.P. (2003) “Portable High-Voltage Power Supply and Electrochemical Detection Circuits for Microchip Capillary Electrophoresis.” Analytical Chemistry, 75, 3643-3649.

Jacobson, S.C., Ramsey, J.M. (1997) “Electrokinetic Focusing in Microfabricated Channel Structures.” Analytical Chemistry, 69, 3212-3217.

Johann, R., Renaud, P. (2004) “A Simple Mechanism for Reliable Particle Sorting in a Microdevice with Combined Electroosmotic and Pressure-Driven Flow.” Electrophoresis, 25, 3720-3729.

Jorgensen, A.M., Mogensen, K.B., Kutter, J.P., Geschke, O. (2003) “A Biochemical Microdevice with an Integrated Chemiluminescence Detector.” Sensors and Actuators B, 90, 15-21.

Kamei, T., Paegel, B.M., Scherer, J.R., Skelley, A.M., Street, R.A., Mathies, R.A. (2003) "Integrated Hydrogenated Amorphous Si Photodiode Detector for Microfluidic Bioanalytical Devices." Analytical Chemistry, 75, 5300-5305.

Kanagasabapathi, T.T., Dalton, C., Kaler K.V.I.S. (2005) "An Integrated PDMS Microfluidic Device for Dielectrophoretic Separation of Malignant Cells." 3rd International Conference on Microchannels and Minichannels, Toronto, Canada, June 13-15, 2005.

Kruger, J., Singh, K., O'Neill, A., Jackson, C., Morrison, A., O'Brien, P. (2002) "Development of a Microfluidic Device for Fluorescence Activated Cell Sorting." Journal of Micromechanics and Microengineering, 12, 486-494.

Kuo, J.S., Kuyper, C.L., Allen, P.B., Fiorini, G.S., Chiu, D.T. (2004) "High-Power Blue/UV Light-Emitting Diodes as Excitation Sources for Sensitive Detection." Electrophoresis, 25, 3796-3804.

Lee, G-B., Hung, C-I., Ke, B-J., Huang, G-R., Hwei, B-H., Lai, H-F. (2001) "Hydrodynamic Focusing for a Micromachined Flow Cytometer." Journal of Fluids Engineering, 123, 672-679.

Lee, G-B., Lin, C-H., Chang, G-L. (2003) "Micro Flow Cytometers with Buried SU-8/SOG Optical Waveguides." Sensors and Actuators A, 103, 165-170.

Lee, G-B., Chang, C-C., Huang, S-B., Yang, R-J. (2006) "The Hydrodynamic Focusing Effect Inside Rectangular Microchannels." Journal of Micromechanics and Microengineering, 16, 1024-1032.

Li, D. (2004) Electrokinetics in Microfluidics, Elsevier Academic, San Diego, CA.

Li, P.C.H., Harrison, D.J. (1997) "Transport, Manipulation, and Reaction of Biological Cells On-chip Using Electrokinetic Effects." Analytical Chemistry, 69, 1564-1568.

Li, P.C.H. (2006) Microfluidic Lab-on-a-Chip for Chemical and Biological Analysis and Discovery, Taylor & Francis Group, Boca Raton, FL.

Lin, C-H., Lee, G-B. (2003) "Micromachined Flow Cytometers with Embedded Etched Optic Fibers for Optical Detection." Journal of Micromechanics and Microengineering, 13, 447-453.

Lin, J-Y., Fu, L-M., Yang, R-J. (2002) "Numerical Simulation of Electrokinetic Focusing in Microfluidic Chips." Journal of Micromechanics and Microengineering, 12, 955-961.

Masliyah, J.H. (1994) Electrokinetic Transport Phenomena, AOSTRA, Edmonton, AB.

McClain, M.A., Culbertson, C.T., Jacobson, S.C., Ramsey, J.M. (2001) "Flow Cytometry of *Escherichia coli* on Microfluidic Devices." Analytical Chemistry, 73, 5334-5338.

McDonald, J.C., Duffy, D.C., Anderson, J.R., Chiu, D.T., Wu, H., Schueller, O.J.A., Whitesides, G.M. (2000) "Fabrication of Microfluidic Systems in Poly (dimethylsiloxane)." Electrophoresis, 21, 27-40.

Melamed, M.R., Lindmo, T., Mendelsohn, M.L. (1990) Flow Cytometry and Sorting, 2nd Edition, John Wiley & Sons, New York, NY.

Miyake, R., Ohki, H., Yamazaki, I., Takagi, T. (1997) “Investigation of Sheath Flow Chambers for Flow Cytometers (Micro Machined Flow Chamber with Low Pressure Loss).” JSME International Journal Series B, 40, 106-113.

Miyaki, K., Guo, Y., Shimosaka, T., Nakagama, T., Nakajima, H., Uchiyama, K. (2005) “Fabrication of an Integrated PDMS Microchip Incorporating an LED-Induced Fluorescence Device.” Analytical and Bioanalytical Chemistry, 382, 810-816.

Mogensen, K.B., El-Ali, J., Wolff, A., Kutter, J.P. (2003) “Integration of Polymer Waveguides for Optical Detection in Microfabricated Chemical Analysis Systems.” Applied Optics, 42:19, 4072-4079.

Mogensen, K.B., Klank, H., Kutter, J.P. (2004a) “Recent Developments in Detection from Microfluidic Systems.” Electrophoresis, 25, 3498-3512.

Mogensen, K.B., Eriksson, F., Gustafsson, O., Nikolajsen, R.P.H., Kutter, J.P. (2004b) “Pure-Silica Optical Waveguides, Fiber Couplers, and High-Aspect Ratio Submicrometer Channels for Electrokinetic Separation Devices.” Electrophoresis, 25, 3788-3795.

Paul, P.H., Garguilo, M.G., Rakestraw, D.J. (1998) “Imaging of Pressure- and Electrokinetically Driven Flows through Open Capillaries.” Analytical Chemistry, 70, 2459-2467.

Pekas, N., Granger, M., Tondra, M., Popple, A., Porter, M.D. (2005) “Magnetic Particle Diverter in an Integrated Microfluidic Format.” Journal of Magnetism and Magnetic Materials, 293, 584-588.

Qiao, R., Aluru, N.R. (2002) “A Compact Model for Electroosmotic Flows in Microfluidic Devices.” Journal of Micromechanics and Microengineering, 12, 625-635.

Quake, S.R., Scherer, A. (2000) “From Micro- to Nanofabrication with Soft Materials.” Science, 290, 1536-1540.

Recktenwald, D., Radbruch, A. (1998) Cell Separation Methods and Applications, Marcel Dekker Inc., New York, NY.

Ren, L., Escobedo-Canseco, C., Li. D. (2002) “A New Method of Evaluating the Average Electro-osmotic Velocity in Microchannels.” Journal of Colloid and Interface Science, 250, 238-242.

Ren, L., Sinton, D., Li, D. (2003) “Numerical Simulation of Microfluidic Injection Processes in Crossing Microchannels.” Journal of Micromechanics and Microengineering, 13, 739-747.

Ren, X., Bachman, M., Sims, C., Li, G.P., Allbritton, N. (2001) “Electroosmotic Properties of Microfluidic Channels Composed of Poly (dimethylsiloxane).” Journal of Chromatography B, 762, 117-125.

Reyes, D.R., Iossifidis, D., Auroux, P-A., Manz, A. (2002) “Micro Total Analysis Systems. 1. Introduction, Theory, and Technology.” Analytical Chemistry, 74, 2623-2636.

Rieseberg, M., Kasper, C., Reardon, K.F., Scheper, T. (2001) “Flow Cytometry in Biotechnology.” Applied Microbiology and Biotechnology, 56, 350-360.

Rolland, J.P., Hagberg, E.C., Denison, G.M., Carter, K.R., De Simone, J.M. (2004) "High-Resolution Soft Lithography: Enabling Materials for Nanotechnologies." Angewandte Chemie International Edition, 43, 5796-5799.

Schrum, D.P., Culbertson, C.T., Jacobson, S.C., Ramsey, J.M. (1999) "Microchip Flow Cytometry Using Electrokinetic Focusing." Analytical Chemistry, 71, 4173-4177.

Shapiro, H.M. (2003) Practical Flow Cytometry, 4th Edition, John Wiley & Sons, Hoboken, NJ.

Sinton, D. (2003) "Flow Visualization in Microchannels." PhD Thesis, University of Toronto.

Spehar, A-M., Koster, S., Linder, V., Kulmala, S., de Rooij, N.F., Verpoorte, E., Sigrist, H., Thormann, W. (2003) "Electrokinetic Characterization of Poly (dimethylsiloxane) Microchannels." Electrophoresis, 24, 3674-3678.

Stone, H.A., Stroock, A.D., Ajdari, A. (2004) "Engineering Flows in Small Devices: Microfluidics Toward a Lab-on-a-Chip." Annual Review of Fluid Mechanics, 36, 381-411.

Struder, V., Jameson, R., Pellereau, E., Pepin, A., Chen, Y. (2004) "A Microfluidic Mammalian Cell Sorter Based on Fluorescence Detection." Microelectronic Engineering, 73-74, 852-857.

Tabeling, P. (2005) Introduction to Microfluidics, Oxford University Press, New York, NY.

Takahashi, K., Hattori, A., Suzuki, I., Ichiki, T., Yasuda, K. (2004) "Non-Destructive On-Chip Cell Sorting System with Real-Time Microscopic Image Processing." Journal of Nanobiotechnology, 2:5.

Tung, Y-C., Zhang, M., Lin, C-T., Kurabayashi, K., Skerlos, S.J. (2004) "PDMS-Based Opto-Fluidic Micro Flow Cytometer with Two-Color, Multi-Angle Fluorescence Detection Capability Using PIN Photodiodes." Sensors and Actuators B, 98, 356-367.

Veal, D.A., Deere, D., Ferrari, B., Piper, J., Attfield, P.V. (2000) "Fluorescence Staining and Flow Cytometry for Monitoring Microbial Cells." Journal of Immunological Methods, 243, 191-210.

Verpoorte, E. (2003) "Chip Vision – Optics for Microchips." Lab on a Chip, 3, 42N-52N.

Vilkner, T., Janasek, D., Manz, A. (2004) "Micro Total Analysis Systems. Recent Developments." Analytical Chemistry, 76, 3373-3386.

Walker, G.M., Beebe, D.J. (2002) "A Passive Pumping Method for Microfluidic Devices." Lab on a Chip, 2, 131-134.

Wang, H-Y., Lu, C. (2006) "Electroporation of Mammalian Cells in a Microfluidic Channel with Geometric Variation." Analytical Chemistry, 78, 5158-5164.

Wang, M.W., Tu, E., Raymond, D.E., Yang, J.M., Zhang, H., Hagen, N., Dees, B., Mercer, E.M., Forster, A.H., Kariv, I., Marchand, P.J., Butler, W.F. (2005) "Microfluidic Sorting of Mammalian Cells by Optical Force Switching." Nature Biotechnology, 23, 83-87.

Wang, Z., El-Ali, J., Engelund, M., Gotsaed, T., Perch-Nielsen, I.R., Mogensen, K.B., Snakenborg, D., Kutter, J.P., Wolff, A. (2004) "Measurements of Scattered Light on a Microchip Flow Cytometer with Integrated Polymer Based Optical Elements." Lab on a Chip, 4, 372-377.

White, F.M. (1999) Fluid Mechanics, 4th Edition, McGraw-Hill, New York, NY.

Wu, H., Wheeler, A., Zare, R.N. (2004) "Chemical Cytometry on a Picoliter-Scale Integrated Microfluidic Chip." Proceedings of the National Academy of Sciences of the United States of America, 101:35, 12809-12813.

Xia, Y., Whitesides, G.M. (1998) "Soft Lithography." Angewandte Chemie International Edition, 37, 550-575.

Xuan, X., Xu, B., Sinton, D., Li, D. (2004) "Electroosmotic Flow with Joule Heating Effects." Lab on a Chip, 4, 230-236.

Xuan, X., Li, D. (2005) "Focused Electrophoretic Motion and Selected Electrokinetic Dispensing of Particles and Cells in Cross-Microchannels." Electrophoresis, 26, 3552-3560.

Yamaguchi, N., Sasada, M., Yamanaka, M., Nasu, M. (2003) "Rapid Detection of Respiring *Escherichia coli* O157:H7 in Apple Juice, Milk, and Ground Beef by Flow Cytometry." Cytometry Part A, 54A, 27-35.

Yang, R-J., Chang, C-C., Huang, S-B., Lee, G-B. (2005) "A New Focusing Model and Switching Approach for Electrokinetic Flow Inside Microchannels." Journal of Micromechanics and Microengineering, 15, 2141-2148.

Yang, S-Y., Hsuing, S-K., Hung, Y-C., Chang, C-M., Liao, T-L., Lee, G-B. (2006) "A Cell Counting/Sorting System Incorporated with a Microfabricated Flow Cytometer Chip." Measurement Science and Technology, 17, 2001-2009.

Yao, B, Luo, G-A., Feng, X., Wang, W., Chen, L-X., Wang, Y-M. (2004) "A Microfluidic Device Based on Gravity and Electric Force Driving for Flow Cytometry and Fluorescence Activated Cell Sorting." Lab on a Chip, 4, 603-607.

Yi, C., Li, C-W., Ji, S., Yang, M. (2006) "Microfluidics Technology for Manipulation and Analysis of Biological Cells." Analytica Chimica Acta, 560, 1-23.

Appendix A

Chip Fabrication Procedure

The PDMS microfluidic chips were fabricated using the soft-lithography technique developed by Xia and Whitesides (1998). Chip fabrication was conducted in the Microfluidics and Biochips Laboratory. Two primary procedures were used to create planar, single-layer chips and multiple-layer chips. The steps associated with these processes are as follows:

Single Layer

1. **Substrate Cleaning**
   One of two following cleaning procedures was performed:
   i. Microscope glass slides pre-cleaned with Piranha solution
      - Rinse with DI water
      - Blown dry with nitrogen gas.
   ii. Uncleaned microscope glass slides
      - 5 minutes 1 M H_2SO_4 bath with agitation.
      - 5 minutes 1 M NaOH bath with agitation.
      - Rinse with DI water.
      - Blown dry with nitrogen gas.
2. **Dehydration Bake**
   To remove H_2O molecules from substrate surface:
   - 10 minutes on 200 °C hotplate.
3. **SU-8 Dispensing onto Substrate**
   - SU-8 de-gassed in sealed 30ml scintillation bottles by heating for ~30 minutes on 65 °C hotplate.
   - SU-8 is poured directly from scintillation bottle onto glass slide. 3-5 ml is dispensed per slide.
4. **Spin Coating**
   25 μm depth – SU-8 25:
      - 0-500 rpm @ 100 rpm/s ramping speed – hold for 20 s.
      - 500-1000 rpm @ 100 rpm/s ramping speed – hold for 10 s.
      - 1000-2000 rpm @ 100 rpm/s ramping speed – hold for 30 s.
5. **Soft Bake**
   25 μm depth – SU-8 25:
      - 3 minutes on 65 °C hotplate.
      - 7 minutes on 95 °C hotplate.
6. **UV Exposure**
   25 μm depth – SU-8 25:
      - Mask and substrate are placed in vacuum contact (~ 15 inHg).
      - 850 mJ/cm^2 exposure dose setting (actual measured dose ~ 530 mJ/cm^2).

7. **Post Exposure Bake**
   25 μm depth – SU-8 25:
   - 1 minute on 65 °C hotplate.
   - 3 minutes on 95 °C hotplate.
   - 1 minute on 65 °C hotplate.
   - 1 minute on 50 °C hotplate.
   - Air-cooled > 10 minutes to reduce cracks resulting from thermal contraction.

8. **SU-8 Developing**
   - 2.5 minute bath in PGMEA developer with light agitation.
   - Remove from developer and rinse with isopropanol. If present, undeveloped, uncross-linked photoresist appears white at this stage and additional developing is required.
   - Rinse with DI water.
   - Blown dry with nitrogen gas.

9. **PDMS Replication**
   - The liquid PDMS base and curing agents are mixed in a 10:1 ratio (w/w) for approximately 17 g per petri dish containing the slide master.
   - The elastomer is poured on the master and de-gassed in the vacuum oven at 27 inHg vacuum pressure for 1 hour with no heat.
   - PDMS is cured at 80 °C for 1 hour.
   - Cured PDMS is lifted from the master and cut to shape. Reservoirs are also punched in the appropriate locations with a leather punch tool.

10. **O_2 Plasma Treating & Bonding**
    - The PDMS replica and a cleaned glass slide are plasma treated for 35 s at high setting.
    - The two layers are placed in contact immediately after plasma treating to bond the materials and form enclosed channels.
    - The channels are filled with filtered DI water to prevent the surface properties from reverting back to their natural, unfavourable state. The chip is sealed to prevent evaporation of the water.

Multi-Layer

Steps 1-3: Remain the same as single layer fabrication.

4. **Spin Coating – 1st Layer**
   5 μm depth – SU-8 5:
   - 0-500 rpm @ 100 rpm/s ramping speed – hold for 20 s.
   - 500-2000 rpm @ 100 rpm/s ramping speed – hold for 10 s.
   - 2000-3000 rpm @ 100 rpm/s ramping speed – hold for 30 s.

5. **Soft Bake – 1st Layer**
   5 μm depth – SU-8 5:
   - 2 minutes on 65 °C hotplate.
   - 4 minutes on 95 °C hotplate.

6. **UV Exposure – 1st Layer**
   5 μm depth – SU-8 5:
   - Mask and substrate are placed in vacuum contact (~ 15 inHg).
   - 350 mJ/cm^2 exposure dose setting (actual measured dose ~ 220 mJ/cm^2).

7. **Post Exposure Bake – 1st Layer**
   5 μm depth – SU-8 5:
   - 1 minute on 65 °C hotplate.
   - 1 minute on 95 °C hotplate.
   - 30 seconds on 200 °C hotplate.
   - 30 seconds on 95 °C hotplate.
   - 30 seconds on 65 °C hotplate.

8. **SU-8 Dispensing – 2nd Layer**
   Repeat Step 3 with SU-8 25.

9. **Spin Coating – 2nd Layer**
   Same as Step 4 of single layer fabrication.

10. **Soft Bake – 2nd Layer**
    Same as Step 5 of single layer fabrication.

11. **UV Exposure – 2nd Layer**
    30 μm total depth – SU-8 5 + SU-8 25:
    - Mask and substrate are placed in vacuum contact (~ 15 inHg).
    - 900 mJ/cm^2 exposure dose setting (actual measured dose ~ 560 mJ/cm^2).

12. **Post Exposure Bake – 2nd Layer**
    30 μm total depth – SU-8 5 + SU-8 25:
    - 1 minute on 65 °C hotplate.
    - 5 minutes on 95 °C hotplate.
    - 1 minute on 65 °C hotplate.
    - 1 minute on 50 °C hotplate.
    - Air-cooled > 10 minutes to reduce cracks resulting from thermal contraction.

Steps 13-15: Same as Steps 8-10 of single layer fabrication.

Appendix B

Transient Model for Reservoir Levels

A compact transient model to determine the pressure driven flow contributions in a microchannel was developed. The model calculates the hydrostatic and Laplace pressure forces acting on the channel fluid and predicts the time dependent volumetric flow in a domain that includes two reservoirs connected by a single microchannel (Figure B.1).

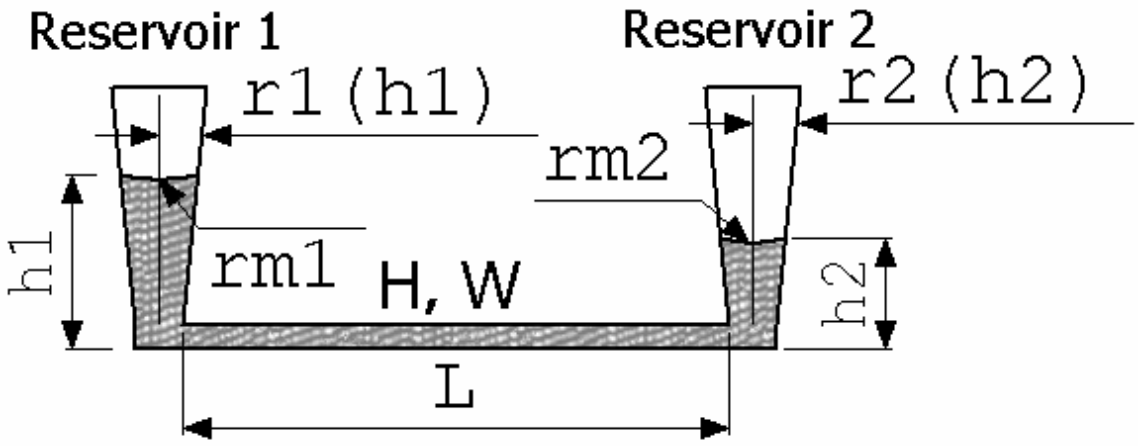

Figure B.1 Schematic of transient model domain and critical dimensions.

The reservoir can be cylindrical or conical, where the radius varies with height. The geometry of reservoir 1 is illustrated in Figure B.2. The radius $r(h)$ of the reservoir at the fluid height is

$$r(h) = h \cdot \tan\theta + R_B \qquad \textbf{(B.1)}$$

where h is the height of the fluid in the reservoir, θ is the angle of slope of the reservoir wall, and R_B is the radius at the bottom of the reservoir. The volume corresponding to the fluid level is

$$V(h) = \frac{\pi}{3}\left[\frac{r(h)^3}{\tan\theta} - R_B{}^2\left(\frac{r(h)}{\tan\theta} - h\right)\right] \quad ; \quad \theta \neq 0 \qquad \textbf{(B.2)}$$

$$V(h) = \pi \cdot r(h)^2 h \quad ; \quad \theta = 0 \qquad \textbf{(B.3)}$$

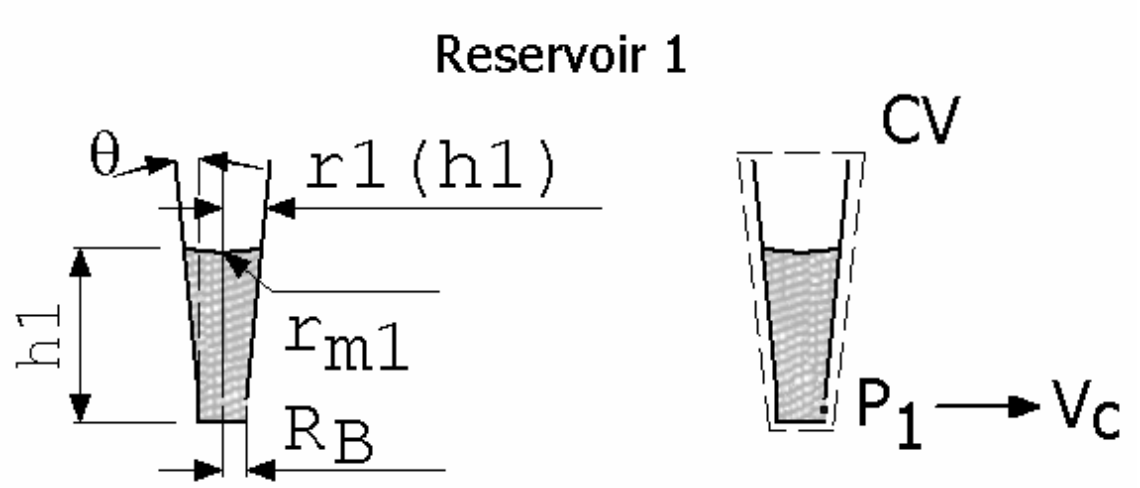

Figure B.2 Schematic of reservoir 1 and the reservoir control volume.

The radius r_m of the meniscus occurring in the reservoir is estimated by the contact angle θ_{ca}:

$$r_m = \frac{r(h)}{\cos(\theta_{ca})} \tag{B.4}$$

The resulting Laplace pressure contribution P_L is

$$P_L = \frac{2\gamma}{r_m} \tag{B.5}$$

where γ is the surface tension. The hydrostatic pressure P_{hyd} at the mid-height location of the microchannel is

$$P_{hyd} = \rho g\left(h - \frac{H}{2}\right) \tag{B.6}$$

where ρ is the fluid density, g is the gravitational field strength, and H is the height of the channel. The overall pressure P is the sum of the hydrostatic and Laplace pressures:

$$P = P_L + P_{hyd} \tag{B.7}$$

The mass balance for the control volume in the reservoir gives,

$$\frac{d}{dt}\left(\int_{CV} \rho dV\right) = -\rho A_c V_c \tag{B.8}$$

where A_c is the cross-sectional area of the channel and V_c is the average velocity of the fluid leaving the reservoir. Assuming the cross-sectional area of the reservoir does not change significantly with time ($r(h) \approx r_{ave}$), Equation B.8 can be approximated as

$$\frac{dh}{dt} \approx -\frac{A_c V_c}{\pi \cdot r_{ave}^{\,2}} \tag{B.9}$$

For a discrete time period Δt, we get,

$$\frac{h_{new} - h_{old}}{\Delta t} \approx -\frac{A_c V_c}{\pi \cdot \left(\frac{r_{new} - r_{old}}{2}\right)^2} \tag{B.10}$$

where h_{new} and h_{old} are the fluid levels at the start and end of the time Δt and r_{new} and r_{old} are the reservoir radii corresponding to these levels.

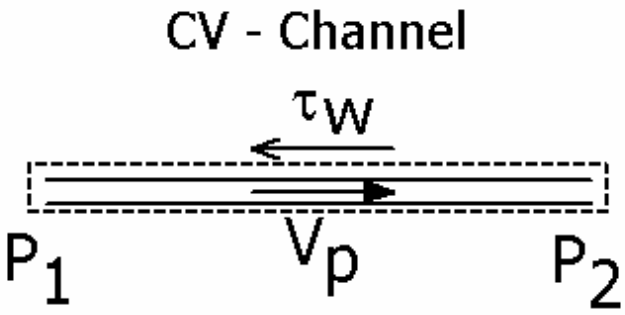

Figure B.3 Schematic of the microchannel control volume.

Performing a force balance on the channel, for which the control volume is shown in Figure B.3, we get,

$$(P_1 - P_2)A_c = -\tau_w (2H + 2W)L \tag{B.11}$$

where P_1 is the pressure in the channel at reservoir 1, P_2 is the pressure in the channel at reservoir 2, L is the length of the channel, and τ_w is

$$\tau_w = \left(\frac{64}{\mathrm{Re}_d}\right)\rho\frac{V_p^2}{8} \tag{B.12}$$

where V_p is the pressure velocity component and Re_d is the Reynolds number for flow in a duct. Substituting Equation B.12 for a non-circular duct into Equation B.11 provides the following expression for V_p:

$$V_p = \frac{A_c\left(P_1 - P_2\right)}{2\mu\left(2H + 2W\right)^2 L} \quad \textbf{(B.13)}$$

where μ is the fluid viscosity and W is the width of the channel. A slip velocity V_{eof} is assumed for the electroosmotic flow; therefore the overall fluid velocity is

$$V_c = V_p + V_{eof} \quad \textbf{(B.14)}$$

The pressures at the ends of the channel are calculated and used to determine the velocity of the fluid and the resulting change in volume in each reservoir. The new fluid levels and the radius of the reservoir at this height are found by iteration. The pressure at the next time interval is then calculated and the process repeats for the duration of the transient solution.

Appendix C

Circuit Equivalency Model Solution

The circuit equivalency model was applied to various chip configurations to solve the potential field and flow field. The procedure for different chips is essentially identical; however, the number of junctions and channels at each node vary. A 5-reservoir chip is used to illustrate the solution of this compact model. The equivalent circuit is shown in Figure C.1.

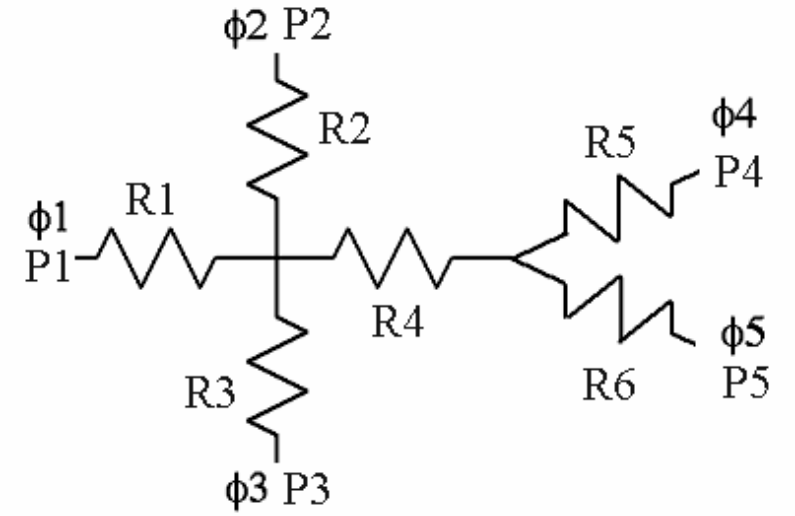

Figure C.1 Equivalent circuit schematic for the 5-reservoir chip design containing 1 sample channel, 2 focusing channels, and 2 collection channels. Electrical potentials and pressures are applied at the reservoirs.

The potential field is solved by applying Kirchoff's law at the junctions for the current I determined by,

$$I = \frac{\Delta\phi}{R_V} \qquad \textbf{(C.1)}$$

where $\Delta\phi$ is the potential drop along the channel and R_V is the electrical resistance of the channel. At Junction 1 Kirchoff's law gives,

$$I_1 + I_2 + I_3 = I_4 \qquad \textbf{(C.2)}$$

where I_1 , I_2 , I_3 , and I_4 are the currents in channels 1, 2, 3, and 4, respectively. Substituting Equation C.1 into Equation C.2 gives,

$$A_1\frac{(\phi_1-\phi_{J1})}{L_1}+A_2\frac{(\phi_2-\phi_{J1})}{L_2}+A_3\frac{(\phi_3-\phi_{J1})}{L_3}=A_4\frac{(\phi_{J1}-\phi_{J2})}{L_4} \qquad \textbf{(C.3)}$$

where A_1, A_2, A_3, and A_4 are the cross-sectional areas of channels 1, 2, 3, and 4, respectively, ϕ_1, ϕ_2, ϕ_3, ϕ_{J1}, and ϕ_{J2} are the potentials at reservoir 1, reservoir 2, reservoir3, junction 1, and junction 2, respectively, and L_1, L_2, L_3, and L_4 are the lengths of channels 1, 2, 3, and 4, respectively. Kirchoff's law applied at junction 2 provides the following equation:

$$A_4\frac{(\phi_{J1}-\phi_{J2})}{L_4}=A_5\frac{(\phi_{J2}-\phi_4)}{L_5}+A_6\frac{(\phi_{J1}-\phi_5)}{L_6} \qquad \textbf{(C.4)}$$

where A_4, A_5, and A_6 are the cross-sectional areas of channels 4, 5, and 6, respectively, ϕ_4 and ϕ_5 are the potentials at reservoirs 4 and 5, respectively, and L_4, L_5, and L_6 are the lengths of channels 4, 5, and 6, respectively. The system of equations formed by Equations C.3 and C.4 is converted to matrix form and solved for the potentials at the junctions:

$$\begin{bmatrix} -\frac{A_1}{L_1}-\frac{A_2}{L_2}-\frac{A_3}{L_3}-\frac{A_4}{L_4} & \frac{A_4}{L_4} \\ \frac{A_4}{L_4} & -\frac{A_4}{L_4}-\frac{A_5}{L_5}-\frac{A_6}{L_6} \end{bmatrix}\begin{bmatrix}\phi_{J1}\\ \phi_{J2}\end{bmatrix}=\begin{bmatrix} -\frac{A_1\phi_1}{L_1}-\frac{A_2\phi_2}{L_2}-\frac{A_3\phi_3}{L_3} \\ -\frac{A_5\phi_5}{L_5}-\frac{A_6\phi_6}{L_6}\end{bmatrix} \qquad \textbf{(C.5)}$$

The electric field strength can be subsequently calculated for each channel.

Mass continuity is applied at the junctions to solve the flow field. The volumetric flow rate Q is estimated by,

$$Q=u_{slip}hw-\frac{\Delta P w h^3}{12\mu L}\left[1-\frac{h}{w}\left(\frac{192}{\pi^5}\sum_{n=1,3,5}^{\infty}\frac{1}{n^5}\tanh\left(\frac{n\pi w}{2h}\right)\right)\right] \qquad \textbf{(C.6)}$$

where u_{slip} is the electroosmotic velocity defined by,

$$u_{slip}=\mu_{eof}E_x \qquad \textbf{(C.7)}$$

where μ_{eof} is the electroosmotic mobility of the fluid, E_x is the electric field along the channel, h is the channel height, w is the channel width ($w > h$), μ is the fluid viscosity, and ΔP is the pressure drop along the length of the channel. Assuming uniform density, conservation at junction 1 gives,

$$Q_1+Q_2+Q_3=Q_4 \qquad \textbf{(C.8)}$$

where Q_1 , Q_2 , Q_3 , and Q_4 are the flow rates in channels 1, 2, 3, and 4, respectively. Substituting Equation C.6 into Equation C.8 gives,

$$\begin{aligned}
&u_{slip1}h_1w_1 - \frac{(P_{J1}-P_1)w_1{h_1}^3}{12\mu L_1}\left[1-\frac{h_1}{w_1}\left(\frac{192}{\pi^5}\sum_{n=1,3,5}^{\infty}\frac{1}{n^5}\tanh\left(\frac{n\pi w_1}{2h_1}\right)\right)\right] \\
&+u_{slip2}h_2w_2 - \frac{(P_{J1}-P_2)w_2{h_2}^3}{12\mu L_2}\left[1-\frac{h_2}{w_2}\left(\frac{192}{\pi^5}\sum_{n=1,3,5}^{\infty}\frac{1}{n^5}\tanh\left(\frac{n\pi w_2}{2h_2}\right)\right)\right] \\
&+u_{slip3}h_3w_3 - \frac{(P_{J1}-P_3)w_3{h_3}^3}{12\mu L_3}\left[1-\frac{h_3}{w_3}\left(\frac{192}{\pi^5}\sum_{n=1,3,5}^{\infty}\frac{1}{n^5}\tanh\left(\frac{n\pi w_3}{2h_3}\right)\right)\right] \\
&=u_{slip4}h_4w_4 - \frac{(P_{J2}-P_{J1})w_4{h_4}^3}{12\mu L_4}\left[1-\frac{h_4}{w_4}\left(\frac{192}{\pi^5}\sum_{n=1,3,5}^{\infty}\frac{1}{n^5}\tanh\left(\frac{n\pi w_4}{2h_4}\right)\right)\right]
\end{aligned} \qquad \textbf{(C.9)}$$

where u_{slip1}, u_{slip2}, u_{slip3}, and u_{slip4} are the electroosmotic velocities in channels 1, 2, 3, and 4, respectively, h_1, h_2, h_3, and h_4 are the heights of channels 1, 2, 3, and 4, respectively, P_1, P_2, P_3, P_{J1}, and P_{J2} are the pressures at reservoir 1, reservoir 2, reservoir 3, junction 1, and junction 2, respectively, and w_1, w_2, w_3, and w_4 are the widths of channels 1, 2, 3, and 4, respectively. Continuity applied at junction 2 provides the following equation:

$$\begin{aligned}
&u_{slip4}h_4w_4 - \frac{(P_{J2}-P_{J1})w_4{h_4}^3}{12\mu L_4}\left[1-\frac{h_4}{w_4}\left(\frac{192}{\pi^5}\sum_{n=1,3,5}^{\infty}\frac{1}{n^5}\tanh\left(\frac{n\pi w_4}{2h_4}\right)\right)\right] \\
&=u_{slip5}h_5w_5 - \frac{(P_4-P_{J2})w_5{h_5}^3}{12\mu L_5}\left[1-\frac{h_5}{w_5}\left(\frac{192}{\pi^5}\sum_{n=1,3,5}^{\infty}\frac{1}{n^5}\tanh\left(\frac{n\pi w_5}{2h_5}\right)\right)\right] \\
&+u_{slip6}h_6w_6 - \frac{(P_5-P_{J2})w_6{h_6}^3}{12\mu L_6}\left[1-\frac{h_6}{w_6}\left(\frac{192}{\pi^5}\sum_{n=1,3,5}^{\infty}\frac{1}{n^5}\tanh\left(\frac{n\pi w_6}{2h_6}\right)\right)\right]
\end{aligned} \qquad \textbf{(C.10)}$$

where u_{slip4}, u_{slip5}, and u_{slip6} are the electroosmotic velocities in channels 4, 5, and 6, respectively, h_4, h_5, and h_6 are the heights of channels 4, 5, and 6, respectively, P_4 and P_5 are the pressures at reservoirs 4 and 5, respectively, and w_4, w_5, and w_6 are the widths of channels 4, 5, and 6, respectively. Equations C.9 and C.10 form a system of equations that was solved for the

pressures at the junctions, similar to the potential field. The known pressure field allows the linear flow rates in each channel to be calculated.

Appendix D

Experimental Operating Conditions

The potential distributions applied for cell sorting were guided by numerical simulations, but were ultimately selected based on experimental results. The typical voltage combinations for the chips used experimentally and numerically are as follow:

Design E-1b

Exp: $[\phi_S = 500, \phi_{F1} = \phi_{F2} = 650, \phi_{D1} = 225, \phi_{D2} = 400, \phi_{C1} = 0, \phi_{C2} = 300]$ V

Design E-2b

Exp: $[\phi_S = 500, \phi_{F1} = \phi_{F2} = 625, \phi_{D1} = 250, \phi_{D2} = 450, \phi_{C1} = 0, \phi_{C2} = 300]$ V

Num: $[\phi_S = 400, \phi_{F1} = \phi_{F2} = 525, \phi_{D1} = 350, \phi_{D2} = 450, \phi_{C1} = 0, \phi_{C2} = 300]$ V

Design F-1

Exp: i. $[\phi_S = 500, \phi_{F1} = \phi_{F2} = 625, \phi_{D1} = 275, \phi_{D2} = 450, \phi_{C1} = 0, \phi_{C2} = 300]$ V

ii. $[\phi_S = 400, \phi_{F1} = \phi_{F2} = 525, \phi_{D1} = 225, \phi_{D2} = 400, \phi_{C1} = 0, \phi_{C2} = 250]$ V

iii. Focusing values were increased to increase particle velocity:

$[\phi_S = 700, \phi_{F1} = \phi_{F2} = 800]$ V

$[\phi_S = 1000, \phi_{F1} = \phi_{F2} = 1150]$ V

Num: $[\phi_S = 400, \phi_{F1} = \phi_{F2} = 525, \phi_{D1} = 350, \phi_{D2} = 450, \phi_{C1} = 0, \phi_{C2} = 300]$ V

Design F-2

Exp: i. $[\phi_S = 500, \phi_{F1} = \phi_{F2} = 625, \phi_{C1} = 0, \phi_{C2} = 325]$ V

ii. $[\phi_S = 400, \phi_{F1} = \phi_{F2} = 525, \phi_{C1} = 0, \phi_{C2} = 250]$ V

Num: $[\phi_S = 400, \phi_{F1} = \phi_{F2} = 525, \phi_{C1} = 0, \phi_{C2} = 300]$ V

Design F-3

Exp: $[\phi_S = 500, \phi_{F1} = \phi_{F2} = 600, \phi_{D1} = 300, \phi_{D2} = 450, \phi_{C1} = 0, \phi_{C2} = 325]$ V

Num: $[\phi_S = 400, \phi_{F1} = \phi_{F2} = 525, \phi_{D1} = 350, \phi_{D2} = 450, \phi_{C1} = 0, \phi_{C2} = 300]$ V

Design F-4

Exp: [ϕ_S = 500, ϕ_{F1} = ϕ_{F2} = 650, ϕ_{D1} = 300, ϕ_{D2} = 500, ϕ_{C1} = 0, ϕ_{C2} = 225] V

Num: [ϕ_S = 400, ϕ_{F1} = ϕ_{F2} = 525, ϕ_{D1} = 350, ϕ_{D2} = 450, ϕ_{C1} = 0, ϕ_{C2} = 300] V

The experimental switching durations tested for these conditions are as follows:

Design E-1a

T = 250 ms

Design E-2b

T = 300 ms, 400 ms, and 500 ms

Design F-1

i. and ii. T = 200-500 ms

iii. T = 50 ms and 100 ms were attempted at higher velocities, but cell distinguishing at these velocities was too difficult.

Design F-2

i. and ii. T = 200-500 ms

Design F-3

[T_D = 300 ms directing pulse after 0 ms delay & T_S = 300 ms sorting pulse after 300 ms delay]

[T_D = 300 ms directing pulse after 0 ms delay & T_S = 200 ms sorting pulse after 300 ms delay]

[T_D = 300 ms directing pulse after 0 ms delay & T_S = 200 ms sorting pulse after 200 ms delay]

[T_D = 300 ms directing pulse after 0 ms delay & T_S = 100 ms sorting pulse after 100 ms delay]

[T_D = 200 ms directing pulse after 0 ms delay & T_S = 100 ms sorting pulse after 400 ms delay]

Design F-4

[T_D = 300 ms directing pulse after 0 ms delay & T_S = 300 ms sorting pulse after 200 ms delay]

T = 200 ms, 300 ms, 400 ms, and 500 ms